Master Thesis in Petroleum Technology – Reservoir Chemistry

Simulation Study of Polymer Injectivity and Rheology in Radial Models

Lars Christian Kjær

Department of Chemistry

uniCIPR

Centre for Integrated Petroleum Research

University of Bergen

June 2017

Acknowledgments

First and foremost, I would like to express my gratitude towards my supervisor, Professor Arne Skauge, for his excellent guidance, great support and helpful discussions during the work on this thesis.

Further, I would also like to thank Iselin Salmo and Nematollah Zamani who could always be counted on to offer support and instructions with the thesis.

I would also like to thank Centre for Integrated Petroleum Research at the University of Bergen (Uni CIPR) for providing me with an office space and essential equipment during my time as a master's student.

Furthermore, I would like to express my gratitude towards fellow master's students and friends, Jørgen Gausdal Jacobsen and Tonje Nielsen, for the countless discussions, both on and off topic, and hours spent together throughout our Master's degree.

Finally, I would like to thank my family and friends for their motivation and encouragement during my years as a student. The support has been greatly appreciated. Special recognition goes to Katy Elizabeth Rengel for her outstanding patience, support and motivation.

Lars Christian Kjær

Bergen, June 2017

Abstract

The simulation study conducted in this thesis was carried out at the Centre for Integrated Petroleum Research (Uni CIPR) at the University of Bergen (UiB). The main objective in this thesis was to study polymer rheology and injectivity in a radial Bentheimer disk by history matching experimental polymer flooding data. As radial models emulate the flow field encountered in field applications, characterised by a successive flow velocity reduction, studying the rheological behaviour of polymers in radial disks is an important field of study for planning of future field scale polymer flooding operations.

The rheological behaviour of two polymers were studied; the synthetic polymer HPAM and the biopolymer xanthan. The polymers displayed rheological behaviour earlier reported in the literature characteristic to the molecular conformation of the polymers.

Results from the history matches of HPAM pressure data revealed a dominating shear thickening behaviour at high velocities in the near-well vicinity. Newtonian and slight shear thinning was also observed for lower injection rates. HPAMs rheological behaviour was found to be dependent on the deformational history experienced during the flooding sequence, showing different rheological behaviour in the radial model at different injection rates.

History matching pressure data collected during xanthan flooding sequences showed a rheological behaviour dominated by shear thinning behaviour at high and intermediate velocities. Further, at lower injection rates a lower Newtonian plateau was attained at low velocities away from the injection well. This lower Newtonian plateau commonly encountered in bulk rheological measurements has been reported to be difficult to attain in linear core experiments. The results observed in this thesis therefore indicate that radial disk experiments may be an improved geometry for studying xanthan rheology which may aid in planning future xanthan flooding applications.

Comparison of the polymers injectivity further revealed improved injectivity characteristics of the shear thinning xanthan polymer owing to a reduced pressure drop occurring in the near-well vicinity. As expected, injectivity characteristics heavily depended on the rheological behaviour of the polymers.

In this simulation study two reservoir simulation tools were utilized; STARS by CMG and MRST with an Ensemble Kalman Filter module extension. By using these simulation tools Bentheimer disks were modelled and polymer flooding sequences simulated. By history

matching pressure data both manually using STARS and automatically using the MRST simulator, increased confidence was reached from the simulation results as agreement was obtained between the simulated results.

Nomenclature

Variables

A	Cross-sectional area	$[m^2]$
A	Area	$[m^2]$
dp/dx	Pressure drop over distance x	$[Pa \cdot m^{-1}]$
dv/dr	Velocity gradient	$[s^{-1}]$
E_A	Areal sweep efficiency	dimensionless
E_D	Microscopic displacement efficiency	dimensionless
E_R	Overall recovery efficiency	dimensionless
E_V	Vertical sweep efficiency	dimensionless
E_{vol}	Volumetric sweep efficiency	dimensionless
F	Force	$[kg \cdot m \cdot s^{-2}]$
h	Height	[m]
I	Injectivity	$[m^3 \cdot Pa^{-1} s^{-1}]$
K	Absolute permeability	$[m^2]$ (1-D = $0.98692 \cdot 10^{-12}$ m^2]
k_e	Effective permeability	[D]
k_r	Relative permeability	dimensionless
L	Length	[m]
M	Mobility ratio	dimensionless
m	Mass	[kg]
n	Power law index	dimensionless
n_2	empirical constant	dimensionless
N_{De}	Deborah number	dimensionless
p	Pressure	[Pa]
Q	Volumetric flow rate	$[m^3 \cdot s^{-1}]$
r	Radius	[m]
RF	Resistance factor	dimensionless
RRF	Residual resistance factor	dimensionless
S	Saturation	dimensionless
S	Skin factor	dimensionless

v	Velocity	[$m \cdot s^{-1}$]
v	Darcy velocity	[$m \cdot s^{-1}$]
α	Correction factor	Dimensionless (assumed=2)
μ	Viscosity	[Pa·s] (1Pa·s=10^3cP)
τ	Shear stress	[Pa]
τ_E	porous media characteristic time	[s]
τ_R	relaxation time	[s]
φ	Porosity	dimensionless
λ	empirical time constant	[s]
λ	Mobility	[$m^2 \cdot Pa^{-1} \cdot s^{-1}$]
π	Pi	dimensionless
x	Mole fraction	dimensionless
$\dot{\gamma}$	Shear rate	[s^{-1}]

Subscripts

abs	absolute
b	bulk
e	boundary
e	effective
eff	effective
i	component (phase)
ineff	ineffective
iw	irreducible water
max	Maximum shear thickening
o	oil
or	irreducible oil
p	pore
p	polymer
r	relative

R	Permeability region
skin	skin zone
tot	total
vol	volumetric
w	water
w	well
0	zero shear rate
∞	infinite shear rate

Abbreviations

CIPR	Centre for Integrated Petroleum Research
CMG	Computer modelling group
EnKF	Ensemble Kalman filter
EOR	Enhanced oil recovery
HPAM	Hydrolysed polyacrylamide
IOR	Improved oil recovery
IPV	Inaccessible pore volume
MATLAB	Matrix laboratory
MRST	Matlab Reservoir Simulation Toolbox
MWD	Molecular weight distribution
NSC	Norwegian continental shelf
PAM	Polyacrylamide
PDI	Probability distribution
ppm	Parts per million
RF	Resistance factor
RRF	Residual resistance factor
STARS	Steam, Thermal and Advanced Process Reservoir Simulator
UiB	University of Bergen

STARS Keywords

ADMAXT	Maximum adsorption capacity rock	[gmol· cm^{-3}]
ADRT	Residual adsorption level	[gmol· cm^{-3}]
ADSCOMP	Component adsorption function apply	dimensionless
ADSTABLE	Tabular adsorption input	[gmol· cm^{-3}]
AVISC	Liquid viscosities	[cP]
CMM	Component molecular mass	[kg/mol
PORFT	Accessible pore volume	dimensionless
RPT	Rock type number	dimensionless
RRFT	Residual resistance factor	dimensionless
SHEARTAB	Polymer viscosity Darcy velocity effect table	[cm/min]/[cP]
VSMIXCOMP	Viscosity nonlinear mixing rule	Dimensionless
VSMIXENDP	Minimum and maximum mole fraction of component specified in VSMIXCOMP	Dimensionless

Table of Contents

List of Figures

List of Tables

1 Introduction

The demand for energy is increasing worldwide, with population growth and rise in living standards in emerging economies such as China and India acting as drivers. Globally, oil accounts for 32.9% of total energy consumption and showed an increasing demand in 2016. [1] However, discovery of new oil fields cannot be guaranteed, and as any such discoveries are likely located in challenging production areas, the ability to increase oil recovery from existing fields is necessary to handle increasing global energy demand. [2]

On the Norwegian continental shelf (NCS) production of oil is conventionally supported by injection of water which displaces oil towards producing wells and maintains reservoir pressure. Though practical and economically viable due to its ease of accessibility and abundance in most production environments, water tends to travel through high permeable conduits in the reservoir bypassing regions of oil residing at lower permeable areas. [3]

On average 46% of oil is therefore recovered from NCS reservoirs, and globally this figure drops to only 35% on average.[4, 5] When reservoirs contain heavy oil, limitations on oil recovery experienced during waterflooding processes are exacerbated as a result of unfavourable mobility ratios. In such instances recovery from heavy oil fields is often as low as between 10% to 20%. [6] Alain Labastie, former president of Society of Petroleum Engineers stated that “Increasing the average ultimate recovery factor from 35% to 45% would bring about 1 trillion barrels of oil”. [7].

Therefore, there is a significant economic incentive and potential for increasing oil recovery from existing fields over what is accomplished through conventional recovery methods.

Polymers are repetitive chains of high-molecular weight macromolecules used to viscosify injection water. This improves reservoir sweep and increases the amount of areas contacted in the reservoir while accelerating oil production. The increase in polymer solution viscosity further improves production in heavy oil reservoirs as a result of improved mobility ratios over that experienced during waterflooding processes. [3] The application of polymer flooding in the field has shown promising results in countries including China, Angola, Oman and Turkey. Wang et al (2002) [8] reported that since implementing polymer flooding EOR in 1998 the Daqing field in China had increased its incremental recovery by 12% ~ 15%.

The most commonly used polymers for EOR applications are the synthetic polymer polyacrylamide in its partially hydrolysed form (HPAM) and the biopolymer xanthan. Both

polymers display non-Newtonian behaviour when exposed to increased velocities. However, due to differences in molecular structure their non-Newtonian behaviour in porous media differs significantly. Whereas xanthan display a shear thinning behaviour where viscosity decreases with increasing velocities, HPAM is a viscoelastic polymer displaying shear thickening behaviour when exposed to high velocities in porous media. [9]

Because of the viscous nature of the polymer solutions, increased pressures occur during injection compared to that of pure water limiting the rate at which the solutions may be injected. This in turn results in slower propagation in the reservoir and later arrival of produced oil, and is factors which may erode the economic value of the EOR process. Increased injection pressures may also induce fracture growth in the near well region and can in worst case result in loss of injection wells if not accounted for. [10] Thus, due to complications arising during polymer flooding processes in the field, polymer injectivity has gained significant attention from the industry.

1.1 Scope of Study

In this thesis, polymer rheology in radial flow geometry has been investigated for a synthetic polymer and a biopolymer through simulations based on experimental flooding data. Further, a comparison of how the respective polymer rheology affect the injectivity in the models has been undertaken. Due to the radial geometry used in this study both the rheology and injectivity are studied in a flow regime commonly encountered in the field where flow velocities successively decrease with increasing radial distance from injection point. This flow condition differs from most studies which are conducted in linear cores characterized by steady-state conditions.

The experimental data provided forming the basis for the work conducted in this thesis, comprise of pressure recordings which were collected during flooding sequences of the polymers in separate Bentheimer disks. Through simulations of the polymer flooding sequences and history matching provided pressure data, the polymers rheological behaviour has been studied using two separate simulation tools.

This thesis consists of 9 chapters. Chapter 2 presents necessary theory and concepts forming the basis for the simulation study conducted. Chapter 3 give a short review of the experimental data subsequent simulations are modelled on. Chapter 4 presents the simulation tools used throughout the study, and Chapter 5 includes a verification and sensitivity study

carried out on parameters which may influence the water and polymer flooding simulations. Chapter 6 will present the results and discussions on the simulation results, while Chapter 7 gives a conclusion to the undertaken study. Chapter 8 will give advice for further study on polymer flooding in radial geometries.

2 Theory

This chapter reviews the main theory and concepts of relevance for the simulation study conducted in this thesis.

2.1 Petrophysical Properties

The main petrophysical properties of interest for flooding applications relates to a rocks porosity and permeability, which are measures of a rocks ability to store fluids and transmit these through its interconnected network of pores respectively. The absolute permeability of a rock is for simplicity referred to as permeability throughout this thesis.

2.1.1. Porosity

The porosity of a porous medium is a measure of the void space within a rock matrix available for fluids to occupy. [11] Porosity can be divided into two types; effective and ineffective porosity. Effective porosity constitutes interconnected pores available for fluid flow, whereas ineffective porosity refers to pores with no interconnections remaining closed off for fluids. [12] Absolute porosity constitutes the sum of effective and ineffective porosity;

$$\varphi_{abs} = \varphi_{eff} + \varphi_{ineff} = \frac{V_{p,abs}}{V_b} \tag{2.1}$$

Where φ_{abs} is absolute porosity, φ_{eff} is effective porosity, φ_{ineff} is ineffective porosity, $V_{p,abs}$ is total void space and V_b is rock bulk volume. [13]

Ineffective porosity will not influence fluid flow and can be neglected when considering flooding applications, consequently reducing equation (2.1) to;

$$\varphi_{eff} = \frac{V_{p,eff}}{V_b} \tag{2.2}$$

Where $V_{p,eff}$ is the total volume of interconnected pores. Effective porosity depends on factors such as rock type, grain size, grain packaging and orientation. [13]

Porosity is usually reported as a percentage, but the fraction is always used for calculations. Most naturally occurring porous mediums have porosity values ranging from 10% to 40%, although values outside of this range occur.[12]

2.1.2. Permeability

The permeability of a porous medium is a measure of the mediums capability to transmit fluids through its network of interconnected pores by the application of a pressure gradient. [14] Permeability can be defined through Darcy's law;

$$Q = -\frac{K \cdot A}{\mu}\frac{dp}{dx} \tag{2.3}$$

Where Q is the volumetric flow rate, K is the permeability, A is the cross-sectional area, μ is the fluid viscosity and $\mathrm{dp/dx}$ is the pressure gradient over the porous medium. The minus sign accounts for flow in direction of decreasing pressure. [13] Equation (2.3) is valid for a horizontal, laminar, incompressible, Newtonian single-phase flow in which no chemical interaction occurs between fluid and surrounding rock matrix.

The permeability can be regarded as a constant property of the porous medium during single fluid flow and depends on physical properties such as ratio between pore throats and pore volumes, pore size distribution and medium tortuosity. [13] Permeability is commonly given in Darcy units which is equivalent to;

$$1\ \text{Darcy} = \frac{1\text{cm}^3/\text{s} \cdot 10^{-3}\text{Pa·s}}{1\text{cm}^2 \cdot 1.01325 \cdot 10^5\text{Pa/cm}} = 0.98692 \cdot 10^{-8}\text{cm}^2$$

The study conducted in this thesis deals with single-phase flooding in radial geometry where flow is radially away from a cylindrical well driven by a bottomhole pressure towards a circumferential outlet boundary as illustrated in Figure 2.1**.**

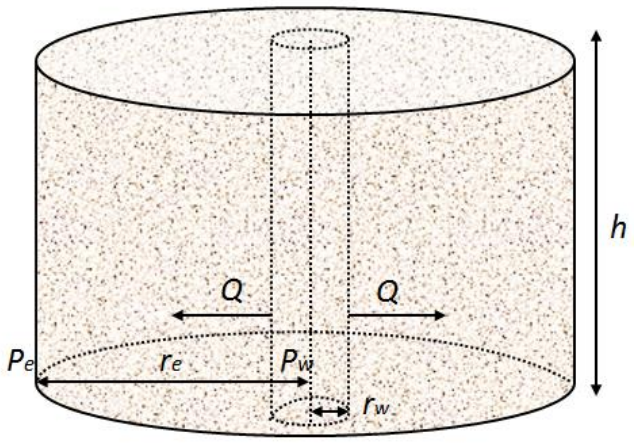

Figure 2.1 Radial flow away from central well in a cylinder shaped model (modified from Lien (2014) [14])

Darcy's law for radial flow is given by;

$$Q = \frac{2 \cdot h \cdot \pi \cdot K}{\mu} \frac{p_w - p_e}{ln\left(\frac{r_w}{r_e}\right)} \tag{2.4}$$

Where p_w is the bottomhole pressure at wellbore radius r_w and p_e is the external boundary pressure at boundary radius r_e. Equation (2.4) is derived in appendix B.1 and is valid in radial flow geometries in which an incompressible Newtonian fluid propagates from a centre well towards a circumferential outlet boundary. [15]

As mentioned, this study deals with single-phase flooding in radial geometry and the permeability definitions above is sufficient for describing this process. However, due to definitions and discussions arising later in this text the effective permeability and relative permeability is also defined in this section. These permeability notions relate to flow of several fluids simultaneously in porous rocks.

When two or more fluids are present in the porous medium, the fluids hinder each other's free flow and consequently reduce the permeability available for each fluid. Thus, an effective permeability, $k_{e,i}$, can be defined for each fluid in the multiphase flow as;

$$Q_i = \frac{k_{e,i} \cdot A}{\mu_i} \cdot \frac{dp}{dx} \tag{2.5}$$

The effective permeability is strongly dependent on the relative saturations of the fluids present in the porous medium. [13]

Relative permeability, $k_{r,i}$, is defined as the ratio of the effective permeability for a given fluid to the permeability of the medium;

$$k_{r,i} = \frac{k_{e,i}}{K} \tag{2.6}$$

Relative permeability is a dimensionless property which is a function of the rock properties, fluid saturations and the wetting characteristics of the formation. [14]

2.2 Fluid Properties and Fluid Dynamics

2.2.1. Fluid Rheology

Molecules of flowing fluids are subject to frictional interactions, between molecules of the fluid and between adjacent surroundings, consequently acting as forces resisting fluid movement. [13] Viscosity is a measure of this internal resistance, and can be defined through Newton's law for viscosity when considering a fluid in steady shear flow as illustrated in figure 2.2.

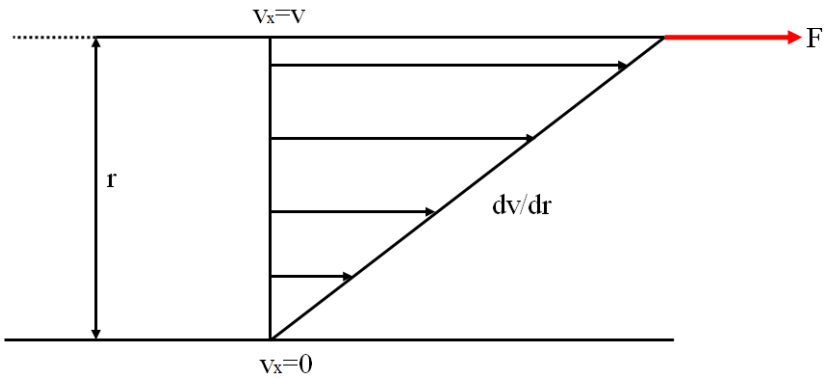

Figure 2.2 Simple shear flow schematic (modified from Walters and Jones(2010)[16])

In figure 2.2, a fluid at rest consisting of individual fluid layers is confined between two parallel horizontal plates of area A separated by a distance r. If a horizontal force, F, is applied to the top plate it is set in motion attaining a velocity, v, whereas the lower plate remains stationary. The fluid between the plates is sheared and a velocity gradient, dv/dr, develops between the fluid layers. The fluid layer adjacent to the top plate attains velocity v whereas the bottom fluid layer, adjacent to the lower plate, remains stationary. The force applied per area A is known as the shear stress, τ, and is proportional to the velocity gradient dv/dr. The velocity gradient is also known as the shear rate denoted $\dot{\gamma}$ [17];

$$\tau \propto \dot{\gamma} \tag{2.7}$$

The constant of proportionality between applied shear stress and resulting shear rate is the viscosity, μ, which expresses the fluids resistance to this shearing force. Newton's law of viscosity is defined as;

$$\tau = \frac{F}{A} = \mu\dot{\gamma} = \mu\frac{dv}{dr} \tag{2.8}$$

Where τ is shear stress, F is applied force in horizontal direction, A is plate area, μ is the fluid viscosity, $\dot{\gamma}$ is the shear rate and dv/dr is the velocity gradient.

Rheology is the study of fluid flow behaviour when subjected to deformational forces, for instance shear, and fluids exhibiting a direct proportionality between viscosity and shear rate (i.e., μ independent of shear rate) in equation (2.8) are known as Newtonian fluids. Newtonian fluids therefore display a constant viscosity when subjected to increasing shear rates. [13, 17]

Fluids not following a linear relationship between viscosity and shear rate are called non-Newtonian, and for these fluids the viscosity varies when subjected to increasing deformational forces, as illustrated in figure 2.3. For non-Newtonian fluids equation (2.8) may therefore be rewritten as;

$$\tau = \mu(\dot{\gamma})\dot{\gamma} \tag{2.9}$$

Where the viscosity is now a function of applied shear rate. [3]

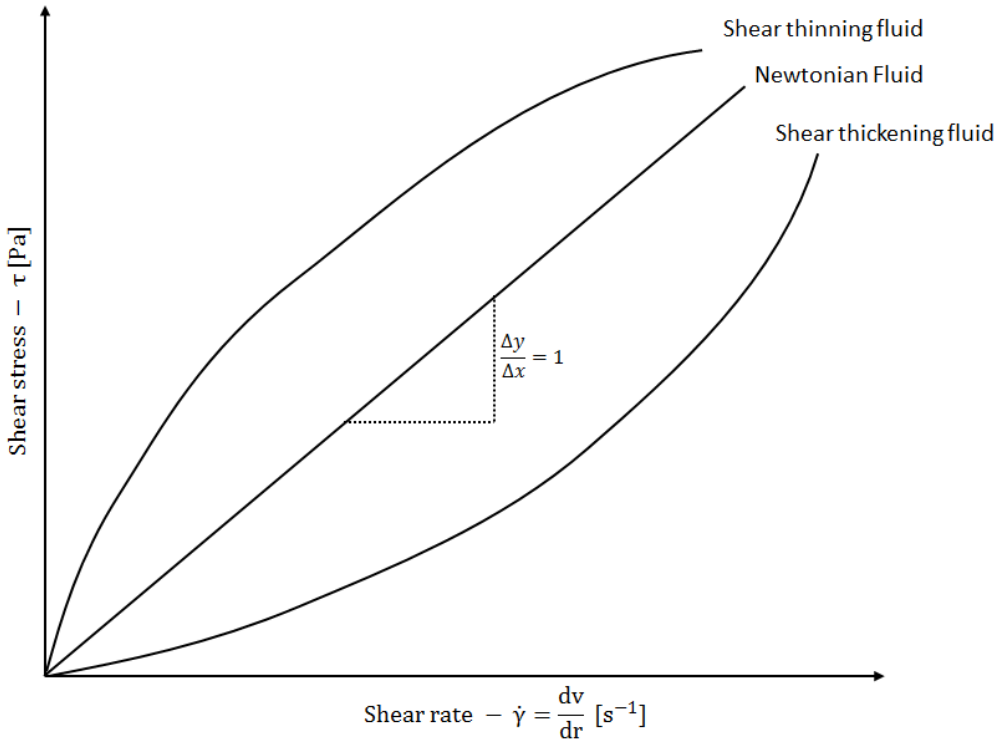

Figure 2.3 Relationship between shear rate and viscosity for different fluid classes (modified from Sorbie (1991) [3])

In figure 2.3 Newtonian fluids display a constant slope at increasing shear rates and viscosity is therefore independent of applied shear rate. Two types of non-Newtonian behaviour are illustrated in figure 2.3; shear thickening and shear thinning behaviour. Shear thickening

fluids display an increasing slope with increasing shear rate corresponding to an increasing viscosity with increasing deformational forces. Shear thinning fluids, on the other hand, display a decreasing slope with increasing shear rate corresponding to a decreasing viscosity with increasing shear rate. Polymer solutions, discussed in later sections, virtually always display shear thinning behaviour in simple shear flow as illustrated in Figure 2.2. [3]

Following from equation (2.9), the SI-unit for viscosity is $N \cdot s/m^2$, but by convention viscosity is usually given in centipoises (cP) where $1cP = 10^{-3}\ N \cdot s/m^2 = 1mPa \cdot s$.

2.2.2. Fluid Mobility

Fluid mobility is a measure of the ease at which a fluid flow through interconnected pores at a given saturation in the presence of other fluids. The mobility for any fluids is defined as the ratio of effective permeability to the viscosity for a given fluid denoted by i [18];

$$\lambda_i = \frac{k_{e,i}}{\mu_i} = \frac{K \cdot k_{r,i}}{\mu_i} \tag{2.10}$$

Where λ_i is mobility, $k_{e,i}$ is effective permeability, $k_{r,i}$ is relative permeability and μ_i is the viscosity of phase i. K is the permeability of the porous medium.

Following from equation (2.10), the viscosity term in the denominator indicate that fluids of lower viscosity, for instance water, have a high mobility in porous medium whereas more viscous fluids, like oil, have lower mobility and therefore experience higher flow resistance at given saturation.

2.2.3. Mobility Ratio

The mobility ratio, M, is defined as the mobility of a displacing fluid to the mobility of a displaced fluid, and for water displacing oil during a waterflooding sequence it is defined as [18];

$$M = \frac{\lambda_w}{\lambda_o} = \frac{k_{e,w} \cdot \mu_o}{k_{e,o} \cdot \mu_w} \tag{2.11}$$

Mobility ratio is an important parameter for displacement processes, affecting areal and vertical sweep efficiency, discussed in later sections, and the stability of the displacement process. [19]

The impact of the mobility ratio on a displacement process of oil by water is shown schematically in figure 2.4. In figure 2.4, the curves illustrate the displacement front as a function of different residence times, denoted by t, whereas S_{or} and S_{iw} denote irreducible oil and water saturation respectively. The injection and production terms denote well names, in which water is injected through the injection well and fluids are produced at the production well.

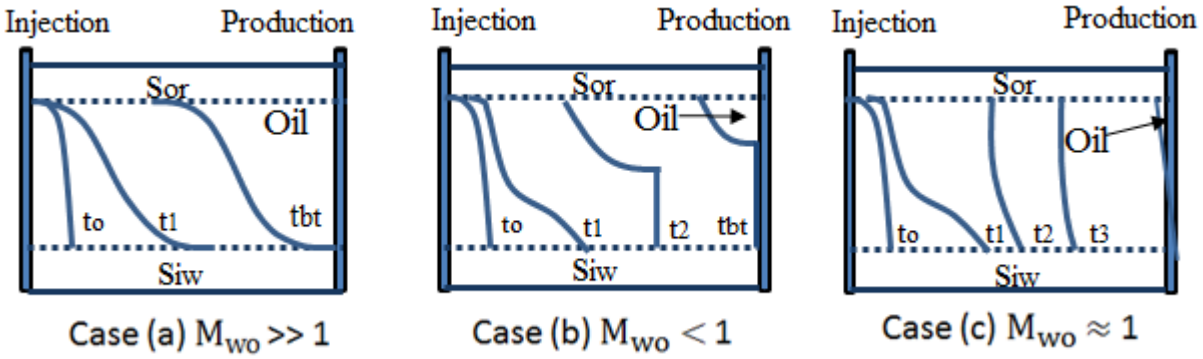

Figure 2.4 Illustration of mobility ratio impact during waterflooding of oil (modified from Lien (2010) [20])

Case (a) in figure 2.4 illustrates an unfavourable mobility ratio scenario. As the mobility ratio is much larger than unity the displacing water moves quicker through the reservoir than the less mobile oil. At breakthrough of water at the producing well, at time t_{bt}, large quantities of oil remain within the reservoir corresponding to the area over the last curve.

Case (b) in figure 2.4 illustrates an opposite scenario where the mobility ratio is less than unity. The water is less mobile than the displaced oil promoting a piston-shaped displacement which results in less oil remaining in the reservoir at water breakthrough at the producing well. The recovery of oil is therefore significantly improved over the recovery illustrated for Case (a).

Case (c) illustrates an ideal mobility ratio at unity in which displacing water and displaced oil flows through the porous medium at comparable mobility's. The water drives the oil in front of it and only residual oil remains within the reservoir at breakthrough. [20]

Therefore, stable displacement processes occur in the reservoir when the mobility ratio is close to or less than unity. Higher mobility ratios, however, promote early water breakthrough at producing wells and a long tail production of oil. [11]

2.2.4. Fluid Flow Regimes and Flow Equations in Porous Media

For a fluid to flow in a porous media a pressure gradient must exist over the medium. Three types of flow regimes can be identified describing both the flow behaviour and the pressure distribution in the reservoir as a function of time and position; transient flow, semi-steady flow and steady-state flow. [21]

The pressure regimes existing in a reservoir can be described by considering a cylindrical reservoir with a central well, as illustrated in figure 2.1. As fluids are injected in the well, a pressure disturbance is created in the reservoir, and the rate of change of pressure with respect to time at any position in the reservoir is a function of both the position, i, and the time, t, and may be expressed as [14];

$$\left(\frac{\partial p}{\partial t}\right)_i = f(i,t) \tag{2.12}$$

Equation (2.12) implies that the rate of change of pressure with respect to time at any position within the reservoir is not constant.

The pressure disturbance radius, radius at which disturbance have propagated, is continuously increasing with time. Until the pressure disturbance reaches the reservoir boundary, r_e, in Figure 2.1 the reservoir act as if it is infinite in size. Thus, the boundary has no effect on the pressure behaviour during this transient regime. [21]

As the pressure disturbance reaches the circumferential boundary two regimes may be identified depending on whether the pressure is supported, by water influx for instance, or not.

The semi-steady state flow regime is characterised by a linear pressure decline with time and occur when the reservoir pressure is not supported by external forces, thus, it may be expressed as;

$$\left(\frac{\partial p}{\partial t}\right)_i = constant \tag{2.13}$$

Equation (2.14) thus indicates that reservoir pressure is declining at a constant rate within the reservoir. The pressure at various locations in the reservoir declines as a function of time and remains constant at every point [21]

When the pressure at every location in the reservoir remains constant with time the flow is characterized by steady-state flow conditions;

$$\left(\frac{\partial p}{\partial t}\right)_i = 0 \tag{2.14}$$

Equation (2.14) states that the rate of change of pressures with respect to time at any location i is zero. [14] The various flow regimes are illustrated in figure 2.5.

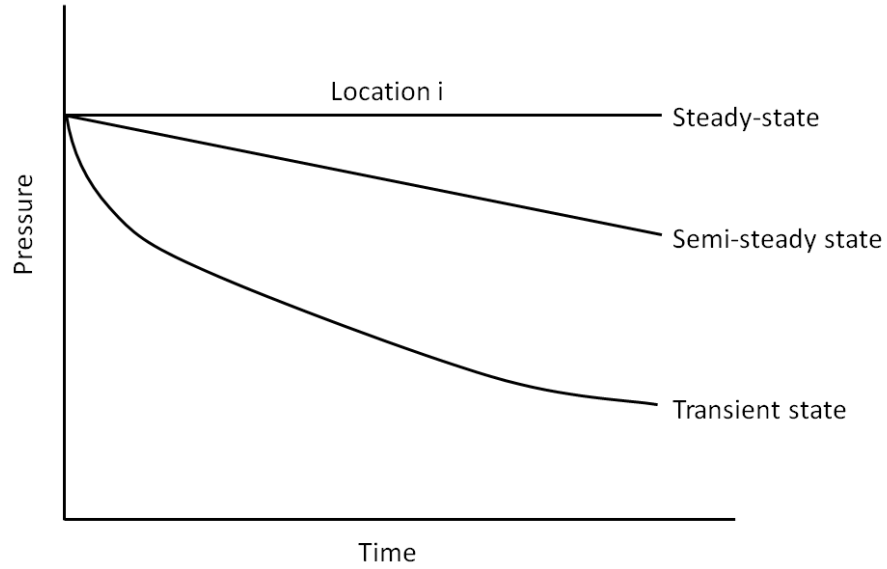

Figure2.2.5 Pressure decline at well in a circular reservoir at constant injection rate (Modified from Ahmed (2010) [21])

Following from equation (2.3), the velocity of a fluid in a porous medium is proportional to the pressure gradient and inversely proportional to the fluid viscosity. For a horizontal linear system, the relationship is expressed as;

$$v = \frac{Q}{A} = -\frac{K}{\mu}\frac{dp}{dx} \tag{2.15}$$

Where v is Darcy velocity, Q is volumetric flow rate, A is cross-sectional area, K is permeability, μ is fluid viscosity and dp/dx is the pressure gradient over the reservoir.

For a horizontal-radial system, equation (2.15) is expressed as;

$$v = \frac{Q_r}{A_r} = \frac{K}{\mu}\left(\frac{\partial p}{\partial t}\right)_r \tag{2.16}$$

Where Q_r is the volumetric flow rate at radius r, $A_r$is the cross-sectional area to flow at radius r, $(\partial p/\partial t)_r$ is the pressure gradient at radius r and v is the apparent velocity at radius r.[21]

2.3 Enhanced Oil Recovery

Enhanced oil recovery (EOR) is techniques applied to further increase oil recovery from a reservoir beyond what is achieved through conventional recovery methods. EOR techniques commonly involve injection of special fluids, such as chemicals, miscible gases and/or thermal energy into the reservoir. [2] A related definition is improved oil recovery (IOR), which encompasses EOR plus a broad range of other techniques including hydraulic fracturing, infill drilling and well stimulation. [11]

Recovery of oil from a producing reservoir can be divided into three distinct recovery phases; primary, secondary and tertiary, in which primary recovery and secondary recovery constitutes conventional recovery methods. [11]

During primary recovery, natural energy present in the reservoir is utilized to displace oil towards producing wells caused by the expansion of reservoir fluids as reservoir pressure decreases. Natural forces involved in the displacement are called reservoir drives and includes water drive, solution-gas drive and gas-cap drive. [22] The gradual decline of reservoir pressure results in decreasing oil recovery rates and low ultimate recovery when the natural energy tapers off. Secondary recovery through injection of fluids, most commonly water, is used to maintain reservoir pressure and increase reservoir drive. Due to reservoir heterogeneities, unfavourable mobility ratios and well-siting issues large quantities of oil are still left unrecovered as secondary recovery reach its limit. Tertiary recovery is any technique applied after secondary recovery, and usually involves injection of special fluids. EOR is therefore commonly referred to as tertiary recovery, but is not restricted to a distinct phase of the producing life of a reservoir. [19] The aim when implementing EOR techniques is to increase volumetric sweep efficiency and enhance the microscopic sweep efficiency, defined below, to further increase oil recovery from reservoirs. [13]

The overall recovery efficiency, E_R, for any secondary or tertiary oil recovery method is defined as [21];

$$E_R = E_D \cdot E_{vol} = E_D \cdot (E_A \cdot E_V) \tag{2.17}$$

Where E_D is microscopic displacement efficiency, E_{vol} is volumetric displacement efficiency and E_A and E_V are areal and vertical sweep efficiency respectively.

The microscopic displacement efficiency is defined as;

$$E_D = \frac{Volume\ oil\ displaced}{Volume\ of\ oil\ contacted} \tag{2.18}$$

Following from equation (2.18), microscopic displacement efficiency is therefore a measure of the effectiveness displacing fluids contact the oil during flooding processes.

Volumetric displacement efficiency is defined as;

$$E_{vol} = \frac{Volume\ of\ oil\ contacted}{Volume\ of\ oil\ originally\ in\ place} \tag{2.19}$$

The volumetric displacement efficiency is a measure of the efficiency displacing fluids sweeps the reservoir volume, both areally and vertically, and E_{vol} is therefore usually decomposed into the product of areal and vertical sweep efficiency, as indicated by equation (2.17). Areal sweep efficiency principally depends on the mobility ratio between displacing and displaced fluid, whereas the vertical sweep efficiency is primarily dependent on permeability and heterogeneities within vertical zones. The parameters are also dependent on each other. [23]

2.3.1. Chemical EOR Polymer Flooding

Polymer flooding is a chemical EOR method in which long repetitive chains of high-molecular weight polymers are dissolved in water to viscosify injection water. Injection of a viscous polymer solution results in a reduced mobility ratio leading to improved areal and vertical sweep efficiency. Thus, limitations encountered in waterflooding applications due to unfavourable mobility ratios and early watercut at producing wells can be decreased during polymer flooding EOR. [19]

Increased oil displacement efficiency is achieved mainly through increased volumetric sweep by reducing the mobility ratio. As illustrated in figure 2.6 development of a more favourable mobility ratio results in increased areal displacement efficiency.

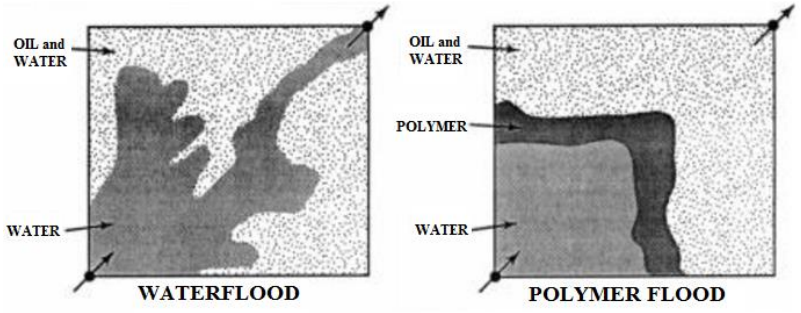

Figure 2.6 Improved areal sweep efficiency by polymer flooding (Green and Willhite (1998) [19])

In figure 2.6, due to the unfavourable mobility ratio (M>1) the more mobile water bypasses areas of oil, residing in lower permeable regions, promoting early water breakthrough and a long tail production of oil as the water finger through the oil zones. The polymer flooding process, on the other hand, occurs at more favourable mobility ratios ($M \leq 1$) due to the more viscous polymer solution. This suppresses the fingering effects and early water breakthrough caused by more mobile displacing fluids, resulting in increased areal sweep efficiency. [3] For this reason, polymer flooding applications are favourable in reservoirs consisting of highly viscous oil.

Reservoir heterogeneities are also of concern during oil recovery processes, where variations in permeability within reservoir rocks result in the injected fluids travelling through the most permeable channels. Thus, oil filled lower permeable areas are bypassed and early water breakthrough results. [18]

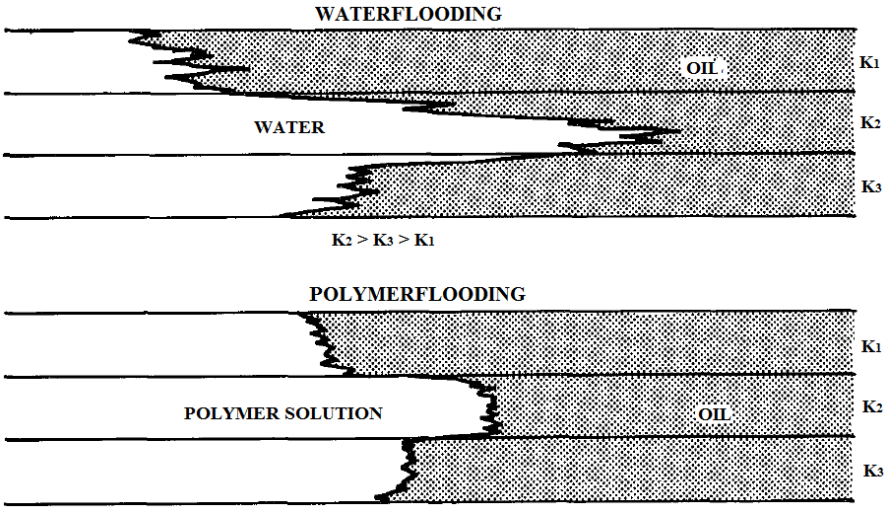

Figure 2.7 Waterflooding and polymer flooding processes in a vertically stratified reservoir with contrasting permeabilities (modified from Sorbie (1991) [3])

As seen in figure 2.7, water travels through the most permeable layers during the waterflooding process and less water flows through the lower permeable layers, resulting in

low vertical sweep efficiency. In contrast, the polymer solution flows in a much more uniform manner through the layers accomplished by a combination of two mechanisms; improved mobility control and adsorption on rock walls resulting in local permeability reduction. Both these mechanisms alter fluid flow patterns in the reservoir and lead to improved vertical sweep efficiency. [3]

2.4 Polymers for EOR

Two types of polymers are commonly employed for polymer flooding applications; synthetic polymers and biopolymers. Field applications have most frequently been carried out using the synthetic polymer HPAM due to its relatively low price and availability from other industries. Among the biopolymers xanthan has been most frequently used for EOR purposes. [13] The viscosifying ability of polymers is mainly a consequence of their high molecular weights. [10]

Research and literature have focused on characterisation of HPAM and xanthan properties owing to their extensive usage in EOR applications compared to other polymers. However, the generic behaviour of other synthetic polymers is qualitatively similar to that of HPAM, whereas other biopolymers have behaviour qualitatively similar to xanthan. [3]

2.4.1. Synthetic Polymers

Polyacrylamide (PAM) was the first polymer used to viscosify aqueous solutions for EOR applications, and may be manufactured through polymerization of acrylamide monomers producing macromolecules with average molecular weights ranging from 0.5 million Dalton to 30 million Dalton. [19] However, due to excessive adsorption and poor stability in the reservoir polyacrylamide is hydrolysed to produce the widely most used synthetic polymer HPAM.

HPAM is a synthetic straight chain polymer of partially hydrolysed acrylamide monomers as shown in figure 2.8. Figure 2.8 also include the primary structure of unhydrolysed polyacrylamide.

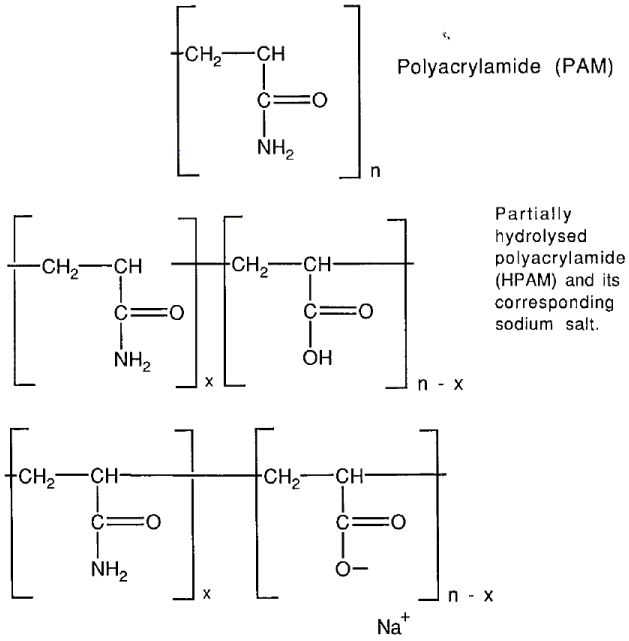

Figure 2.8 Primary structure of HPAM and PAM (Sorbie (1991) [3])

As seen in figure 2.8, hydrolysis introduces negative charges from carboxyl groups (COO^-) on the backbone in favour of positively charged amide groups (NH_2). This effectively reduces adsorption on anionic mineral surfaces within the reservoir rock. Normal hydrolysis degree for commercially available HPAM ranges from 15% to 35% and are selected to optimize properties like water solubility, viscosity and retention. [19] The molecular weight range for HPAM polymers utilized for EOR purposes are commonly in the range from $2 \cdot 10^6$ Dalton to $20 \cdot 10^6$ Dalton. [3]

The presence of electrostatic charges along the backbone causes stretching of the polymer in solution due to repulsion of the negative backbone causing the polymer chains to extend and result in a strong viscosifying power. [24] However, increasing solution salinity and hardness (in particular Mg^{2+} and Ca^{2+}) reduce the backbone repulsions due to shielding of the negative charges. This leads to a flexible coiled conformation of lower hydrodynamic size and viscosifying power as illustrated in Figure 2.9. [12]

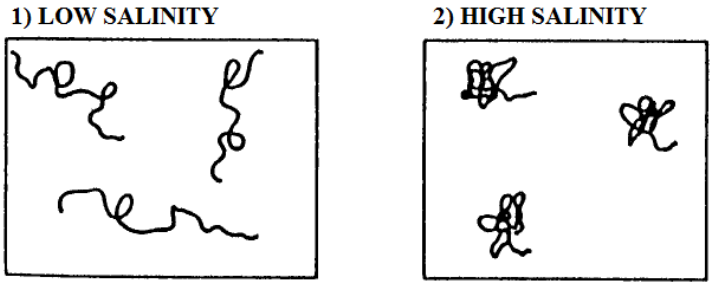

Figure 2.9 Effect of solution salinity on HPAM solution conformation (Modified from Sorbie (1991) [3])

2.4.2. Biopolymers

Among biopolymers, by far the most frequently used polymer for EOR applications is xanthan which was also used in the radial flooding experiment simulated in this thesis. Xanthan consists of a backbone chain of repeating glucose monomer units with a trisaccharide chain of mannose-glucuronic acid-mannose substituted onto every second glucose monomer, as illustrated in Figure 2.10. The mannose closest to the backbone contains an O-acetyl group, whereas the terminal mannose is pyruvaleted in a varying degree. [25]

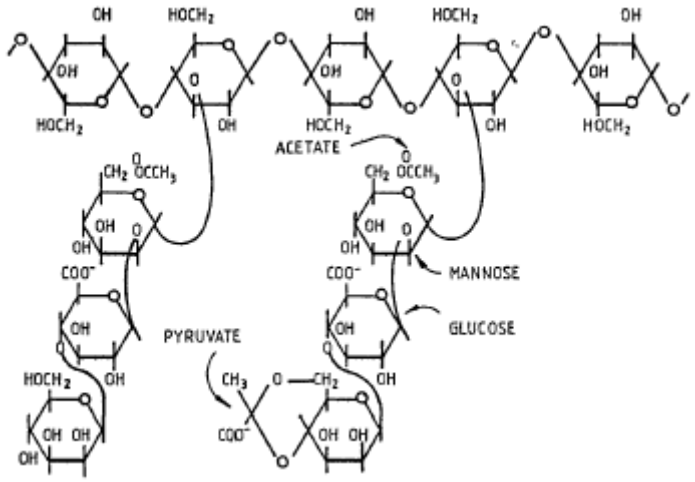

Figure 2.10 Xanthan primary molecular structure (Sorbie (1991) [3])

Xanthan does not display typical polyelectrolyte behaviour. In contrast to synthetic flexible coil polymers increasing solution salinity causes the xanthan polymer to undergo a conformational change from that of a flexible coil to a rigid rod. [24] In saline solutions of sufficient salinity and hardness, xanthan's molecular conformation is that of a rigid rod in which intertwining polymer molecule chains create a double-helical structure affording it rigidity. [12] Therefore, the polymers double-helical structure is retained in most injection and reservoir brines. [26, 27]

Average reported molecular weight for xanthan used in EOR processes ranges from 1 million Dalton to 15 million Dalton. [19]

2.5 Polymer Flow in Porous Media

Several factors influence polymer flow in porous mediums. As briefly mentioned in section 2.2.1, polymers are non-Newtonian and show a shear-rate dependent viscosity. However, the shear-rate dependency varies for different types of polymers owing to their respective molecular conformation in solution.

Rigid rod biopolymers like xanthan generally show shear-thinning behaviour during flow through porous media whereas the more flexible synthetic polymers like HPAM show a viscoelastic behaviour in which both shear-thickening and shear-thinning may occur. [9, 24, 28] The non-Newtonian behaviour and molecular conformation is important for the EOR flooding efficiency, but also influences factors such as polymer injectivity and polymer degradation.

Polymer flow in porous media is therefore complex and involves several mechanisms as it traverses the tortuous pore network of a porous media consisting of variation in both pores and pore throats. The following theory, however, will limit to concepts and mechanisms of importance for the simulation study conducted in this thesis.

2.5.1. In-situ Polymer Rheology

The main property of interest for polymer solutions for EOR applications are their solution viscosity in porous media. Polymer viscosity in porous media is referred to as their apparent viscosity, and much effort have been focused on describing and characterizing the porous media rheology, referred to as polymers in-situ rheology.

A common way of representing polymer rheology is in a plot of viscosity as a function of shear rate as shown in Figure 2.11. Figure 2.11 does not describe the rheological behaviour for all types of polymers, and only serves as a visual illustration and reference to rheological behaviours discussed below.

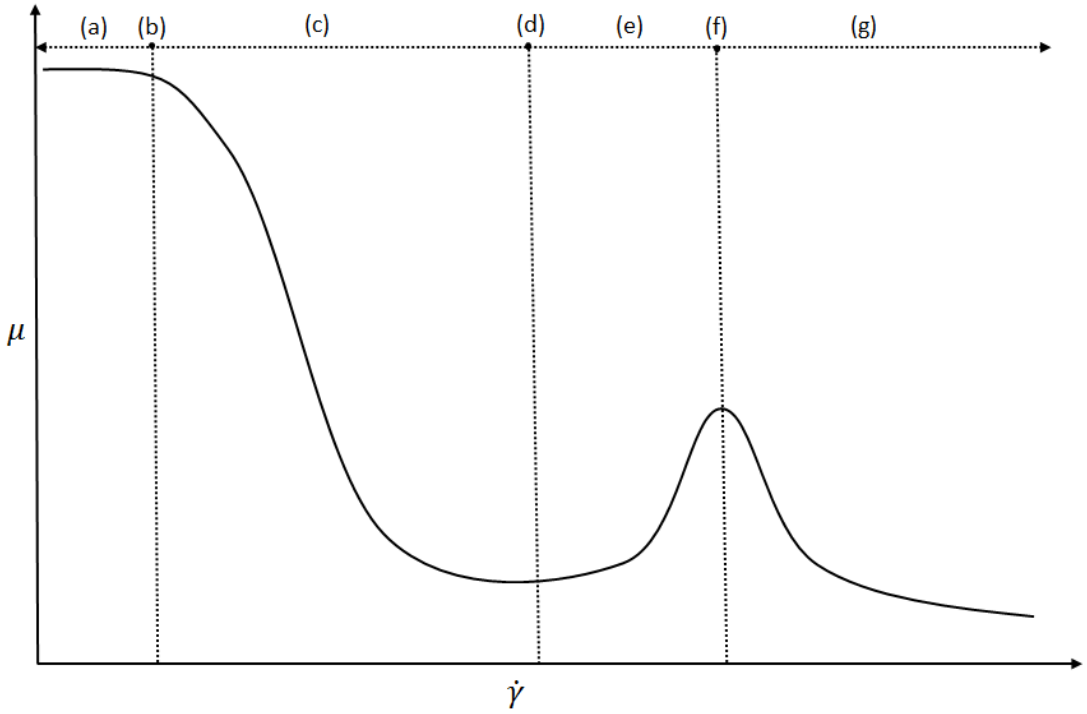

Figure 2.11 General polymer rheology curve (modified from Skauge et al. (2016) [29])

In porous media, xanthan display both Newtonian and shear thinning behaviour. At low shear rates a Newtonian plateau, referred to as the lower Newtonian plateau and denoted μ_0, is attained where the polymer molecules are randomly oriented and exert a constant viscosity not affected by the shear rate. However, as shear rates increases the xanthan molecules start to align themselves with the flow direction resulting in reduced molecular interactions and a gradual viscosity reduction. This region of decreasing viscosity with increasing shear rate is a consequence of the xanthan polymers shear thinning characteristic owing to its rigid rod molecular conformation. [13] At the highest shear rates all molecules are aligned with the flow field resulting in another Newtonian plateau, referred to as the upper Newtonian plateau and denoted μ_∞, of constant minimum viscosity again unaffected by prevailing shear rate. [19] Therefore, xanthan display the rheological behaviour from region (a) to region (d) in Figure 2.11. Figure 2.12 illustrates the transition in rheological behaviour for the rigid rod xanthan molecule described above.

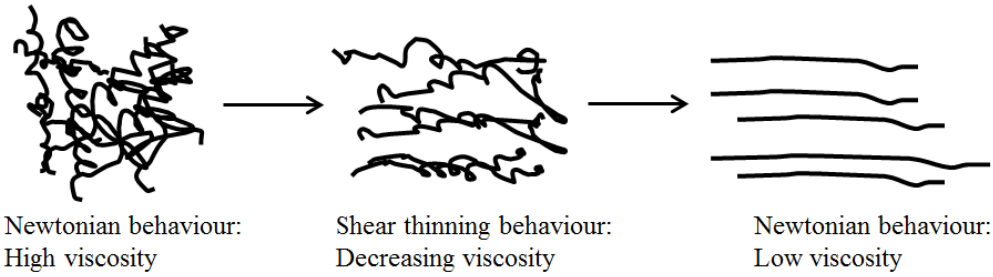

Figure 2.12 Shear thinning polymer behaviour (modified from Zolothukin and Ursin (2000) [13])

Viscoelastic fluids are fluids showing characteristics of both viscous fluids and elastic solids which enable them to elastically recover after deforming forces are removed. [17] Ghoniem (1985) [30] studied viscoelastic response of EOR polymers, including polyacrylamide polymers and xanthan, and found that viscoelastic response were present for polyacrylamides due to their flexible coil conformation. Xanthan, on the other hand, showed little viscoelastic response due to its rigid rod molecular structure.

Synthetic polymers are generally viscoelastic and the behaviour arises during flow through tortuous pore networks of varying cross-sections at high velocities. The flowing polymer molecules are subject to deformational forces acting both parallel (shear forces described in section 2.2.1) and perpendicular to the flow field. These perpendicular forces are referred to as elongational forces and are associated with the converging-diverging flow paths encountered as polymers enter and leave pores. [31]

To adjust to the flow field, the elongational forces stretch the polymer when flowing through constrictions as seen in figure 2.13. As a consequence of this highly extended conformation the apparent viscosity of the viscoelastic polymer increases. [32] If the transient time between consecutive constrictions is large relative to the time required for the polymer to relax and attain its random coil conformation the polymer is shear thinning. The time required for the polymer to attain this equilibrium configuration is called the polymers relaxation time, denoted τ_r, and is characteristic for the polymer. [3]

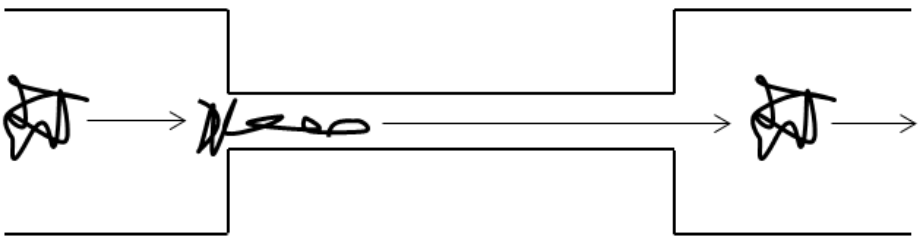

Figure 2.13 Synthetic polymer coil-stretch in elongational flow (modified from Zaitoun (2011) [33])

At high flow rates, however, the transient time between consecutive pore throats may be of the same order or smaller than the polymer relaxation time, consequently preventing the polymer from attaining its equilibrium configuration. The polymer therefore remains elongated during the flow resulting in an increase in polymer viscosity. This pulling and contraction is a result of the polymers elastic characteristic leading to higher apparent viscosity and a shear thickening behaviour. [31]

The ratio of the relaxation time to the average residence time in the porous media is called the Deborah number defined as [3];

$$N_{Deb} = \frac{\tau_r}{\tau_E} \tag{2.20}$$

Where N_{De} is Deborah number, τ_r is polymer relaxation time and τ_E is the porous media characteristic time. Equation (2.20) thus characterizes the onset of viscoelastic effects, where a large Deborah number indicates solid-like behaviour dominated by the elastic character resulting in shear thickening behaviour. Small Deborah numbers, on the other hand, result in shear thinning behaviour dominated by the viscous fluid nature. [9] Thus, viscoelastic polymers, such as the synthetic polymers described in section 2.4.1, display the full range of rheological behaviour illustrated in figure 2.11.

In Figure 2.11, the region at the highest shear rates extending from (f) and outwards indicate mechanical degradation where the polymer undergoes chain scission resulting in an irreversible loss of viscosity.[34] This concept is further described in subchapter 2.5.5.

2.5.2. Empirical rheology models

Several models have been proposed to correlate polymers bulk rheology, rheology measured in experimental rheometers, with their in-situ rheology. The most common empirical model describing this dependency is the power-law model [35];

$$\mu = K\dot{\gamma}^{(n-1)} \tag{2.21}$$

Where μ is polymer viscosity, K is a power law constant, $\dot{\gamma}$ is shear rate and n is the power-law exponent. In the shear thinning region n<1 and for a Newtonian fluid n=1. The power-law model produces satisfactory results in describing polymers shear thinning region, but is unsuitable for describing rheological behaviour at high and low shear rates. [3]

The Carreau model is a more general model producing an improved description at low and high shear regimes compared to the power-law model. The Carreau model is defined by [19];

$$\frac{\mu - \mu_\infty}{\mu_0 - \mu_\infty} = [1 + (\lambda\dot{\gamma})^\alpha]^{\frac{n-1}{\alpha}} \tag{2.22}$$

Where μ is polymer viscosity, μ_∞ is the upper Newtonian viscosity, μ_0 is the lower Newtonian viscosity, λ is a relaxation constant and n is the power-law exponent from equation (2.21). The parameter α is generally taken as 2, an assumption used throughout this thesis. Figure 2.14 illustrate the improved polymer rheology modelling resulting from the Carreau model compared to the power-law model.

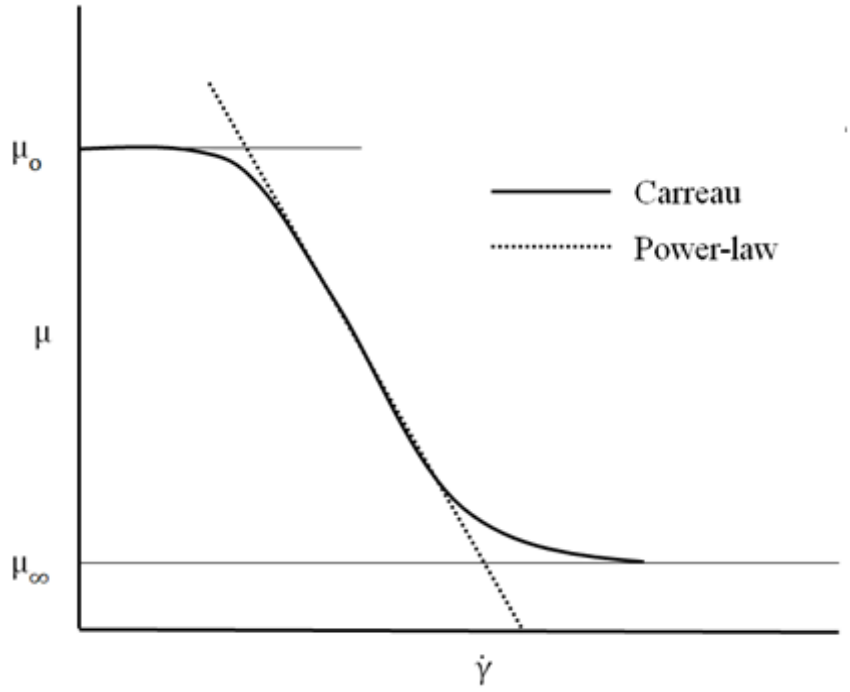

Figure 2.14 Comparison of Carreau and power law models (modified from Sorbie)

An unified apparent viscosity model accounting for both shear-thinning and shear-thickening behaviour has been developed by Delshad et al. [36] The model is a composite of the Carreau model (equation (2.22)) and an empirical model correlating shear-thickening viscosity with the Deborah number (equation (2.20)). The model constructed by Delshad et al. assumes that apparent viscosity dependence on Darcy velocity consists of two parts; one-shear viscosity dominant part, μ_{sh}, and an elongational viscosity dominant part, μ_{el};

$$\mu = \mu_{sh} + \mu_{el} \tag{2.23}$$

In equation (2.23) the shear-thinning part, μ_{sh}, is the Carreau model (equation (2.22)). The elongational viscosity dominant part,μ_{el}, is included to account for shear-thickening behaviour assuming μ_{el} is an empirical function of the Deborah Number, N_{De};

$$\mu_{el} = \mu_{max}[1 - exp(-(\lambda_2 N_{Deb})^{n_2 - 1}] \tag{2.24}$$

Where μ_{max} is the maximum shear thickening viscosity and λ_2 and n_2 are empirical constant. The Deborah number was defined in equation (2.20), however; in the model developed by Delshad et al. the assumption is that the average residence time, τ_E, is proportional to the inverse of the effective shear rate, $\dot{\gamma}_{eff}$;

$$N_{Deb} = \tau_r \dot{\gamma}_{eff} \tag{2.25}$$

Combining equation (2.23), equation (2.24) and equation (2.25) produces a unified apparent viscosity model covering the full range of rheological behaviour observed in porous media and illustrated in Figure 2.11;

$$\mu = \mu_\infty + (\mu_0 - \mu_\infty)[1 + (\lambda\dot{\gamma})^2]^{\frac{n_1 - 1}{2}} + \mu_{max}\left[1 - exp(-(\lambda_2 \tau_r \dot{\gamma}_{eff})^{n_2 - 1}\right] \tag{2.26}$$

Equation (2.26) is used extensively in the work conducted in this thesis to generate apparent viscosity values for polymer simulations. An important note, however, is that the Darcy velocity is used in place of the effective shear rate for calculations. This is a valid assumption as the Darcy velocity is connected to the effective shear rate through the equation;

$$\dot{\gamma}_{eff} = C\left[\frac{3n + 1}{4n}\right]^{\frac{n}{n-1}}\left[\frac{v}{\sqrt{K k_{rw} S_w \varphi}}\right] \tag{2.27}$$

Where v is Darcy velocity, K is permeability, k_{rw} is relative permeability, S_w is water saturation and φ is porosity, n is the power-law exponent and C is a fitting parameter.

2.5.3. Polymer Retention

As mentioned earlier, the main task for polymers during EOR flooding applications is to viscosify injection water and facilitate favourable oil displacement conditions. During flow in porous media, interactions between polymer molecules and the surrounding rock matrix cause polymers to be retained within the medium. As a consequence, polymer solution viscosity decreases leading to a reduced flooding efficiency. Retention of polymer may contribute positively to the flooding process due to a lowering of the permeability, however; the

decrease in solution viscosity tends to reduce oil recovery despite the permeability reduction. [3] Polymer retention varies with polymer type, concentration and molecular weight, rock characteristic and composition, and brine properties (salinity, hardness, pH). [19]

Figure 2.15 illustrate the three main polymer retention mechanisms; adsorption, mechanical entrapment and hydrodynamic retention.

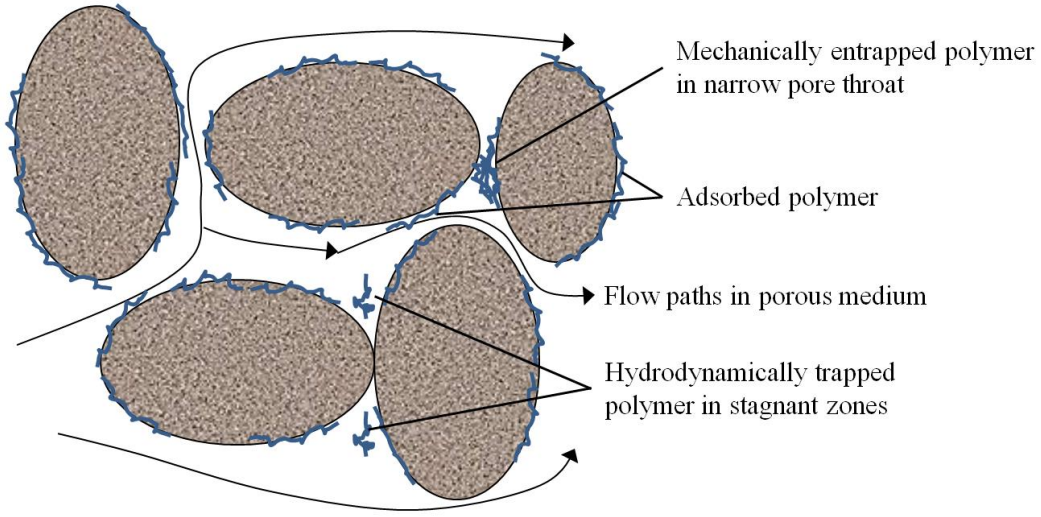

Figure 2.15 Schematic of polymer retention mechanisms (Modified from Sorbie (1991) [3])

Adsorption of polymer is the result of interactions occurring between polymer molecules and surrounding rock surface causing polymers to be bound to the rock by physical adsorption mechanisms (van der Waal forces and hydrogen bonding). The amount of adsorption depends on surface area; the larger the surface area available the higher the adsorption levels. [2] Further, polymer adsorption results in decreased rock permeability dependent on original permeability and thickness of adsorbed layer. The thickness of the adsorbed layer in turn is dependent on the polymer molecular weight (i.e., size of polymer coil) and polymer concentration. [10] Adsorption of polymer on the pore walls will also act to delay the propagation of the polymer solution within the porous media. [37] Generally, xanthan display less adsorption than HPAM in porous media due to a reduced degree of positively charged groups in its molecular structure. [3]

Mechanical entrapment of polymers arises when large polymer molecules become lodged in narrow flow channels. Therefore, mechanical entrapment is dependent on the molecular sizes present in the polymer solution. [37] Further, due to the nature of mechanical entrapment it is also heavily dependent on the rocks pore size distribution, and is a more likely mechanism in low-permeability formations. [38] Polymers are polydisperse indicating molecular size

variation and a wide molecular weight distribution, thus; reported polymer molecular weights is an average of the molecular weight distribution. If the entrapment process acts on the polymer down to the average size in the distribution a build-up of material close to the injection well occur leading to pore blocking and well plugging. [2]

Hydrodynamic retention is a less understood mechanism, but is believed to be the result of polymer molecules becoming temporarily trapped in stagnant zones. However, polymer retention resulting from hydrodynamic retention is more prevalent in core experiments and is thought to be of neglecting importance in field applications. [2]

2.5.4. Inaccessible Pore Volume

The polymer molecular size is large relative to molecules of the water which it travels in and to the porous medium if flows through. As a consequence, polymer molecules only flow through pores larger than their molecular size leading to an accelerated flow through the porous medium. [3] Inaccessible pore volume (IPV) is defined as the fraction of the pore space not contacted by the polymer solution, and can range from 1% to 2% to as much as 25% to 30% depending on polymer type and porous medium. [19]

The effect of IPV generally becomes more pronounced with increasing polymer molecular weight and decreasing characteristic pore size (ratio of permeability to porosity). However, the effect of accelerated flow of the polymer solution through the porous medium due to IPV tends to be concealed due to the delay of the polymer flow caused by polymer retention. [2]

2.5.5. Polymer Degradation

Polymer degradation refers to processes which break down the polymer molecular structure. Of importance for EOR applications are the chemical, mechanical and biological degradation pathways. [2] For the simulation study conducted in this thesis only mechanical degradation is of importance, therefore other degradation mechanisms will only be briefly mentioned.

Mechanical degradation occurs in high velocity flow fields, as encountered in the injection well vicinity, causing breakdown of the polymer molecules. As flow velocity falls of rapidly at increasing distances from injection point little mechanical degradation occur within the reservoir itself. [12] Mechanical degradation is more severe at lower permeabilities as the pore throat diameter is smaller resulting in higher stresses acting on the polymer. [2] As mentioned in section 2.5.1, synthetic polymers, such as those containing polyacrylamide,

display viscoelastic characteristics and shear thickening behaviour when exposed to elongational flow within the porous medium. The shear thickening behaviour of these polymers yields very high elongational stresses acting on the polymer molecule, which in turn mechanically pulls the molecule apart. [3] Rigid rod polymers, such as the xanthan biopolymer, have limited capacity for stretching due to its slight flexibility and therefore will not experience a large build-up of elongational stresses. Rigid rod polymers are therefore resistant to mechanical degradation owing to their rigid molecular conformation and do not degrade under the same conditions as the flexible coil polymers. [32]

Larger molecules are more prone to mechanical degradation due to the increased flow resistance and consequent larger elongational or shear stresses experienced by larger species. [2] Therefore, when mechanical degradation occur the molecular weight distribution of the polymer solution is altered as high molecular weight species are broken down into smaller species. HPAM samples experiencing degradation at high flow rates display a lower molecular weight distribution after the flooding sequence as seen in figure 2.16. [3]

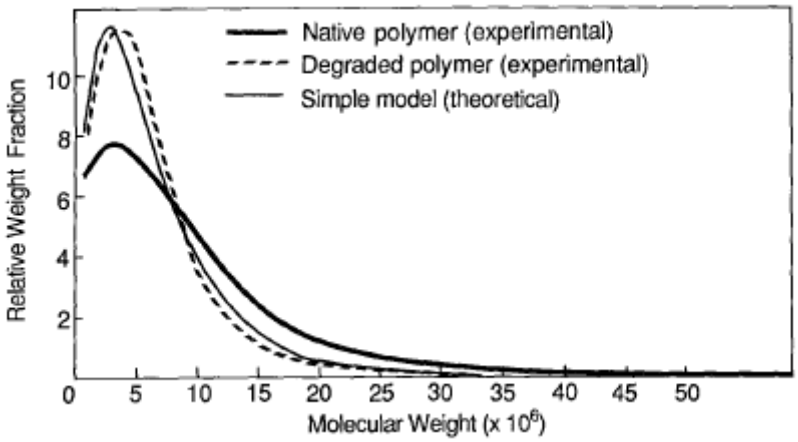

Figure 2.16 Molecular Weight Distribution before/after degradation (Sorbie (1991) [3])

To avoid significant mechanical degradation polymers which are prone to mechanical degradation may be pre-sheared before injection. [19]

Chemical degradation refers to processes which break down the polymer molecule during short-term attack by contaminants, such as oxygen or iron, or through longer-term attack to the molecular backbone by processes such as hydrolysis. [2]

Degradation of polymer may also occur from bacterial attack. Biopolymers are more susceptible to biological attack due to its carbohydrate backbone, which when attacked result

in loss of solution viscosity. However, biological degradation may be decreased by the use of an effective biocide. [12]

2.5.6. Mobility Reduction in Porous Media

Because of increased solution viscosity and reduced permeability due to polymer retention polymer solutions experience greater resistance to flow compared to pure water. To describe this mobility reduction in porous mediums for polymer solutions three factors have been defined; resistance factor, residual-resistance factor and permeability-reduction factor. [11]

The resistance factor, RF, was first proposed by Pye [39] and is defined as the ratio of the brine mobility in porous medium before polymer exposure to the polymer mobility in the same porous medium.

$$RF = \frac{\lambda_w}{\lambda_p} = \frac{k_w \cdot \mu_{app}}{k_p \cdot \mu_w} \tag{2.28}$$

Where λ_w and λ_p are the water and polymer mobility respectively. Following from equation (2.28), the resistance factor describes the decrease in polymer mobility compared to water mobility flowing in the same porous medium. [40]

Equation (2.28) is derived directly from Darcy's law, thus, the resistance factor may be expressed as the pressure drop in a porous medium during polymer flooding relative to the pressure drop occurring during the waterflood but before polymer exposure [19];

$$RF = \frac{dp_p}{dp_w} \tag{2.29}$$

Where dp_p and dp_w is the pressure drop for polymer and water before polymer exposure respectively.

Assuming constant permeability throughout the flooding sequences and combining equation (2.28) and equation (2.29) the apparent viscosity for the polymer flowing in the porous medium can be expressed as;

$$\mu_{app} = RF \cdot \mu_w = \frac{dp_p}{dp_w} \cdot \mu_w \tag{2.30}$$

Residual resistance factor, RRF, is defined as the ratio of the water mobility before polymer exposure to the water mobility after polymer exposure, consequently indicating the decrease in water mobility following a polymer flooding sequence [40];

$$RRF = \frac{\lambda_w}{\lambda_{wp}} = \frac{k_w}{k_{wp}} = \frac{k_w}{k_p} \tag{2.31}$$

Where $\lambda_w$and $\lambda_{wp}$is the water mobility before and after polymer exposure, k_w and k_{wp} is water effective permeability before and after polymer exposure. The denominator of the last term in equation (2.31) is based on the assumption that brine permeability after polymer exposure is the same as the permeability of the porous medium to the flow of polymer, k_p. [19]

2.5.7. Polymer Injectivity

From the previous subchapters, it has been described how polymers are added to injection water during polymer flooding EOR to facilitate for improved oil recovery conditions. The improved oil recovery conditions are a consequence of decreasing water mobility and resulting mobility ratio which result in an improved sweep efficiency of the reservoir. However, as a consequence of the polymers non-Newtonian behaviour in porous media their apparent viscosity when subjected to deformational forces will significantly influence their injectivity into porous media. [41]

Injectivity can be defined as the injection rate divided by the experienced injection pressure drop;

$$I = \frac{Q}{\Delta P} \tag{2.32}$$

Where I is the well injectivity, Q is the volumetric injection rate, ΔP is the pressure drop between the bottom-hole well pressure and some arbitrary reference pressure. [42]

Following from equation (2.4) and equation (2.32) the injectivity in radial geometry can be written as for a Newtonian fluid;

$$I = \frac{Q}{\Delta P} = \frac{2 \cdot \pi \cdot h \cdot K}{\mu \cdot ln\left(\frac{r_w}{r_e}\right)} \tag{2.33}$$

.

During fluid injection into porous media characterized by a radial flow pattern, the near-well vicinity will be the region where fluids experience the highest velocities. Consequently, this region heavily influences the in-situ rheology of non-Newtonian fluids, following from the discussion in subsection 2.5.1. Further, due to the radial flow pattern the velocities successively decrease with increasing radial distance from injection point. This, in turn, promotes different rheological response for the rigid rod polymers and the flexible coil polymers.

For synthetic flexible coil polymers, like the polymers described in section 2.4.1, the high velocities near the injection well promotes shear thickening viscoelastic response due to the high deformational forces experienced in this region. Due to the proportionality existing between pressure drop and viscosity this will result in an increasing pressure drop in the injection well as the polymer solution viscosity increases. Further, as the high velocities in this region also yields the highest elongational stresses on the polymer chains, mechanical degradation of the flexible coil polymers is also restricted to this region. Seright (1983) [42] associated mechanical degradation of polymers occurring in this region with an additional pressure drop, which will act to reduce the experienced injection pressure drop due to viscosity reductions. The highest fluxes and greatest mechanical degradation occur just as the polymer enters the formation. Thereafter fluxes decrease and no further significant mechanical degradation of the polymer occur. [3]

Rigid rod polymers, on the other hand, like xanthan described in section 2.4.2, high velocities near the injection well induces the polymers shear thinning behaviour. Thus, following the same rationale as for the previous paragraph, an decreased pressure drop occur for the polymer solution as the apparent viscosity decreases with increasing porous media velocities compared to the flexible coil polymer. Mechanical degradation of the rigid rod polymers will also be significantly reduced compared to the flexible coil polymers following from the discussion in section 2.5.5. Further, despite rigid rod polymers offer increased injectivity as their viscosity decreases with higher velocities, this is not necessarily a positive. As the low viscous solution propagates in the porous media it can bypass large quantities of oil due to the low viscosity.

From the following discussion, it is clear that the polymer solutions non-Newtonian behaviour is a significant contributor to the polymer injectivity in porous media. Adsorption and mechanical entrapment can also further result in loss of injectivity due to excessive adsorption

and plugging in the near-well region. [10] This consequently results in a decreased permeability which, due to the inverse proportionality with the pressure drop, increases the injection pressure drop.

3 Review of Experimental Data

Pressure recordings from waterflooding and polymer flooding sequences in radial Bentheimer disks were provided by Uni CIPR. These have been simulated and history matched in this thesis. Two separate experiments were conducted, one using the synthetic polymer HPAM, hereafter denoted experiment H-1, and one using the biopolymer xanthan, hereafter denoted experiment X-1. The radial flooding experiment is shown schematically in figure 3.1.

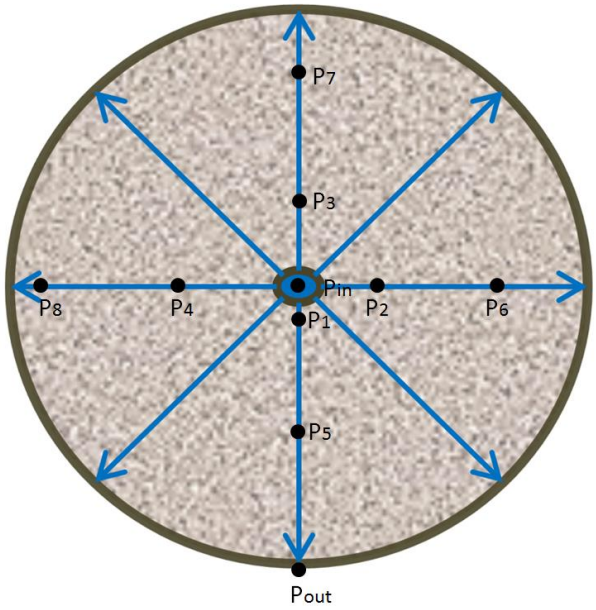

Figure 3.1 Radial flooding experiment schematic (modified from Skauge et al., 2016 [29]).

Figure 3.1 illustrate the radial flow of the fluids and the distribution of pressure ports rotated successively 90 degrees away from the centre. In radial flow geometry, fluids experience velocity reductions as they propagate away from the injection well towards an circumferential outlet boundary. As the cross-sectional area increases as the fluid propagates away from the injection well, radial flow is characterised as an unsteady state process going through both transient and semi-transient pressure regimes. The injection of fluids was performed at a constant rate and pressures were recorded once the pressure drop over the core stabilized.

The experimental data reviewed in this chapter forms the basis for the simulation study, and simulation results from subsequent chapters will be anchored to these experimental data. Due to its importance for the simulations conducted in this thesis, the following subsections will review the experiments and the provided data which have been simulated and history matched in later chapters.

3.1 H-1 Flooding Experiment

An initial waterflooding sequence was followed by HPAM solution injections at various rates in a radial Bentheimer disk. The HPAM polymer was diluted to a concentration of 1000 ppm, and the Bentheimer disk properties are summarized in table 3.1. Rock properties listed in Table 3.1 were used for modelling the radial disk in Chapter 5 and Chapter 6.

Table 3.1 Experiment H-1 Bentheimer disk properties.

Diameter [cm]	Height [cm]	Well radius [cm]	Porosity [%]
30	3.08	0.3	22.8

Pressure recordings from the waterflooding sequences are shown in Figure 3.2 as a function of logarithmic radial distance from injection well. The dotted lines connecting coloured dots are only added to aid in the identification of collected pressure values from the same injection rate.

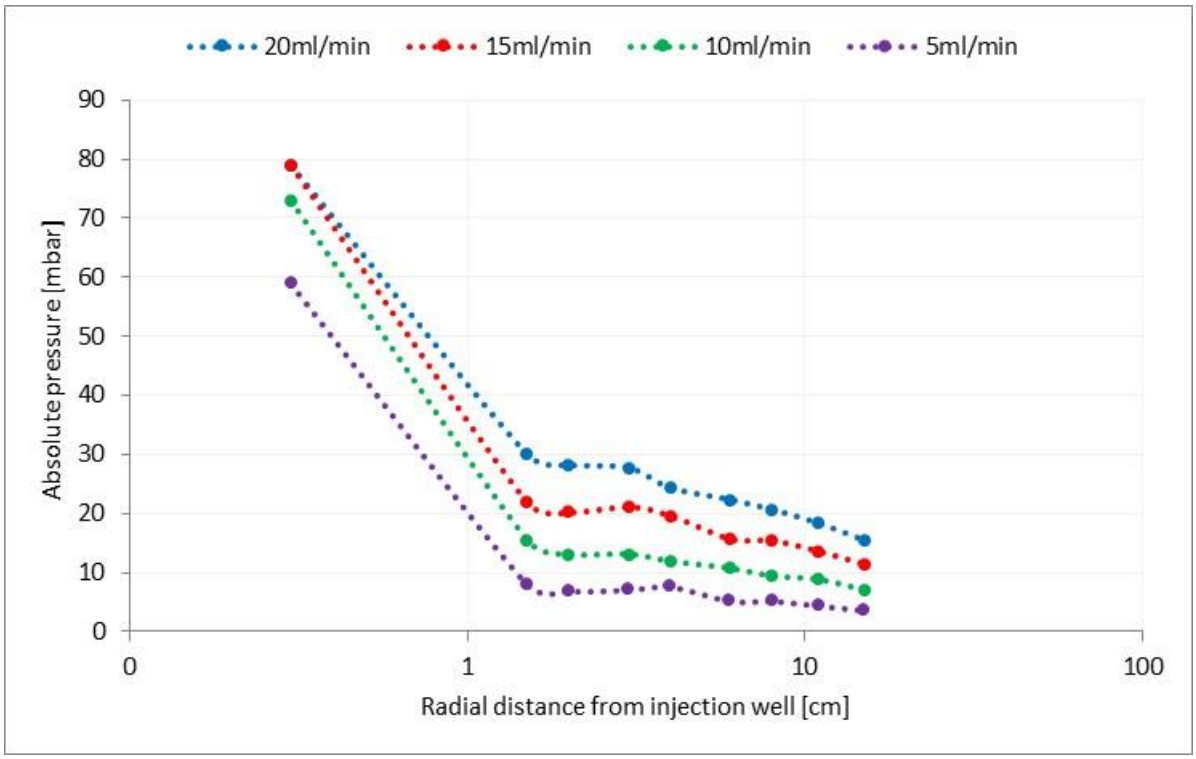

Figure 3.2 Recorded pressure during initial waterflooding in experiment H-1 as a function of log radial distance.

Darcy's law for radial flow, equation (2.4), predicts a logarithmic relationship between pressure and radial distance. However, from Figure 3.2 it is seen that the first pressure point in the injection well deviates from this relationship and is much higher than expected. Reasons for this pressure discrepancy are discussed in section 6.1.1.

Figure 3.3 show the pressure recordings in another plot where the first pressure recording has been omitted.

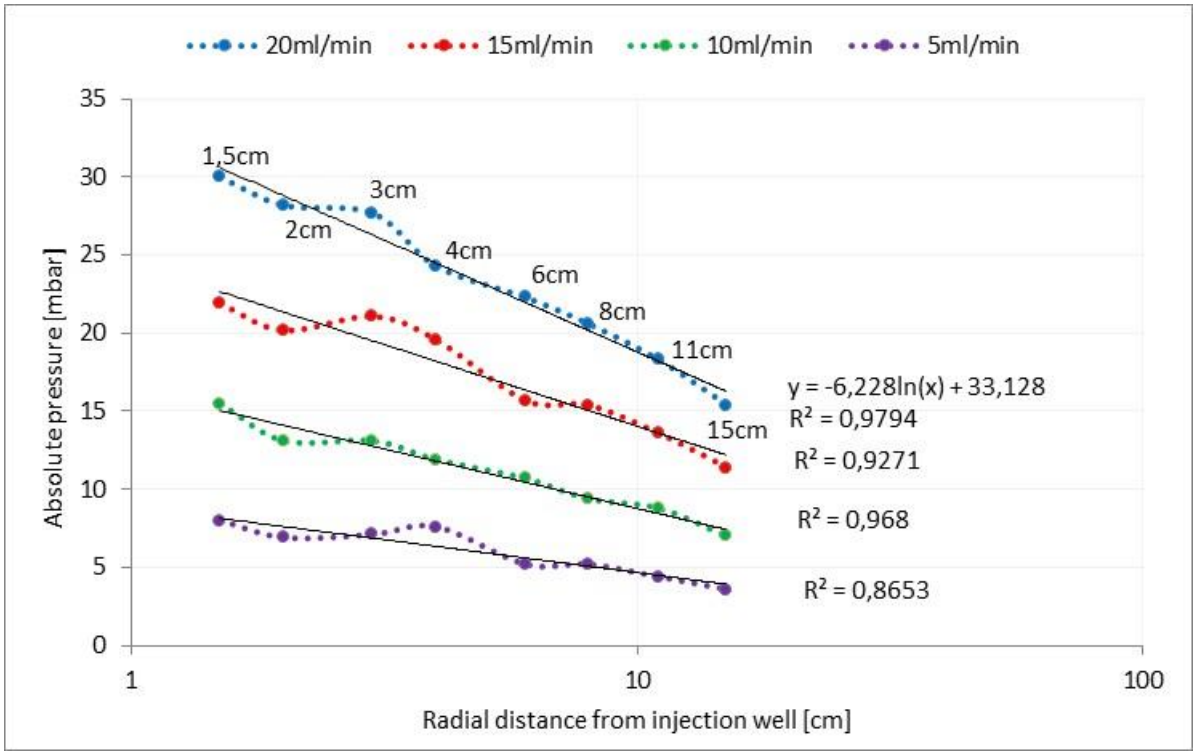

Figure 3.3 Recorded pressure during initial waterflooding in experiment H-1 as a function of log radial distance omitting first pressure recording.

From Figure 3.3, the remaining pressure points follow the logarithmic relationship predicted by Darcy's law, and hence confirm the radial symmetry of fluid inflow. The R squared value in Figure 3.3 is a statistical measure indicating the fit of the regression line on a scale of 0 to 1 where; 0 indicate that the regression line explains none of the variance in the data and a value of 1 indicate that the regression line explains all the variance in the data. Hence, a value of 1 would match every points in Figure 3.3. The R squared value in Figure 3.3 hence show good correlation between the pressures recorded from 1.5 cm to the outlet rim. The regression line equation for the 20ml/min injection rate in Figure 3.3 is included as an example for later us in this thesis.

Permeabilities for the Bentheimer rock were calculated for each injection rate using equation (2.4). Results from these calculations are listed in Table 3.2, and include calculations with the first pressure point (0.3cm-outlet rim) and when this pressure have been omitted (1.5cm-outlet rim), indicated by the permeability subscripts.

Table 3.2 Calculated Bentheimer permeabilities from various injection rates in experiment H-1.

Injection rate	$K_{0.3cm - Outlet\ rim}$ [D]	$K_{1.5cm - outlet\ rim}$ [D]
$Q_{5ml/min}$	0.31	2.29
$Q_{10ml/min}$	0.51	2.36
$Q_{15ml/min}$	0.78	2.87
$Q_{20ml/min}$	1.08	2.76

As seen in Table 3.2, inclusion of the deviating pressure point result in a significant permeability reduction compared to calculations in which it is omitted. This deviation and its implications are discussed in detail in Chapter 6.1.1. It should be noted, however, that the low permeability arises due to the unexpectedly high pressure recorded in the injection well and can be understood from the inverse proportionality between differential pressure and permeability in equation (2.4).

Pressures from the HPAM flooding sequence were collected in the same manner as the initial waterflooding sequence when pressure stabilized. Figure 3.4 shows the recorded pressure drop in the injection well during the HPAM polymer flooding and the initial waterflooding as a function of injection rate.

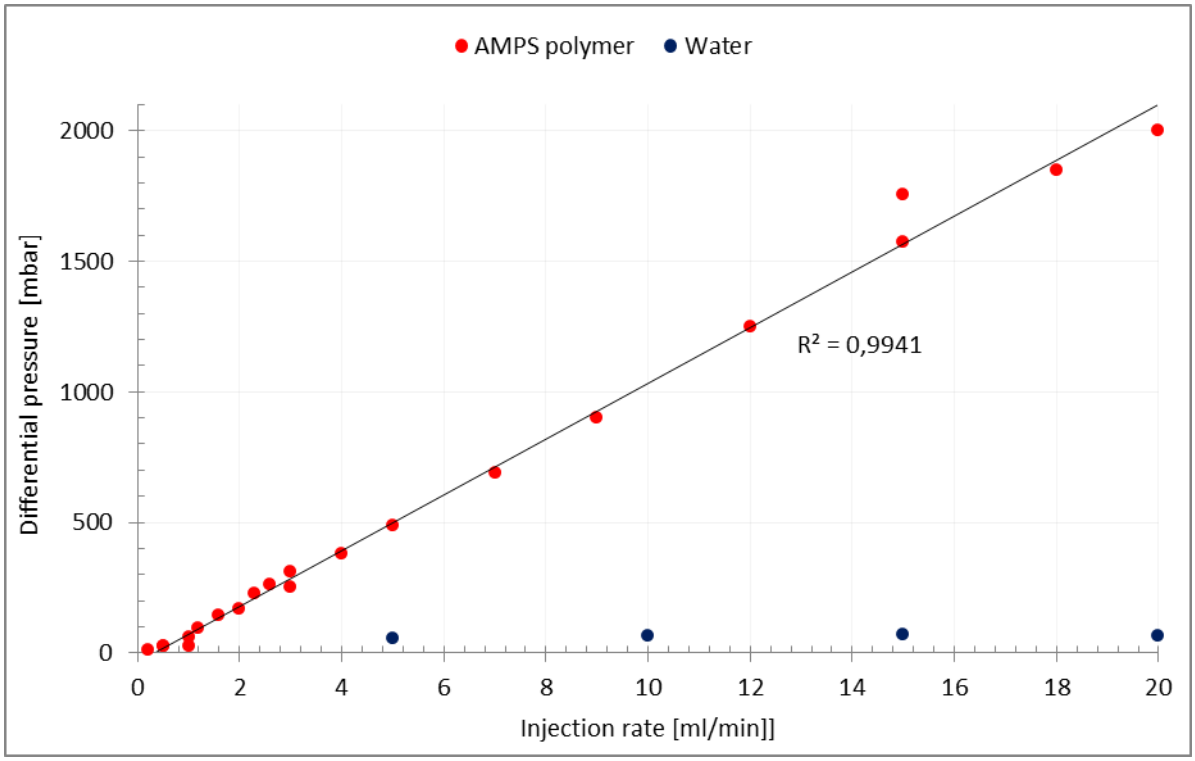

Figure 3.4 Differential pressure drop recorded during HPAM flooding and waterflooding by first pressure port as a function of injection rate.

As seen in Figure 3.4, recorded pressures increases significantly as injection rate increase during the HPAM flooding, showing a significant increase over the pressure drop recorded during the initial waterflooding sequence performed in the same porous medium. Following from the description in section 2.5.1, the increased pressure during the HPAM flooding can be attributed to the non-Newtonian rheology of the polymer and the shear thickening occurring as velocities increases. Further, the recorded pressure can also be enhanced by polymer retention in the porous media. In comparison, the Newtonian water displays an almost constant pressure drop independent of the injection rate during the flooding sequence. Due to the low viscosity of the water the pressure drop is also significantly lower than the recorded pressure drop for the polymer solution. There also appear to be a strong linear correlation between recorded pressure drop and injection rate during the HPAM flooding, as indicated by the R squared value from the linear regression line.

Bulk viscosity measurements were performed for selected effluent samples after flowing in the porous media at different velocities. Figure 3.5 show bulk rheology data collected for the injected polymer solution, before exposure to the porous media, and effluent samples collected after flooding through the Bentheimer disk.

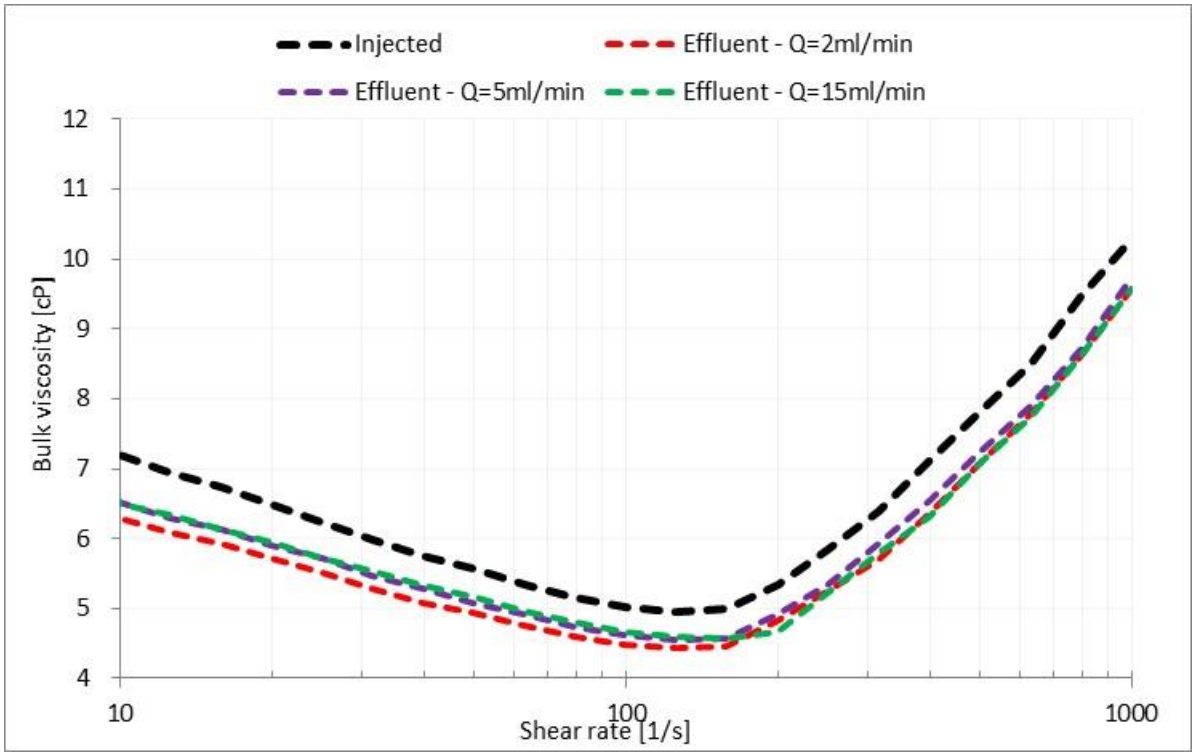

Figure 3.5 Bulk viscosity as a function of log shear rate for injected polymer and effluent polymer samples.

From Figure 3.5, the effluent samples collected after flowing through the radial disk show loss of viscosity compared to the injected polymer solution. The viscosity loss for each injection

rate is listed in Table 3.3 at $10s^{-1}$ and $100s^{-1}$ shear rate. In Table 3.3 Injected refers to the viscosity measurement conducted on the polymer solution before porous media exposure.

Table 3.3 Bulk viscosity measurement on injected and effluent HPAM samples.

	μ_{10s}^{-1} [cP]	% loss	μ_{100s}^{-1} [cP]	% loss
Injected	7.2	-	5.0	-
$Q_{2ml/min}$	6.3	12.5	4.5	10
$Q_{5ml/min}$	6.5	9.7	4.6	8
$Q_{15ml/min}$	6.5	9.7	4.7	7

As seen in Table 3.3 the effluent samples all display loss of viscosity following flow in the radial disk. The 2ml/min injection rate show the greatest loss of viscosity in the bulk viscosity measurement, however; as this rate was the first during the flooding experiment this rate likely experienced a higher degree of adsorption and entrapment within the Bentheimer disk. As a note, Table 3.3 does not account for measurement errors or uncertainties related to instrument limitations used for measuring the bulk rheology. These uncertainties were not provided along with the experimental data. Therefore, discussions involving values from Table 3.3 arising in this thesis will treat the viscosity values as they are listed in Table 3.3 without further discussions on uncertainties related to the values.

Dupas et al (2013) [34] referred to a 10% loss of effluent viscosity as indication of mechanical degradation occurrence during polymer flooding. Therefore, as the percentage viscosity loss from Table 3.3 show effluent viscosity values close to 10% for the HPAM solutions tested this may indicate that the polymer have experienced mechanical degradation in the injection well vicinity during the radial flooding experiment. Further, as was observed in Table 3.2 the permeability appeared to be significantly decreased in the near-well region which consequently increases the likelihood of polymer entrapment.

Another waterflooding sequence followed the polymer flooding sequence. Figure 3.6 show the differential pressure recorded for the 5ml/min water injection rate before and after the polymer flooding sequence.

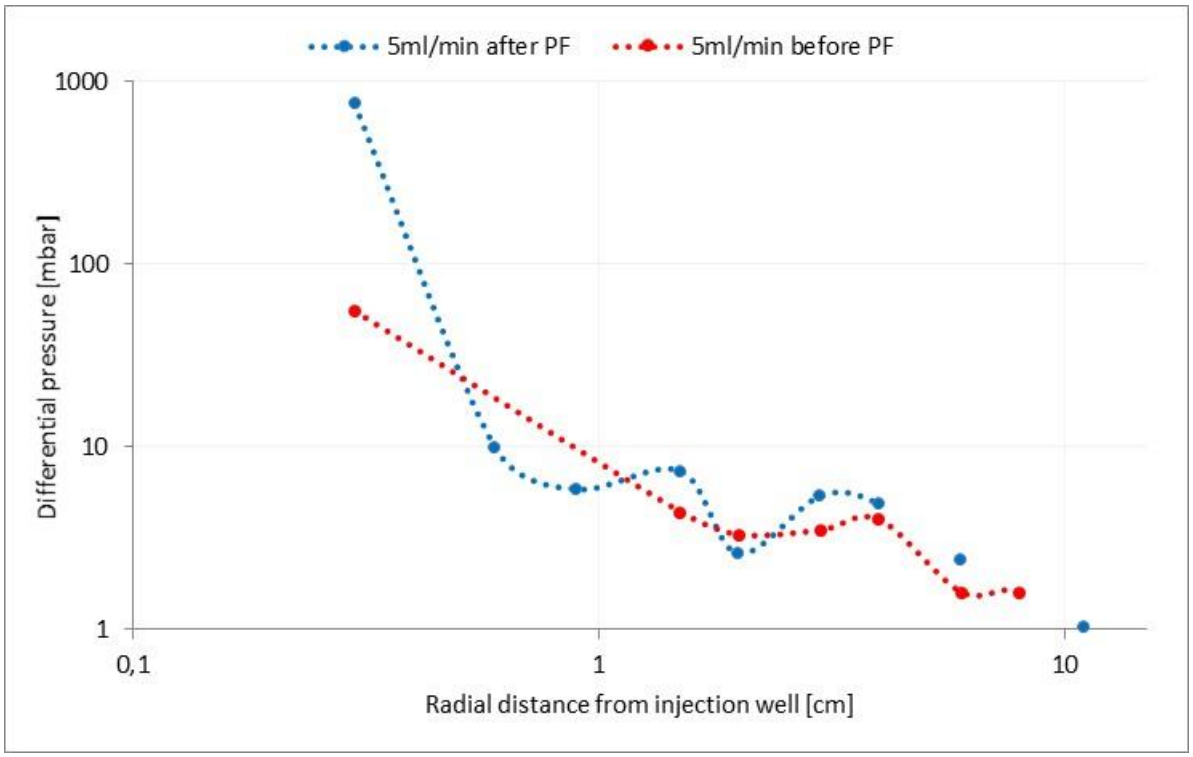

Figure 3.6 Recorded differential pressures from 5ml/min waterflooding performed before and after polymer flooding sequence.

From Figure 3.6, it is observed that the first pressure recording is significantly higher in the second waterflooding, indicative of a significant permeability decrease in the near-well region. Likely mechanisms for the permeability decrease and resulting increased pressure response are adsorption and/or mechanically entrapment of polymer molecules near the injection well. It was seen in Table 3.2 above that the analytical permeability when including the near-well pressure point in the calculations deviated significantly from permeability calculations in which it was omitted. Consequently, the permeability appears to be decreased in the near-well region compared to the remainder of the core, hence, facilitating for increased entrapment conditions. Table 3.3 also showed that the polymer solution had experienced a viscosity loss during the flooding sequence, thus, the loss of viscosity experienced is likely a consequence of polymer entrapment in the near well vicinity.

3.2 X-1 Flooding Experiment

An 890ppm xanthan solution was used during the X-1 flooding experiment and was conducted in a similar manner as the HPAM experiment for a wide range of injection rates. The flooding experiment was performed in another Bentheimer disk with properties listed in Table 3.4, properties which were also utilized for later modelling of the radial disk in Chapter 5 and Chapter 6.

Table 3.4 Experiment X-1 Bentheimer disk properties.

Diameter [cm]	Height [cm]	Well radius [cm]	Porosity [%]
29.8	2.2	0.3	28.2

Pressure recordings from the waterflooding sequences are shown in Figure 3.7 as a function of radial distance from injection well. Again, the dotted line is added only to aid the reader towards other pressure values collected for an injection rate.

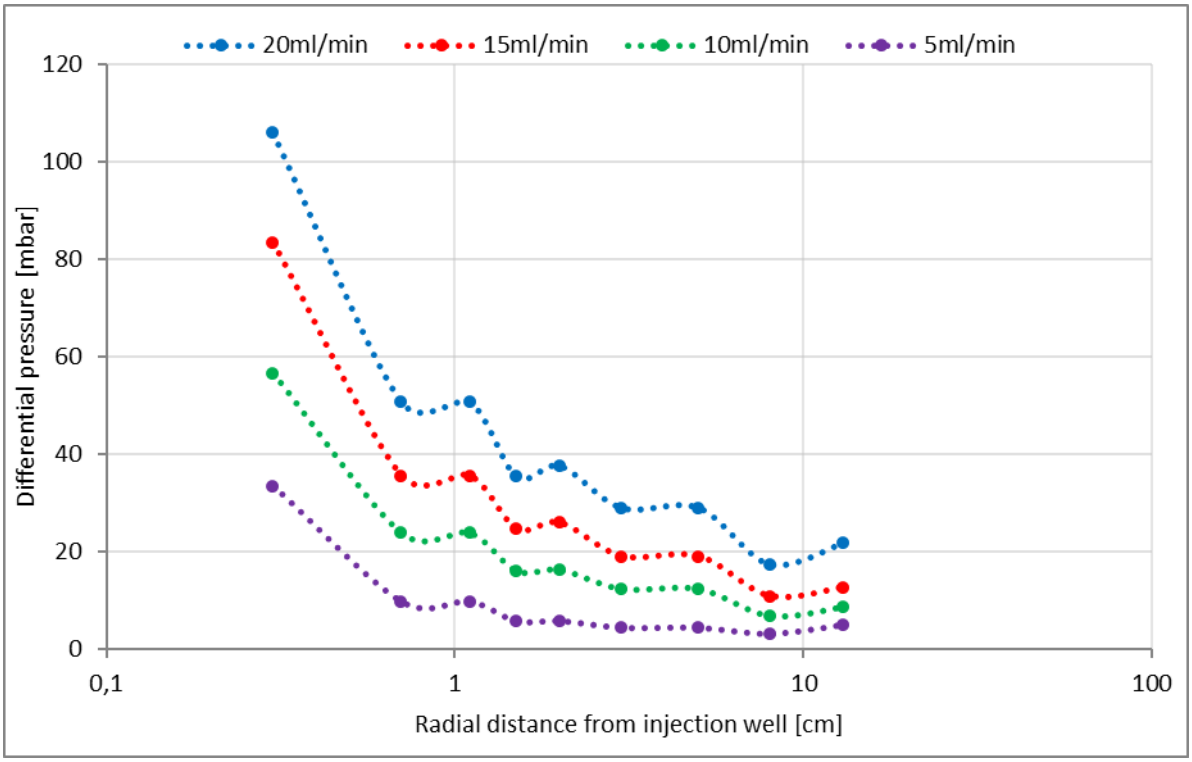

Figure 3.7 Recorded pressure during initial waterflooding in experiment X-1 as a function of log radial distance.

In Figure 3.7 it is observed that the recorded well pressure deviates from the relationship predicted by Darcy's law, as for experiment H-1. Following from the discussion in the previous subsection this indicates lower near-well permeability compared to the rest of the radial disk.

Figure 3.8 show the pressure recordings in another plot omitting the first pressure point.

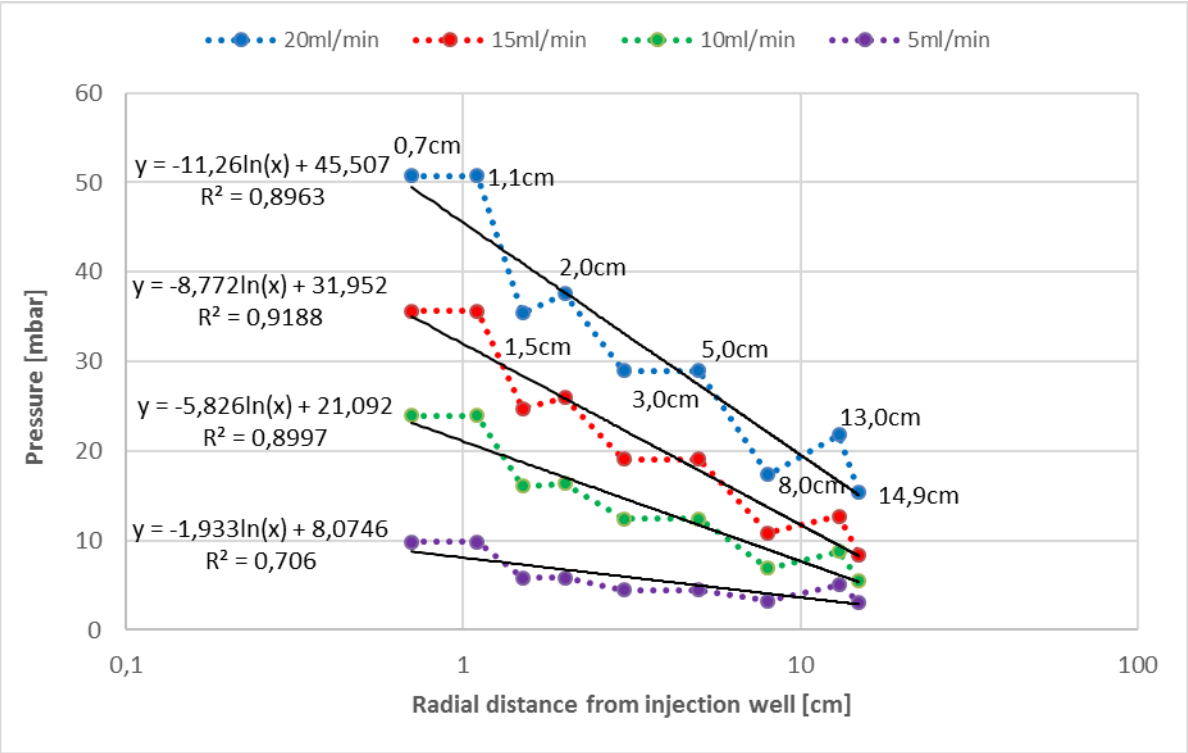

Figure 3.8 Recorded pressure during initial waterflooding in experiment X-1 as a function of log radial distance omitting first pressure recording.

As seen in Figure 3.8, recorded pressures from the flooding experiments fluctuate far more than corresponding recordings collected from the H-1 experiment. This is also confirmed by the lower R squared value obtained from the logarithmic regression line. A possible reason for the fluctuations may be because of insufficiently accurate pressure transducers employed in this experiment. Another explanation may stem from local variations within the radial disk used in experiment X-1 not present during the flooding sequences in experiment H-1. Nevertheless, recorded pressures appear to be more uncertain than the corresponding pressure values obtained from experiment H-1 floodings.

Further, there was some uncertainty as to how the experimental data was collected. According to info provided along with the experimental data, pressure values recorded during the xanthan flooding experiment was collected with differential pressure transducers. Therefore, the pressure at the rim should be 0 millibar at the outlet rim after offset correction. However, this appear to be questionable. Inspection of the experimental data collected during the waterflooding sequences in experiment H-1, collected by absolute pressure transducers in a comparable Bentheimer disk, and pressure recordings from experiment X-1 reveal that the pressures are of the same order. Further, calculating the pressure at the rim using the logarithmic regression line equation in Figure 3.8 reveal that, for instance, the rim pressure for the 20ml/min injection rate would be approximately 15.1 mbar. As the pressure values are to

be backpressure corrected to satisfy Dirichlet boundary condition (i.e., 0 mbar at the outlet rim) not having pressure values collected at the outlet rim result in history matching of pressure values which do not follow this boundary condition. As this issue is not easily circumvented as calculating synthetic values for non-Newtonian fluids is not appropriate, further elaborated on in section 6.2.2, the boundary condition of 0mbar at outlet rim will be defined for experiment X-1, although this is questionable due to the missing pressure values at the outlet rim. Therefore, the values will be treated as differential pressure values, and further implications of this discrepancy will discussed in detail in Chapter 6.

Nevertheless, as a consequence of these uncertainties and the fluctuating pressure data used for the simulations of this experiment, a larger degree of uncertainty than the corresponding H-1 simulations results. Due to the functional relationship between pressure and permeability the uncertainties from the pressure recordings in experiment X-1 will be transferred to the permeabilities estimated during later waterflooding simulations. Ultimately the uncertainties coupled with the pressure data and transferred to the permeability will affect the polymer rheology curves investigated in Chapter 6. However, as history matching of the pressure points adjust the curve to all pressure points, this has the effect of averaging over the data and uncertainties, this will result in reduction of uncertainties from the pressure data.

Permeabilities for the Bentheimer rock was calculated from equation (2.4) for each injection rate listed in Table 3.5. Synthetic pressure values were estimated for the outlet rim based on the regression line equation in Figure 3.8 due to missing pressure data at this location.

Table 3.5 contains permeability values both including the first pressure recording and permeabilities calculated omitting this pressure as indicated by the permeability subscripts.

Table 3.5 Calculated Bentheimer permeabilities for various injection rates in experiment X-1.

Injection rate [ml/min]	$K_{0.3cm - Outlet\ rim}$ [D]	$K_{0.7cm - outlet\ rim}$ [D]
$Q_{5ml/min}$	0.78	2.76
$Q_{10ml/min}$	0.93	2.03
$Q_{15ml/min}$	0.95	2.06
$Q_{20ml/min}$	1.05	2.11

From Table 3.5 it is seen that permeabilities are lowered significantly when including the first pressure point in the calculations compared to calculations in which it is omitted. Thus, as for the H-1 experiment the near-well permeability appear to be lower than for the remainder of

the Bentheimer disk. Again, an explanation for this deviation is discussed further in Chapter 6. However, a comparison of near-well permeabilities for experiment X-1 with permeabilities calculated for the H-1 experiment in table 4.2 indicate that the deviation resulting from the inclusion of the first recorded pressure is not as heavily affected by the injection rate as the case was for the H-1 experiments. Further, it is seen that the calculated pressure from the 5ml/min injection rate deviates significantly from the other analytical permeabilities.

The X-1 experiment consisted of fewer injection rates than the H-1 experiment. Pressure measurements were again collected once pressure stabilized during each flooding procedure and injection at a different rate was initiated. Figure 3.9 shows the recorded pressure drop at the injection well as a function of injection rate for the xanthan solution and the initial water.

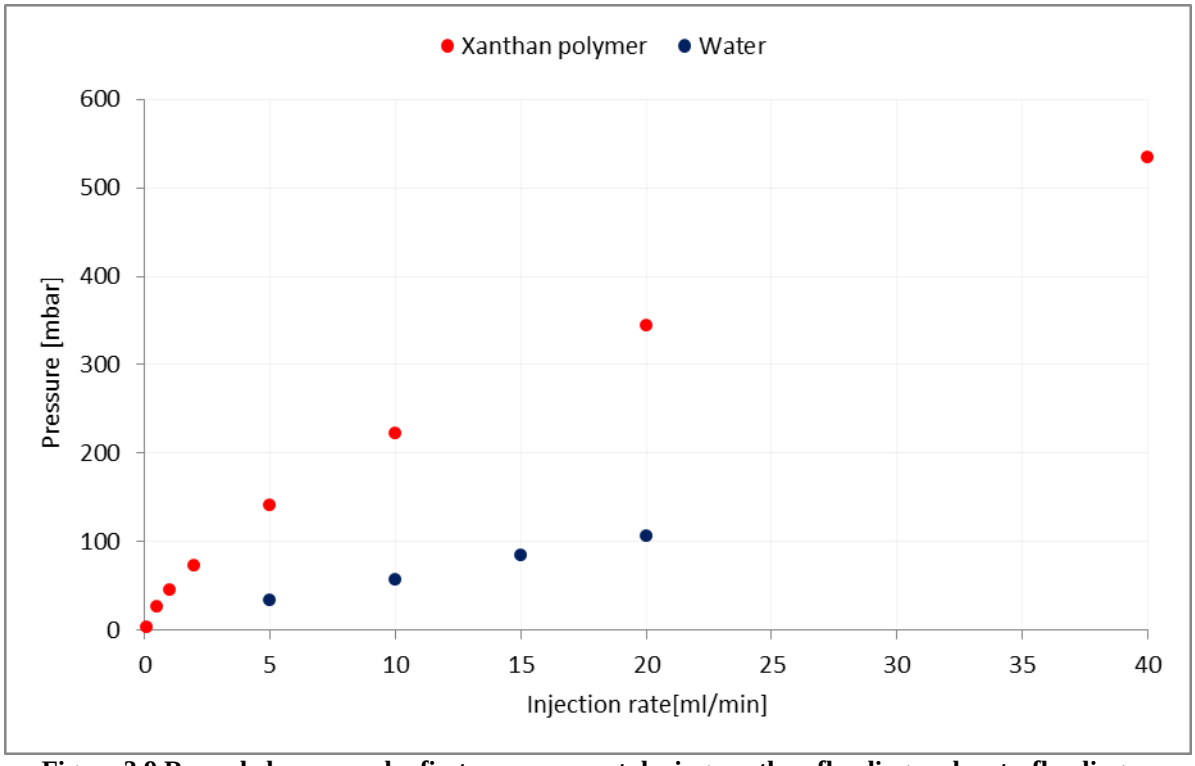

Figure 3.9 Recorded pressure by first pressure port during xanthan flooding and waterflooding as a function of injection rate.

Comparison of the recorded pressure during the xanthan flooding sequence with the recorded pressure during the HPAM flooding sequence shows that recorded pressure is significantly lowered in experiment X-1. This is to be expected, due to different rheological behaviour of the polymers in porous media, as described in section 2.5.1. The shear thinning xanthan polymer will display a significantly lower entrance pressure than the shear thickening HPAM polymer due to the lower viscosity expected at high velocities near the injection well.

Due to limitations in the pressure transducers in the xanthan flooding sequences, only a total of 5 transducers were able to record the pressure drop occurring between consecutive ports. As a result, during the history matches performed in chapter 6 only 5 points were utilized for the matching and no backpressure correction was performed as for the pressure data in experiment H-1. Consequences of the limited pressures available for the history matches are discussed in detail in Chapter 6.2.2.

No bulk viscosity measurement was performed on any xanthan samples. Therefore, assessing the degree of mechanical degradation occurring during injection of xanthan is difficult to accomplish. However, as described in 2.5.5 the rigid rod xanthan polymer is much more resistant to mechanical degradation than the flexible coil synthetic polymer used in experiment H-1.

After the xanthan flooding sequence the Bentheimer disk was again flooded with water. However, like for the xanthan flooding sequence the pressure transducers were only able to record the pressure at 5 positions within the Bentheimer disk. In Figure 3.10 synthetic pressure values have been calculated based on a regression line equation fitted to the experimental pressure data collected during the second waterflooding.

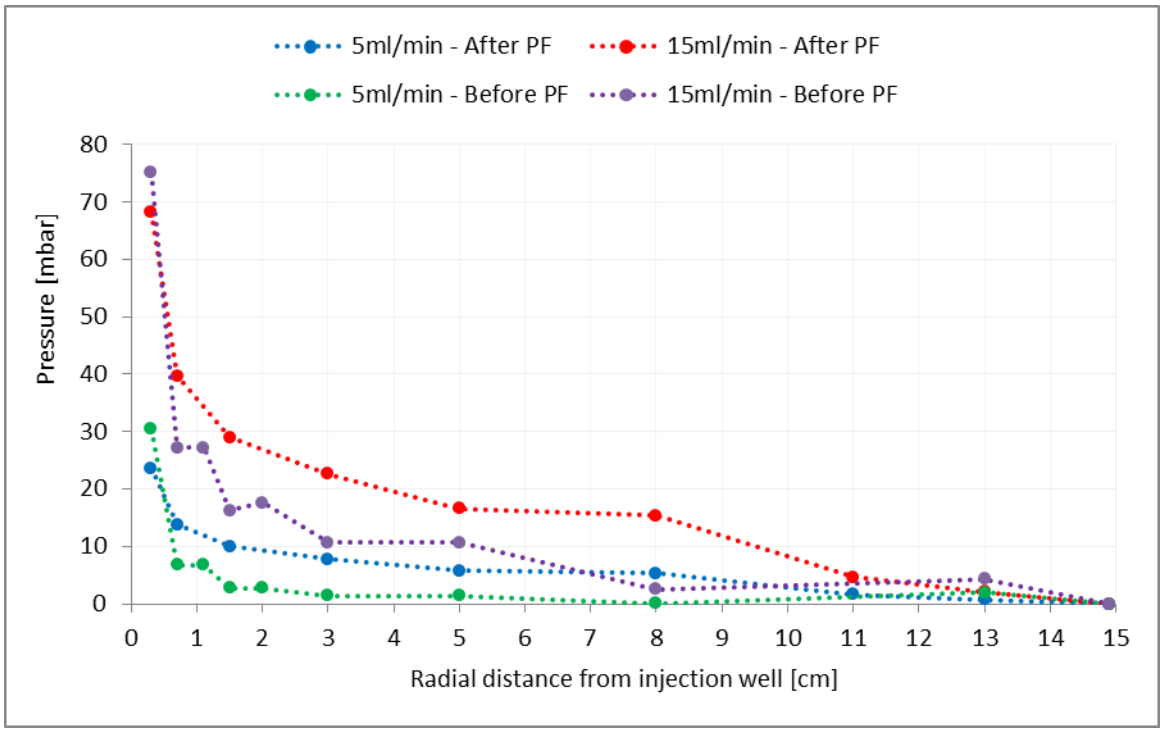

Figure 3.10 Recorded differential pressures from 5ml/min and 15ml/min waterflooding performed before and after polymer flooding sequence as a function of radial distance.

As seen in Figure 3.10, the pressure did not significantly change after the polymer flooding sequence in the near well region, indicative of little adsorption and mechanical entrapment.

The first pressure point is actually seen to be lowered after the polymer flooding sequences. However, for the remainder of the core the pressure is increased compared to the initial waterflooding sequence, thus; some adsorption and retention have likely occurred during the xanthan flooding sequence.

4 Simulation Tools

This thesis deals with the simulation study of polymer rheology and injectivity in radial geometry where the experiments presented in Chapter 3 form the basis for the study. Two simulation tools have been utilized during this work; STARS by Computer Modelling Group (CMG) and MATLAB Reservoir Simulation Toolbox (MRST), referred to as MRST throughout this thesis, developed by SINTEF. The MRST simulator will utilize an Ensemble Kalman Filter (EnKF) module extension developed by Uni CIPR.

The following subsections review the reservoir simulation tools and the procedures followed to achieve history matches of the provided pressure measurements recorded during water and polymer flooding sequences.

4.1 STARS

STARS is an advanced thermal and processes reservoir simulator which includes a range of options and functionalities for simulating EOR processes such as chemical injection of polymers and surfactants, steam injection and thermal applications.

For the work conducted in this thesis, STARS proved to be a suitable tool for simulating single phase polymer injection due to its capability of including polymer characteristics, most importantly shear rate viscosity dependency, while modelling the radial Bentheimer disks.

For the simulations, input files containing pertinent reservoir information and rock and fluid properties were initialized and simulated. The input files were grouped in an order which had to be honoured in which reservoir model, component properties and rock-fluid data were defined separately in individual groups. Output data was also limited to properties of interest, such as pressure development in specific grid blocks, through special keywords in the input/output control group. Other groups included in the input files were initialization, numerical control and well and recurrent data. These groups are easily identified in the provided input files provided in appendix C.1

Keywords and the process of initializing the input-files used for modelling the water and polymer flooding sequences are not reviewed in this chapter, but is covered in the sensitivity study conducted in Chapter 5. Further description of keywords used in the STARS input-files such as keywords defining rock properties can be found in the STARS user guide. [43, 44]

However, an important and desirable feature offered in the STARS simulator was the option of inputting polymer rheology data in tabular form using the SHEARTAB keyword. By selecting this option, rheology data was inputted in two columns; one column containing Darcy velocities in cm/min and the second column containing corresponding polymer apparent viscosities in centipoises. This allowed for great flexibility in specifying and investigating the polymers in-situ rheology during the simulation study. During the history matching process the simulation files were initialized with polymer apparent viscosity values generated using the extended Carreau equation, equation (2.26), and Darcy velocities from equation (2.16). The extended Carreau parameters were then tuned until a satisfactory pressure match was achieved.

The STARS reservoir simulator is included in the CMG Technologies Launcher which also includes the "Results 3D" tool allowing for graphical representation of simulation output. Properties like viscosity development, fluid velocity and pressure propagation in the model could therefore be viewed as a function of time and distance in both 2D and 3D for the radial model and for specific grid blocks. Simulation output could also be exported to Excel through this tool making comparison and graphical handling more efficient.

During the simulations an issue which arose in the STARS simulator was problems related to Darcy velocities in the near well vicinity. The simulator was incapable of including Darcy velocities at 0.3 cm, the same distance as the well radius, which is also the region of highest velocities. Therefore, the highest apparent viscosity of the polymer solution was not included in the output results from STARS. The reason for this issue is unclear. It is believed that the simulator is not able to include the well in the simulations, and therefore velocities occurring at same distance as defined well radiuses cannot be modelled as it would indicate same velocities occurring at different positions. Further, due to limitations in defining the near-well region

4.2 MRST

MRST simulations were conducted using the EnKF module to obtain history matches of inputted pressure values. The iterations and calculations performed by EnKF during the simulation runs are complex and requires knowledge of both mathematical and statistical concepts for description of the history match process. Therefore, details of the underlying

EnKF method will not be reviewed in this thesis and reference is made to Evensen (2003) [45] and Krymskaya et al (2009) [46] for a detailed description.

In short, EnKF uses a Monte Carlo approach to estimate parameter values based on an iteration scheme which produces a probability distribution (PDI) of specified parameter values based on an initial best guess finite value range. The iterative EnKF scheme allow for parameter estimation by conducting several iteration runs on an initial best guess range continuously improving results found during previous iterations. The probability distribution resulting from the iterative EnKF scheme is illustrated in figure 4.2.

The process of obtaining a history match for the polymer flooding sequence using MRST can therefore be described by the flowchart in figure 4.1. The procedure for history matching the waterflooding sequences is performed in a similar manner and is therefore not covered in detail. Not included in figure 4.1 is the initial MRST script initialization which included providing the simulator with pertinent information regarding rock properties (listed in table 3.1 and table 3.4 for the respective experiments), injection rates, desired number of EnKF iterations and ensemble members. In this thesis, 4 iteration runs were performed based on 100 ensemble members. Further, the experimental data (backpressure corrected differential pressures) forming the basis for the EnKF iterations are also included in a separate file.

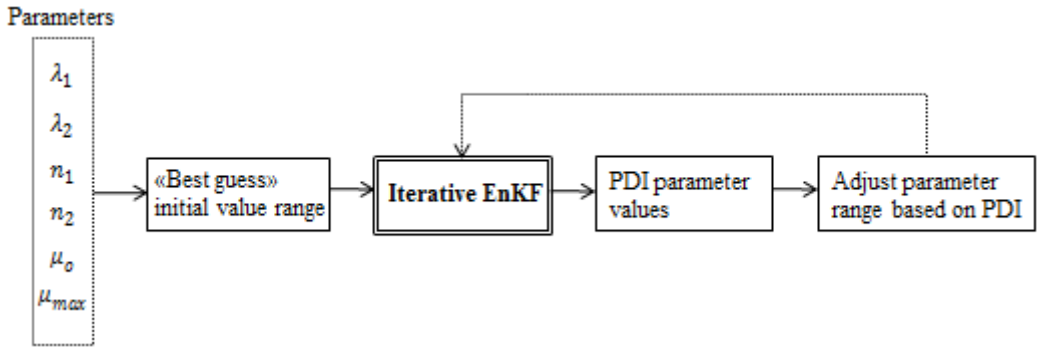

Figure 4.1 MRST history match flowchart

For the history matches, the extended Carreau equation (2.26) is utilized to history match the experimental pressure data and consequently determining the polymers in-situ rheology. For the waterflooding history matches Darcy's law for radial flow is utilized, equation 2.4. The parameter values are defined within a finite range closed by a minimum and maximum value for each parameter, thus; defining the initial best guess range for the iterations. Few limitations exists for the parameters in equation (2.26) which explains why manual history matching using the extended Carreau equation is tedious and uncertain as an unlimited amount of combinations of parameter values can produce an satisfactory history match.

Generally, the power-law exponent (n_1) is bound within the range 0<n_1<1 and the relaxation time constants follow$\lambda_1 < \lambda_2$. For MRST the empirical constant n_2 is also recommended to be within the range $1 < n_2 < 2.5$ to avoid numerical computation issues. It was observed during simulations using MRST that not following the n_2 recommendation lead to significantly longer simulation runs. Further, the initial best guess range was based on the values from the manual history matches for the polymer flooding simulations. The range, however, was defined significantly wider than the values from the manual simulations as to not limit the MRST simulations.

After defining the parameters and parameter value ranges, the simulator ran a total of 4 iteration runs for the 100 ensemble members. The ensemble members can be explained as the 100 random values, for each parameter, selected by the simulator from the initial best guess range to run the first initial iteration run. Based on this first iterative run from the first 100 ensemble members, the simulator narrows the initial range of values and select another 100 ensemble members for the next iteration run from this new narrower range of parameter values. This process continues until the fourth and final iteration run where the MRST simulator produces a PDI of the values for each separate parameter. Figure 4.2 show an example of a probability distribution from simulation of a 15ml/min HPAM flooding using EnKF.

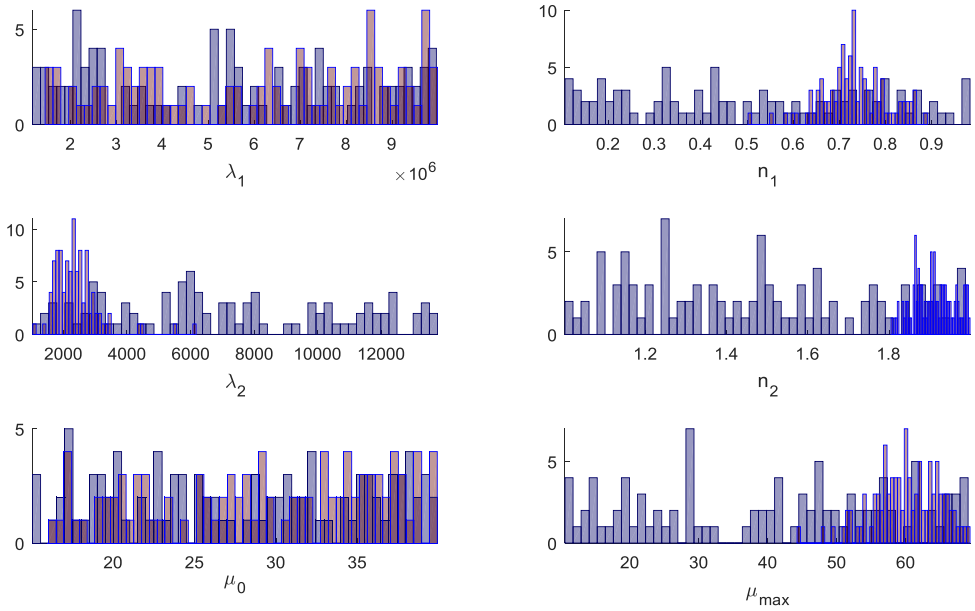

Figure 4.2 EnKF variable probability distribution for 20ml/min polymer flooding

As mentioned, based on the initial best guess range the simulator selects 100 values for each parameter from the specified range for the first iteration run. This is the randomly selected values and corresponds to the grey bars in Figure 4.2. The fourth, and final, iteration sequence yields a PDI for the parameters values as seen in Figure 4.2 as the coloured bars. From Figure 4.2 it is seen that some PDI yields a Gaussian distribution of the estimated parameters. This indicate that the value for the parameter likely reside within the range the iterative scheme have been able to narrow down. Thus, this indicates certainty of the parameter value. Further, as seen for λ_1 and μ_0 in figure 4.2 the initial interval is not defined sufficiently wide for the fourth iteration run to distinguish a distinctive interval range for the parameters. This, on the other hand, reduces the value uncertainty as the scheme is not able to clearly identify the value range.

This last point was of great importance during the simulations conducted in chapter 6. By defining a narrow range for the parameters MRST is given less degree of freedom for the iteration runs and the results will consequently be coupled with uncertainties. Therefore, the specified range for each parameter during the iterations was kept sufficiently wide during each iteration scheme as to ensure that the MRST simulator was given sufficiently freedom to narrow down the range the parameter likely reside in.

Figure 4.3 and figure 4.4 show the pressure matches and corresponding rheology curves obtained from the MRST simulations.

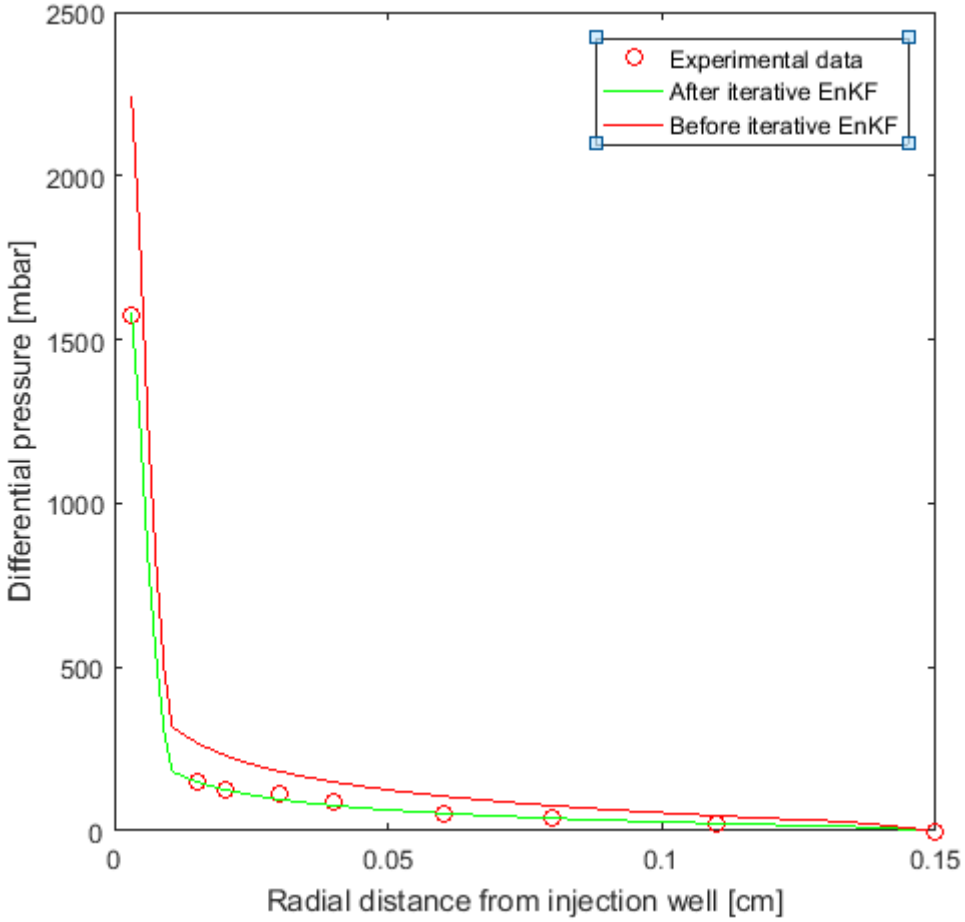

Figure 4.3 Differential pressure match before and after iterative EnKF

In figure 4.3 and figure 4.4 the results include results from the initial best guess range before initiating the iterative process, and the fourth and final result after the iteration scheme has finished. Another note on the MRST EnKF scheme is that though the range can be altered during iteration runs by the user this is not very straight forward. As a consequence of altering the range for the best guess interval provided for MRST, subsequent iteration runs can result in deviating results from what was obtained during preceding iteration run. During the MRST simulations the initial best guess range was kept intact and only altered when needed after several iteration runs produced unsatisfactory results.

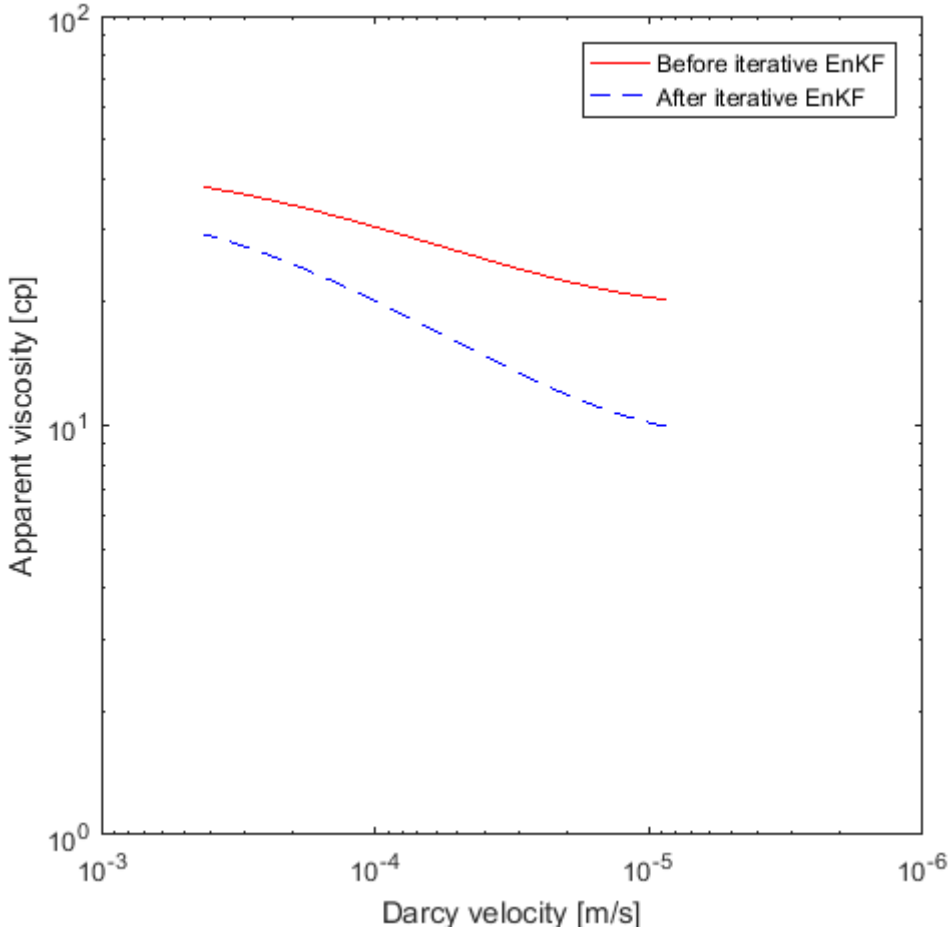

Figure 4.4 20ml/min rheology curve before and after iterative EnKF

5 Sensitivity Study

A sensitivity study was conducted before simulating and history matching the experimental data presented in Chapter 3. The purpose of this study was to investigate influence of certain parameters on the pressure matches while initializing and verifying input-files for subsequent simulations.

As a base case, a 5ml/min injection rate was initialized with rock properties from table 3.1 and 2D permeability. Flow conditions will not vary considerably between HPAM and xanthan simulations and it is assumed that factors influencing HPAM simulations also influence xanthan simulations, and vice versa. No sensitivity study was therefore performed for xanthan and results from the HPAM sensitivity also applies for the xanthan simulations.

During the sensitivity study it was imperative that parameters of interest were not varied simultaneously. This way the impact of each parameter could be assessed, thus; only one parameter is changed for each step of the sensitivity study keeping all other factors constant and equal between sensitivity cases.

Simulation output from the sensitivity study conducted in this chapter is mostly reported in terms of the effect parameters have on individual grid blocks within the model. This has been done to enhance graphical representation and avoid axis scaling caused by inclusion of higher pressure points. Further, individual grid block reporting also allows for displaying parameters influence on simulation time before stabilized pressure conditions is reached. Therefore, when results are reported for pressure build-up in grid block (17,1,1), for instance, this refers to the effect sensitivity parameters have on grid block 17 radially away from the injection well in horizontal direction. When different sensitivity cases result in equal stabilized pressure values in a grid block, regardless of the time used to attain stabilized conditions, it is implied that the cases also yield the same pressure distribution over the entire model at stabilized pressure conditions.

Summary of findings in this sensitivity study and final values used for the final input-file used in subsequent simulations is provided in table 5.12.

5.1 Time-step and Grid Size

Large time-steps and few grid blocks in simulation models can result in poor grid resolution and issues related to numerical dispersion. Numerical dispersion is a numerical effect arising

from time and space discretization causing smearing of sharp fronts which can influence reported simulation output. [22] Larger time-steps can additionally result in convergence failure of the Newton iterations performed by the simulator due to excessive material balance errors (MBE). An example of excessive numerical dispersion is illustrated for the blue curve in figure 5.3.

Small maximum time-steps and a large amount of grid blocks (i.e. narrow grid blocks), however, can significantly increase simulation time and demands more computational power to simulate and store output. The purpose of this study was therefore to initialize input-files with time-step and grid block sizes minimizing numerical dispersion effects while decreasing simulation time.

The maximum time-step size allowed during the simulations is defined by DTMAX and was studied by initializing the radial grid with 147 grid blocks of 0.1cm width in horizontal direction for all cases. A Newtonian-fluid of 10 centipoises was defined to investigate the effect of pressure build-up in grid-block (77,1,1). Table 5.1 lists time-step cases investigated.

Table 5.1 Time-step sensitivity cases and corresponding MBE output

	Time-step [min]	MBE [%]
Case 1	10	12e-3
Case 2	1	0.25
Case 3	0.1	0.29
Case 4	0.01	0.29

Figure 5.1 show the effect cases listed in table 5.1 have on pressure development in grid block (77,1,1) in the model.

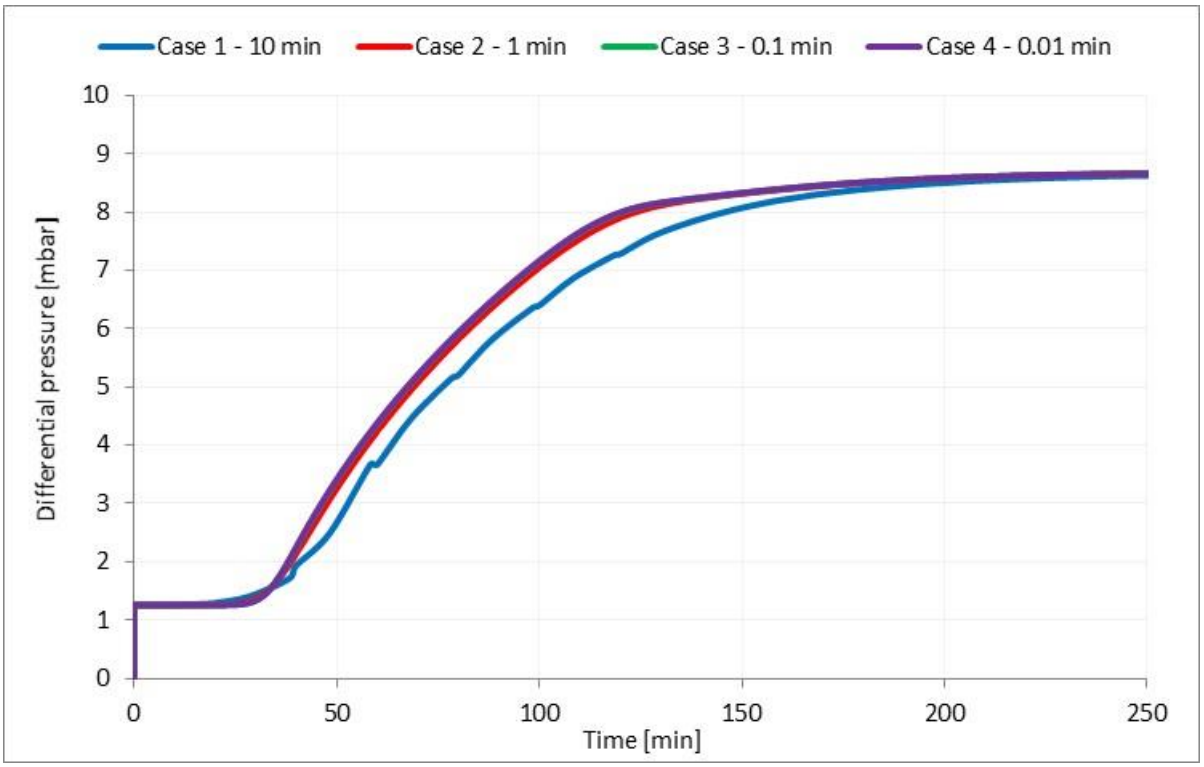

Figure 5.1 Time-step sensitivity simulation output on pressure build-up in block (107,1,1)

Case 1 simulated the largest time-step of the cases tested and consequently displays poor grid resolution and smearing of the pressure front, indication of numerical dispersion. Cases 2, 3 and 4 show little numerical dispersion and simulation time would be improved using the time-step from case 2, however; as computational time and output file size was not severely affected and minimal numerical dispersion was achieved when lowering the time-step to Case 4 this was preferred going forward to ensure optimal grid resolution and accurate simulation output. Further, as observed in figure 5.1 time-step size had no influence on the pressure build-up in block (77,1,1).

For the Bentheimer disk modelling it was imperative that the simulation model matched the experimental Bentheimer disk dimensions listed in table 3.1. Inclusion of the pressure port positions was also desirable. Therefore, only cases which could model the stated conditions were considered for the sensitivity study. It was further assumed that the radial model consisted of 1 layer, and the only direction of interest is therefore in horizontal direction during the sensitivity study.

Grid size is defined in the reservoir description group in the input-file and was studied by initializing the radial grid with grid blocks matching the Bentheimer disk dimensions. This implies that some cases (Case 1 and Case 2) required varying grid block lengths to match disk dimensions. Case 3 and Case 4 was initialized with grid blocks of uniform size. As a

reminder, simulation input-file was initialized with Case 4 time-step from table 5.1 and a Newtonian fluid of 10 centipoises viscosity. Table 5.2 summarize grid block numbers investigated along with individual grid block sizes. The grid block size row should be read as number of grid blocks (#) times corresponding size in centimetres; # * size in centimetres.

Table 5.2 Grid size sensitivity cases and corresponding MBE output

	Number of grid blocks	MBE [%]
Case 1	(8,1,1)	0.29
Grid block size (#*size) [cm]	1*1.2 1*0.5 2*1 2*2 1*3 1*4	-
Case 2	(67,1,1)	0.29
Grid block size (#*size) [cm]	12*0.1 54*0.25 0.5	-
Case 3	(147,1,1)	0.29
Grid block size (#*size) [cm]	147*0.1	-
Case 4	(1461,1,1)	0.29
Grid block size (#*size) [cm]	1461*0.01	-

Figure 5.2 shows sensitivity on differential pressure collected at a time when pressure stabilized (i.e., increasing time with decreasing grid size) as a function of radial distance.

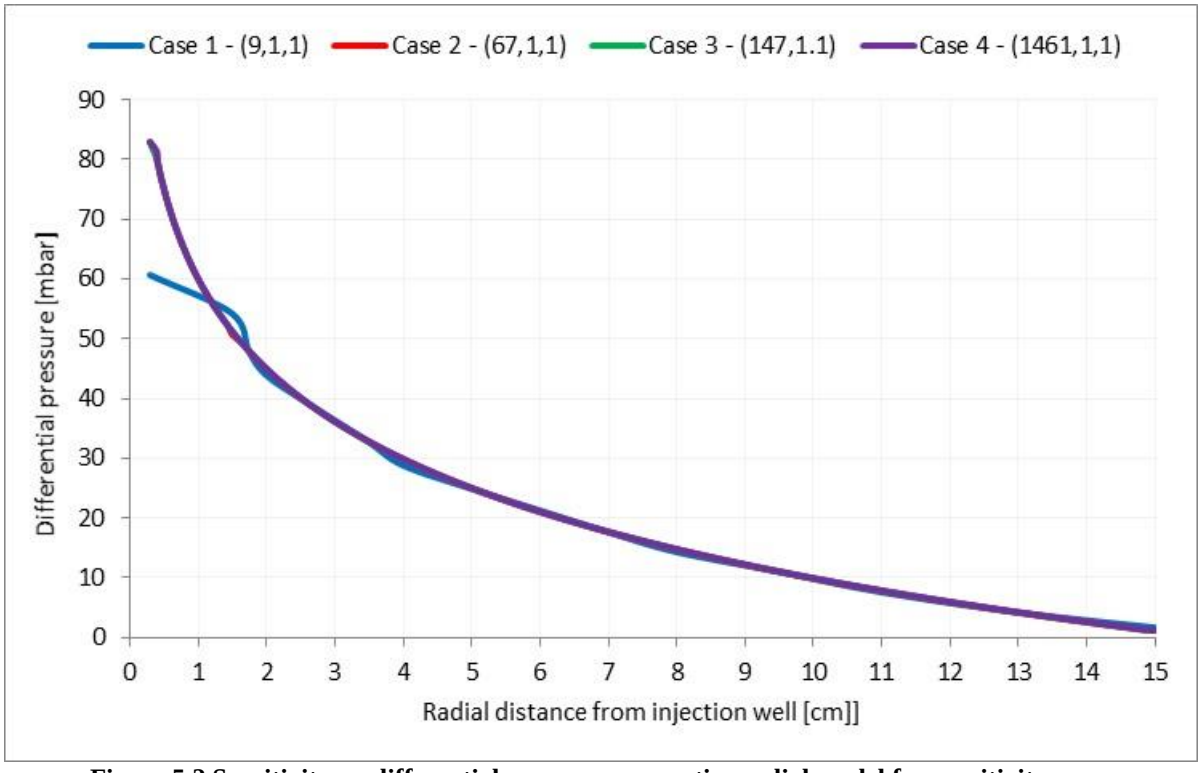

Figure 5.2 Sensitivity on differential pressure over entire radial model for sensitivity cases

Figure 5.2 demonstrates that Cases 2, 3 and 4 returns almost identical pressure build-ups. This indicates that once pressure is stabilized, Case 2 grid resolution is sufficient to return pressure values which do not improve significantly in Case 3 and Case 4, which consists of finer grid resolution (i.e., increasing number of grid blocks). Case 1 output, however, deviates significantly from the other sensitivity cases tested. The explanation for this can be made by considering how STARS returns pressure values. As reported pressure is an average pressure collected at the centre of each grid block, increasing the width of grid blocks consequently increase the pressure range within these blocks. Therefore, as Case 1 only consists of 9 wide grid blocks, compared to other cases; the reported average pressure from each block comprises a larger range of pressure values including lower pressures resulting in lower average block pressure.

Figure 5.3 shows viscosity development in a grid block 8 cm from the injection well for all cases listed in table 5.2.

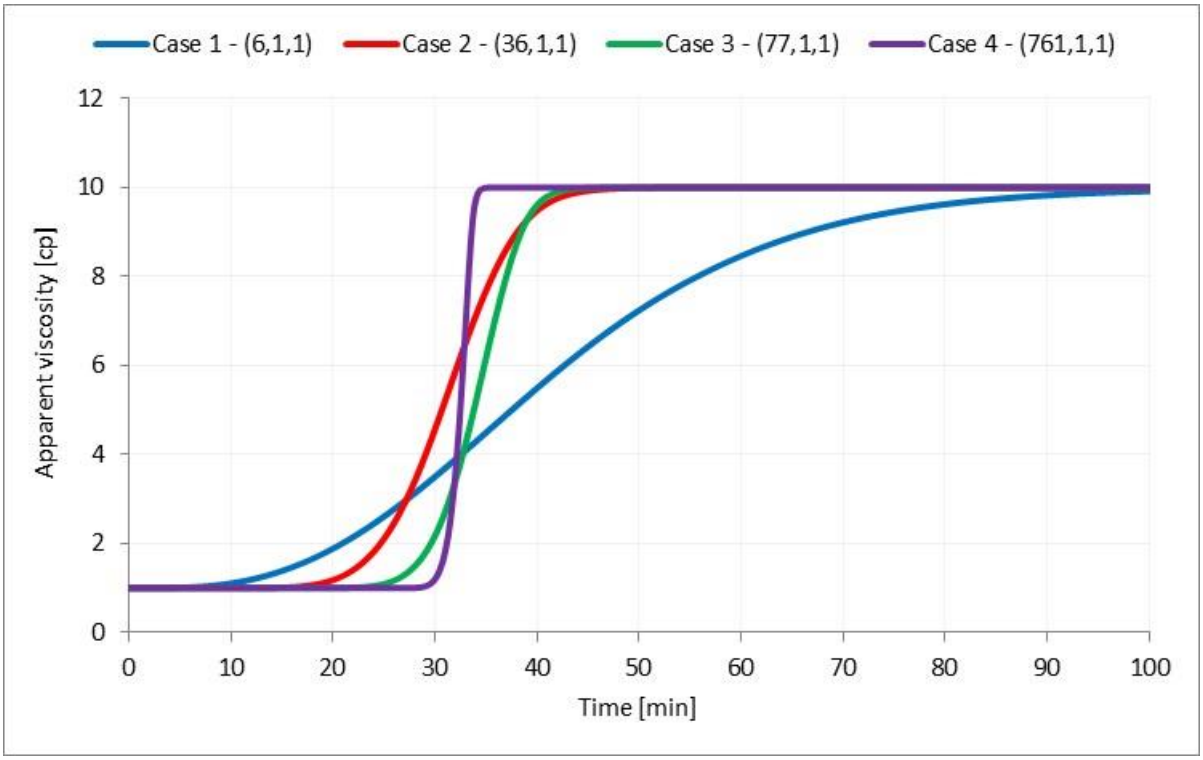

Figure 5.3 Grid size sensitivity simulation output on viscosity development in specific grid block

As seen in figure 5.3, significant numerical dispersion is present for simulation output of Case 1 and Case 2, showing decreasing effects with increasing number of grid blocks. For Case 4 the numerical dispersion effect is of neglecting magnitude. This is in accordance with the numerical dispersion effect description given by Fanchi (2006) [22] where numerical dispersion is said to decrease with increasing grid resolution.

Based on the findings in figure 5.2 and figure 5.3, Case 3 was selected for input-file initialization. This is based on the significant simulation time and computer memory required for Case 4, despite having the least numerical dispersion effect.

5.2 Polymer Molecular Mass and Mole Fraction

Molecular weight is defined in kg/mol in STARS and is specified by the CMM keyword in the input-file. STARS limit the molecular weight range to not exceed 15 000kg/mol, thus; molecular weights over this value were not tested. Molecular weights commonly used in polymer EOR applications, as described in section 2.4.1, was used for input-file initialization. Mole fractions in the input-file rely heavily on molecular weights, and was therefore calculated accordingly and tested by initializing corresponding mole fractions in the input file using equation (5.1). [47] An example of mole fraction calculation based on provided polymer concentrations is provided in appendix B.2.

$$x_i = \frac{n_i}{n_{tot}} \tag{5.1}$$

Table 5.3 Molecular weight sensitivity cases and corresponding MBE output

	Molecular Weight [kg/mol]	Mole fraction	MBE [%]
Case 1	15 000	1.20e-09	27.21
Case 2	10 000	1.80e-9	38.91
Case 3	8000	2.25e-9	19.17
Case 4	2000	9.00e-9	9.99

As seen in table 5.3, high molecular weight polymers return unacceptably large material balance errors resulting in poor convergence of the Newton iterations performed by the simulator. Therefore, comparison of these results graphically was not pursued as further simulation input-files would not be based such high material balance errors. Material balance errors between 0.1-1 percent indicate that convergence is under control, whereas errors greater than 5 percent indicate considerable convergence errors requiring remediation. [43] Therefore, running subsequent simulations with MBE of the magnitude experienced in table 5.3 is not appropriate as simulation results would be coupled with large uncertainties.

STARS offer an option for dealing with material balance errors by lowering convergence tolerance values. However, overwriting default convergence tolerance values result in additional iterations during the simulations. Remedying errors of the magnitude experienced in table 5.3 would therefore result in longer simulation runs which were not desirable.

Another sensitivity run was therefore performed to investigate if the material balance error could be circumvented without increasing simulation time. Following the trend observed in table 5.3, this was conducted by decreasing molecular weights and corresponding mole fractions while examining that pressure build-up was unaffected by the decreasing molecular weights. Cases for the new sensitivity run are listed in table 5.4 in which the 10 000kg/mol case was scaled by a factor of 10 for each run.

Table 5.4 Molecular weight and mole fractions for second sensitivity run and corresponding MBE output

	Molecular weight [kg/mol]	Mole fraction	MBE [%]
Case 1	10 000	1.8e-09	28.97
Case 2	1000	1.8e-08	7.42
Case 3	100	1.8e-07	0.25
Case 4	10	1.8e-6	34e-04

Figure 5.4 show the effect on pressure development in block (17,1,1) from cases listed in table 5.4.

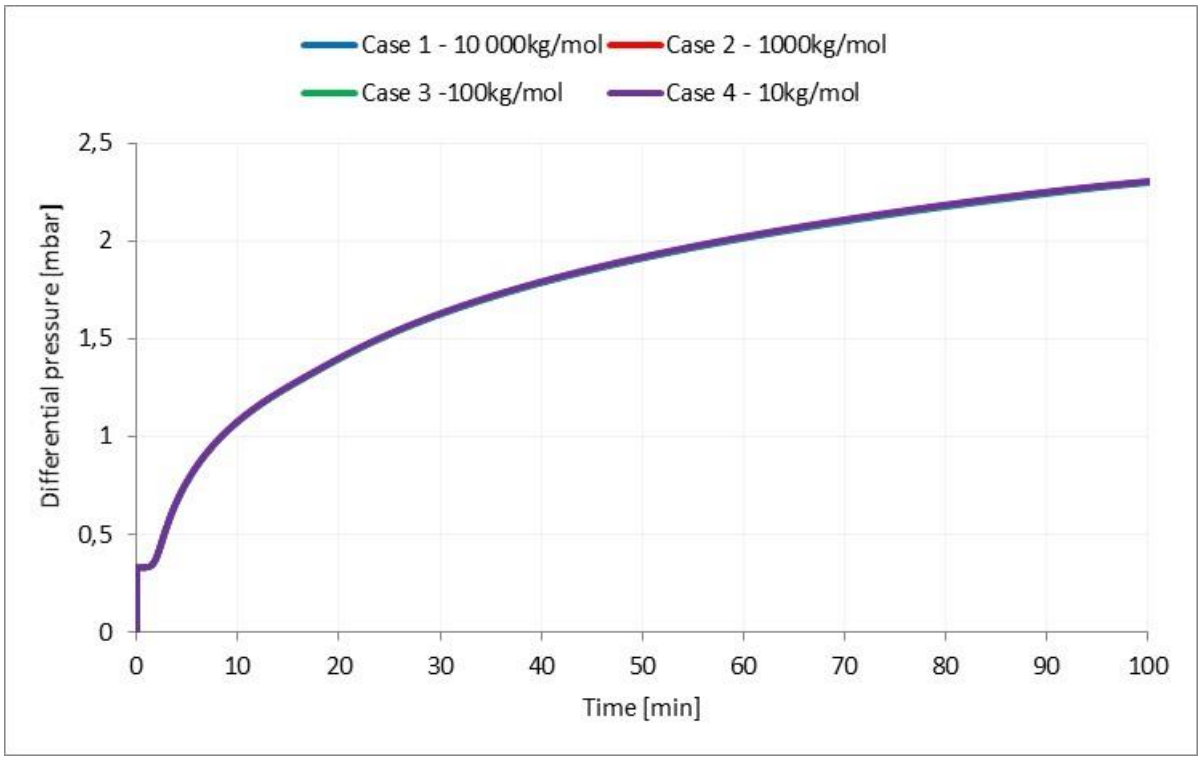

Figure 5.4 Molecular weight sensitivity on pressure development in block (17,1,1)

As seen in figure 5.4 molecular weights and mole fractions have an insignificant effect on the pressure development in the block. However, as in table 5.4 the material balance error is significantly decreased when lowering molecular weights and corresponding mole fractions. Therefore, the procedure of scaling molecular weights was an efficient way of circumventing significant material balance errors, lowering simulation time while returning results not associated with large uncertainties.

Going forward, the 10kg/mol value was used for subsequent simulations to minimize material balance errors and improve confidence in simulation output.

5.3 Polymer Adsorption

Polymer adsorption characteristics are included in several ways by STARS, associated with the specific adsorption of the polymer, defined in ADSTABLE, and by the adsorption capacity of the modelled rock, defined by ADMAXT. [43] Further, pertaining to the adsorption characteristics in the simulation model is also the reversibility of the polymer adsorption, specified through ADRT, and the polymer residual resistance factor, specified by RRFT. Sensitivity studies on these adsorption related keywords are conducted in the order in which they appear in the input-file in appendix C.2.

Due to limited experimental adsorption data, the preferred option for investigating polymer adsorption effect on the simulations was to input adsorption values in tabular form, thus, allowing for greater flexibility during the study. This was achieved using the ADSTABLE keyword. Another option was to use a Langmuir isotherm composition dependency specified via ADSLANG. As this option was not pursued the procedure of including adsorption by Langmuir isotherms is not described further. Description of the ADSLANG keyword can, however, be found in the STARS User Guide (2016). [43]

As it was necessary to include all keywords in the input-file while conducting the sensitivity study other keywords were lowered sufficiently to not influence the simulation runs. Initially the values associated with each keyword was specified as listed in table 5.5

Table 5.5 Initial adsorption related keyword values

	Value
ADSTABLE [mol/cm^3]	1.8e-10
ADMAXT [mol/cm^3]	1.8e-10
ADRT [mol/cm^3]	1.8e-10
RRFT	1

5.3.1. Polymer Adsorption

Polymer adsorption was specified by the ADSTABLE keyword in STARS. Resulting adsorption of the polymer is specified in tabular form in which input is entered in two columns; one containing mole fractions and the other containing corresponding adsorption at specified mole fraction. Input in the adsorption table for all cases listed in table 5.6 was entered as adsorption at 0 mole fraction (consequently implying no adsorption) to adsorption at mole fraction 1.8e-6 found during the sensitivity study in subsection 5.2.

The sensitivity study was conducted by assuming the polymer adsorbed by a specific percentage of its mole fraction, listed in table 5.6. In table 5.6, stated ADSTABLE values are corresponding percentage value of 1.8e-6 mole fraction.

Table 5.6 Polymer concentration adsorption cases

	Percent adsorbed [%]	ADSTABLE	MBE [%]
Case 1	5	9.8e-8	23e-4
Case 2	10	1.8e-7	23e-4
Case 3	15	2.7e-7	23e-4
Case 4	30	5.4e-7	23e-4

Figure 5.5 shows pressure development in block (17,1,1) from the simulation output for cases listed in table 5.6.

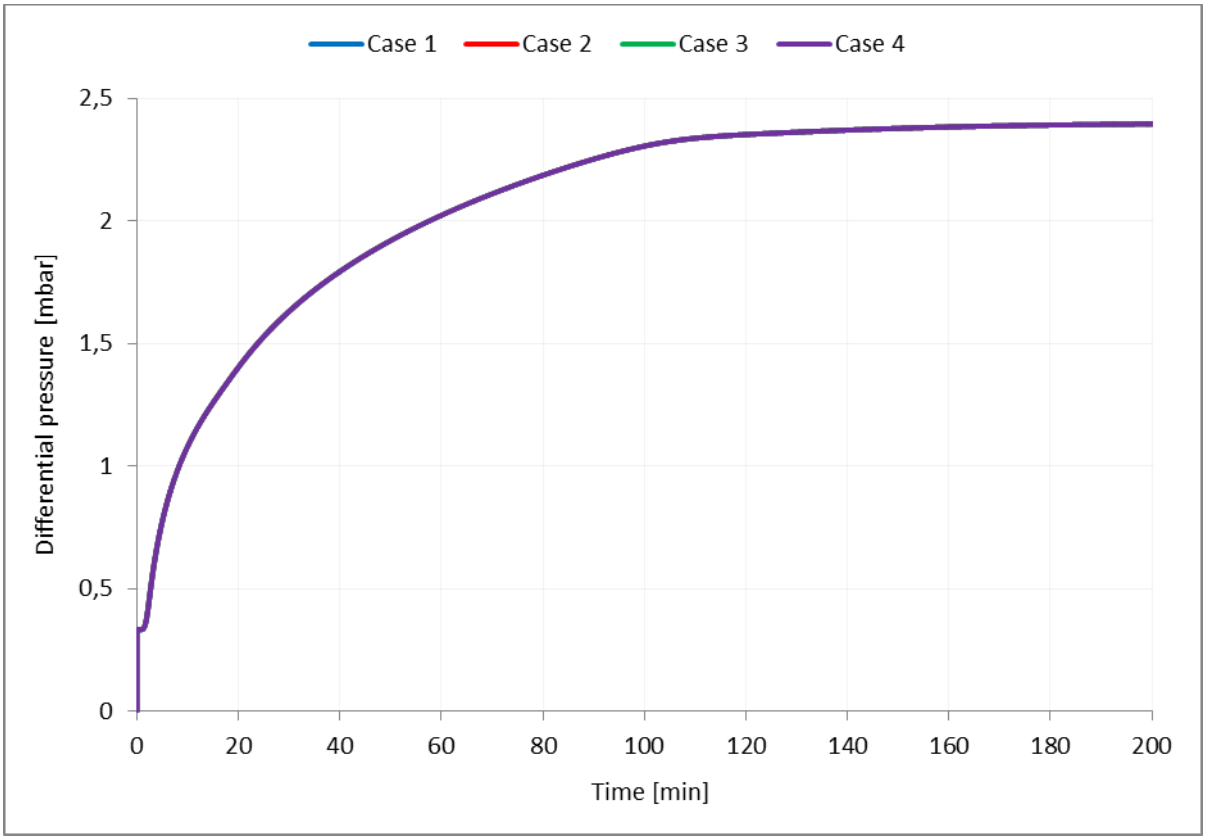

Figure 5.5 Polymer concentration adsorption sensitivity on pressure build up in block (17,1,1)

As seen in figure 5.5, polymer adsorption specified in table 5.6 has no influence on the polymer propagation. The reason for the insignificant effect is the dependency on the porous rock adsorption capacity, defined through ADMAXT. If the adsorption capacity is specified by a certain value, no adsorption occur when this value is reached, as shown graphically in figure 5.6 in a plot of polymer adsorption as a function of radial distance from injection well. As mentioned, adsorption capacity was specified as 1.8e-10gmol/cm^3 for all sensitivity runs.

Figure 5.6 Polymer adsorption as a function of radial distance from injection well

In figure 5.6, all sensitivity cases tested in the simulation runs return the same amount of adsorbed polymer due to the adsorption limitation set by the porous media, specified by the ADMAXT keyword.

5.3.2. Porous Rock Adsorption Capacity

The amount of polymer which can be adsorbed at the modelled porous rock surface is defined by ADMAXT in the input-file. For the sensitivity study the polymer adsorption values listed in table 5.7 were kept constant and ADMAXT was set equal to corresponding values listed in table 5.7.

Table 5.7 Concentration adsorption and maximum rock adsorption sensitivity run

	ADSTABLE	ADMAXT	MBE [%]
Case 1	9.8e-8	9.8e-8	23e-4
Case 2	1.8e-7	1.8e-7	23e-4
Case 3	2.7e-7	2.7e-7	23e-4
Case 4	5.4e-7	5.4e-7	23e-4

Figure 5.7 show pressure development in block (17,1,1) from the sensitivity cases listed in table 5.7

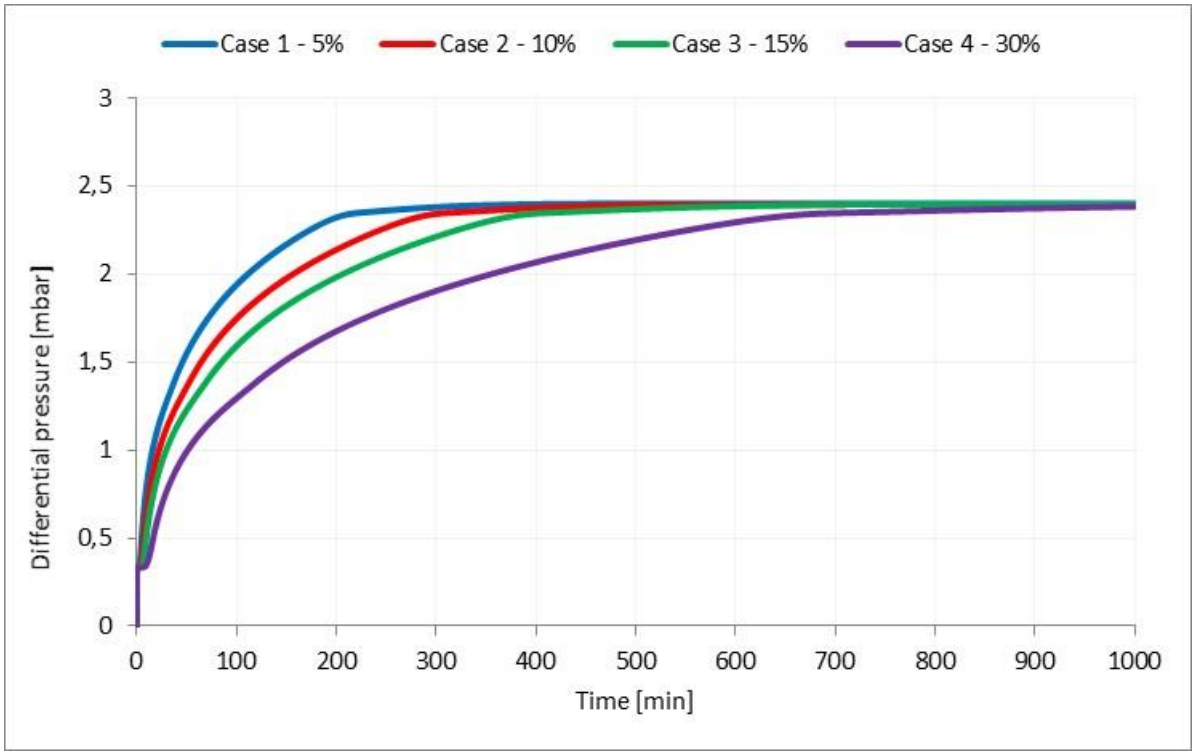

Figure 5.7 Rock adsorption capacity sensitivity on pressure build up in block (17,1,1)

Comparison of figure 5.7 and figure 5.5 show equal stabilized pressure values for all sensitivity cases as rock adsorption capacity increases, however; the time before reaching stabilized pressure conditions is significantly increased when adsorption increases. Thus, as polymer adsorption increases, the resulting polymer propagation is significantly delayed and requires injection of more polymer solution to reach stabilized pressure conditions.

However, as polymer adsorption has an insignificant role on stabilized pressures in the model, history matched in Chapter 6, adsorption is kept low as to decrease simulation time.

5.3.3. Reversible and Irreversible Polymer Adsorption

Residual adsorption level is defined by ADRT in the input-file. If ADRT is set equal to 0 adsorption is completely reversible, whereas an ADRT value equal to ADMAXT specifies completely irreversible polymer adsorption. ADRT values within these extremes specify partial reversible adsorption. All scenarios are tested in the sensitivity study to investigate the effects on stabilized pressure as listed in table 5.8..

Following the sensitivity study in the previous subsection, the input files are initialized with adsorption values of Case 1 from table 5.7 to minimize simulation time.

Table 5.8 Polymer adsorption reversibility sensitivity cases

	ADRT	MBE [%}
Case 1	0	0.68
Case 2	4.9e-8	0.68
Case 3	ADMAXT (=9.8e-8)	0.68

Figure 5.8 show pressure development in block (17,1,1) from sensitivity cases listed in table 5.8.

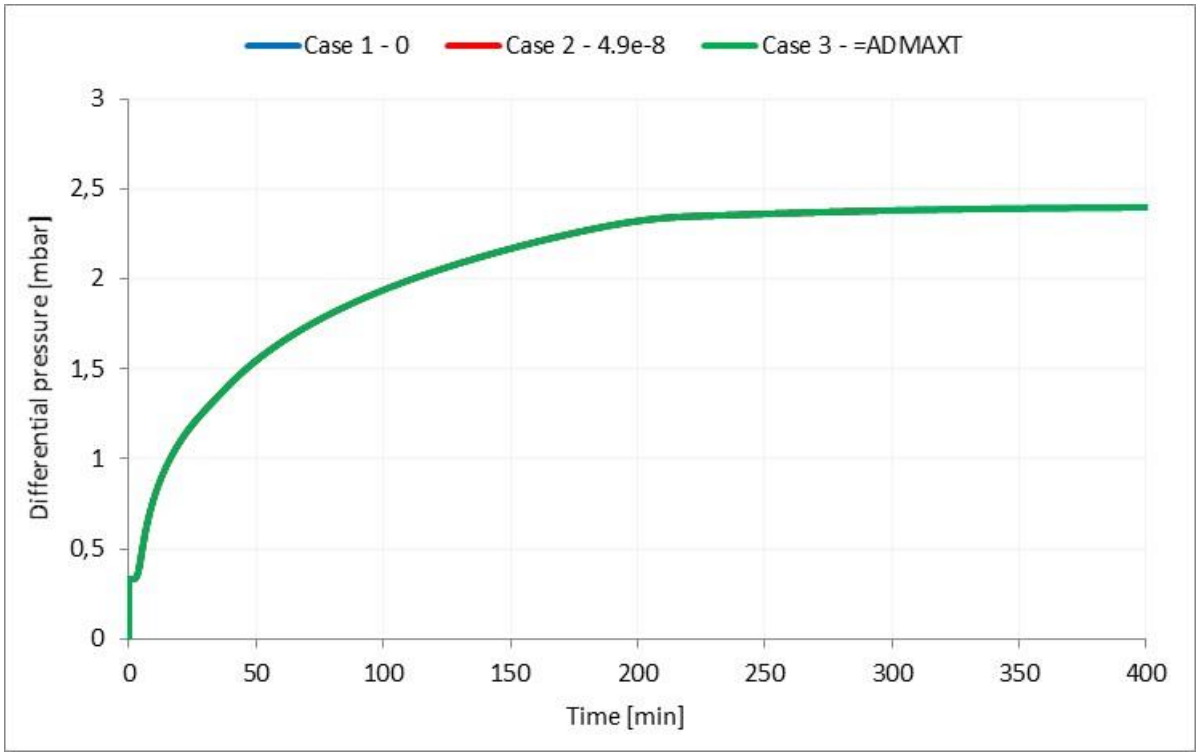

Figure 5.8 Adsorption reversibility sensitivity on pressure build up in block (17,1,1)

In figure 5.8, adsorption reversibility has a neglecting effect on polymer propagation and pressure development. As polymer is the only phase injected the consequence of the polymer adsorption reversibility is not detectable and do not influence neither the polymer propagation nor the pressure response during the polymer flooding.

5.3.4. Residual resistance factor

The residual resistance factor for the adsorbing polymer component is defined by RRFT in the input-file. The residual resistance factor was described in section 2.5.6, and is a measure of the permeability reduction caused by adsorption and mechanical entrapment.

To investigate the effect of residual resistance factor three cases were tested, listed in table 5.9. An RRFT value of 1 is the STARS default value and indicate no permeability reduction during the flooding sequence. However, increasing RRFT results in larger permeability reductions during the fluid flow.

Table 5.9 Residual resistance factor sensitivity cases

	RRFT	MBE [%]
Case 1	1	0.13
Case 2	3	0.13
Case 3	5	0.13

Figure 5.9 show pressure development in block (17,1,1) from the sensitivity cases listed in table 5.9.

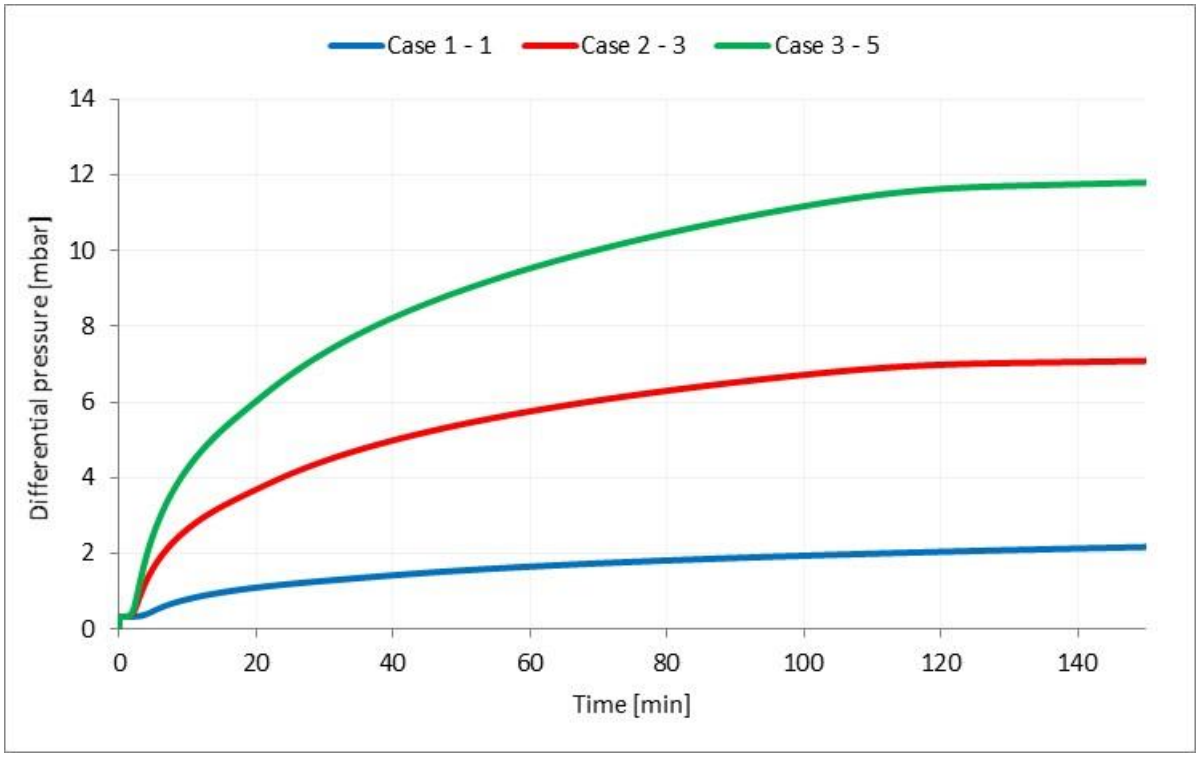

Figure 5.9 Residual resistance factor sensitivity simulation output

Figure 5.9 show that the residual resistance factor has a significant impact on the stabilized pressure value, and is considerably higher for increasing resistance factor. Clearly, the effect of residual resistance factor has to be accounted for due to its importance for the pressure matches in subsequent pressure history matches.

It is desirable to limit the amount of matching parameters, and a way to circumvent the influence of the residual resistance factor is to incorporate the permeability reduction into the

apparent viscosity. The viscosity is directly proportional to the permeability, and instead of varying the residual resistance factor during the history matches, the apparent viscosity will be utilized to account for any permeability reductions and consequent increased differential pressures. Therefore, the apparent viscosity values found from the history matches will likely be overestimated.

5.4 Inaccessible Pore Volume

IPV was discussed in section 2.5.4 and is included by specifying the PORFT keyword in the STARS input-file. Four cases were tested as listed in table 5.10.

A PORFT value of 1 indicates that all pores are accessible, whereas a value of 0.7 indicates that 70% of the pore volume is accessible. In the literature, IPV values of 30% have been recorded for some porous rocks, thus this extreme is also included in the test.

Table 5.10 Inaccessible pore volume sensitivity cases

	Accessible Pore Volume
Case 1	1
Case 2	0.9
Case 3	0.8
Case 4	0.7

The results from the simulation runs using the cases listed in table 5.10 are shown in figure 5.10 as a function of time for grid block 12 in the radial model.

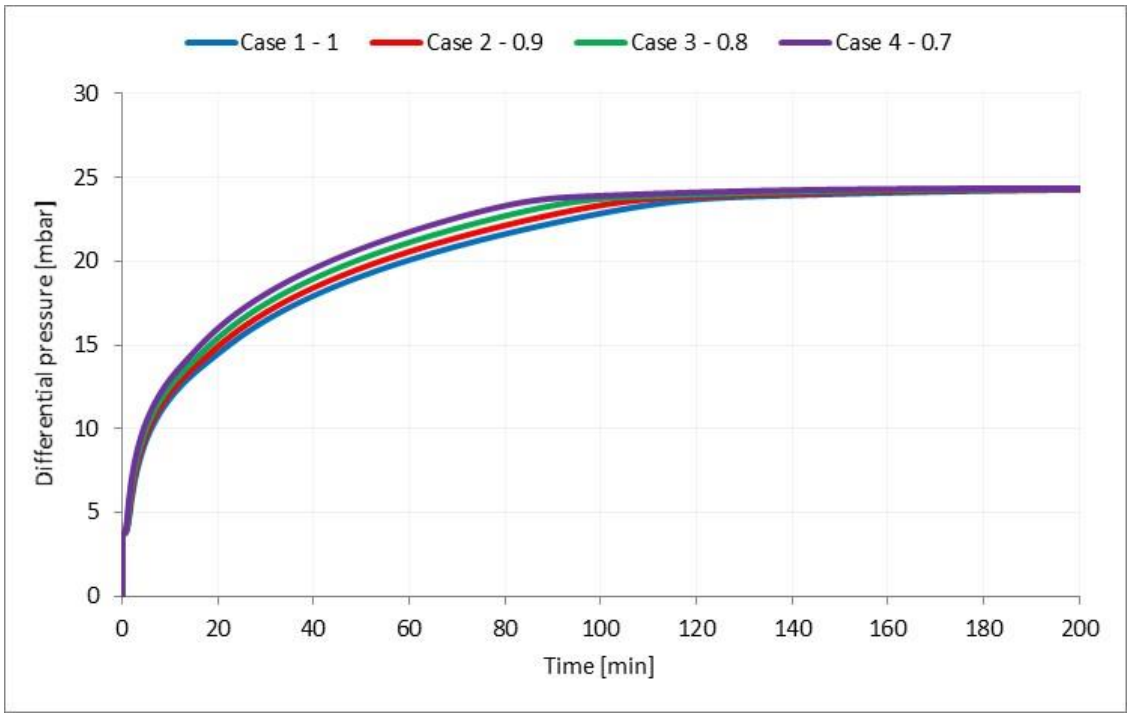

Figure 5.10 Inaccessible pore volume sensitivity simulation output

As seen in figure 5.10, higher IPV values promote accelerated polymer propagation through the radial model, in accordance with theory discussed in section 2.5.4. However, the influence of IPV is negligible once stabilized pressure is attained showing convergence at the same stabilized pressures for all cases. Thus, IPV affect the pressure in an insignificant way and the input-file is therefore initialized with an IPV value of 1, indicating all pores available for the polymer.

5.5 Polymer Viscosity

To verify that the input file was properly initialized following the sensitivity study in previous subchapters, a sensitivity study was carried out on the initialized viscosity behaviour defined in the SHEARTAB. Sensitivity cases listed in table 5.11 were tested during this study.

Table 5.11 Polymer apparent viscosity sensitivity cases

	Viscosity [cp]	MBE [%]
Case 1	1	0.29
Case 2	5	0.29
Case 3	20	0.29
Case 4	50	0.29

The results from the simulation runs using the cases listed in table 5.11 are shown in figure 5.11 as a function of time for grid block 12 in the radial model. As mentioned, the aim for conducting this sensitivity study was to investigate if the simulator was properly initialized to accurately model the defined polymer rheology.

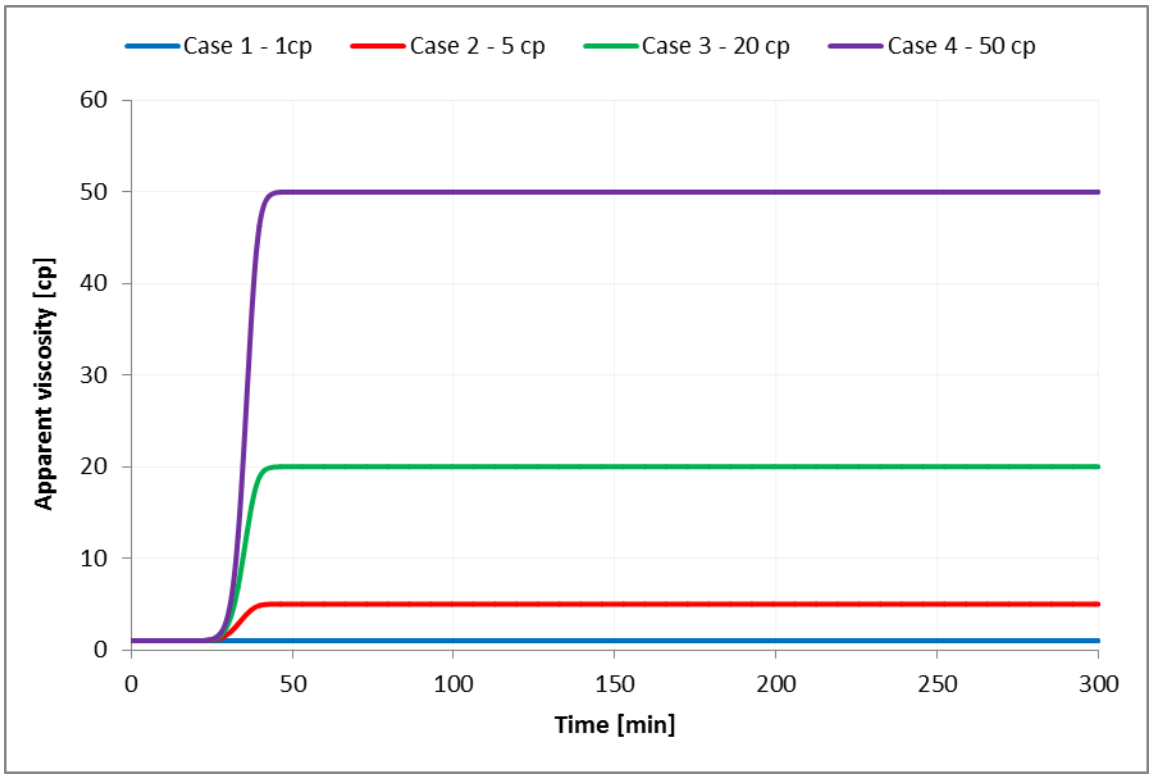

Figure 5.11 Sheartab viscosity sensitivity simulation output

As seen in figure 5.11 the defined viscosity is attained for all cases, indicating that the simulator follow the specified viscosity input in the SHEARTAB. Further, numerical dispersion is also minimized for all cases in figure 5.11 and the material balance error is seen to be within the recommended limits for the STARS simulations.

5.6 Summary Sensitivity Study

Based on the sensitivity study in the previous subsections the input-file was initialized with pertinent keywords and values from these findings. As observed, few parameters affected the pressure build-up in the model and it was therefore focused on minimizing material balance error and simulation time.

Table 5.12 lists results from sensitivity studies conducted in previous subchapters with values used for initialization of the input-files for the HPAM and xanthan simulations.

Table 5.12 Initialization parameters for polymer simulation scripts

	HPAM	Xanthan
DTMAX	0.01	0.01
GRID	(148,1,1)	(147,1,1)
CMM [kg/mol]	10	10
Mole fraction	1.8e-06	1.60e-06
ADSTABLE [gmol/cm^3]	9.8e-8	9.8e-8
ADMAXT [gmol/cm^3]	9.8e-8	9.8e-8
ADRT	9.8e-8	9.8e-8
RRF	1	1
PORFT	1	1

Figure 5.12 show the radial model created in STARS during the sensitivity study. The radial disk is as listed in table 5.12 modelled using 148 grids in horizontal direction during HPAM flooding and 147 grids in horizontal direction for xanthan simulations, each with a width of 0.1 cm. Hence, the radial model matches the Bentheimer disk dimensions listed in table 3.1 and table 3.4. Further the radial model consists of 1 layer in vertical direction.

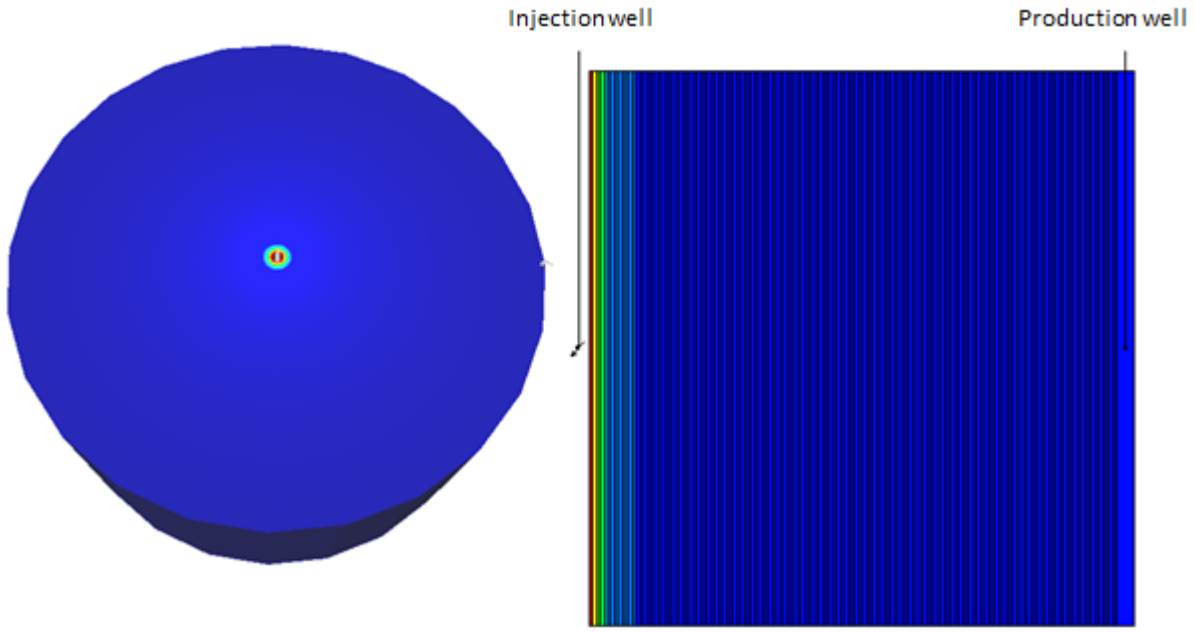

Figure 5.12 STARS radial simulation model

6 Results and Discussion

Waterflooding and polymer flooding sequences performed in experiment H-1 and X-1 have been simulated and pressure recordings history matched. Input-files for the STARS simulator were created based on findings in the sensitivity study conducted in Chapter 5. History matching of recorded pressures was first conducted manually using the STARS simulator before automatic history matching using MRST with the EnKF module was performed.

Pressure recordings in experiment H-1 have been corrected for backpressure, pertaining to both waterflooding and polymer flooding pressures, giving a boundary condition of 0 millibar at the outlet rim. This boundary condition was applied for the xanthan simulations, however; these values were not backpressure corrected due to the limited pressure recordings near the outlet rim from the xanthan flooding sequences. Nevertheless, results are reported as differential pressures in graphs due to the defined boundary condition.

History matching of waterflooding pressures were performed using the permeability as tuning parameter. This follows from Darcy's law for radial flow, equation (2.4) in which permeability is the only free variable in the single phase simulation model. The waterflooding simulations therefore allowed for determination of rock permeabilities.

From the sensitivity study in Chapter 5 it was noted that no parameters, except for the residual resistance factor, influenced the pressure distribution within the radial model apart from polymer viscosity. As no permeability reduction is considered during the simulation study, by reasons discussed in subsection 5.3.4, and assuming all properties of the medium constant the polymer apparent viscosity is used to history match the experimental pressure values.

6.1 Waterflooding Simulations

Input-files used for waterflooding simulations were created based on the sensitivity study file from Chapter 5 by inhibiting all polymer related keywords in table 5.12 and defining a Newtonian fluid of 1 centipoise. MRST simulations were performed following the procedure outlined in section 4.2.

6.1.1. H-1 Waterflooding History Match – STARS simulations

Differential pressures from waterflooding sequences performed in experiment H-1 was history matched using permeability values listed in table 6.1. From the history matches the radial disk was divided into three regions, region radiuses are indicated by the permeability subscripts in table 6.1, of local permeability.

Table 6.1 H-1 radial model permeabilities from STARS waterflooding history matches

	$K_{R1(0.6\ cm)}$ [D]	$K_{R2(5.1cm)}$ [D]	$K_{R3(9cm)}$ [D]
$Q_{5ml/min}$	0.08	3.15	2.40
$Q_{10ml/min}$	0.15	3.15	2.40
$Q_{15ml/min}$	0.23	3.15	2.40
$Q_{20ml/min}$	0.36	3.15	2.40

Figure 6.1 show the history matched result for the 10ml/min injection rate using permeability values listed in table 6.1 compared to calculated analytical permeability solution from 1.5 cm to outlet rim listed in table 3.2. History matches from other injection rates are located in appendix A.1.

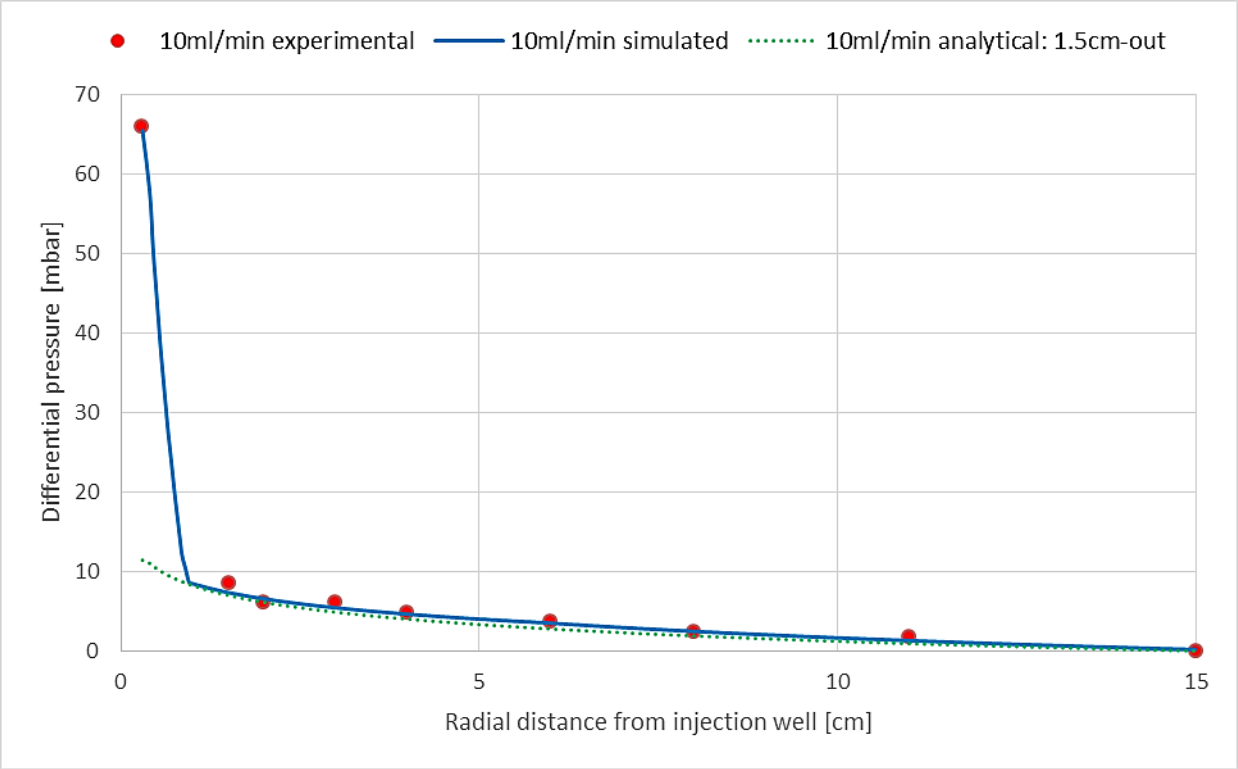

Figure 6.1 H-1 differential pressure matched 10ml/min waterflooding injection rate as a function of radial distance compared to analytical solution

An improved pressure match is seen in figure 6.1 when using a heterogeneous permeability field compared to the uniform 10ml/min analytical solution. In accordance with theory, described in subsection 2.1.2, the permeability in region 2 and region 3 are independent of flow rate and constant. However, permeabilities in region 1 from table 6.1 are significantly lowered compared to region 2 and region 3 permeabilities. Further, region 1 permeabilities display a rate-dependency showing a decreased permeability for decreasing injection rates. This low-permeability region is a result of the deviating pressure recorded by the well pressure transducer, as discussed in section 3.1. Due to the inverse proportionality between permeability and differential pressure in equation (2.4) a significantly lower permeability is required to match this higher-pressure point compared to other pressures in the radial disk.

The region of altered permeability may indicate presence of formation damage near the wellbore, commonly referred to as a skin zone, resulting in an increased pressure drop. [21] As the permeability should be a constant rock property an attempt was made to match the pressure values using a rate-independent permeability field. However, as seen in figure 6.2 when using the 10ml/min permeability field unacceptable matches of the first pressure point resulted for the other injection rates. Figure 6.2 have been scaled to only include the near-well region.

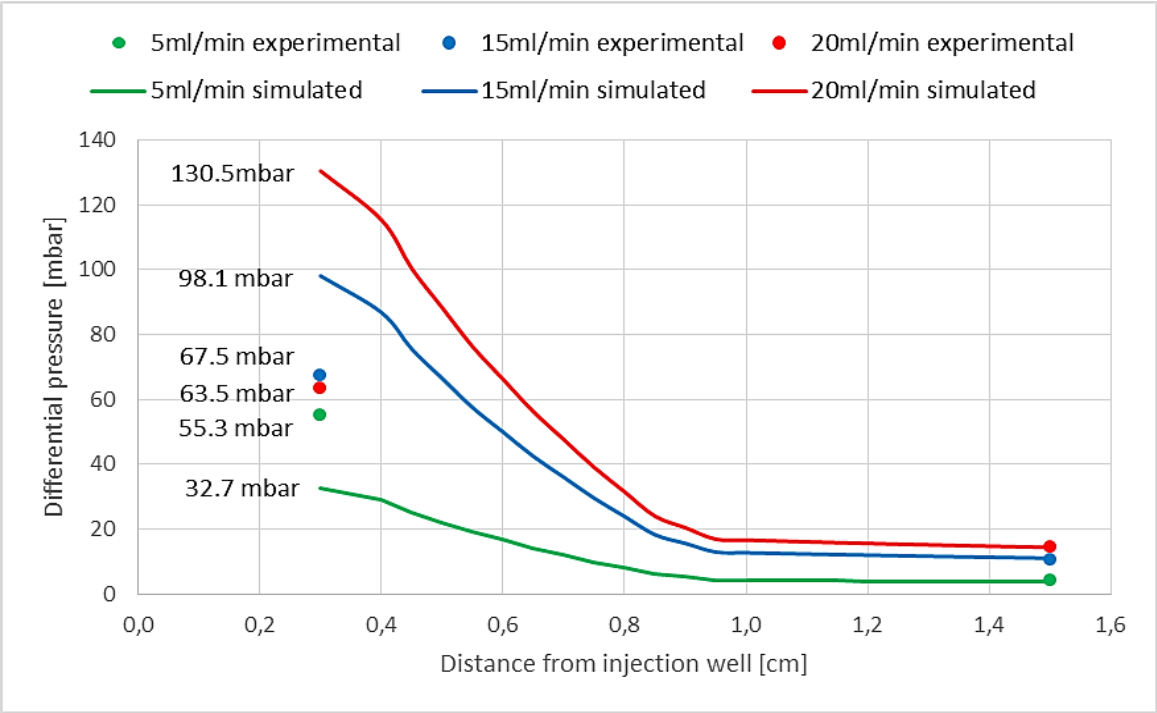

Figure 6.2 Differential pressure match of 5ml/min, 15ml/min and 20ml/min using the 10ml/min permeability field

The injection well region is of great importance when studying polymer rheology due to the high velocities experienced in the near-well vicinity. Following from the proportionality between viscosity and permeability in equation (2.4) it is clear that underestimation of permeability result in an underestimated apparent viscosity, whereas permeability overestimation results in overestimated apparent viscosity values.

The possible near-wellbore skin effect could be corrected for by calculating the increased pressure drop occurring by including the mechanical skin factor, S, to equation (2.4). The skin factor is defined as;

$$S = \left[\frac{K}{K_{skin}} - 1\right] ln\left(\frac{r_{skin}}{r_w}\right) \tag{6.1}$$

Where k_{skin} is skin zone permeability, K is formation permeability, r_{skin} is skin zone radius and r_w is wellbore radius. Inspection of equation (2.4) reveals that the lower permeability in the near-well region yields a positive skin factor, indicative of a damaged zone. [21] However, there are some complications when correcting for the skin effect. The extent of the formation damage in the disk is unknown which would result in uncertainties when correcting the pressure data for the skin factor. Ultimately the polymer rheology resulting from the pressure history matches would be affected by this uncertainty. Further, the first pressure

transducer reside in the injection well and is therefore subjected to conditions of both the well and the porous media adding additional uncertainty to this measurement as it is influenced by other factors than the remaining transducers.

Another approach was therefore pursed instead of correcting for the skin effect to account for this near-well permeability discrepancy. As the first pressure transducer gave an analysis of the near-well conditions this information was utilized for subsequent polymer simulations. Thus, assuming discrepancies influencing the waterfloods also influence the polymer flood in a similar manner, a plot was constructed of the near-well permeabilities from table 6.1 (blue dots in figure 6.3) as a function of injection rate. A linear regression line was then added as shown in figure 6.3.

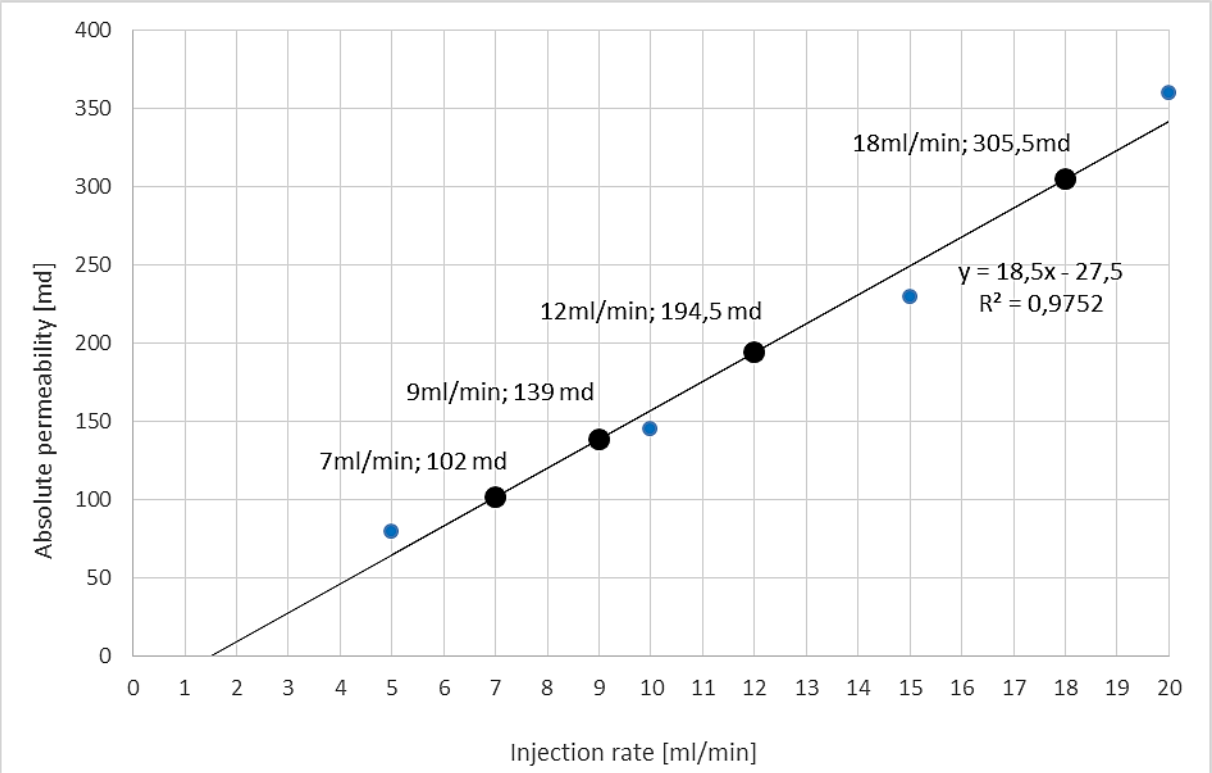

Figure 6.3 Region 1 permeabilities as a function of simulated injection rates and new calculated permeabilities for injection rates in the range 5ml/min to 20ml/min not history matched

From the linear regression line equation in figure 6.3 new permeabilities were calculated (black dots) for injection rates in the range 5ml/min to 20ml/min not previously history matched in the waterflooding simulations. For injection rates below 5ml/min, new permeabilities were not calculated as the permeability tended towards zero for the lowest injection rates yielding unreasonable permeability values corresponding to that of an impermeable rock. Instead the 5ml/min permeability field from table 6.1 was used for injection rates lower than 5ml/min. As seen in figure 6.3 the R squared value of the regression

line, indicating accuracy of the regression line fit, produces a value close to 1 signifying a good fit to the permeability data.

6.1.2. H-1 Waterflooding History Match – MRST Simulations

Differential pressures for the waterflooding sequences were history matched from values listed in table 6.2 using the MRST simulator. R_1, R_2 and R_3 denote radiuses of permeability regions, whereas K_1, K_2 and K_3 denote corresponding permeabilities for respective regions.

Table 6.2 H-1 radial model permeability regions and corresponding permeabilities from MRST waterflooding history matches

	R_1 [cm]	R_2 [cm]	R_3 [cm]	K_1 [D]	K_2 [D]	K_3 [D]
$Q_{5ml/min}$	0.97	12.37	1.37	0.09	2.93	0.75
$Q_{10ml/min}$	0.98	12.36	1.36	0.15	2.86	0.91
$Q_{15ml/min}$	0.97	12.42	1.31	0.24	2.99	1.07
$Q_{20ml/min}$	0.96	12.51	1.23	0.38	2.90	0.98

As seen in table 6.2, permeability values in the near-well region follow the trend observed in the STARS simulations displaying significantly lower values than the other permeability regions. The MRST results also show a rate-dependent permeability effect in the near-well region, with decreasing permeability values for decreasing injection rates. Region 3 permeabilities show a large decrease compared to corresponding permeabilities found in region 3 during STARS simulations, however; this is likely a result of a narrower region 3 in the MRST simulations. Region 2 constitutes most of the radial disk in the MRST simulations and show agreement with the region 2 permeability values from the STARS simulations.

Figure 6.4 show a comparison of the MRST simulation output and STARS simulation output for the 10ml/min injection rate.

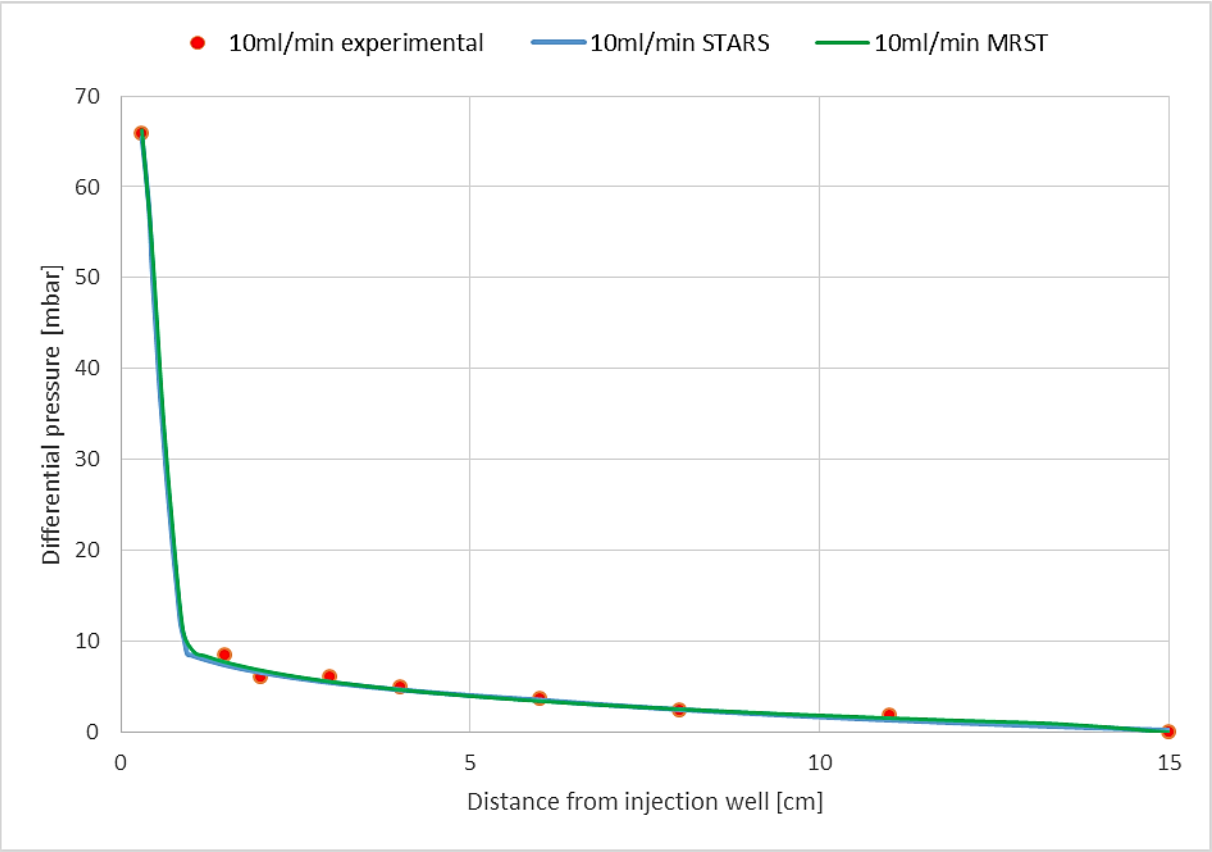

Figure 6.4 10ml/min differential pressure match comparison from STARS and MRST

As seen in figure 6.4 the curves are almost identical and overlap at most points with some very minor deviations occurring in the near-well region and towards the outlet rim. These deviations are likely a consequence of different radiuses for the permeability regions.

The similarities between the simulations enhance the confidence in both results and it is assumed that permeability will have an insignificant effect for rheology curve comparison from STARS and MRST in the polymer flooding sections.

6.1.3. X-1 Waterflooding Simulations – STARS

Table 6.3 lists permeability regions and corresponding permeabilities found from the STARS waterflooding simulations of experiment X-1.

Table 6.3 X-1 radial model permeabilities from STARS waterflooding history matches

	$K_{R1(0.6\ cm)}$ [D]	$K_{R2(0.6\ cm)}$ [D]	$K_{R3(0.6\ cm)}$ [D]	$K_{R4(0.6\ cm)}$ [D]
$Q_{5ml/min}$	0.25	1.80	2.75	0.44
$Q_{10ml/min}$	0.35	1.80	2.75	0.15
$Q_{15ml/min}$	0.37	1.80	2.75	0.15
$Q_{20ml/min}$	0.40	1.80	2.75	0.13

Figure 6.5 show the differential pressure match obtained from STARS for the 10ml/min injection rate using values listed in table 6.3.

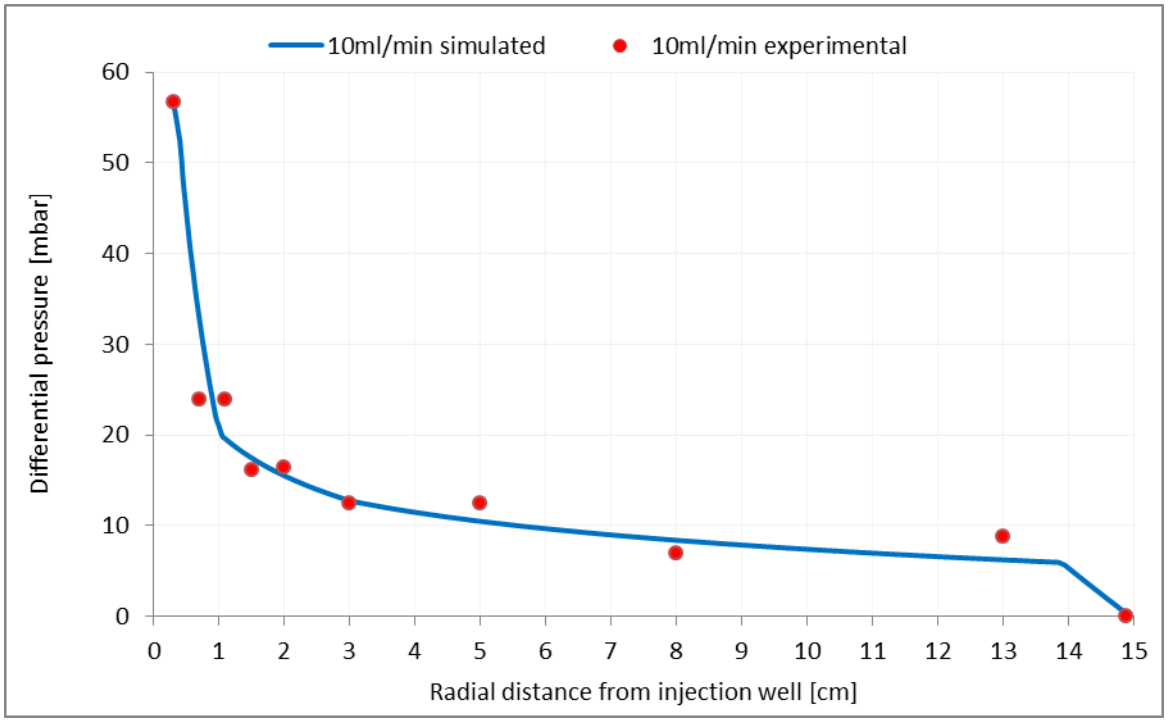

Figure 6.5 X-1 differential pressure matched 10ml/min waterflooding injection rate as a function of radial distance compared to analytical solution

The history match obtained in figure 6.5 gives a satisfactory match with the pressure, but the scattered nature of the data makes it difficult to match every pressure point accurately. The reason for the scattered pressure data was discussed in section 3.2.

From table 6.3 it is seen that the radial disk was divided into 4 regions of permeabilities. Region 4 permeabilities are significantly reduced compared to region 2 and region 3 permeabilities, and the reason for this discrepancy is the limited pressure data available from the xanthan flooding sequences. No backpressure corrections were made for the xanthan pressure data, and for consistency backpressure corrections were not performed for the waterflooding simulations either. Nevertheless, a 0 millibar pressure was defined at the outlet rim. Because of this both the water and polymer solutions experience an additional resistance near the outlet rim, manifested as a low permeability region and observed in Figure 6.5 near the outlet as the steep pressure decrease. This low permeability region was necessary to raise the curve sufficiently to obtain a pressure match for the remaining points. Implications of this condition for subsequent xanthan flooding simulations are further elaborated in section 6.2.2.

Near-well permeabilities are also significantly lower than region 2 and region 3 permeabilities. Discrepancies in the near-well region was discussed in section 6.1.1, and it is believed that factors affecting region 1 permeabilities in experiment H-1 also affect near-well permeabilities in experiment X-1, therefore this discussion is not repeated here. However, near-well permeabilities show significantly less rate-dependency, displaying equivalent values for the 10ml/min, 15ml/min and 20ml/min injection rates.

Figure 6.6 show the results from simulations of the 15ml/min permeability field on the 10ml/min and 20ml/min injection rate.

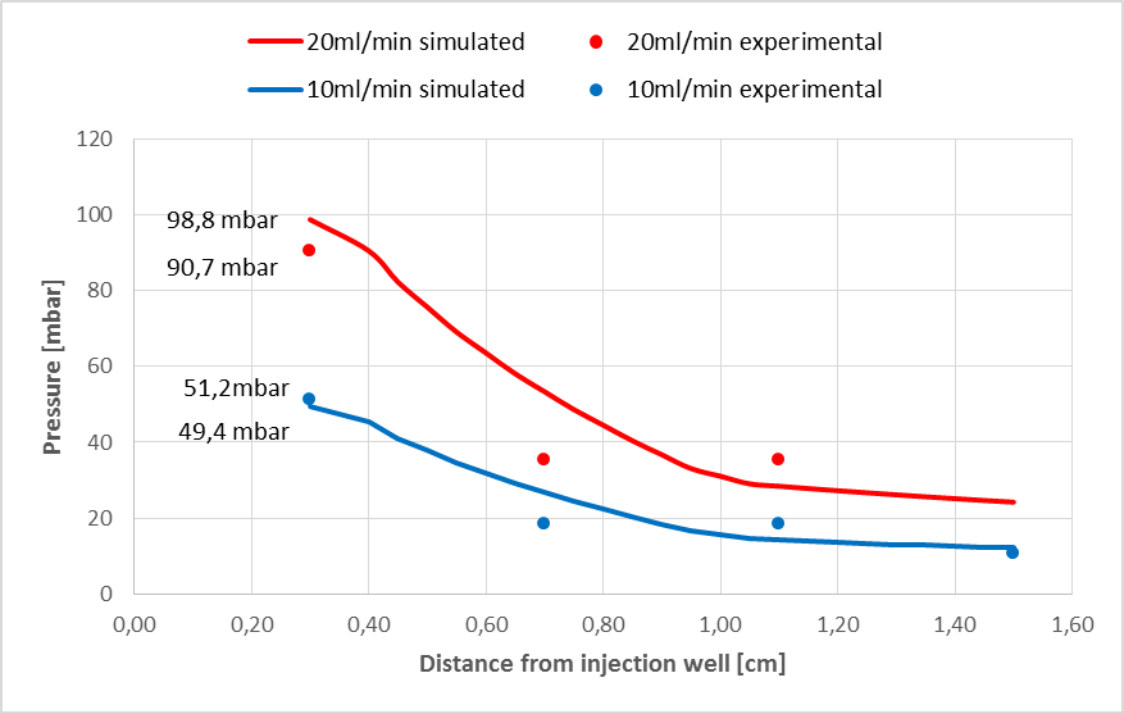

Figure 6.6 Differential pressure match of 10ml/min and 20ml/min using the 15ml/min permeability field

Only small deviations are observed for the 10ml/min and 20ml/min matches using the 15ml/min permeability field. Thus, the 15ml/min permeability field from table 6.3 is used for subsequent pressure matching of the xanthan flooding simulations. However, as seen in figure 6.6 the 5ml/min injection rate was omitted. This was due to severe deviations in the pressure match using the 15ml/min rate permeabilities. Further, as seen in table 6.3 the permeability in region 4 deviates significantly from other rates. Because of the high region 4 permeability the pressure curve is lowered considerably less than other rates, as seen in appendix A.5. Following from subsequent xanthan simulations it was observed that use of the 5ml/min permeability field yielded unsatisfactory pressure matches as the rheology curves from these simulations deviated significantly from the trend observed for rheology curves obtained using

the 15ml/min permeability field. Therefore, it was decided to view the results from the 5ml/min rate as a deviating measurement caused by the limited pressure data near the outlet.

6.1.4. X-1 Waterflooding Simulations – MRST Simulations

MRST permeabilities from the pressure matches are listed in table 6.4**.** R_1, R_2 and R_3 denote permeability region radiuses, whereas K_1, K_2 and K_3 denote corresponding region permeabilities.

Table 6.4 X-1 radial model permeability regions and corresponding permeabilities from MRST waterflooding history matches

	R_1 [cm]	**R_2 [cm]**	**R_3 [cm]**	**K_1 [D]**	**K_2 [D]**	**K_3 [D]**
$Q_{5ml/min}$	0.66	12.87	1.17	0.15	4.13	0.49
$Q_{10ml/min}$	0.65	12.87	1.18	0.23	2.33	0.19
$Q_{15ml/min}$	0.60	12.89	1.21	0.22	2.26	0.19
$Q_{20ml/min}$	0.64	12.86	1.20	0.27	2.90	0.15

Region 1 permeabilities listed in table 6.4 follow a similar trend as the STARS simulations displaying a significantly lower permeability than region 2. Region 3 show permeability values which deviates significantly from the region 2 permeabilities as well, but as mentioned; this is an effect arising from the uncorrected backpressure values.

Figure 6.7 show MRST simulation output for the pressure match of the 10ml/min injection rate compared to corresponding STARS simulation result.

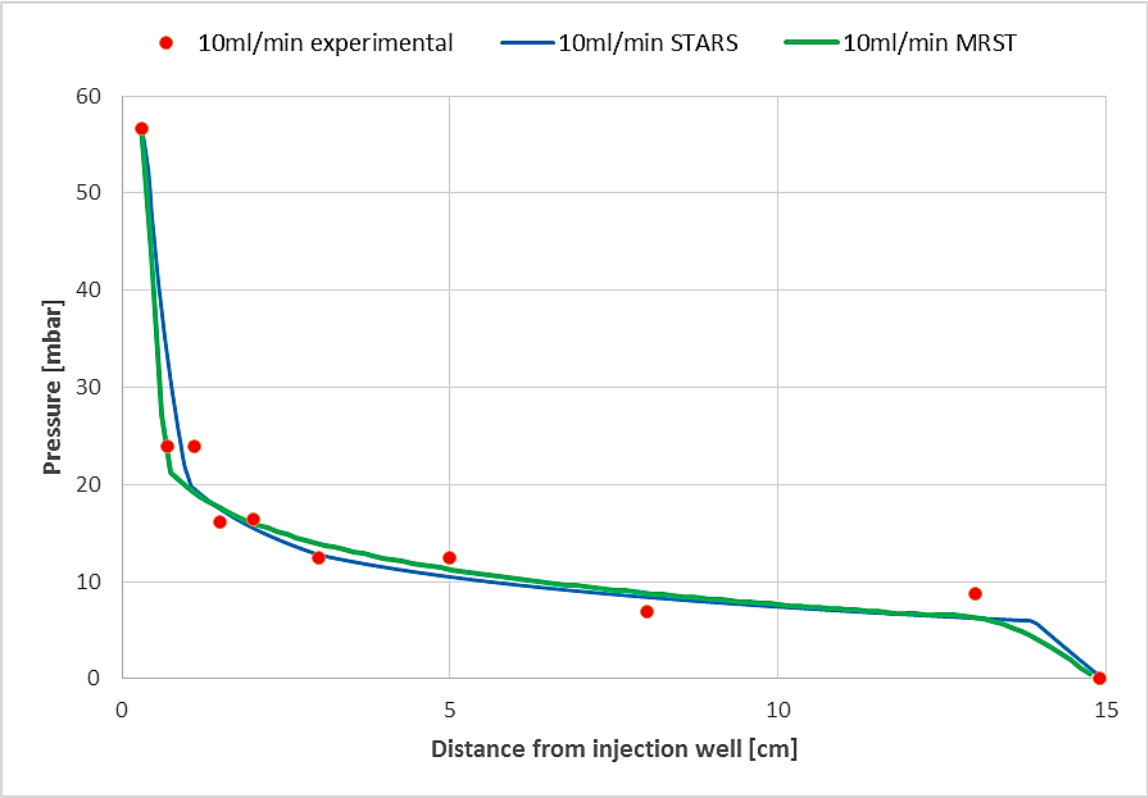

Figure 6.7 10ml/min differential pressure history match from STARS and MRST

Some deviations occur in figure 6.7 between the MRST pressure match and the STARS pressure match. The decrease in pressure towards outlet rim (region 3 in MRST and region 4 in STARS) is less steep in the MRST match due to a wider outlet region. Region 1 from the MRST results is narrower than for the STARS results yielding a steep near-well pressure incline. Further, region 3, extending from the fourth pressure point towards the second last pressure point, show a steeper increase in pressure than the STARS pressure match.

EnKF finds the best match for inputted pressure data based on iterations using equation (2.4) to find the minimum deviation with input data. Therefore, it is surprising that MRST apparently prefer to honour certain pressure points while neglecting others. For the manual simulations in STARS care was taken when finding a pressure match honouring most pressure points as the scattered nature made it difficult to identify potential outliers. An explanation for the poorer MRST match is the permeability region limitation. As region 1 and region 3 in MRST account for the entrance effect and the uncorrected backpressure respectively, only one permeability region is used to match most of the pressure data. Thus, MRST results are not as finely tuned as the manual results from STARS as only one region is available to match data in region 2.

Though there are some deviations in figure 6.7 between the STARS and MRST results, shape similarities between the curves exists apart from a slightly steeper curve from the MRST simulations. For consistency with the STARS simulations, the permeability field obtained for the 15ml/min simulation is used for subsequent xanthan simulations in MRST to compare rheology output at similar conditions from the simulations in section 6.2.2.1.

6.2 Polymer Flooding Simulations

Experimental pressures from polymer flooding sequences are matched using polymer apparent viscosity as tuning parameter. Input-files for STARS were initialized with permeabilities from the waterflooding simulations presented in previous subchapters. Further, pertinent polymer related keywords are included based on the sensitivity study conducted in Chapter 5 and summarized in table 5.12.

Simulation results from HPAM solution sequences are presented first. Due to a large amount of injection rates the results are presented separately in two subchapters; results from high injection rates and from low injection rates. Further, as several injections were performed at the same rate only the first injection rate during the HPAM flooding sequence is included in the rheology curves below. Remaining rheology curves and corresponding pressure matches are located in appendix A.1 and denoted with -2. Because of different rheological behaviours arising at higher and lower rates this also simplifies results discussion. For the xanthan polymer simulations fewer injection rates were simulated and the results are presented as a whole.

An important note, all rheology curves presented in the following subchapters and in the appendix are plotted with Darcy velocities on the x-axis in reverse, hence; velocities decrease along the x-axis. The rationale for presenting rheology curves in this manner is to illustrate the rheological behaviour arising in radial flow when the polymer encounter successive velocity reductions as it flows from injection well towards a circumferential boundary rim.

6.2.1. HPAM Flooding Simulations

6.2.1.1. HPAM Simulations for High Injection Rates – STARS Simulations

Figure 6.8 show HPAM rheology curves from corresponding differential pressure matches at high injection rates in a plot of apparent viscosity as a function Darcy velocity. History matched differential pressure graphs are located in appendix A.1.

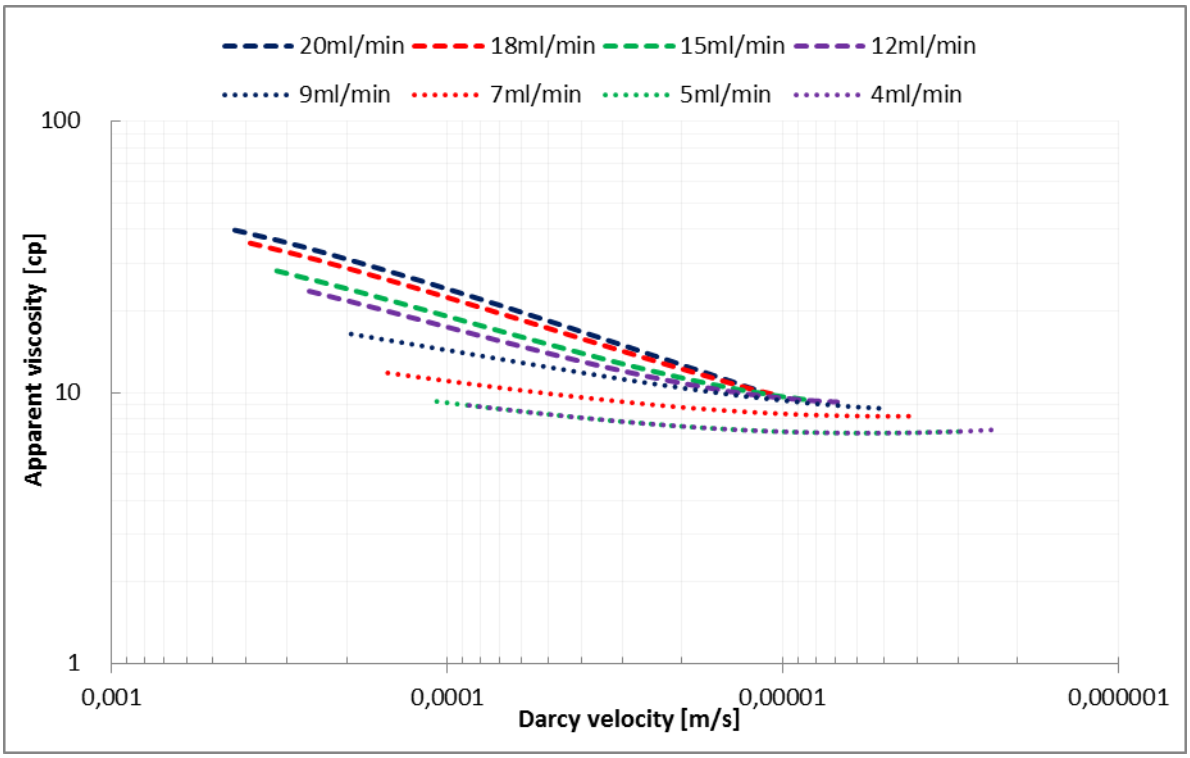

Figure 6.8 Apparent viscosities as a function of Darcy velocity for higher injection rates

In figure 6.8, shear thickening is present for all rates and is more pronounced for increasing injection rates. This is a result of the increasing velocities encountered for higher injection rates in the near well vicinity. Shear thickening behaviour extend the full radial distance from well to outlet for all rates, apart from the 5ml/min and 4ml/min rate, showing a diminishing effect as velocities decrease sufficiently for shear thickening to taper off near the outlet. The 5ml/min and 4ml/min injection rate show slight shear thinning behaviour at the lowest velocities near the outlet. This shear thinning behaviour is only noted in this section and is discussed in more detail in subchapter 6.2.1.2.

The shear thickening behaviour observed in figure 6.8 is in accordance with synthetic polymers viscoelastic character and is a well-documented effect reported by several authors for synthetic polymers flowing in porous media (Pye, 1964 [39]; Hirasaki and Pope, 1974 [48]; Masuda et al., 1992 [49]; Delshad et al., 2008 [36]). As described in section 2.5.1, shear thickening is attributed to flexible coil polymers elastic response when exposed to elongational forces when encountering high velocities in the porous media. If the polymer relaxation time is longer than the transient time between consecutive constrictions the polymer will not have sufficient time to adopt its equilibrium configuration and remains elongated. This conformational change from flexible coil to elongated conformation causes an

increase in the polymers apparent viscosity resulting in the characteristic shear thickening behaviour. This coil-stretch transition was illustrated in figure 2.13.

At high velocities and for lower injection rates little convergence is observed between the rheology curves in figure 6.8. In theory, one would expect the rheology curves to attain the same apparent viscosity when subjected to comparable velocities within the porous medium producing a continuing overlapping rheology curve. However, this is not the case and the curves are shifted upwards for increasing injection rates and curve convergence is only observed for some rates at lower Darcy velocities near the outlet.

This behaviour may be explained by considering the characteristics of viscoelastic polymers. Viscoelastic polymers display a memory effect due to their elasticity, meaning that their present behaviour is dependent on their deformational history. [31] Rheology curves in figure 6.8 are the result of varying injection rates, hence; the polymer are exposed to different deformational regimes in the porous media for each injection rate. Therefore, their rheological behaviour may differ from rheology curves attained from different injection rates (i.e. different deformational history). As velocities increases and the polymer undergoes increasing deformation, the polymer consequently require a longer time to adopt its equilibrium configuration giving rise to the lack of convergence observed in figure 6.8 between rheology curves attained from different deformational histories. Another explanation for the lack of convergence is the varying near-well permeabilities used throughout the simulations. This point is further elaborated in section 6.2.1.3.

From figure 6.8 there is no sign of mechanical degradation in the rheology curves for any rates as illustrated in figure 2.11. However, this is no definite indication on whether mechanical degradation has occurred during the flooding sequences. The extended Carreau model, equation (2.26) used to model the rheological behaviour of the polymers is not able to model the full range of polymer rheological behaviour apart from the mechanical degradation region. Therefore, this model restriction do not allow for mechanical degradation to be included and simulated in STARS, and the rheology curves in figure 6..8 consequently will not display signs of degradation.

RF (described in section 2.5.6) may be interpreted as polymer apparent viscosity from equation (2.30) Polymer apparent viscosity can therefore be approximated as the ratio of the polymer pressure drop to the water pressure drop, recorded before polymer exposure to the porous media.

Figure 6.9 show calculated resistance factors (coloured dots) for 20ml/min, 15ml/min and 5ml/min. 9ml/min is included in figure 6.9, however; the waterflooding pressure drop has been calculated using synthetic simulated values. 18ml/min, 12ml/min and 7ml/min have been omitted to make figure 6.9 more readable. To clarify figure 6.9, the RF values are only the coloured points, and the lines connecting these points have been added to aid the reader to the next RF value.

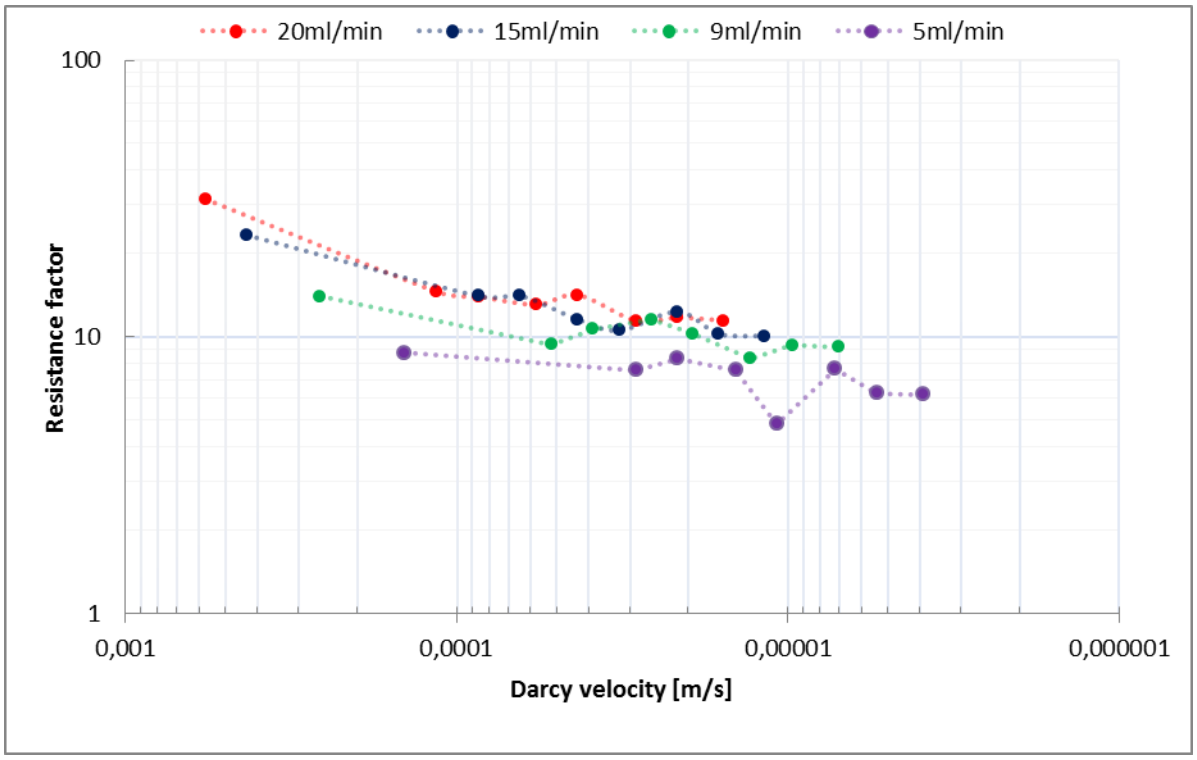

Figure 6.9 Resistance factor values as a function of Darcy velocity

Shear thickening behaviour observed in figure 6.8 is also prominent in figure 6.9, displaying the same trend of decreasing magnitude with decreasing injection rate. The slope of the shear thickening region appear to be steeper in figure 6.9 compared to the simulated results indicating quicker tapering off shear thickening behaviour. Like the simulation results in figure 6.8**,** little convergence between the rheology curves is observed at higher flow velocities, which again can be explained by the viscoelastic memory effect as discussed above. At lower velocities, however, curve convergence appears to be improved relative to the STARS simulation results. Further, no clear apparent shear thinning is observed for the rates in figure 6.9, although one could argue for slight shear thinning occurring at lower velocities for the 9ml/min rate.

Resistance factors in figure 6.9 fluctuates at intermediate to low flow velocities giving the impression of apparent shear thinning. These fluctuations, however, are likely an effect of the

radially distributed pressure transducers. As the transducers are positioned successively rotated 90 degrees with increasing radial distance, illustrated in figure 3.1, recorded pressures can be influenced by local variations in the porous media affecting the measurements. For example, a transducer located in a region experiencing higher degree of retention than other regions with consequent permeability reduction may return unexpectedly high pressures. This in turn affects calculated resistance factors by returning elevated values. The values in figure 6.9 thus further demonstrate the significance of performing simulations on experimental data when investigating polymer rheology compared to the commonly derived resistance factor apparent viscosities found in much of the literature. Nevertheless, resistance factors in figure 6.9 appear to support the overall trend observed from the STARS simulation results.

6.2.1.2. HPAM Simulations for Low Injection Rates - STARS Simulations

Figure 6.10 show rheology curves from lower injection rates in a plot of apparent viscosity as a function of Darcy velocity. Due to the large amount of rates simulated at lower rates, some rheology curves attained at equal injection rate have been omitted from figure 6.10 to make the figure more readable.

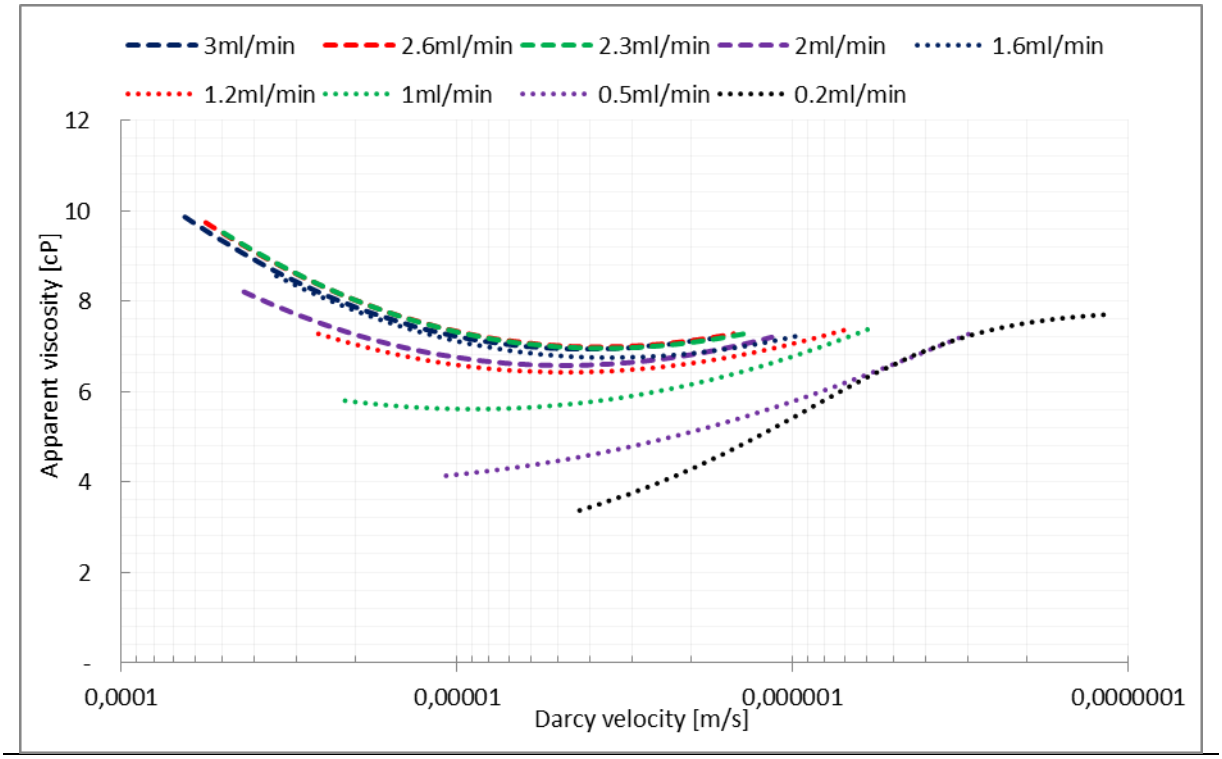

Figure 6.10 Apparent viscosities as a function of Darcy velocity for various lower injection rates

All injection rates in figure 6.10, apart from the 0.5ml/min and 0.2ml/min injection rate, display shear thickening behaviour in the near-well vicinity. The explanation for shear

thickening behaviour for higher injection rates discussed in section 6.2.1.1 also pertains to these lower injection rates and is therefore not repeated here. However, the decreasing shear thickening behaviour with decreasing injection rate trend observed in figure 6.8 is preserved for the lower injection rates. This further demonstrates the viscoelastic character of the HPAM polymer.

At intermediate flow velocities a plateau of lower viscosity is observed in the transition between shear thickening and shear thinning. This intermediate plateau can be interpreted as the region in which the viscous forces start to become dominant over elongational forces in the porous media which cause the apparent shear thickening behaviour. [31] This was described in subsection 2.5.1 as the phenomenon when the polymers viscous fluid nature became dominant over the elastic solid-like behaviour. As a consequence, a plateau of minimum polymer viscosity is observed marking the onset of shear thinning behaviour.

Shear thinning is observed for all rates in figure 6.10, however; this behaviour is slight for most rates down to 2ml/min becoming prominent only for the lowest rates of 2ml/min and below. As described in section 2.5.1, shear thinning occurs as shear forces become dominant over elongational forces during the polymer flow where molecular chains start orienting themselves in flow direction. This result in minimal interactions between the polymer chains and a decreasing polymer solution viscosity. For the 0.2ml/min injection rate, there are also signs of a slight lower Newtonian plateau observed at the lowest Darcy velocities near the outlet rim.

The onset of shear thickening for the synthetic polymer solution was found manually by inspecting rheology output data from the STARS simulations and is shown in figure 6.11.

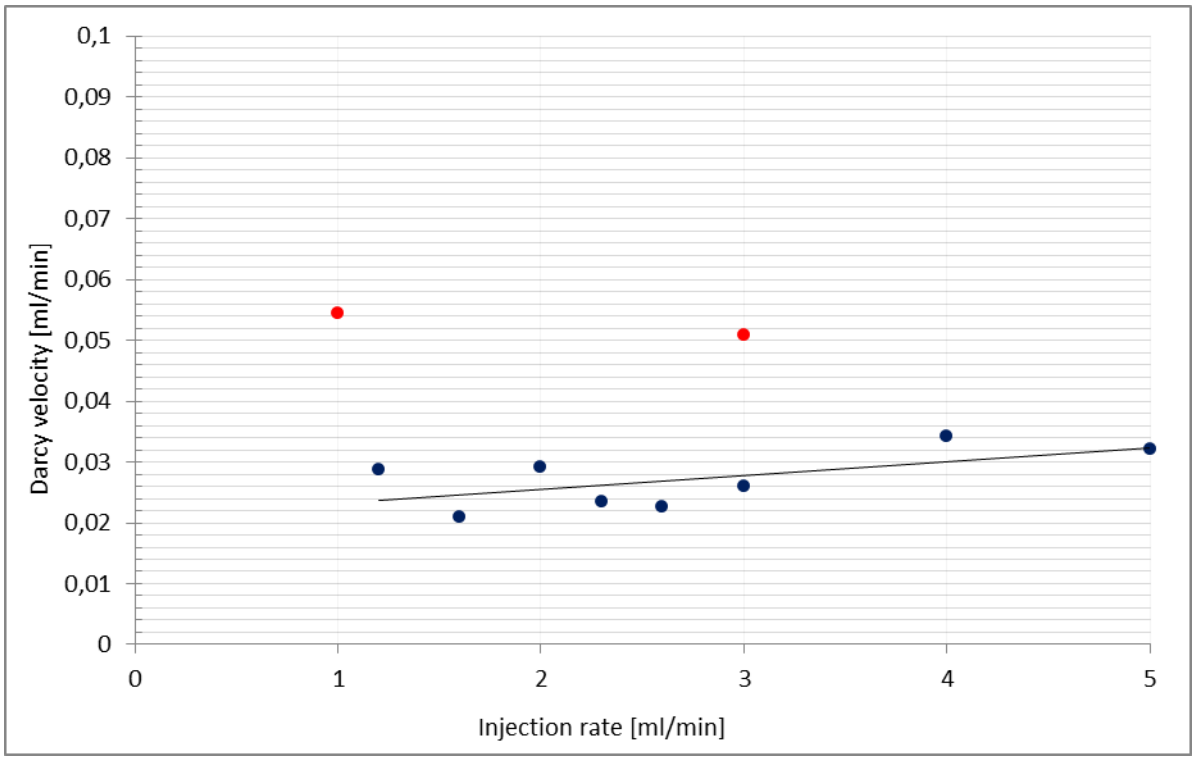

Figure 6.11 Darcy velocity marking onset of shear thickening for various injection rates

As seen in figure 6.11, onset of shear thickening occurs within a narrow range of Darcy velocities between 0.02ml/min and 0.035ml/min. Further, onset of shear thickening appear to occur at decreasing velocities for decreasing injection rates, although there are some fluctuations in the values. This trend of shear thickening onset at decreasing velocities for decreasing injection rates were also observed by Skauge et al. (2016) [29] in radial flooding geometry using a 2000ppm HPAM solution. During injections at 2ml/min and 5ml/min rates it was observed that the onset of shear thickening increased with increasing injection rate.

This was attributed to the viscoelastic character of the polymer and their inherent memory effect. As the polymer is elongated in the flow field, polymers injected at lower rates will experience a shorter shear thickening region due to lower encountered velocities in the well vicinity. Therefore, the time required to attain their equilibrium configuration will be smaller than polymer solutions which have experienced a larger degree of elongation at higher deformational regimes. Consequently, polymers experiencing the smallest degree of deformation returns to their equilibrium state quicker and closer to the wellbore than polymer deformed at higher injection rates. This is also illustrated in figure 6.12 which show the corresponding distance from the well in which the onset of shear thickening occurs.

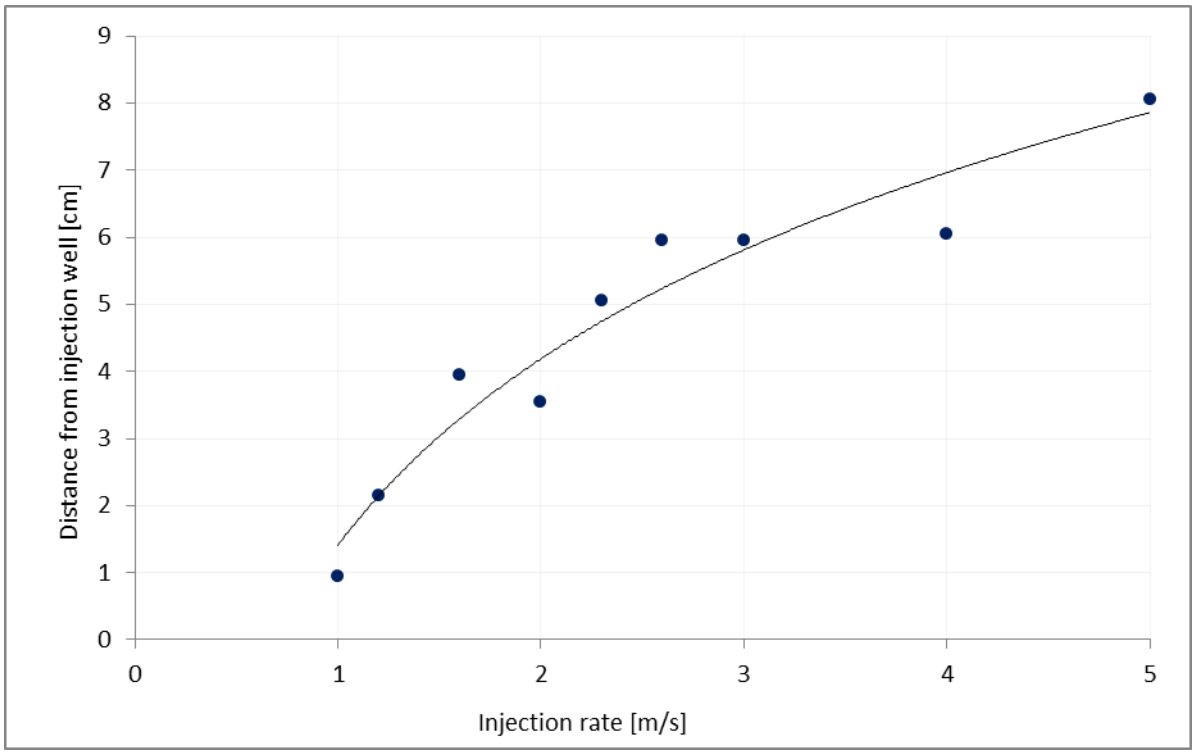

Figure 6.12 Distance from injection well where onset of shear thickening occur for various injection rates

As seen in Figure 6.12, the distance at which onset of shear thickening occur show a clear trend of shear thickening behaviour tapering off closer to the injection well for lower injection rates.

Further, the two red points in figure 6.11 are two deviating points collected during matching of the first 1ml/min injection rate and the first 3ml/min injection rate,. From the experimental data polymer solutions which were injected at equal rates returned significant different pressure drops. This is likely a consequence of retention or degradation affecting some rates more severely than other consequently returning deviating pressure measurements. Thus, obtaining equal rheological behaviour when matching pressures which are deviating from each other is impossible and consequently will result in some deviating rheological behaviours. Inaccurate pressure transducers were also considered as a possible explanation for these discrepancies.

Whereas shear thickening is an established effect for viscoelastic polymers there has been some discussion in the literature regarding their shear thinning behaviour in porous media. Some authors have reported mild shear thinning occurring at lower velocities (Heemskerk et al., 1984 [50]; Masuda et al., 1992 [49]; Delshad et al., 2008 [36]. Dupas et al. (2013) [34]), whereas others have reported apparent Newtonian or near-Newtonian behaviour (Seright et al., 2009, 2011 [51, 52]). Most studies on polymer rheology, however, have been conducted

in linear cores in which the flow regime is characterized by steady state conditions. Skauge et al. (2016) [29] studied the rheological behaviour of a 2000ppm HPAM in both linear and radial Bentheimer outcrop rock, and it was observed different rheological behaviour in the radial flow regime than the steady state flow regime. In the linear model the polymer displayed significantly higher apparent viscosity than in the disk experiment at high velocities. Further, a more pronounced shear thinning behaviour was observed in the radial disk at lower velocities, attributed to the different flow regimes experienced in the two flow geometries. In linear cores the polymer experience a constant cross-sectional area which is not incident in the increasing cross-sectional area experienced in radial flow where velocities decreases as the polymer propagates away from the injection well.

Overall, however, the mild shear thinning occurring in figure 6.10 is in agreement with findings from experiments conducted in both linear cores and results obtained by Skauge et al. (2016) in radial geometry.

The shear thinning observed in figure 6.10 is slight for most injection rates and a possible explanation for the mild shear thinning occurring can be made by considering the Bentheimer disk used in this experiment. As mentioned in previous subchapters, the near-well permeability was significantly reduced compared to the remainder of the disk. As described in section 2.5.3, entrapment of polymers are more likely in low-permeable rocks causing a decrease in the high-molecular weight species as these are most likely to be retained. Further, by inspection of table 3.3 it is observed that the 2ml/min displayed a viscosity loss of 12.5% compared to the injected polymer solution, indicating that retention or degradation occurred even for the lower injection rates. For the 2ml/min a larger viscosity loss was observed than for corresponding measurements at higher flow rates. Further permeability reduction, likely as a consequence of entrapment of polymers in the near-well vicinity, was confirmed by calculation of residual resistance factors in subchapter 6.3. A decrease in high molecular weight species causes a decreasing shear thinning behaviour of the polymer solution. This was observed by Lewandowska (2006) [53] who conducted viscometer measurements on HPAM solutions showing that increasing the amount of high molecular weight species resulted in a more pronounced shear thinning behaviour.

Further indications that shear thinning may not be as pronounced for the HPAM polymer in this experiment can be seen by investigating the provided differential pressure data. Skauge et al. (2016) [29] observed a relative pressure increase near the outlet in their pressure curves

attributed to onset of shear thinning behaviour. This trend of a relative pressure increase is not observed in the pressure data provided, demonstrated for the 5ml/min and 2.6ml/min injection rates in figure 6.13.

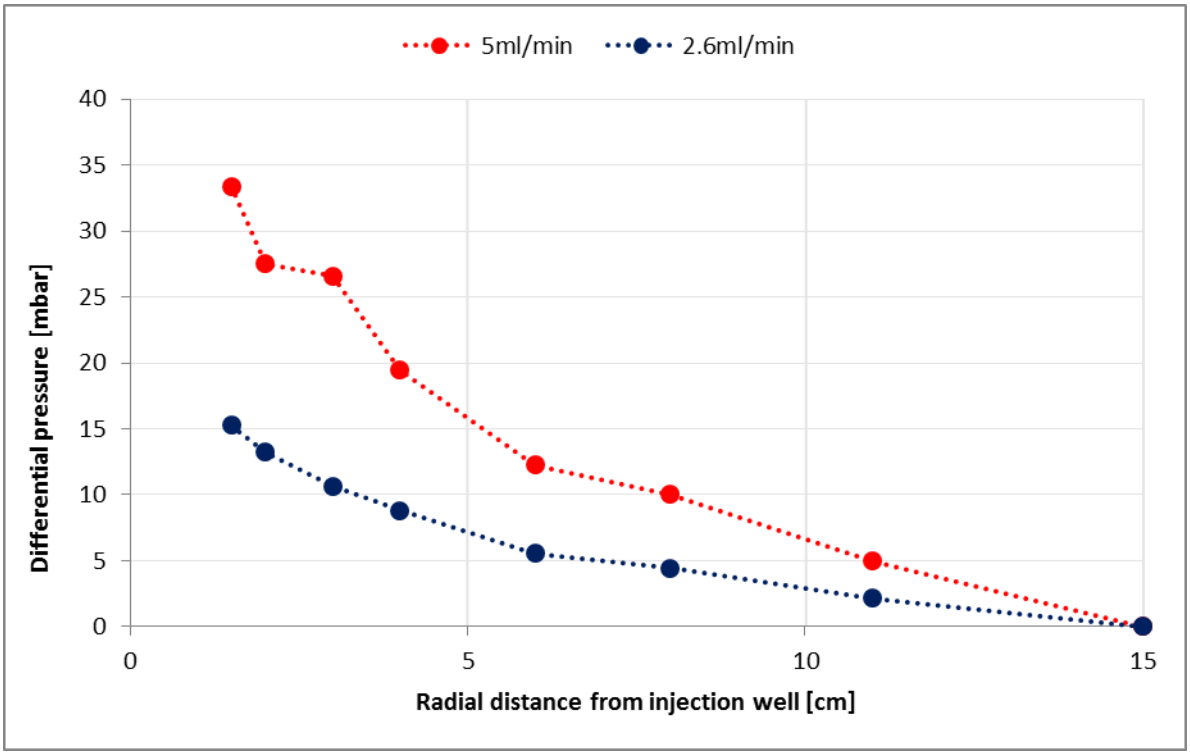

Figure 6.13 Differential pressures as a function of radial distance from injection well for 5ml/min and 2.6ml/min injection rates

In figure 6.13, the pressure drop appears to be continuously decreasing and there is little sign of a relative pressure increase or levelling off towards the outer rim indicating a prominent shear thinning behaviour. However, the absence of a relative pressure increase in the measured pressure from the HPAM flooding experiments may also be a result of too few pressure transducers located in this region of lower velocities. The 2.6ml/min pressures in figure 6.13 show a more gradual decrease in pressure toward the outer rim which may signify some slight degree of shear thinning occurring for the lowest injection rates.

Resistance factor calculations were performed for lower injection rates in the same manner as in section 6.2.1.1. However, these resistance factors fluctuated significantly and no clear trend was possible to distinguish from the values. The fluctuations are possibly a result of inadequate pressure transducers which are not able to accurately record the low pressures occurring for the lowest injection rates away from the injection well. Due to the fluctuating nature of the lower injection rate resistance factors the graphical result has been omitted from this thesis.

6.2.1.3. HPAM Flooding Simulations – Permeability Influence

During the waterflooding simulations it was observed that the near-well permeability showed a rate-dependent value which was accounted for by varying the near-well permeabilities. In theory, the permeability should be a constant rock property during single-phase water flow. Therefore, a simulation run was conducted to investigate the effect that the varying permeability had on the simulation results.

Figure 6.14 show rheology curves from corresponding differential pressure matches for selected injection rates.

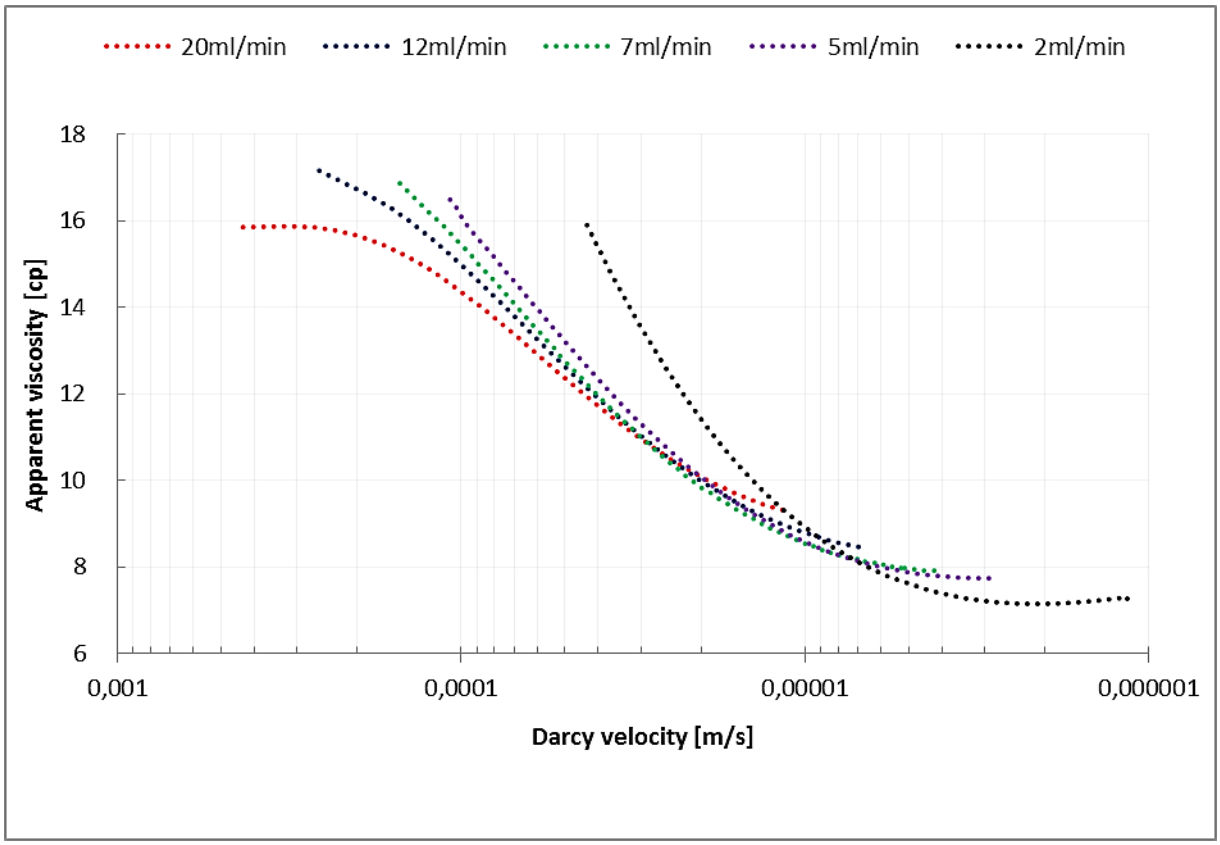

Figure 6.14 Apparent viscosities as a function of Darcy velocity for various injection rates using a constant heterogeneous permeability field.

From figure 6.14 it is observed that the rheology curves attain significantly different viscosity values than rheology curves obtained during simulations where varying near-well permeabilities were included. The 20ml/min injection rate, for instance, displays the lowest apparent viscosity near the injection well, in contrast to the result found in figure 6.8. The 2ml/min injection rate, on the other hand, display a significantly more pronounced shear thickening behaviour compared to results in figure 6.10. Further, using a rate-independent permeability field appears to improve convergence of rheology curves at intermediate

velocities compared to rheology curves from figure 6.8 and figure 6.10. However, the inherent memory effect of the polymers still appear to produce curves dependent on their deformational history, confirming the observations from earlier.

Further, the curves display shape similarities and appear to be parallel shifted left for consecutive injection rates. The slope of the shear thickening region, however, is still steeper for lower injection rates indicating a narrower shear thickening effect, in accordance with results found in previous subsections.

Despite maximum viscosity values in figure 6.14 deviate from previous rate-dependent findings the general rheological behaviour observed appear to be similar to the rheology curves from figure 6.8 and figure 6.10. Higher injection rates still display shear thickening over the full radial distance from injection well to outlet rim, whereas lower rates show slight shear thinning behaviour. Overall, the rate-independent permeability appears to have influenced the simulated rheology behaviour insignificantly, although yielding underestimated viscosity values for the highest injection rates and overestimated viscosity values for the lowest injection rates. This is in accordance with the initial discussion in section 6.1.1.

Based on resistance factor calculations performed in figure 6.9 the pursued method of varying near-well permeabilities appear to have been a correct approach to investigate the synthetic polymers in-situ rheology in the radial model. The lack of convergence experienced in figure 6.8 and figure 6.10, however, may have been enhanced by the permeabilities used during the simulation runs. This section, however, indicate that small variation in the conditions of the porous media when modelling a polymer flooding sequence can significantly influence simulated results. Care should therefore be taken when resolving issues which may arise from experimental data to accurately model polymers rheological behaviour.

6.2.1.4. HPAM Simulations – MRST

During the MRST simulations it was imperative that the EnKF range was defined sufficiently wide so that all rheological behaviours, if present, could be approximated by the MRST iterations. Initially, the range for all cases were defined as listed in table 6.5.

Table 6.5 Initial extended Carreau variable range for HPAM EnKF iterations

Parameter	EnKF range for ensemble members
λ_1	100000 – 100000000
λ_2	1000 – 1000000
n_1	0.1 – 0.99
n_2	1 – 2
μ_o	10 – 200
μ_{max}	10 – 200

Figure 6.15 show polymer rheology curves found from the MRST iterations at higher injection rates.

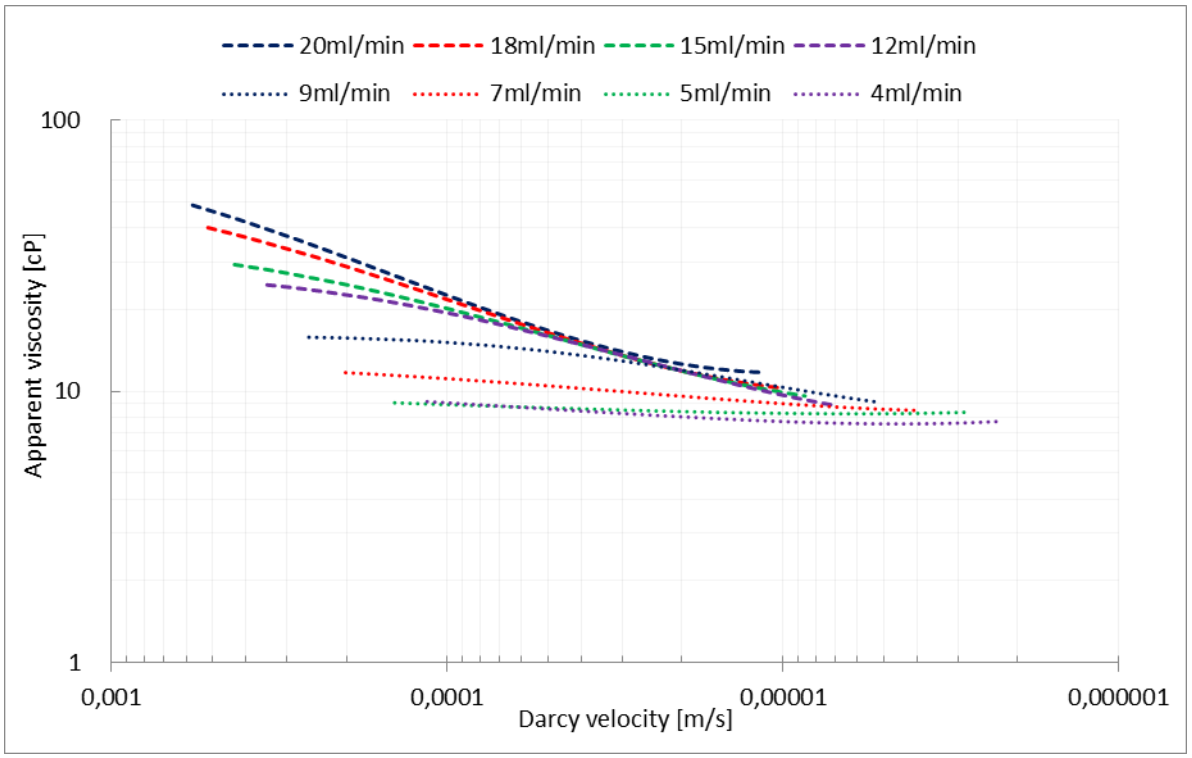

Figure 6.15 Rheology curves for higher injection rates from MRST

From figure 6.15, rheology curves from the MRST simulations produces curves following the same trends observed for the higher injection rates in figure 6.8. Shear thickening is present

for all injection rates, showing a decreasing effect for decreasing injection rates. Further, convergence of the rheology curves appear to be improved during the MRST simulations at intermediate flow velocities for the highest injection rates compared to the simulated results from STARS.

Comparison of selected rates from figure 6.15 are displayed below with corresponding rheology curves from STARS.

Figure 6.16 show results from MRST simulations compared with results from STARS for the 20ml/min injection rate.

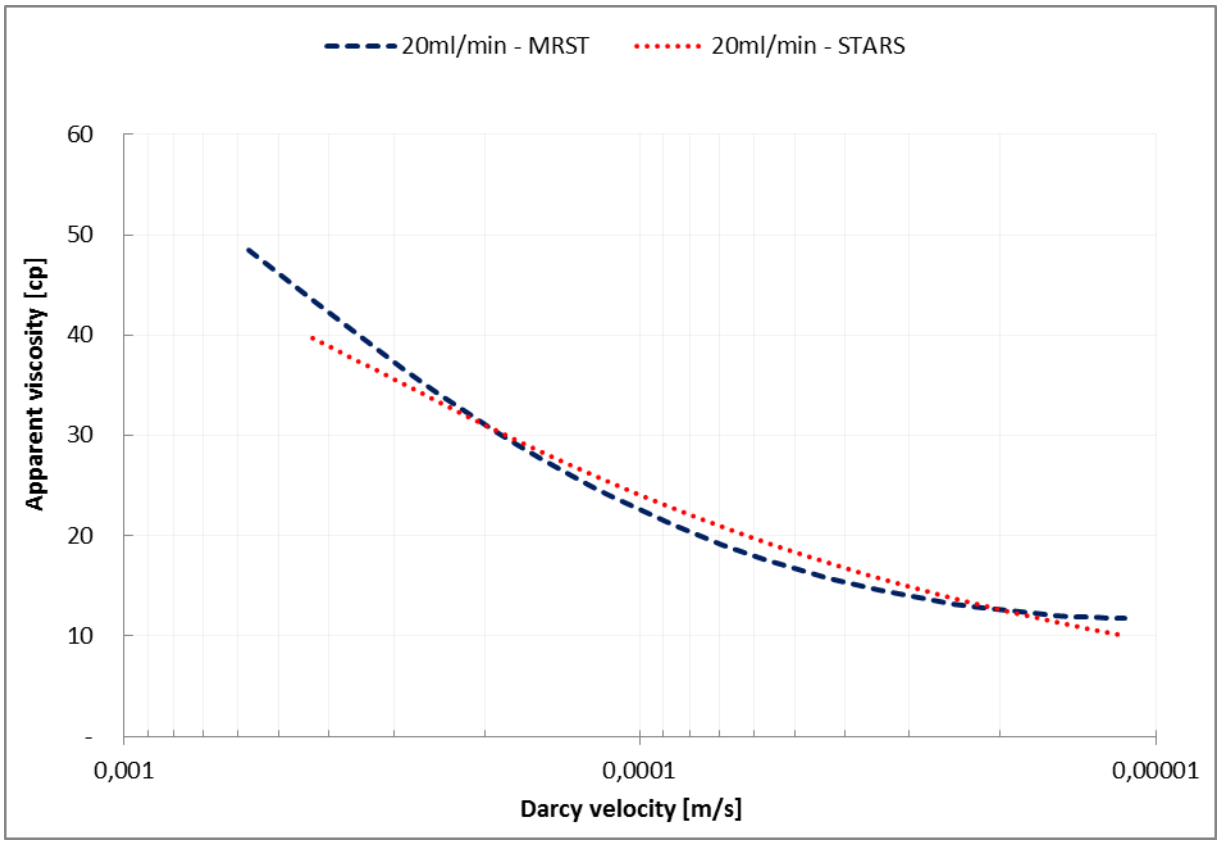

Figure 6.16 Rheology curve comparison for 20ml/min injection rate from MRST and STARS simulations

In figure 6.16 the 20ml/min injection rate from MRST display a higher viscosity in the high-velocity region near the injection well. This higher viscosity, however, is also enhanced by the velocity limitation encountered in STARS as discussed in section 4.1. Further, near the outlet the MRST rheology curve level off and display a slight apparent Newtonian plateau The STARS rheology curve, on the other hand, display a continued decrease in viscosity. Apart from this, the rheology curves display shape similarities and strong shear thickening behaviour.

Figure 6.17

Figure 6.17 show rheology curves obtained from MRST and STARS for the 12ml/min injection rate.

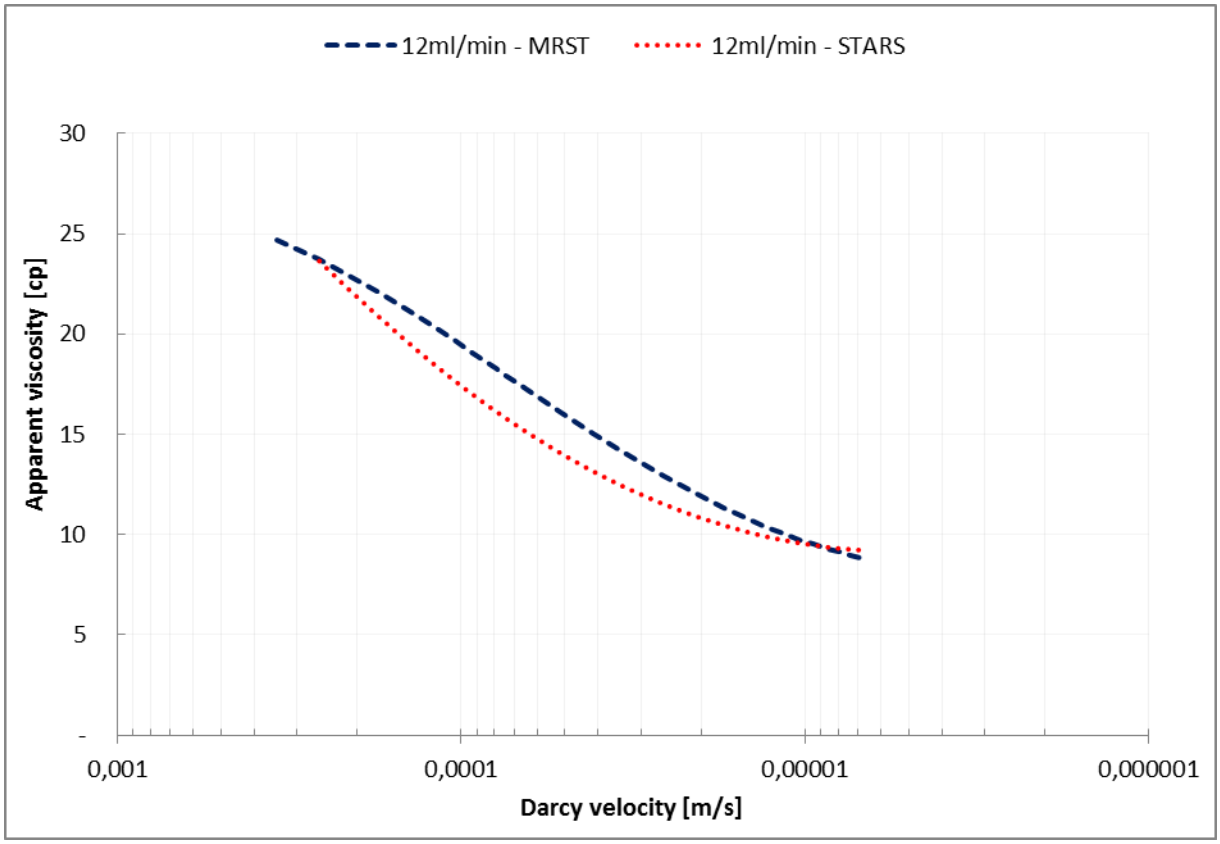

Figure 6.17 Rheology curve comparison for 12ml/min injection rate from MRST and STARS simulations

As seen in figure 6.17, trends observed for the 20ml/min injection rate in figure 6.16 is present also for the 12ml/min injection rate. The MRST simulated rheology curve display the highest apparent viscosity in the near-well vicinity, but as mentioned, this is further enhanced by the STARS limitations. Further, the STARS simulated results display a steeper rheology curve indicating a more rapid tapering off shear thickening behaviour. However, both the MRST and STARS results indicate strong shear thickening behaviour and no presence of shear thinning behaviour

Figure 6.18 shows results from the MRST simulations for lower injection rates.

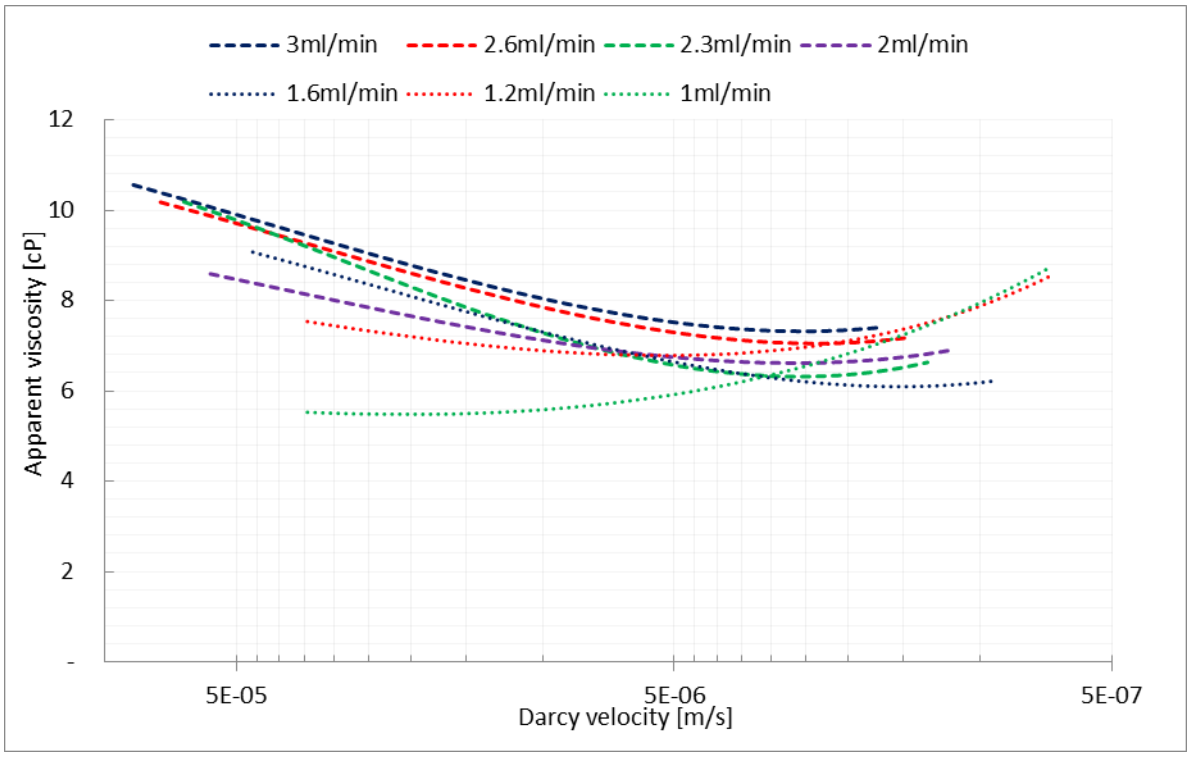

Figure 6.18 Rheology curves for lower injection rates from MRST iterations

From figure 6.18 it is observed that the rheology curves produce a more cluttered graph than was obtained during manual history matches in figure 6.10. The 1.2ml/min and 1ml/min injection rate display significantly more shear thinning than other rates present in the figure. This behaviour was not observed to this extent in the STARS simulations. However, it should be noted that during the MRST simulations the iteration scheme struggled to history match fluctuating pressure values. Therefore, the results produced by MRST for lower rates is more uncertain than for the higher rates as no clear parameter estimation was attained for the lower rates. In figure 6.18, the 0.5ml/min and 0.2ml/min injection rate have been completely omitted as the MRST simulator was unable to handle the fluctuating pressure values for these rates. For each iteration performed by MRST on these lower injection rates new pressure matches and PDI maps was produced deviating significantly from previous iterations.

In figure 6.19, the 1.2ml/min and 1ml/min curves are omitted from the graph to better illustrate the trends which arose for injection rates in the range 3ml/min to 1.6ml/min.

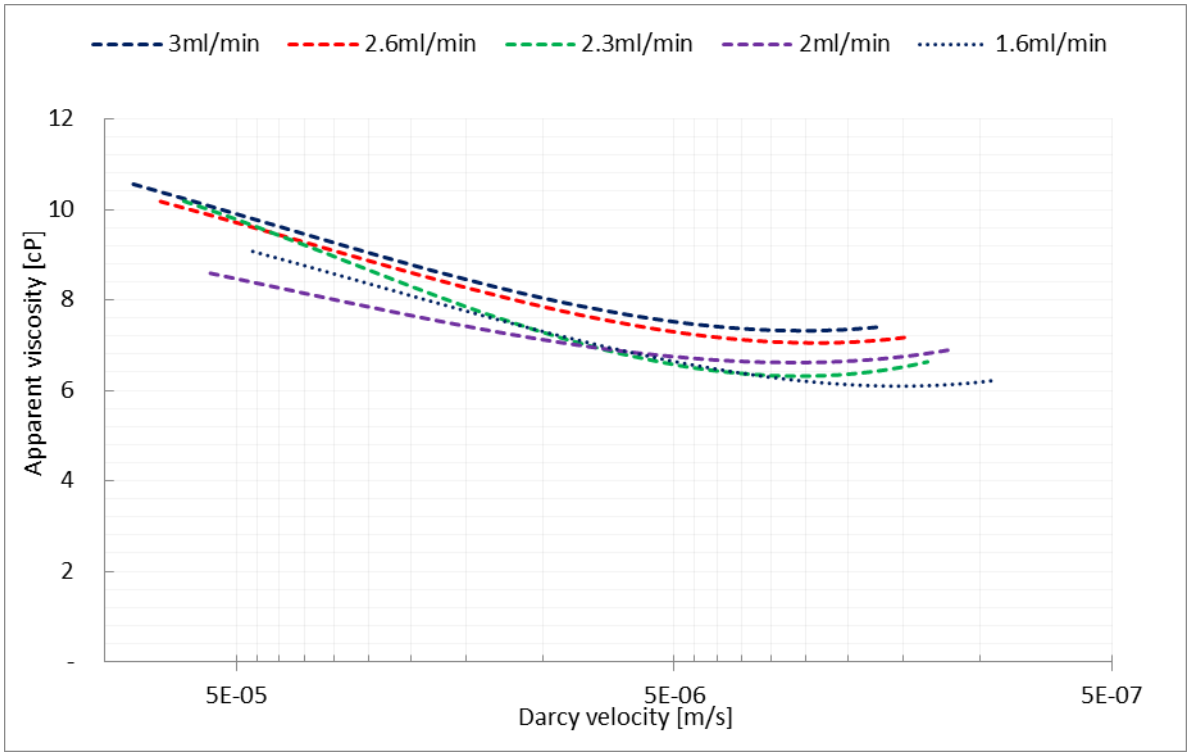

Figure 6.19 Rheology curves for lower injection rates from MRST iterations omitting the lowest injection rates

From figure 6.19 it is seen that a strong shear thickening effect is present for most injection rates, in accordance with the STARS results in figure 6.10. Further, the mild shear thinning behaviour observed from the STARS simulations is maintained from the MRST simulations and only a slight shear thinning behaviour is present towards the outlet rim for most injection rates.

Figure 6.20 shows a comparison of the 2.6ml/min injection rate rheology curve found from the MRST simulations and STARS simulations.

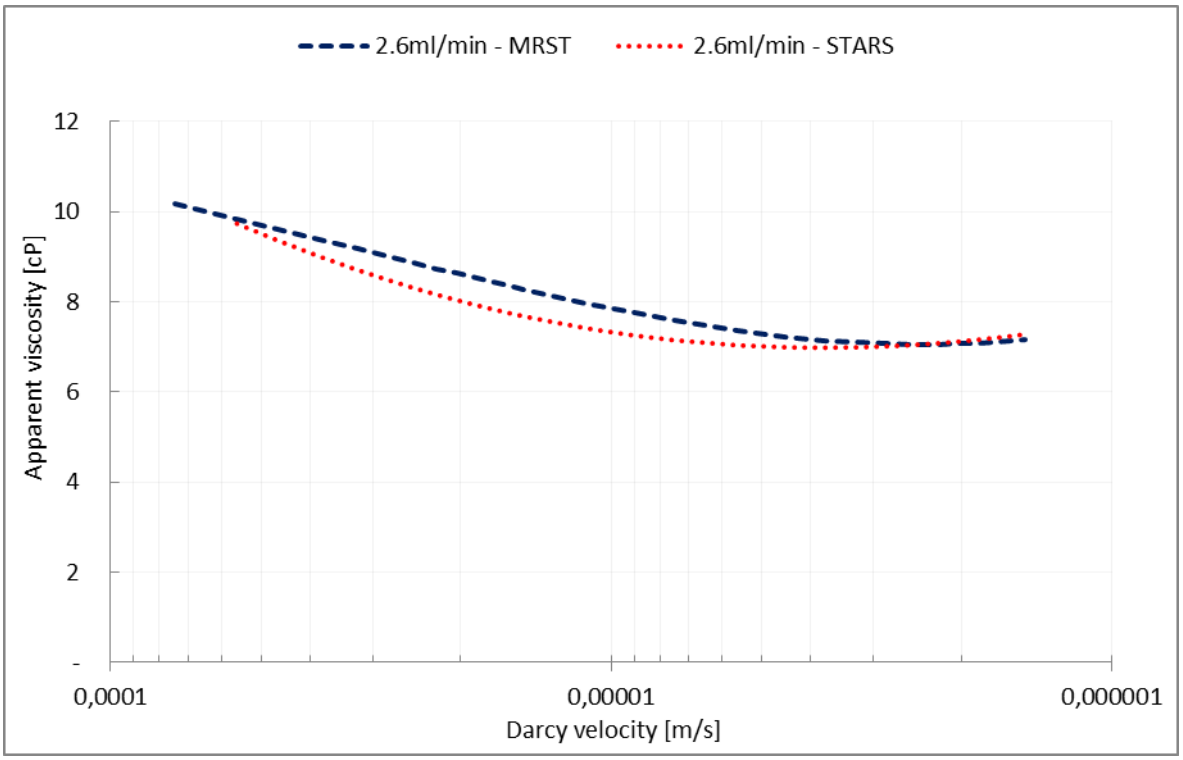

Figure 6.20 Rheology curve comparison for 2.6ml/min injection rate from MRST and STARS simulations

In figure 6.20, correspondence is observed for the rheology curve obtained for the 2.6ml/min injection rate from the MRST simulations and STARS simulations. Shear thickening behaviour is prominent and only slight shear thinning behaviour is observed in both rheology curves. Further, the rheology curve obtained from the manual history matching display a less prominent shear thickening behaviour at intermediate velocities.

Figure 6.21 shows a comparison of the 1ml/min injection rate rheology curve found from the MRST simulations and STARS simulations.

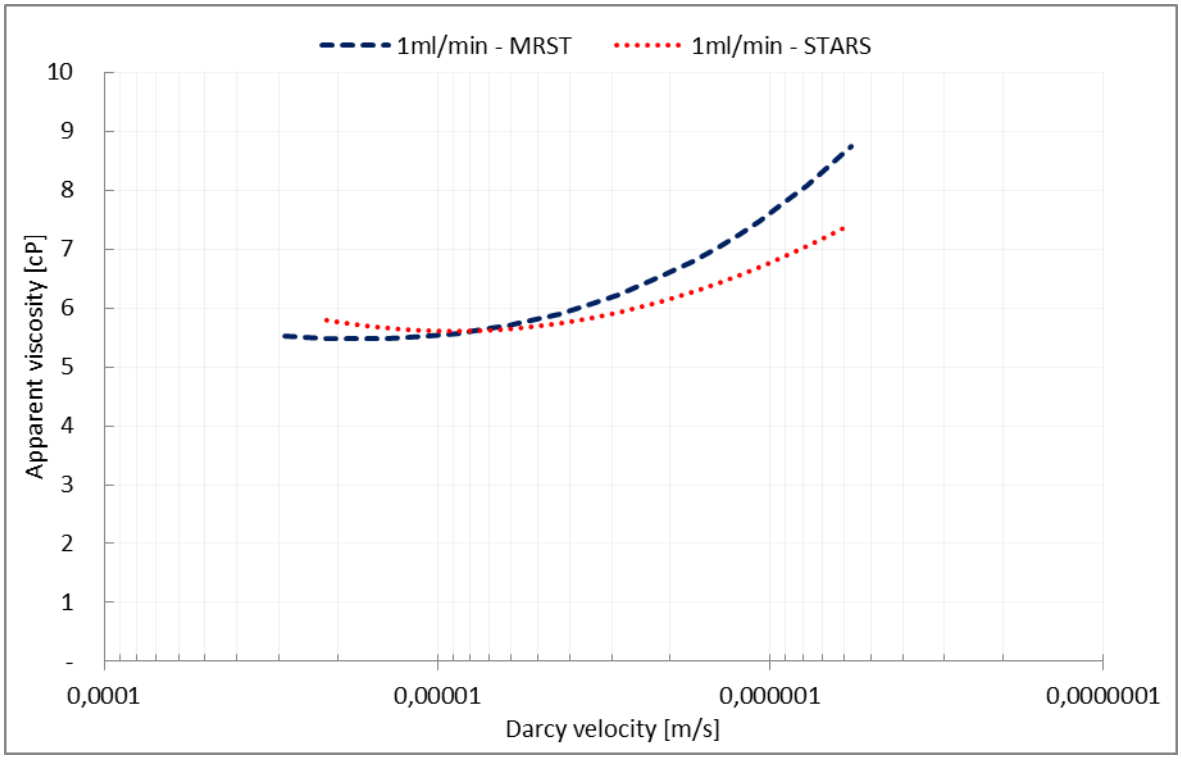

Figure 6.21 Rheology curve comparison for 1ml/min injection rate from MRST and STARS simulations

In figure 6.21, the MRST rheology curve display a more prominent shear thinning behaviour and only very slight shear thickening is observed immediately following the injection. This slight shear thinning behaviour is also observed for the 1ml/min injection rate from STARS. The STARS rheology curve, however displays an intermediate Newtonian plateau before shear thinning becomes prominent as velocities are decreased near the outlet rim.

Figure 6.22 show the onset of shear thickening found by manual inspection of simulated output data from the MRST simulator.

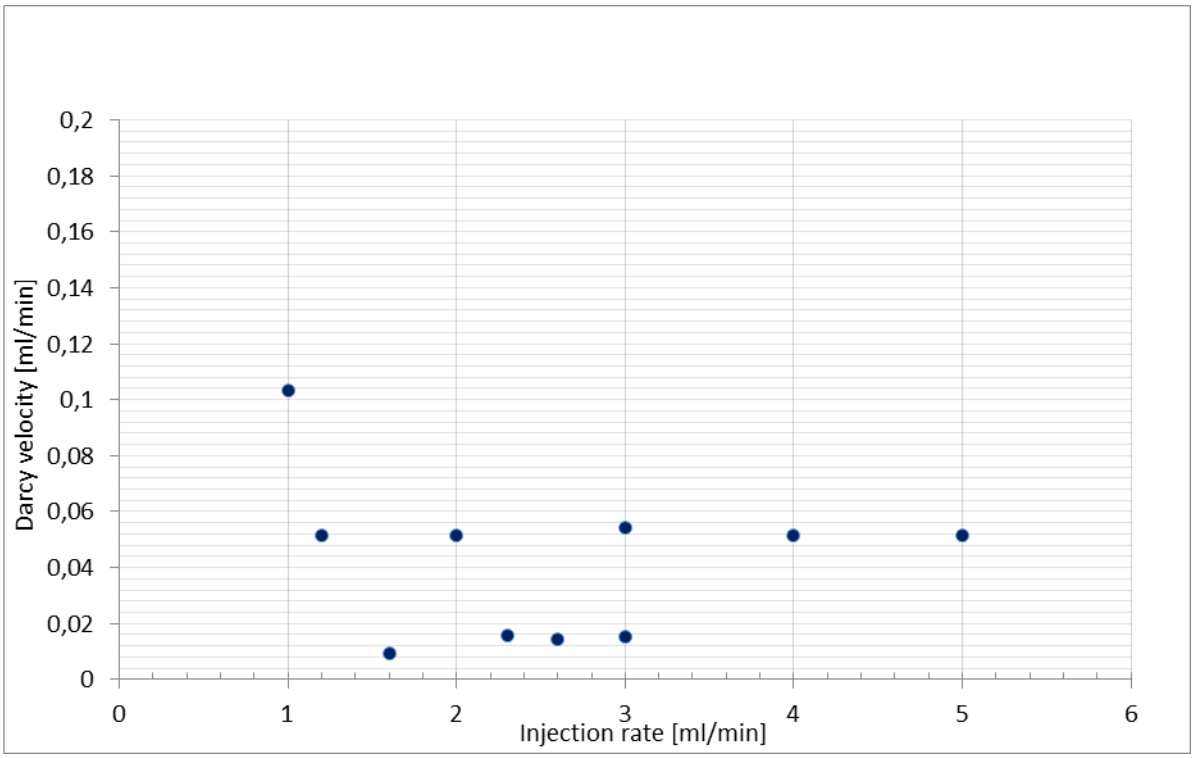

Figure 6.22 Onset shear thickening HPAM MRST

As seen in figure 6.22, the trend of shear thickening onset occurring at decreasing velocity with decreasing injection rate observed in the STARS simulations is not followed in the MRST output. Compared to the shear thickening onset values found in section 6.2.1.2 the values appear to be randomly distributed within a range from 0.01 to 0.05ml/min.

From the simulated results from MRST and STARS, correspondence between rheology curves where observed for most injection rats. This serves to mutually improve the confidence in the simulated rheological behaviour of the HPAM polymer in the radial model. Further, as expected during the history matching, more care was taken to follow trends which arose from the experimental data during the manual tuning. The MRST simulator, on the other hand, though producing adequate pressure matches struggled somewhat to maintain trends in the data set. However, this is also heavily dependent on the quality of the input data provided for MRST.

6.2.2. Xanthan Simulations - STARS Simulations

Figure 6.23 show xanthan rheology curves from the STARS simulations for various injection rates in a plot of apparent viscosity as a function of Darcy velocity. As a remainder, the Darcy velocities are still plotted in reverse on the x-axis. Corresponding pressure matches for the rheology curves are located in appendix A.2. The lowest rates of 0.5ml/min and 0.1ml/min have been omitted from the figure as they produced results which were clearly deviating from the higher rates. These lower rates are located in the appendix.

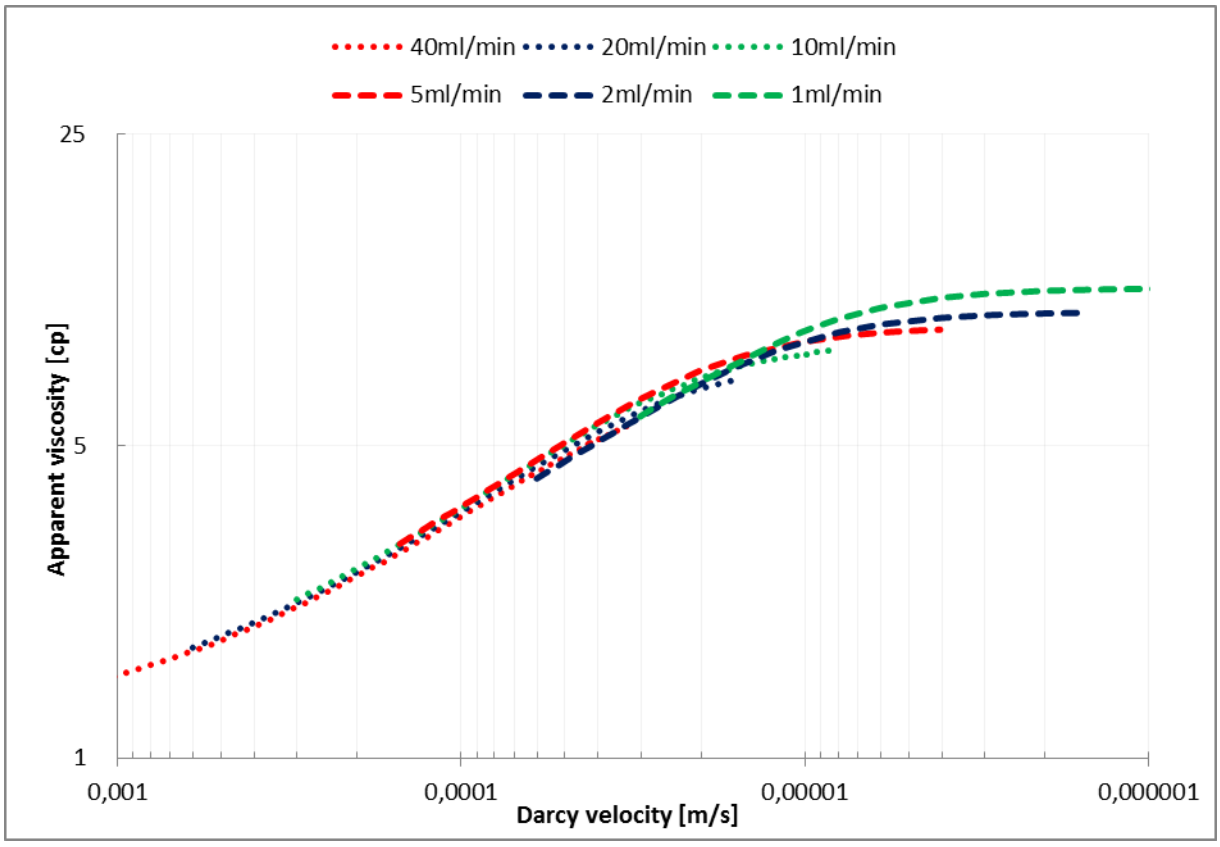

Figure 6.23 Xanthan apparent viscosities as a function of Darcy velocity for various injection rates

Xanthan rheology curves in figure 6.23 are dominated by shear thinning for all injection rates at higher velocities near the injection well. The shear thinning behaviour is more prominent for the highest injection rates due to the higher velocities encountered in the porous medium. For lower injection rates, including 10ml/min and below, a lower Newtonian plateau is observed at lower velocities near the outlet. Further, consistent with literature (Ghoniem, 1985 [30]; Huang and Sorbie, 1992 [54] ; Seright et al., 2011 [52]) the polymer solution display no apparent shear thickening at any velocities in the radial model.

The xanthan rheology curves appear to converge at the same Darcy velocities within the radial model, with an exception occurring at the lowest velocities where the viscosity curve is

shifted upwards for decreasing injection rates. A possible explanation for the convergence of the xanthan rheology curves relates to their lack of viscoelastic response to elongational forces in the porous medium. As described in section 2.5.1, Ghoniem (1985) [30] registered little viscoelastic response from xanthan polymers due to their rigid rod molecular structure, indicative of very slight elasticity. For HPAM little convergence was observed in the presented results in figure 6.8 and figure 6.10 which was thought to be a consequence of the polymers inherent memory effect. As xanthan display only very slight elastic response when subjected to elongational forces the polymer do not have the inherent memory effect of synthetic flexible coil polymers. The convergence of curves would therefore be expected to be improved compared to the HPAM rheology curves as the polymer is not deformed in the same manner as the synthetic flexible coil polymers. This, in turn, is also observed in the xanthan rheology curves presented in figure 6.14 compared to the synthetic polymer rheology curves from figure 6.8 and figure 6.10.

The shear thinning behaviour observed for xanthan was described and illustrated in section 2.5.1, and owes to its rigid rod structure. At higher velocities, the polymer molecules orient themselves in flow direction resulting in reduced chain interactions and a decreasing apparent viscosity. This shear thinning behaviour of rigid rod biopolymers in porous media is a well-established characteristic observed in both bulk rheology measurements and in-situ by several authors (Canella et al., 1988 [28]; Hejri et al., 1991 [55]; Seright et al., 2011 [52]). However, these authors also observed some discrepancies between predicted bulk viscosity behaviour and in-situ rheology at lower velocities in their linear flooding experiments.

Continued apparent shear thinning in porous media were observed by the above authors where bulk measurements predicted Newtonian behaviour. As velocities decreases radially away from the injection well, oil displacement generally occur at lower velocities within the reservoir. Therefore, resolving this rheological discrepancy of xanthan is important for accurate simulations when planning xanthan flooding in the field.

Seright et al. (2011) [52] conducted flooding experiments in short linear cores of both low permeable Berea sandstone cores (0.05D and 0.3D) and high permeable polyethylene (5.1D) using a 600ppm xanthan polymer. From this study, higher resistance factors were reported which surpassed predicted viscosities from bulk measurements and a lower Newtonian plateau was not attained, in accordance with previous studies conducted by Canella et al. (1988) [28] and Hejri et al. (1991) [55]. However, from figure 6.23 it is observed that the

lower Newtonian plateau is attained at lower velocities within the radial model for most injection rates. Seright et al. argued that the continued apparent shear thinning observed in the short linear cores were likely a consequence of high molecular weight species causing unexpectedly high RF values when retained, and was not expected to propagate far into a real reservoir. Further, they recognized that unexpectedly high resistance factors encountered in short linear cores would likely not be experienced in radial flow away from the injection well where velocities are lowest. This is in accordance with the results presented in Figure 6.23.

There are some concerns related to the results presented in figure 6.23. As discussed in section 3.2 and section 6.1.3, the pressure transducers used during the experiment were unable to record pressures at several positions within the Bentheimer disk. This limitation arose as a consequence of a too low pressure drop occurring between consecutive ports which the sensors were not able to register. Thus, only 5 pressure points were recorded and used for the history match.

For a Newtonian fluid the limited pressure values could have been circumvented by calculating synthetic pressure values using Darcy's law for radial flow, equation (2.4), due to the logarithmic relationship existing between expected pressure drop and radial distance. Thus, synthetic pressure values could be generated by fitting a logarithmic regression line to the experimental data, as illustrated in figure 3.3, and calculating new pressure values based on the regression line equation. However, for a non-Newtonian fluid this issue is not as readily circumvented. Following from figure 6.23 and xanthans non-Newtonian characteristics at higher velocities, the apparent viscosity is not constant, and therefore the relation between pressure drop and radial distance will not, in general, be a logarithmic function. [3]

To generate synthetic pressure values for a non-Newtonian fluid one would have to assume the polymer apparent viscosities at certain velocities and distances. Thus, the purpose of history matching measured pressures to study xanthan rheology would be meaningless as the polymer rheology would already be predetermined.

Despite the limited pressure data available hindering backpressure correcting the experimental pressure it is believed that the rheological behaviour is left unaffected.

As the backpressure correction would result in an equal relative pressure reduction for pressures recorded at specific injection rates it is believed that the limited data only affect the magnitude of the viscosity values, not the rheological behaviour itself. Following from the

proportionality between viscosity and differential pressure in Darcy's law, it is implied that an higher differential pressures result in an increased apparent viscosity. Therefore the apparent viscosity values in figure 6.23 may be overestimated. However, since no backpressure correction was performed for the waterflooding simulations and therefore returned lower permeability values this likely remedied or dampened any effect of overestimated apparent viscosity values.

6.2.2.1. Xanthan Flooding Simulations – MRST

The initial range for MRST for all xanthan injection rates was initially defined as listed in table 6.7. The procedure outlined in section 4.2 was followed during the MRST simulation for the xanthan flooding sequence.

Table 6.6 Initial extended Carreau range for xanthan EnKF iterations

Extended Carreau parameter	EnKF range for ensemble members
λ_1	100 – 100 000
λ_2	10 – 1000
n_1	0.1 – 0.99
n_2	1 – 2
μ_o	10 – 200
μ_{max}	10 – 200

Figure 6.24 show the MRST rheology output from the simulations of rates ranging from 40ml/min to 0.5ml/min in a plot of apparent viscosity as a function of Darcy velocity. The 0.5ml/min rheology curve has been included to illustrate the deviations occurring for the lowest injection rates.

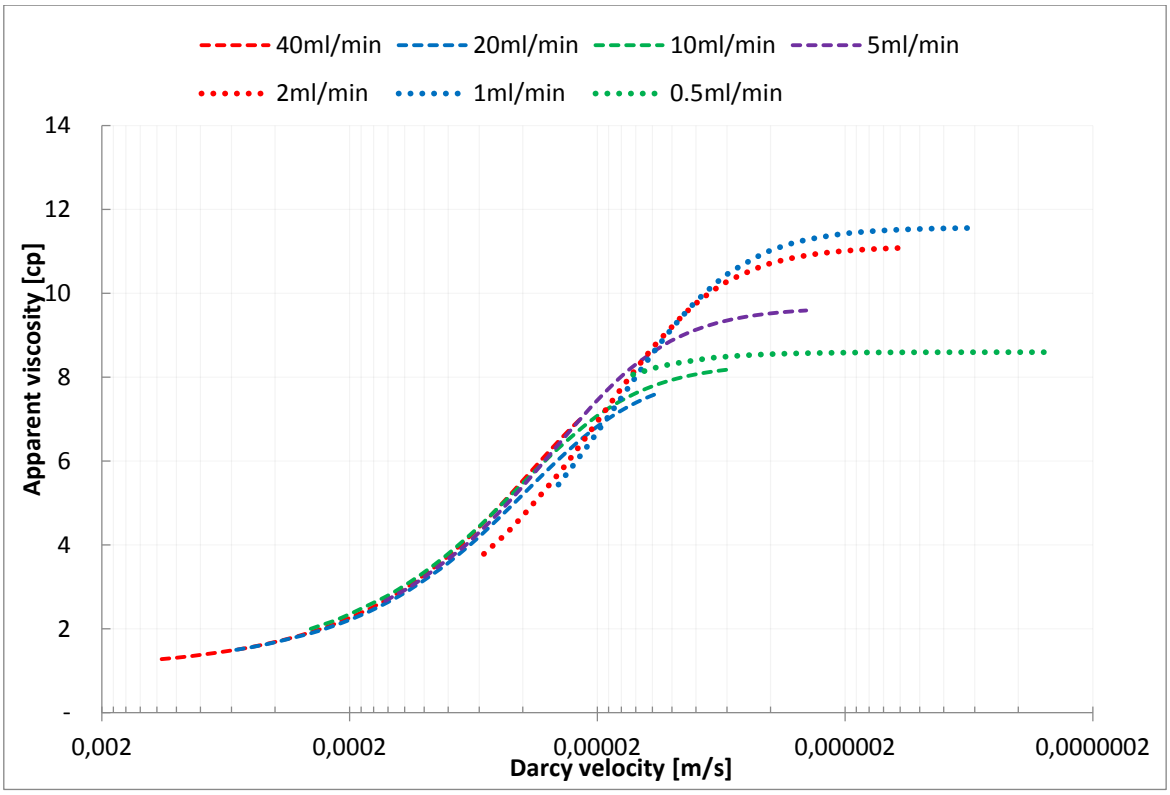

Figure 6.24 Xanthan rheology output from MRST simulations

As seen in 6.24, xanthan rheology curves from the MRST simulations follow the same trends observed during the STARS simulations in 6.23. Shear thinning behaviour is observed for all rates, in accordance with both literature and STARS simulation results, showing a more prominent effect as velocities increases. Further, the lower Newtonian plateau is attained for rates below 10ml/min, though the 10ml/min rate only display a slight levelling off at the lowest velocities, in accordance with the observed rheological behaviour from the STARS simulations.

A more detailed comparison is shown below in which a high rate, intermediate rate and a low rate is compared from the MRST and STARS xanthan simulations. Figure 6.25 show the 20ml/min injection rate rheology output from MRST and STARS in a plot of apparent viscosity as a function of Darcy velocity.

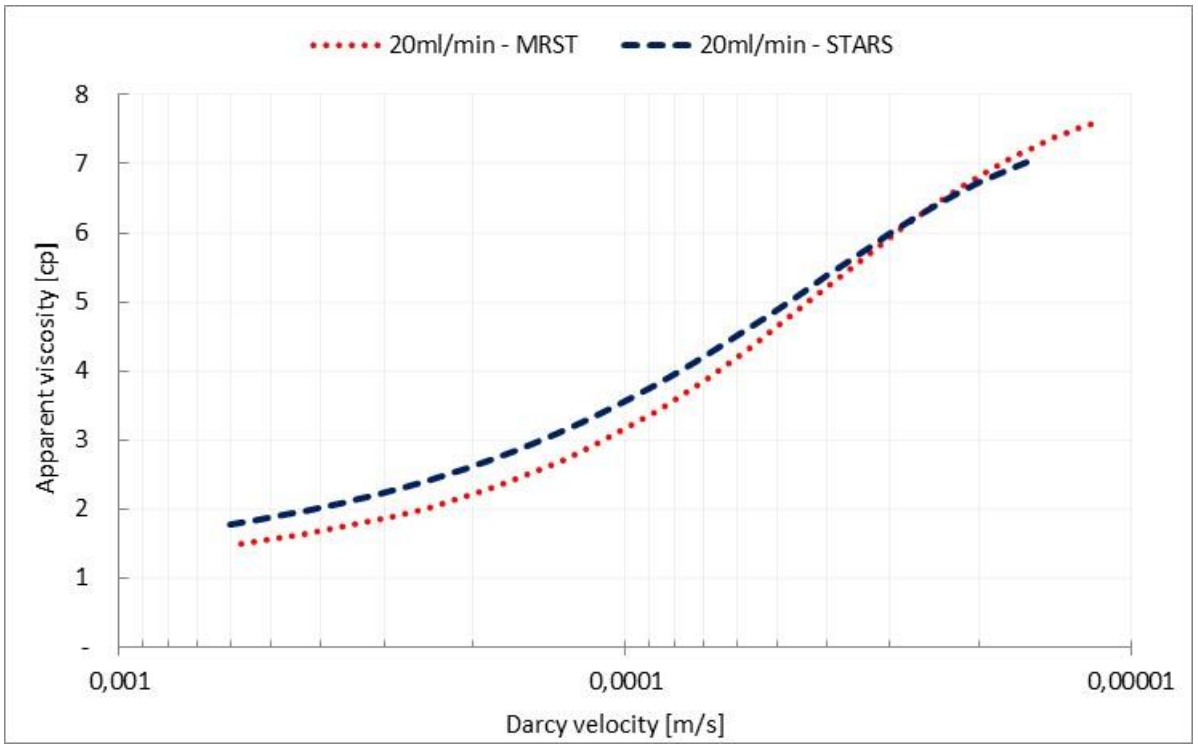

Figure 6.25 Comparison MRST and STARS for 20ml/min rheology curves from xanthan flooding

As seen in figure 6.25, the curves display great shape similarity. The STARS rheology curve is shifted upwards compared to the MRST rheology curve at most velocities, however; as seen on the y-axis the difference in apparent viscosity is slight between the two curves. The MRST simulation further attain a higher maximum apparent viscosity at the lowest velocities near the outlet, although this difference is minor between the two rheology curves. The MRST curve also display a steeper increase in apparent viscosity at intermediate velocities than the STARS simulation output, however; the difference is again very slight.

Figure 6.26 show the 5ml/min injection rate rheology output from MRST and STARS in a plot of apparent viscosity as a function of Darcy velocity

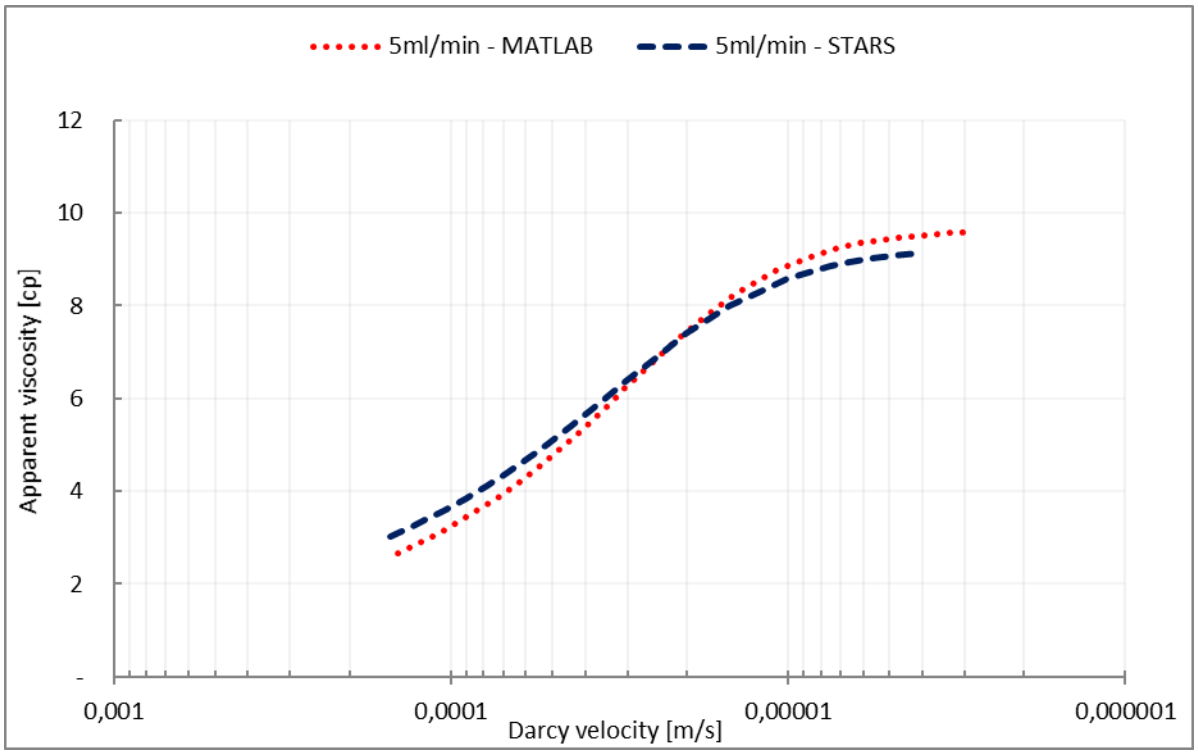

Figure 6.26 Comparison MRST and STARS for 5ml/min rheology curves from xanthan flooding

As seen in figure 6.26, the curves again show great shape similarity from the MRST and STARS rheology output. There is some deviations occurring at the highest and lowest velocities near the injection well and outlet, respectively. However, these deviations are only slight and the curves overall display similar rheological behaviour. Further, for both rheology curves a lower Newtonian plateau is attained at the lowest velocities near the outlet. However, the lower Newtonian plateau is more prominent for the MRST simulation output.

The results from the STARS and MRST simulations appear to mutually enhance the confidence in the simulation results due to the similarities between the rheology curves in figure 6.23 and figure 6.24. The lower Newtonian plateau is present in the results in both the STARS and MRST simulations, shear thinning is present and more prominent for higher injection rates in both simulation outputs, and no shear thickening behaviour is observed.

6.3 Polymer Injectivity

The previous subchapters presented the rheological behaviour of HPAM and xanthan in the radial Bentheimer model. As described in section 2.5.7, consideration of the rheological behaviour of polymers when planning field scale operations is of fundamental importance as it heavily influences the injectivity. To relate the results from section 6.2 to the polymers

injectivity in the model, a comparison of the polymers respective injectivity are presented below.

The injectivity may be calculated using equation (2.32) for HPAM and xanthan based on the polymer solution injection rates and corresponding pressure drops. As reference position, the pressure drop is taken from injection well to 8 cm from injection well for both polymers. Figure 6.27 include both HPAM and xanthan injectivity along with water injectivity of 1 cP from the experiments. A viscous Newtonian fluid of 10 cP is also included as reference.

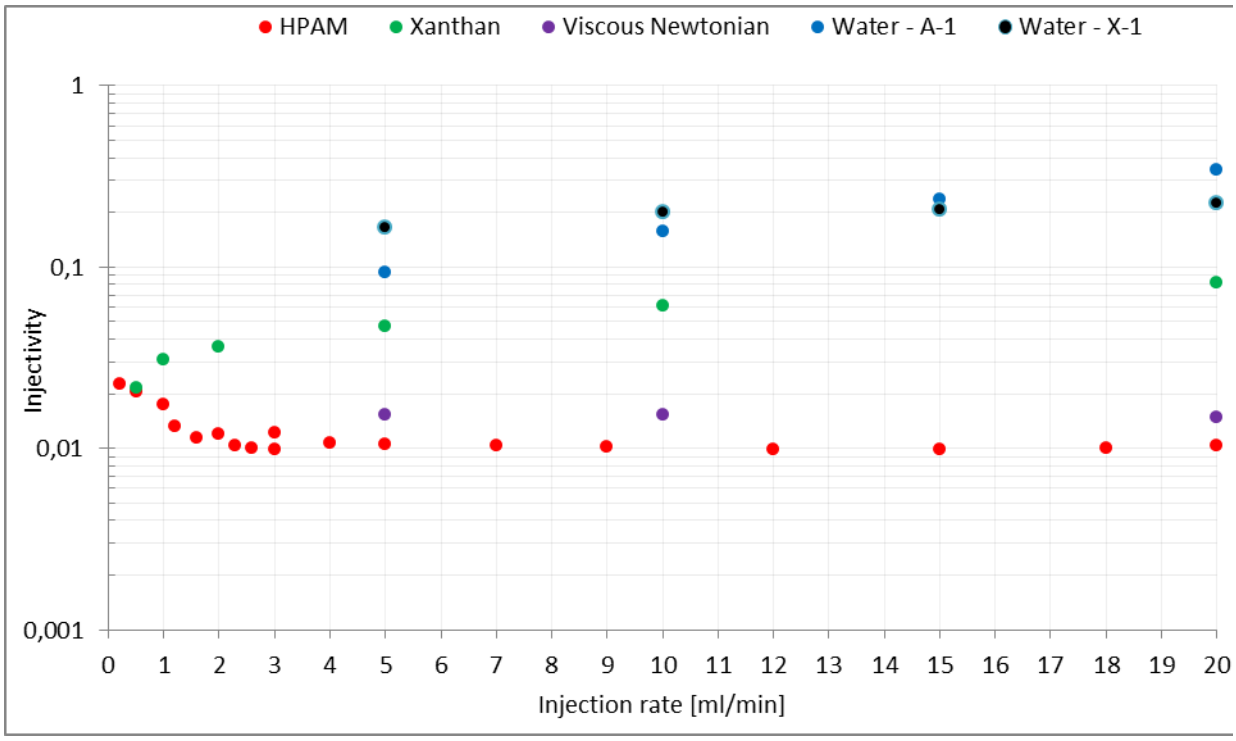

Figure 6.27 Injectivity comparison of HPAM, xanthan, water and viscous Newtonian fluid

In figure 6.27, the injectivity of the Newtonian fluids are seen to be independent of injection rate and display a constant value as injection rate increases. This follows from the constant viscosity displayed by the polymers as they propagate away from the injection well under influence of varying velocities and deformational forces. There are some deviations occurring for the water values from experiment H-1. However, this is likely a consequence of the rate-dependent permeability in the near-well region which was explained in section 6.1.1. As expected, the injectivity is also seen to be improved as viscosity decreases, consequently as a result of the lower pressure drop experienced for fluids of lower viscosity.

The injectivity of HPAM follows from the synthetic polymer characteristics, and is as expected gradually decreasing with increasing injection rates. This is a result of the dominant shear thickening behaviour occurring in the near-well vicinity, as was presented in previous

subchapters. The consequence of shear thickening polymers is an increasing pressure drop occurring at the injection well which decreases the polymer injectivity. However, the poor injectivity characteristic of the HPAM polymer is likely enhanced by the near-well conditions which displayed a significant low permeability value in the near well region, likely as a consequence of formation damage. Due to the low permeable region, the polymer is prone to entrapment in this region causing a gradual permeability decrease near the well during the flooding sequence. This is further discussed below, but will result in an additional pressure increase in the near well vicinity.

Xanthan injectivity, on the other hand, display an increasing value as injection rates increases. Like for HPAM, the improved xanthan injectivity can be explained in terms of the molecular structure and resulting rheological behaviour. In figure 6.23, it was observed that as injection rates increased the polymer displayed decreasing apparent viscosity in the near-well vicinity. Therefore, as the polymer experiences the lowest apparent viscosity at the highest velocities, increasing the injection rate result in improved injectivity conditions for the polymer. However, this improved injectivity characteristic offer some complications during EOR applications. It was mentioned in Chapter 1 that oil usually reside in the low-permeable regions in the reservoir when commencing EOR applications. Therefore, injecting at velocities which induce the lowest xanthan apparent viscosities may result in the polymer bypassing these low-permeable areas.

Using equation (2.29), residual resistance factors are calculated from the waterflooding sequences performed after the HPAM flooding. Rock permeabilities for the 5ml/min and 10ml/min injection rate were calculated and listed in table 3.2, whereas rock permeability after the polymer flooding sequence are calculated in a similar manner as performed in subchapter 4.1. Calculated permeabilities before and after the polymer flooding sequence along with calculated residual resistance factor is listed in table 6.7.

Table 6.7 Residual resistance factors from HPAM flooding sequence

	$K_{w(0.3\text{-out})}$	$K_{wp(0.3\text{-out})}$	**RFF**	$K_{w(1.5\text{-out})}$	$K_{wp(1.5\text{-out})}$	**RFF**
$Q_{5ml/min}$	0.31	0.02	**15.50**	2.29	1.37	**1.67**
$Q_{10ml/min}$	0.52	0.04	**13.00**	2.36	1.19	**1.99**

As seen in table 6.8, residual resistance factors are calculated both from injection well to the outlet rim and from 1.5 cm inside the radial disk to the outlet. The residual resistance factor

values calculated from injection well to the outlet are significantly larger than the corresponding values calculated from 1.5 cm to the outlet. This is indicative of plugging in the near well region caused by the retention of polymer species, and high molecular weight species in particular, in the near-well region. This may further explain the absence of a more dominating shear-thinning behaviour as discussed in section 6.2.1.2. The residual resistance factor calculated after the HPAM flooding sequence also indicate that the apparent viscosity found in the subchapters in 6.2.1 are also overestimated as the apparent polymer viscosity was used to account for the permeability reduction developing during the flooding sequences.

Table 6.8 show calculated residual resistance factors from the injection well to 8 cm inside the radial disk, and from 1.5 cm to 8 cm inside the radial disk for the xanthan polymer.

Table 6.8 Residual reistance factors from xanthan flooding sequence

	$K_{w(0.3-8)}$	$K_{wp(0.3-8)}$	**RFF**	$K_{w(1.5-8)}$	$K_{wp(1.5-8)}$	**RFF**
$Q_{5ml/min}$	0.66	1.10	**0.6**	3.95	2.19	**1.80**
$Q_{10ml/min}$	0.81	1.12	**0.72**	2.23	2.11	**1.06**
$Q_{15ml/min}$	0.83	1.14	**0.73**	2.22	2.26	**0.98**
$Q_{20ml/min}$	0.91	1.15	**0.79**	2.27	2.21	**1.03**

As seen in table 6.8, significantly smaller residual resistance factors have been calculated for the xanthan flooding sequence. In accordance with literature xanthan biopolymer adsorb significantly less to the porous media compared to synthetic polymers. Further, comparing the residual resistance factors calculated from injection well to 8 cm inside the radial disk actually show that the permeability have increased during the xanthan flooding sequence. However, this is likely an experimental artefact.

7 Conclusion

The aim for the simulation study conducted in this thesis was to investigate the rheological behaviour of two polymers; the synthetic polymer HPAM and the biopolymer xanthan. Experimental flooding data conducted on radial Bentheimer disks formed the basis for the simulations in which the polymer solutions were injected at a wide range of rates. The radial geometry of the Bentheimer disks in which the polymers experienced a successive reduction in velocity as they propagated from injection well to outlet rim allowed for studying the rheology and injectivity in conditions commonly encountered in field applications.

The results from the HPAM simulations revealed a predominant shear thickening behaviour at high and intermediate velocities for most simulated injection rates. This behaviour was found in simulations conducted using both the STARS simulator and the MRST simulator. Further, some degree of shear thinning was found at lower injection rates, however, this behaviour was slight for most injection rates. Shear thinning behaviour was found to only display a prominent effect for injection rates of 2ml/min and below. The slight shear thinning behaviour was believed to be a result of high molecular weight species which were retained or degraded in a low-permeable region close to the injection well vicinity.

The results from the HPAM simulations were in agreement with reported results in the literature, conducted both in linear cores and radial disks, and were explained by the viscoelastic character of the synthetic polymer flowing in porous media.

Simulated xanthan solution revealed a prominent shear thinning behaviour at higher and intermediate velocities. Further, for lower velocities near the outlet at intermediate and lower injection rates a lower Newtonian plateau was attained. This rheological behaviour was confirmed by both simulation tools. The rheological behaviour of the xanthan polymer is attributed to the rigid rod structure in which the chains orient themselves in flow direction. The study conducted in this thesis confirms the polymer behaviour.

Literature on xanthan flooding experiments have reported the same shear thinning behaviour which was observed in this simulation study, however; difficulties in attaining the lower Newtonian plateau predicted from bulk viscosity measurements in short linear cores have been reported. Therefore, radial disk experiments may be an improved alternative for studying xanthan rheology as the lower Newtonian plateau was attained for most injection rates studied in this thesis when the flow velocity decreased sufficiently. This could help in aiding the

planning of future field scale applications as avoiding the discrepancies encountered in short linear cores would improve simulations and predicting potential of field scale xanthan polymer flooding.

During the simulation study, decreasing permeabilities were not accounted for during the simulations of the polymer flooding sequences. This has an effect on reported viscosities for both HPAM and xanthan. However; as indicated by calculated residual resistance factor values, the Bentheimer disk used for the HPAM flooding experienced a significant degree of permeability reduction, in particular in the near-well vicinity. As a consequence of the large permeability reduction the reported viscosity values and rheology curves are affected and results in overestimated viscosities. However, incorporating permeability reductions developing during the flooding sequence is difficult to account for based on waterflooding sequences performed after a polymer flooding sequence in simulations and was therefore not pursued. Residual resistance factors calculated for the xanthan flooding sequence, on the other hand, showed significantly less permeability reduction and the reported rheology curves are likely less affected by this effect.

Further, comparison of the polymer injectivity revealed a significantly better injectivity for xanthan at higher injection rates than the viscoelastic HPAM polymer. This is explained from their respective rheological behaviour where an increased pressure drop in the well vicinity is experienced for the shear thickening HPAM polymer compared to the shear thinning xanthan polymer. Whereas the HPAM polymer displayed a decreasing injectivity with increasing injection rates, the xanthan polymer showed an increasing injectivity at increasing injection rates. The increasing injectivity experienced by the xanthan polymer at increasing injection rates is explained by the more prominent shear thinning experienced as injection rates increases.

8 Further Work

There is a lot of improvement and potential for further work on polymer flooding simulations in radial models. As there is very limited literature available more work is needed to fully understand polymer rheology in radial flooding geometries. Some improvements which should be further investigated during later studies are mentioned here.

The simulations of the polymer flooding sequences conducted in this thesis were performed on a radial Bentheimer disk model. A natural extension to this work would be to upscale results to a field scale to further investigate the injectivity in field scenarios. During field scale simulations it would also be appropriate to investigate the influence of different near well conditions on the polymer injectivity. For instance, investigating pressure drops and injectivity in the presence of fracturing conditions could be included. This would help aiding decisions in field applications where injectivity could be greatly improved by fractures in the near well region.

Further, investigating polymer rheology in radial disks of lower permeability could be performed to assess the potential for polymer flooding applications in reservoir rock of lower permeability than the permeable Bentheimer rock. As this thesis only dealt with the single-phase flooding of polymer solutions it would also be interesting to extend the work on radial disks to displacement processes, especially for xanthan who revealed a different rheological behaviour than what is experienced during linear core experiments.

History matching heavily relies on experimental data; therefore it should be of great importance to ensure that data is collected in a manner allowing for simulations with reduced uncertainties. As was experienced during the xanthan history matching, the limited data provided allowed for matching of only five pressure points. Therefore, no pressure correction could be performed and the behaviour towards the outlet rim could not be verified by matching pressures in this region. This is problematic as displacement of oil commonly occurs at lower velocities in the reservoir, thus; accurately resolving the polymer rheology in the low velocity regions are important for planning EOR flooding applications.

The author would also like to credit the MRST simulator with the EnKF module used in this thesis. As manually history matching polymer flooding data is a time consuming activity, achieving reasonable results and parameter estimation from automated history matches from

the MRST tool can significantly improve the efficiency in history matching experimental data.

9 References

1. BP. *BP Statistical Review of World Energy June 2016*. 2016 [cited 2017 1 May]; Available from: http://www.bp.com/content/dam/bp/pdf/energy-economics/statistical-review-2016/bp-statistical-review-of-world-energy-2016-full-report.pdf.
2. Sheng, J., *Modern Chemical Enhanced Oil Recovery*. 2010, Saint Louis, USA: Elsevier Science.
3. Sorbie, K.S., *Polymer-Improved Oil Recovery*. 1991, Glasgow: Blackie & Son LTD. 355.
4. Directorate, N.P. *Opportunities and challenges for producing fields*. 2011 [cited 2017 02.05.2017]; Available from: http://www.npd.no/en/Publications/Resource-Reports/2011/Chapter-5/.
5. BP. *Improving the oil recovery factor*. 2013 [cited 2017 20.05.2017]; Available from: http://www.bp.com/en/global/corporate/bp-magazine/innovations/the-recovery-factor.html.
6. Gao, C.H., *Advances of Polymer Flood in Heavy Oil Recovery*, in *SPE Heavy Oil Conference and Exhibition*. 2011, Society of Petroleum Engineers: Kuwait City, Kuwait.
7. Labastie, A., *En Route: Increasing Recovery Factors: A Necessity*. Journal of Petroleum Technology, 2011. **63**(08).
8. Wang, D., et al., *Producing by Polymer Flooding more than 300 Million Barrels of Oil, What Experiences Have Been Learnt?*, in *SPE Asia Pacific Oil and Gas Conference and Exhibition*. 2002, Society of Petroleum Engineers: Melbourne, Australia.
9. Seright, R.S., M. Seheult, and T. Talashek, *Injectivity Characteristics of EOR Polymers*, in *SPE Annual Technical Conference and Exhibition*. 2008, Society of Petroleum Engineers: Denver, Colorado, USA. p. 14.
10. Glasbergen, G., et al., *Injectivity Loss in Polymer Floods: Causes, Preventions and Mitigations*, in *SPE Kuwait Oil & Gas Show and Conference*. 2015, Society of Petroleum Engineers: Mishref, Kuwait.
11. Skarestad, M. and A. Skauge, *PTEK213 Reservoarteknikk II*. 2013, University of Bergen: Bergen, Norway. p. 173.
12. Lake, L.W., et al., *Fundamentals of Enhanced Oil Recovery*. Vol. 2. 2014, Texas, USA: Society of Petroleum Engineers. 479.
13. Zolothukin, A.B. and J.-R. Ursin, *Introduction to Petroleum Reservoir Engineering*. 2000, Norway: Høyskoleforlaget AS - Norwegian Academic Press. 407.
14. Lien, J.R., *PTEK 212 Reservoarteknikk I*, U.o. Bergen, Editor. 2014, University of Beregn: Bergen, Norway.
15. Lien, J.R., *PTEK211 Grunnleggende Reservoarfysikk (Kjerneanalyse og logging)*. 2004, University of Bergen: Bergen, Norway. p. 76.

16. Walters, K. and W.M. Jones, *Measurement of Viscosity*, in *Instrumentation Reference Book*, W. Boyes, Editor. 2010, Elsevier Science: Burlington. p. 69-75.

17. Hiemenz, P.C. and T.P. Lodge. *Polymer Chemistry*. 2007; 2:[608].

18. Caenn, R., D.B. Burnett, and G.V. Chilingarian, *Enhanced oil recovery, II*. Developments in petroleum science, 17B, ed. E.C. Donaldson, G.V. Chilingar, and T.F. Yen. 1989, Amsterdam ; New York: Elsevier Science Publishers B.V.

19. Green, D.W. and G.P. Willhite, *Enhanced Oil Recovery*. SPE Textbook Series. 1998, USA: Society of Petroleum Engineers. 545.

20. Lien, J.R., M. Jakobsen, and A. Skauge, *PTEK100 Introduksjon til petroleums- og prosessteknologi*. 2007, University of Bergen: Bergen, Norway.

21. Ahmed, T., *Reservoir Engineering Handbook*. 4th ed. 2010, Burlington, USA: Elsevier Science.

22. Fanchi, J.R., *Principles of Applied Reservoir Simulation*. 3 ed. 2006, Burlington, USA

    Oxford, UK: Elsevier Inc. 511.

23. Tiab, D. and E.C. Donaldosn, *Petrophysics*. 3 ed. 2011: Elsevier Science. 971.

24. Wever, D.A.Z., F. Picchioni, and A.A. Broekhuis, *Polymers for enhanced oil recovery: A paradigm for structure–property relationship in aqueous solution.* Progress in Polymer Science, 2011. **36**(11): p. 1558-1628.

25. Chauveteau, G., *Fundamental Criteria in Polymer Flow Through Porous Media*, in *Water-Soluble Polymers*. 1986, American Chemical Society. p. 227-267.

26. Matsuda, Y., Y. Biyajima, and T. Sato, *Thermal Denaturation, Renaturation and Aggregation of a Double-Helical Polysaccharide Xanthan in Aqueous Solution.* Polymer Journal, 2009. **41**(7): p. 526-532.

27. Seright, R.S. and B.J. Henrici, *Xanthan Stability at Elevated Temperatures.* SPE Reservoir Engineering, 1990: p. 52-60.

28. Canella, W.J., C. Huh, and R.S. Seright, *Prediction of Xanthan Rheology in Porous Media*, in *63rd Annual Technical Conference and Exhibition of the Society of Petroleum Engineers*. 1988, Society of Petroleum Engineers: Houston, TX, USA. p. 353-368.

29. Skauge, T., et al., *Radial and Linear Polymer Flow - Influence on Injectivty*, in *SPE Improved Oil Recovery Conference*. 2016, Society of Petroleum Engineers: Tulsa, Oklahoma, USA.

30. Ghoniem, S.A.-A., *Extensional flow of polymer solutions through porous media.* Rheologica Acta, 1985. **24**(6): p. 588-595.

31. Sochi, T., *Non-Newtonian flow in porous media.* Polymer Journal, 2010(51).

32. Southwick, J.G. and C.W. Manke, *Molecular Degradation, Injectivity, and Elastic Properties of Polymer Solutions.* SPE Reservoir Engineering, 1988. **03**(04).

33. Zaitoun, A., et al., *Shear Stability of EOR Polymers.* SPE Journal, 2012. **17**(02).

34. Dupas, A., et al., *Impact of Polymer Mechanical Degradation on Shear and Extensional Viscosities: Toward Better Injectivity Forecasts in Polymer Flooding Operations*, in *SPE International Symposium on Oilfield Chemistry*. 2013, Society of Petroleum Engineers: The Woodlands, Texas, USA.

35. Bird, R.B., W.E. Stewart, and E.N. Lightfoot, *Transport Phenomena*. 2 ed. 2007: John Wiley & Sons, Inc.

36. Delshad, M., et al., *Mechanistic Interpretation and Utilization of Viscoelastic Behavior of Polymer Solutions for Improved Polymer-Flood Efficiency*, in *SPE/DOE Improved Oil Recovery Symposium*. 2008, Society of Petroleum Engineers: Tulsa, Oklahoma, USA. p. 15.

37. Kolodziej, E.J., *Transport Mechanisms of Xanthan Biopolymer Solutions in Porous Media*, in *SPE Annual Technical Conference and Exhibition*. 1988, Society of Petroleum Engineers: Houton, Texas, USA.

38. Dominguez, J.G. and G.P. Willhite, *Retention and Flow Characteristics of Polymer Solutions in Porous Media.* Society of Petroleum Engineers Journal, 1977. **17**(02).

39. Pye, D.J., *Improved Secondary Recovery by Control of Water Mobility.* Journal of Petroleum Technology, 1964. **16**(08): p. 911-916.

40. Jennings, R.R., J.H. Rogers, and T.J. West, *Factors Influencing Mobility Control By Polymer Solutions.* Journal of Petroleum Technology, 1971. **23**(3): p. 391-401.

41. Sorbie, K.S. and L.J. Roberts, *A Model for Calculating Polymer Injectivity Including the Effects of Shear Degradation*, in *SPE Enhanced Oil Recovery Symposium*. 1984, Society of Petroleum Engineers: Tulsa, Oklahoma, USA.

42. Seright, R.S., *The Effects of Mechanical Degradation and Viscoelastic Behavior on Injectivity of Polyacrylamide Solutions.* Society of Petroleum Engineers Journal, 1983. **23**(03): p. 475-485.

43. CMG, *STARS User Guide*. 2016, Calgary, Canada: CMG. 1511.

44. CMG, *Results 3D User Guide*. 2014, Calgary, Alberta, Canada: CMG.

45. Evensen, G., *The ensemble Kalman filter: Theoretical formulation and practical implementation.* Ocean dynamics, 2003. **53**(4): p. 343-367.

46. Krymskaya, M.V., R.G. Hanea, and M. Verlaan, *An iterative ensemble Kalman filter for reservoir engineering applications.* Computational Geosciences, 2009. **13**(2): p. 235-244.

47. Chang, R. and J. Overby, *General Chemisty: The Essential Concepts*. 6th ed. 2011, New York, USA: McGraw-Hill.

48. Hirasaki, G.J. and G.A. Pope, *Analysis of Factors Influencing Mobility and Adsorption in the Flow of Polymer Solution Through Porous Media.* Society of Petroleum Engineers Journal, 1974. **14**(04).

49. Masuda, Y., et al., *1D Simulation of Polymer Flooding Including the Viscoelastic Effect of Polymer Solution.* SPE Reservoir Engineering, 1992. **7**(02).

50. Heemskerk, J., et al., *Quantification of Viscoelastic Effects of Polyacrylamide Solutions*, in *SPE Enhanced Oil Recovery Symposium*. 1984, Society of Petroleum Engineers: Tulsa, Oklahoma, USA.

51. Seright, R.S., M. Seheult, and T. Talashek, *Injectivity Characteristics of EOR Polymers*, in *SPE Annual Technical Conference and Exhibition*. 2009, Society of Petroleum Engineers: Denver, Colorado, USA. p. 1-14.

52. Seright, R.S., et al., *New Insights Into Polymer Rheology in Porous Media.* SPE Journal, 2011.

53. Lewandowska, K., *Comparative studies of rheological properties of polyacrylamide and partially hydrolyzed polyacrylamide solutions.* Journal of Applied Polymer Science, 2007. **103**(4): p. 2235-2241.

54. Huang, Y. and K.S. Sorbie, *The Adsorption and In-situ Rheological Behaviour of Xanthan Solution Flowing Through Porous Media*, in *SPE/DOE Eight Symposium on Enhanced Oil Recovery*. 1992, Society of Petroleum Engineers: Tulsa, Oklahoma.

55. Hejri, S., G.P. Willhite, and D.W. Green, *Development of Correlations To Predict Biopolymer Mobility in Porous Media.* SPE Reservoir Engineering, 1991: p. 91-98.

A. STARS Pressure Matches and Rheology Curves

A.1 HPAM Differential Pressure Matches and Corresponding Rheology Curves

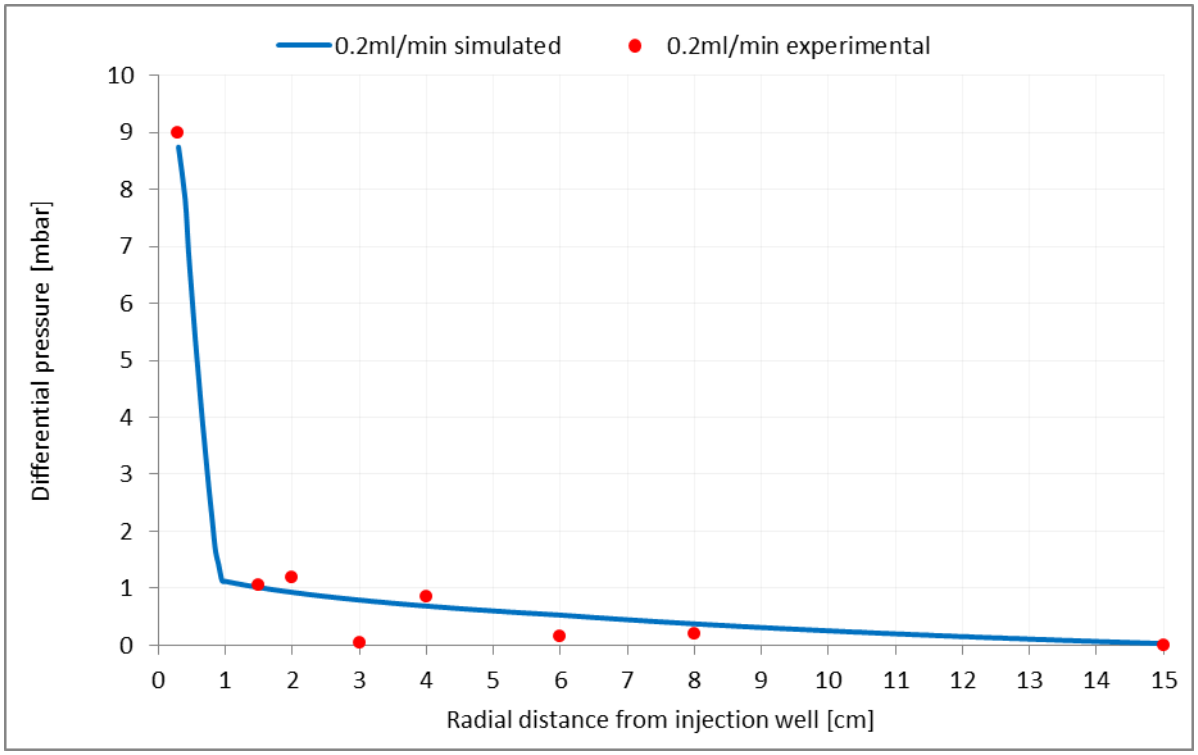

Figure A.1 Differential pressure match for 0.2ml/min HPAM solution injection rate

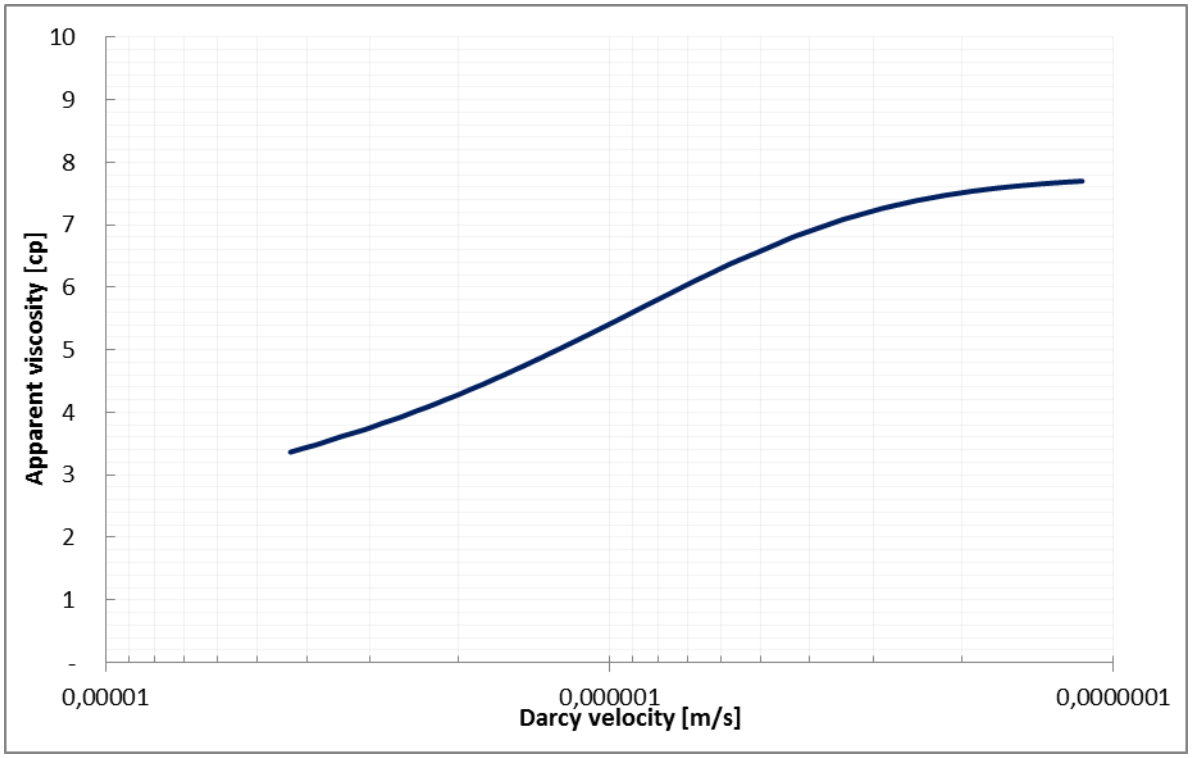

Figure A.2 0.2ml/min HPAM rheology curve

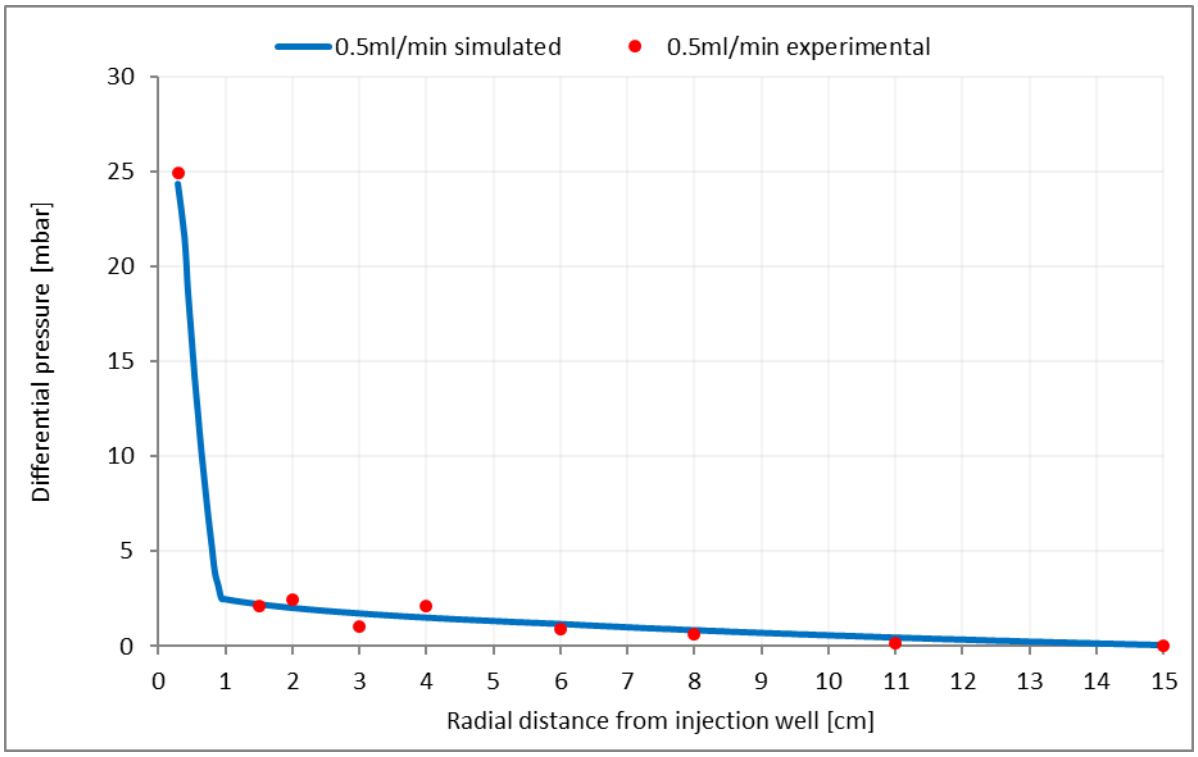

Figure A.3 Differential pressure match for 0.5ml/min HPAM solution injection rate

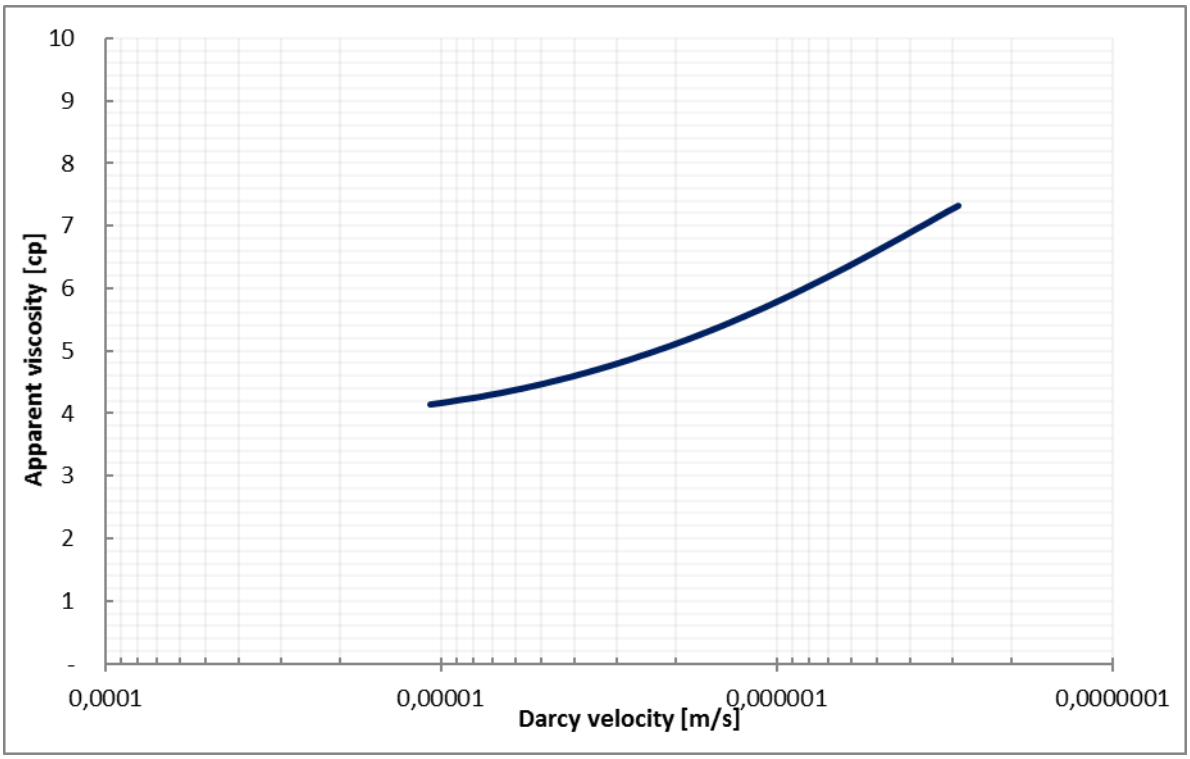

Figure A.4 0.5ml/min HPAM rheology curve

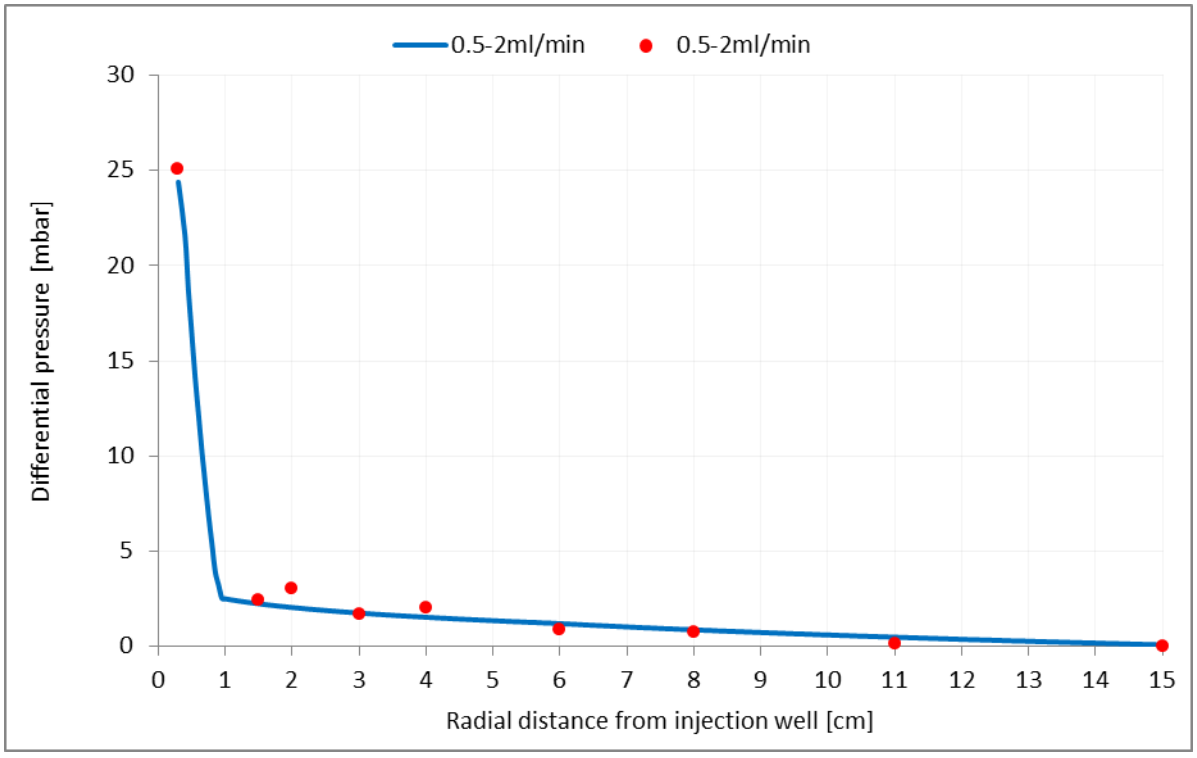

Figure A.5 Differential pressure match for 0.5-2ml/min HPAM solution injection rate

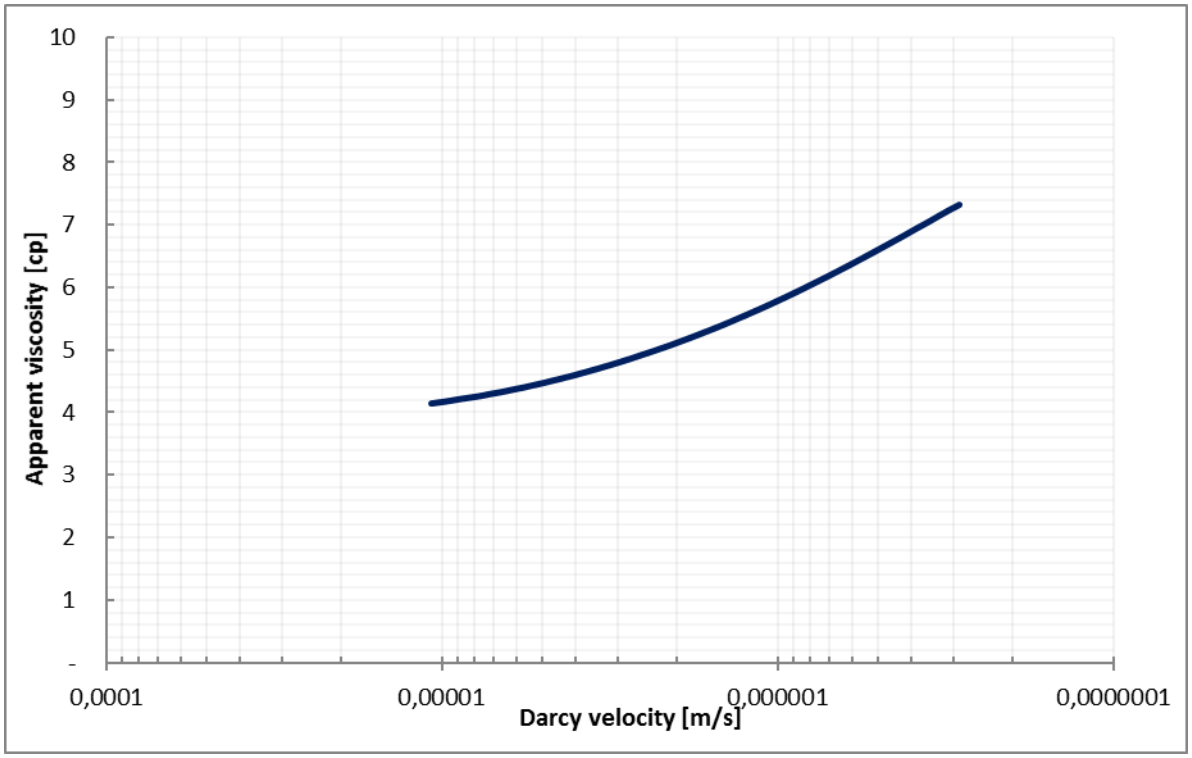

Figure A.6 0.5-2ml/min HPAM rheology curve

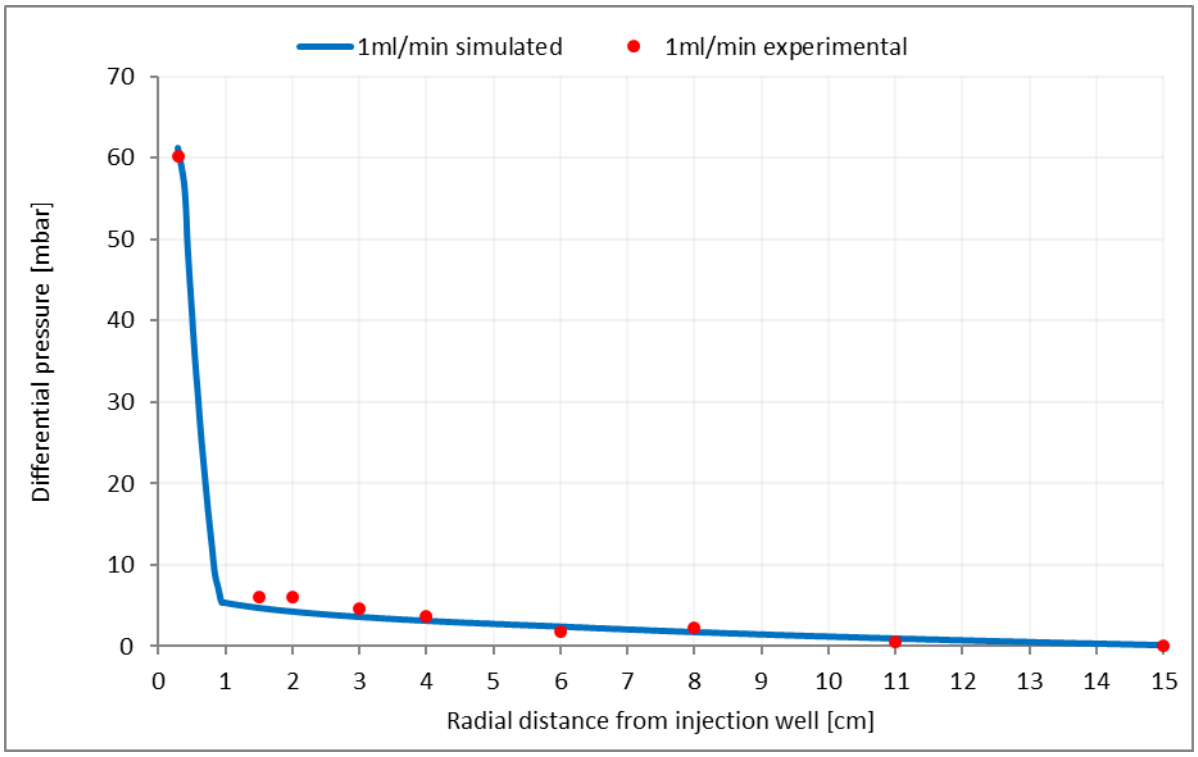

Figure A.7 Differential pressure match for 1ml/min HPAM solution injection rate

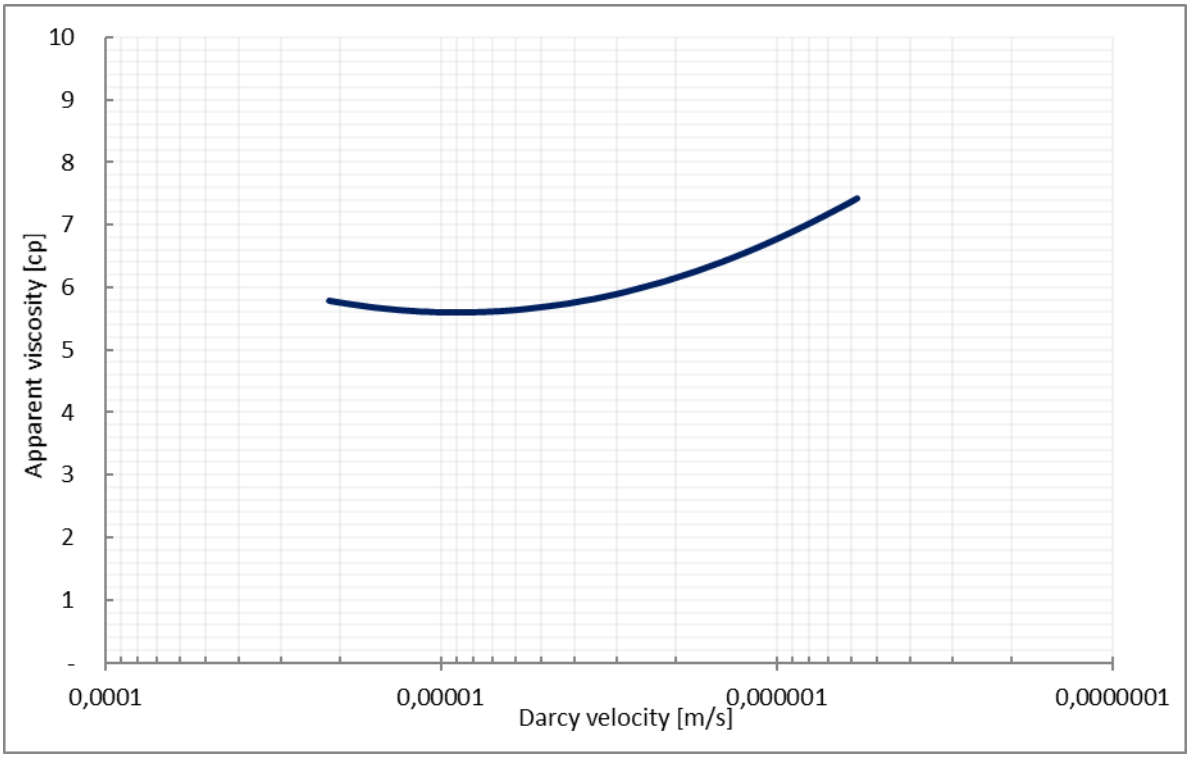

Figure A.8 1ml/min HPAM rheology curve

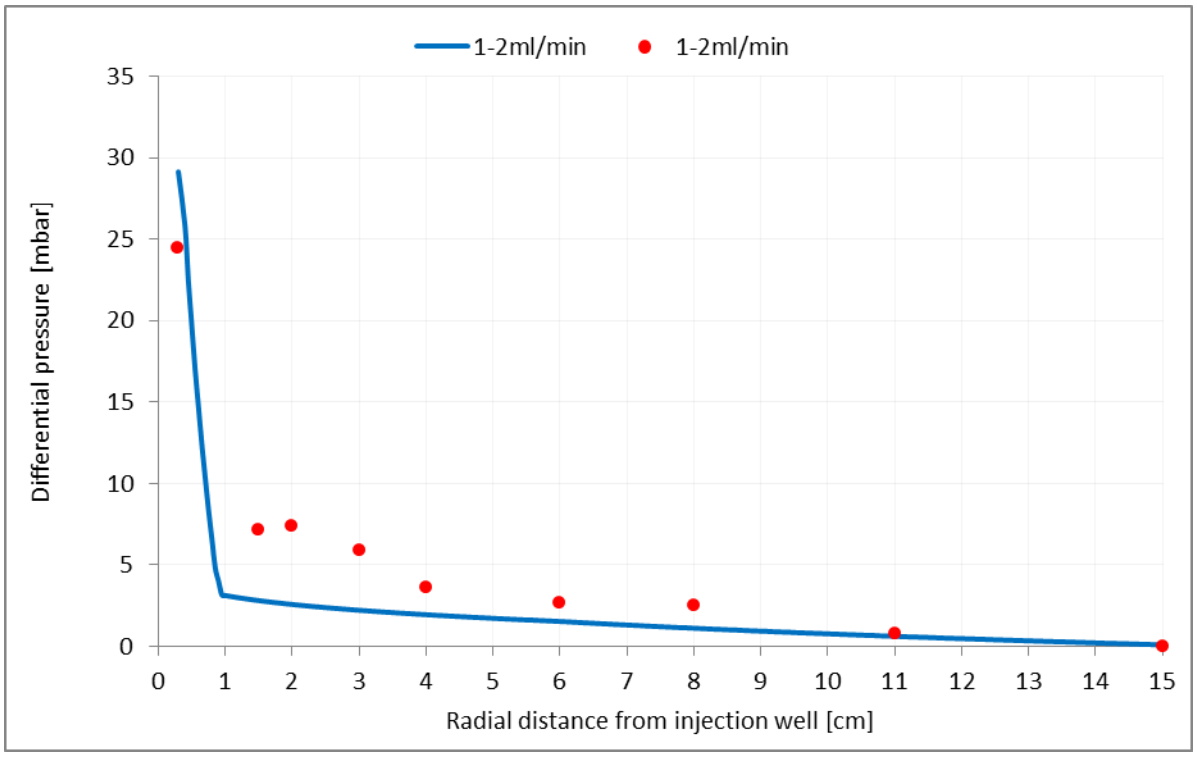

Figure A.9 Differential pressure match for 1-2ml/min HPAM solution injection rate

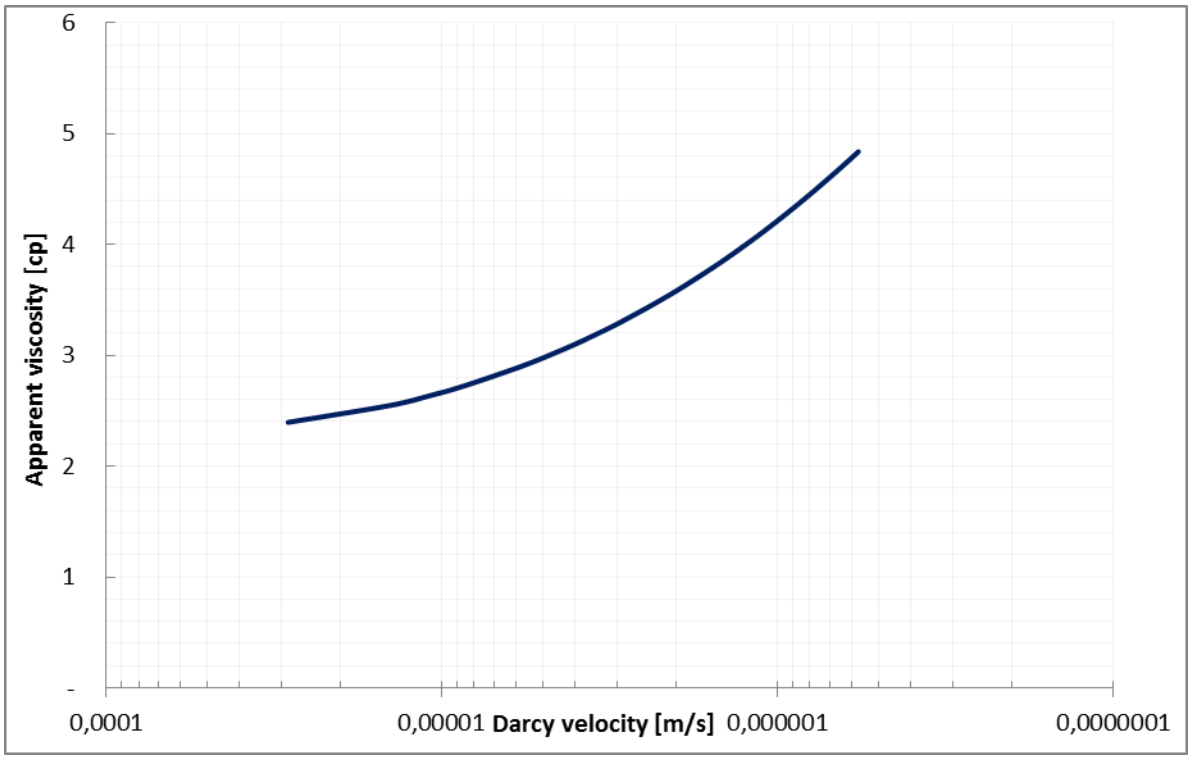

Figure A.10 1-2ml/min HPAM rheology curve

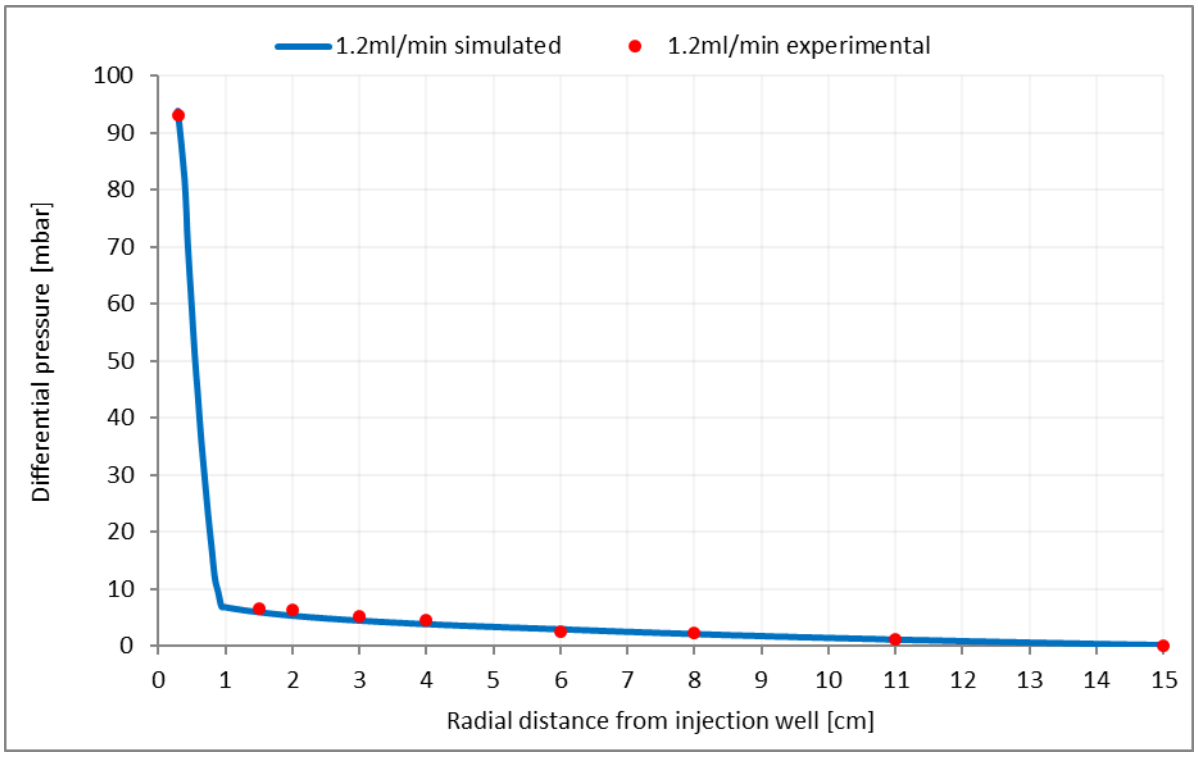

Figure A.11 Differential pressure match for 1.2ml/min HPAM solution injection rate

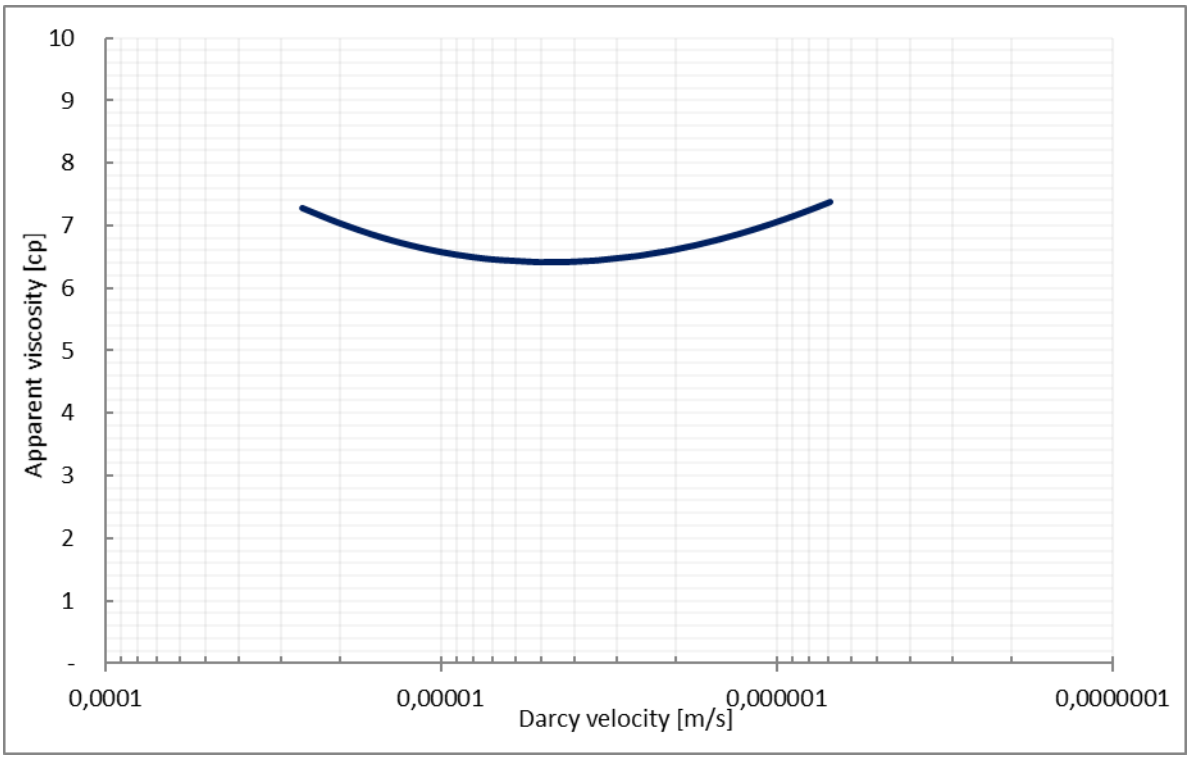

Figure A.12 1.2ml/min HPAM rheology curve

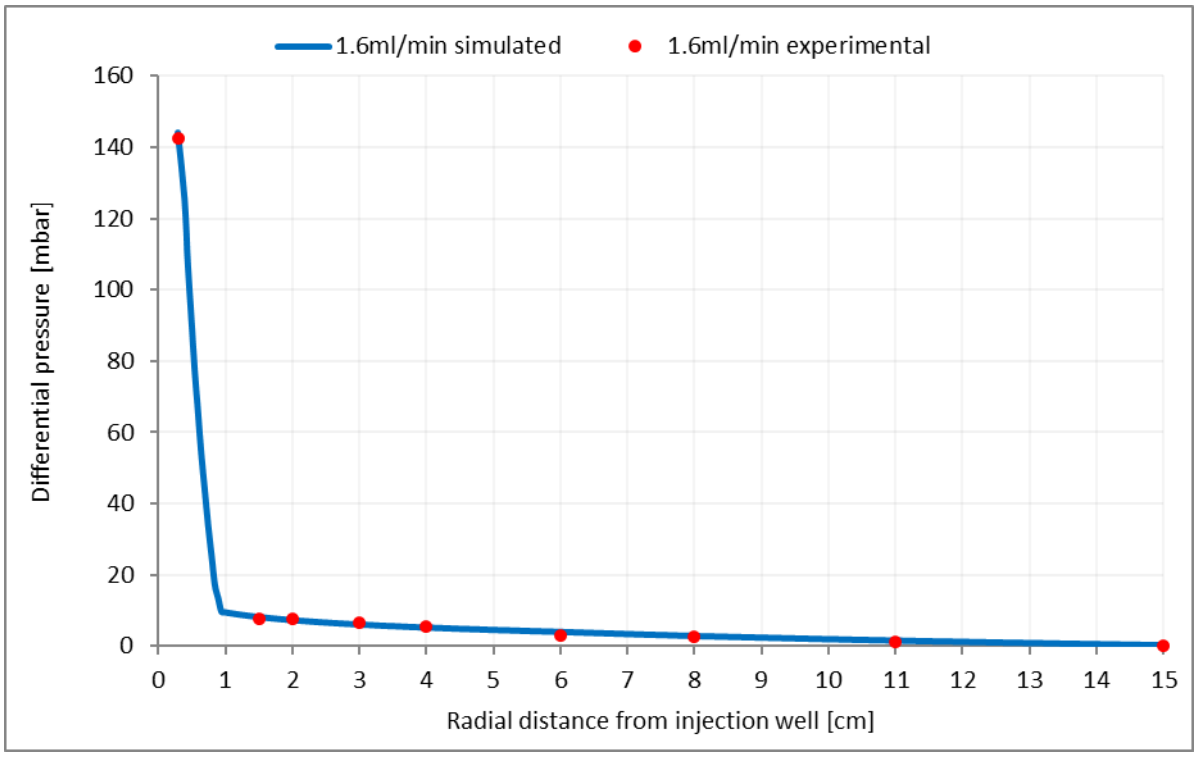

Figure A.13 Differential pressure match for 1.6ml/min HPAM solution injection rate

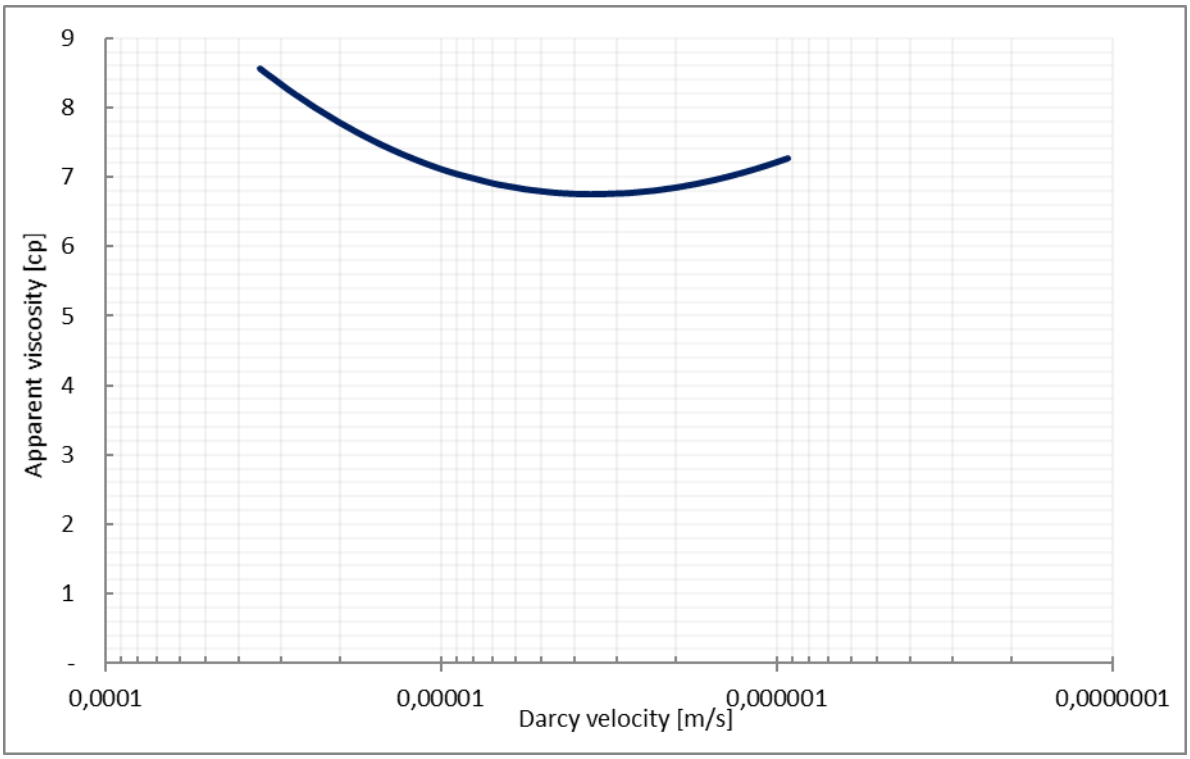

Figure A.14 1.6ml/min HPAM rheology curve

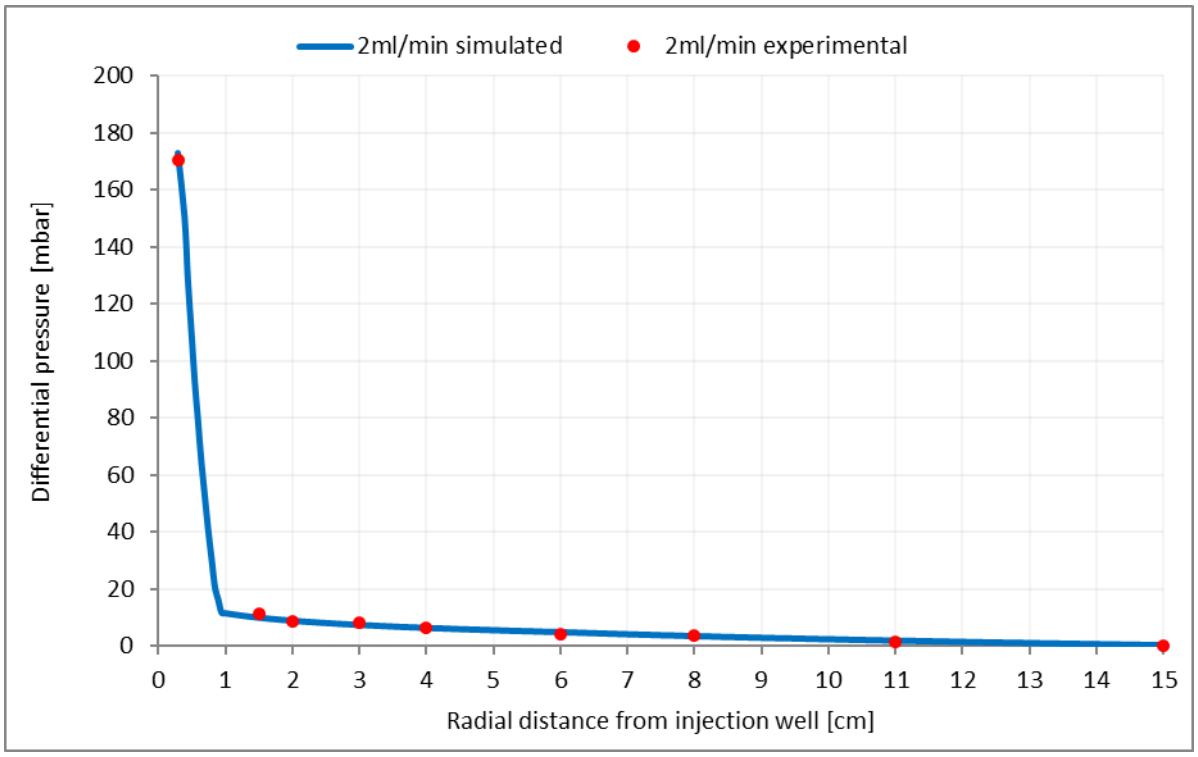

Figure A.15 Differential pressure match for 2ml/min HPAM solution injection rate

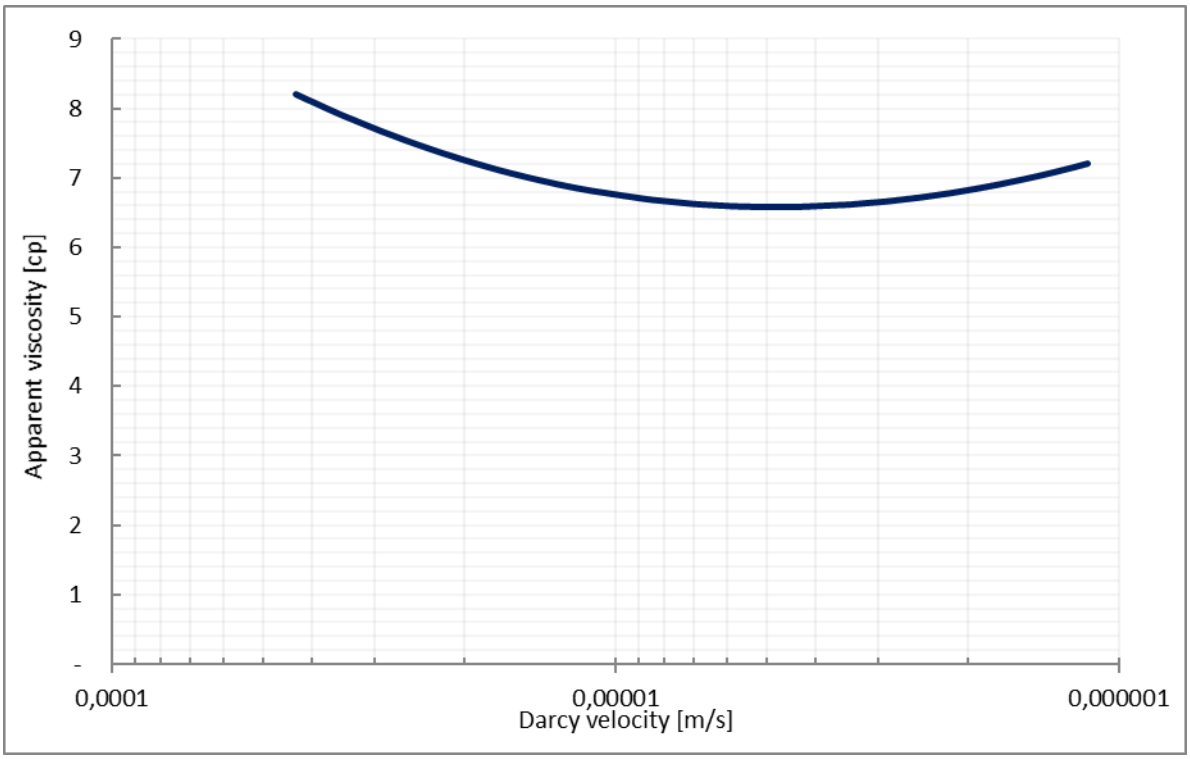

Figure A.16 2ml/min HPAM rheology curve

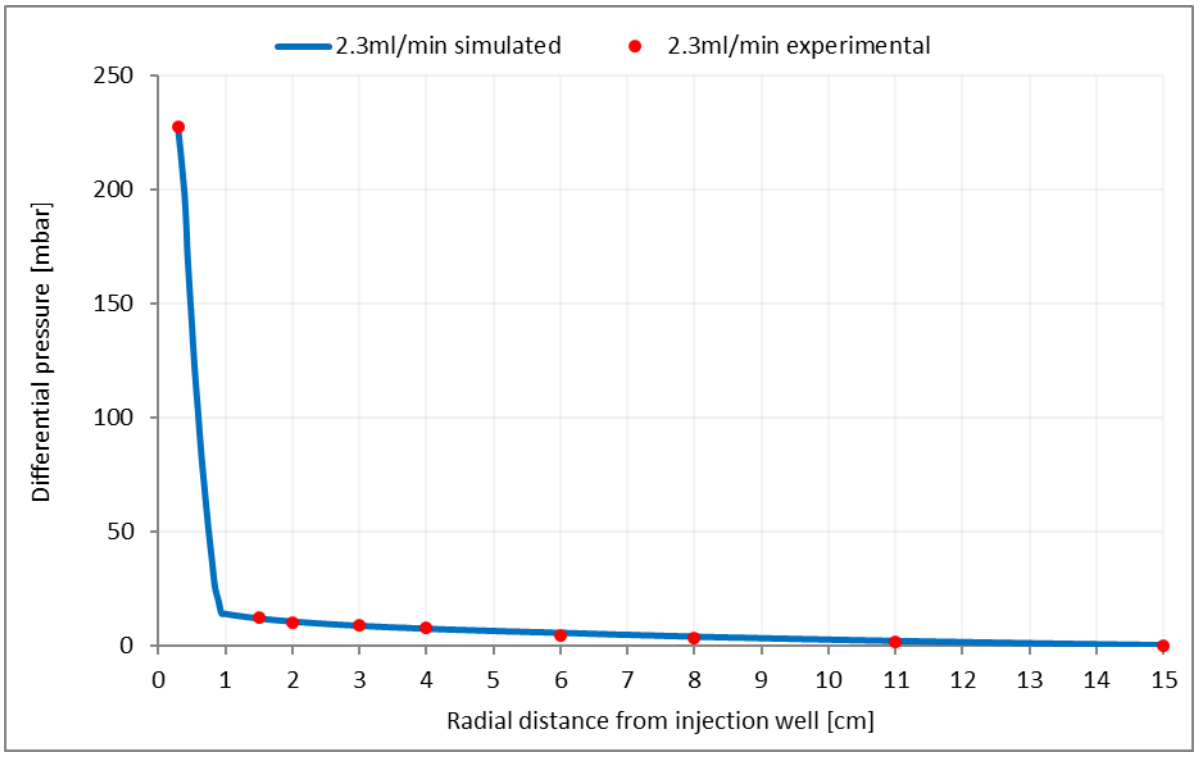

Figure A.17 Differential pressure match for 2.3ml/min HPAM solution injection rate

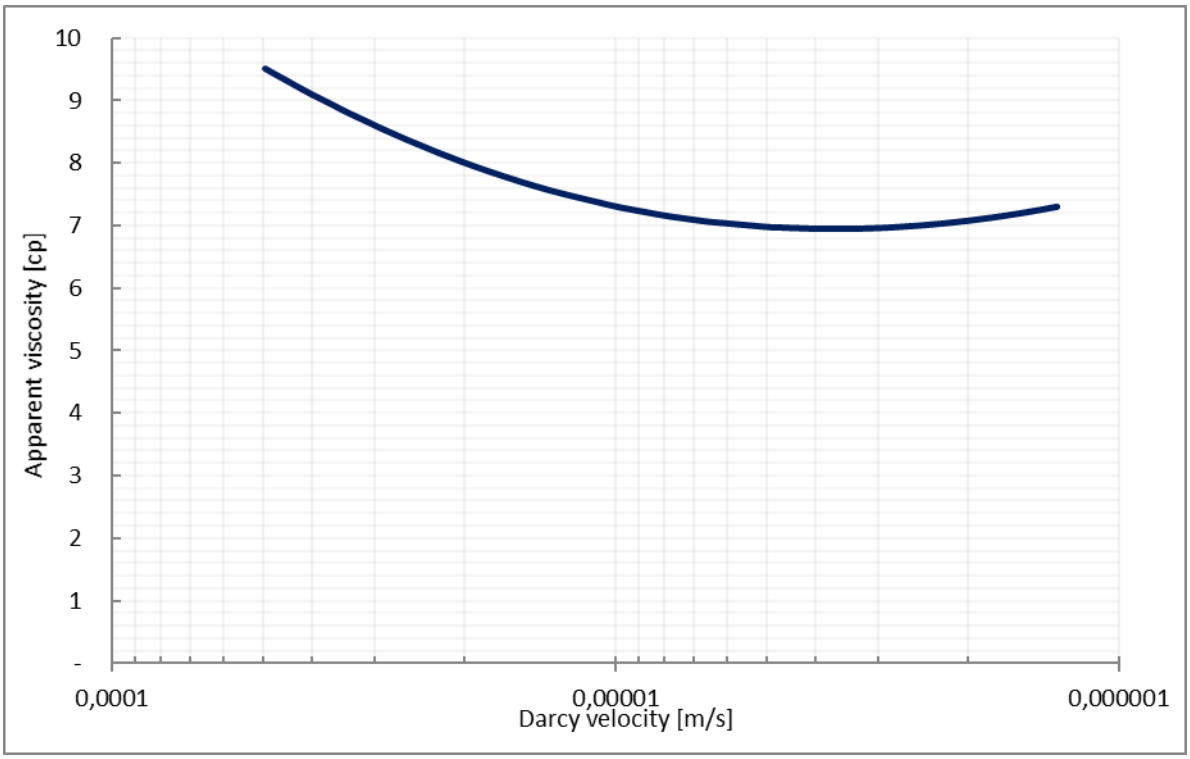

Figure A.18 2.3ml/min HPAM rheology curve

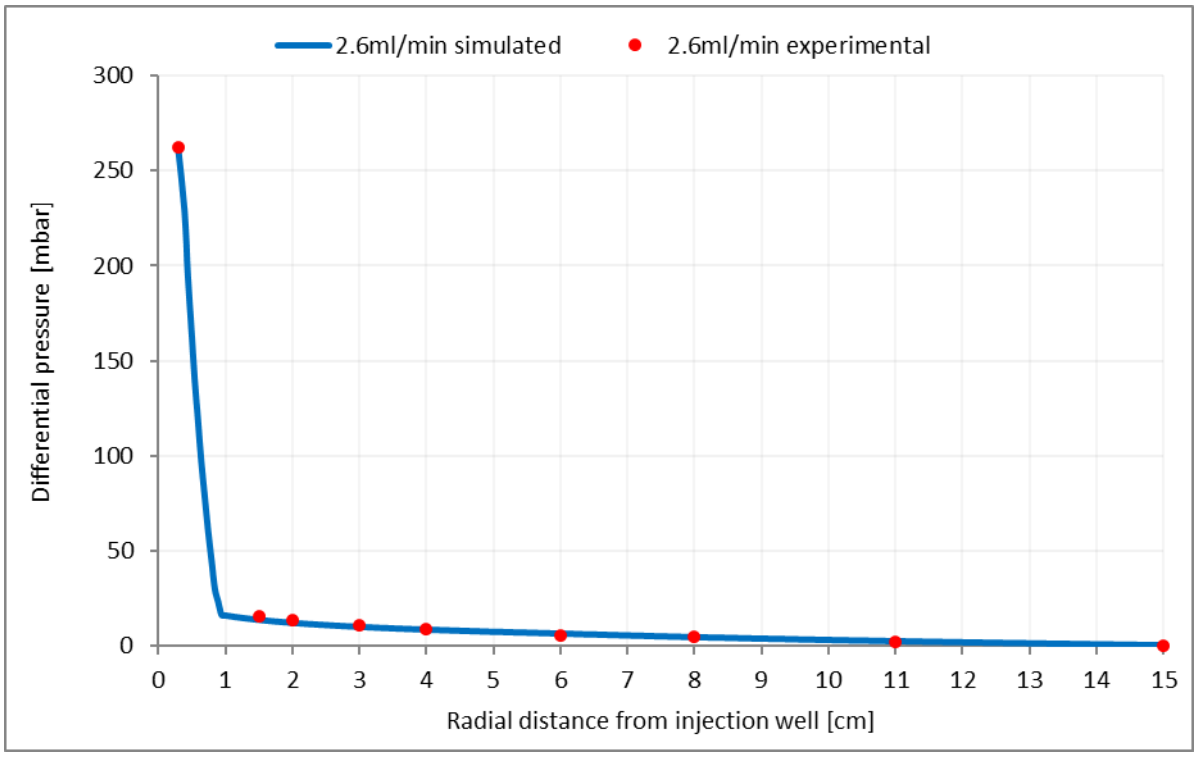

Figure A.19 Differential pressure match for 2.6ml/min HPAM solution injection rate

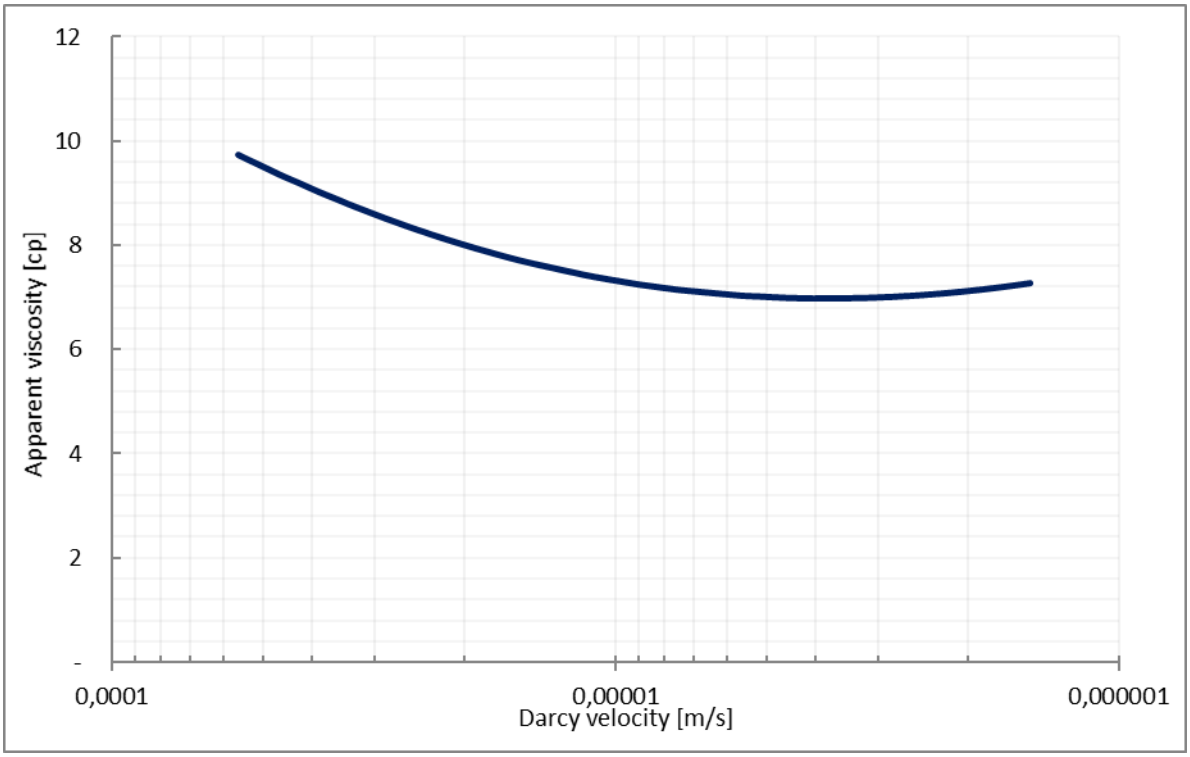

Figure A.20 2.6ml/min HPAM rheology curve

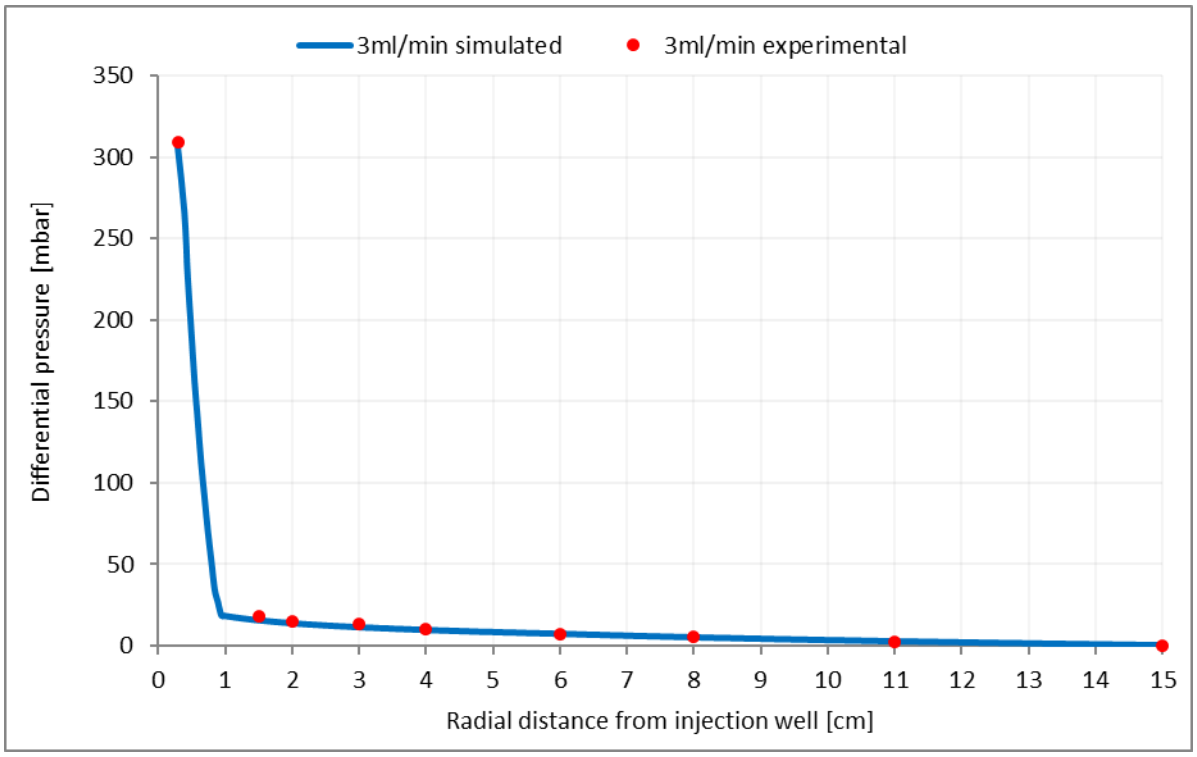

Figure A.21 Differential pressure match for 3ml/min HPAM solution injection rate

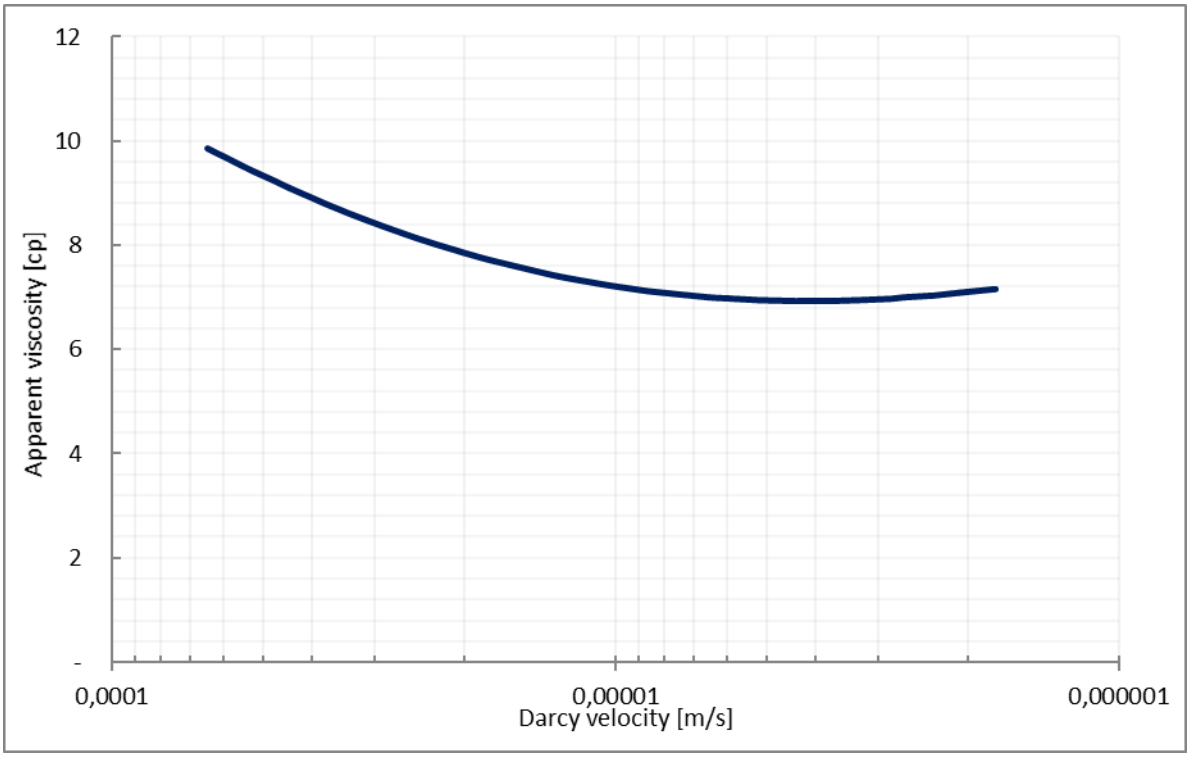

Figure A.22 3ml/min HPAM rheology curve

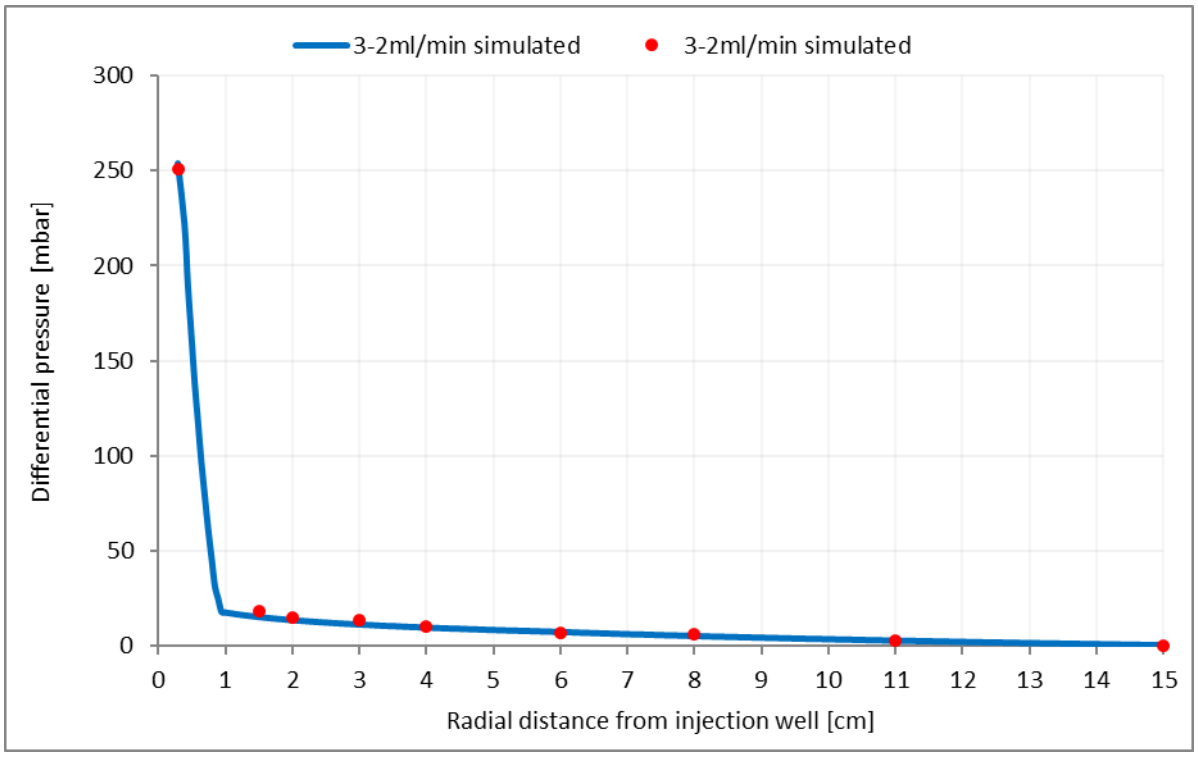

Figure A.23 Differential pressure match for 3-2ml/min HPAM solution injection rate

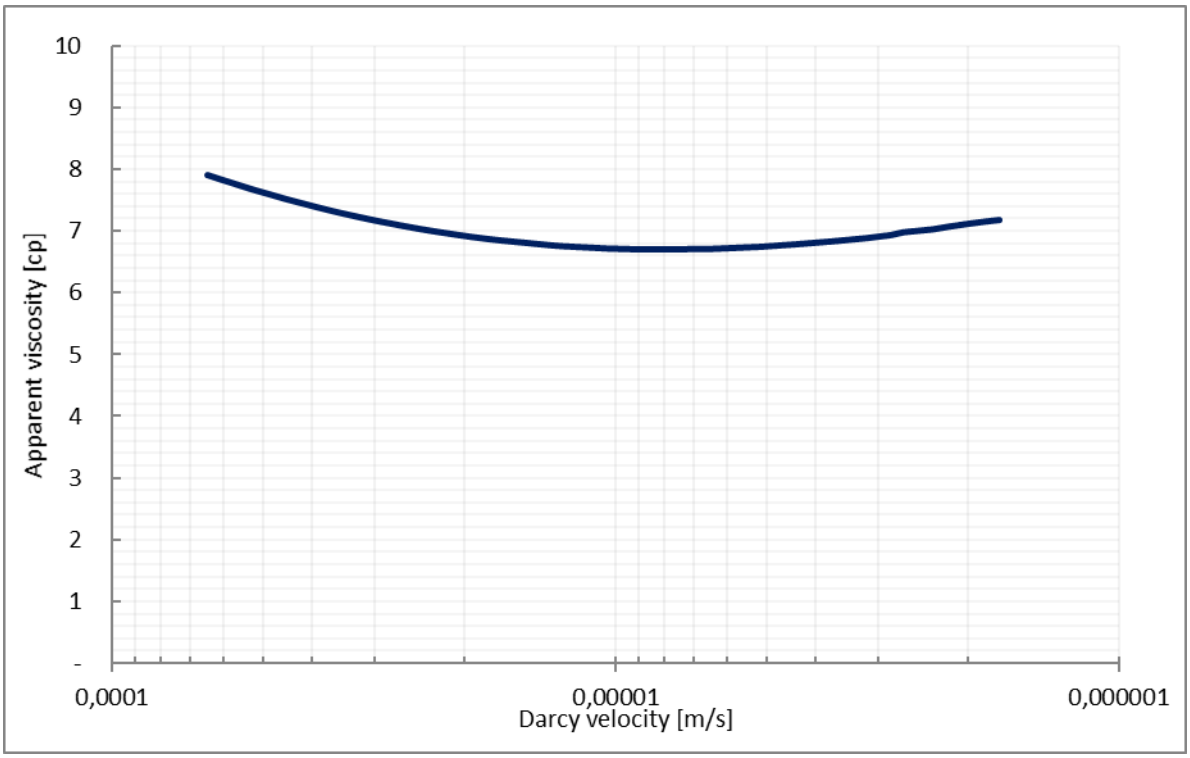

Figure A.24 3-2ml/min HPAM rheology curve

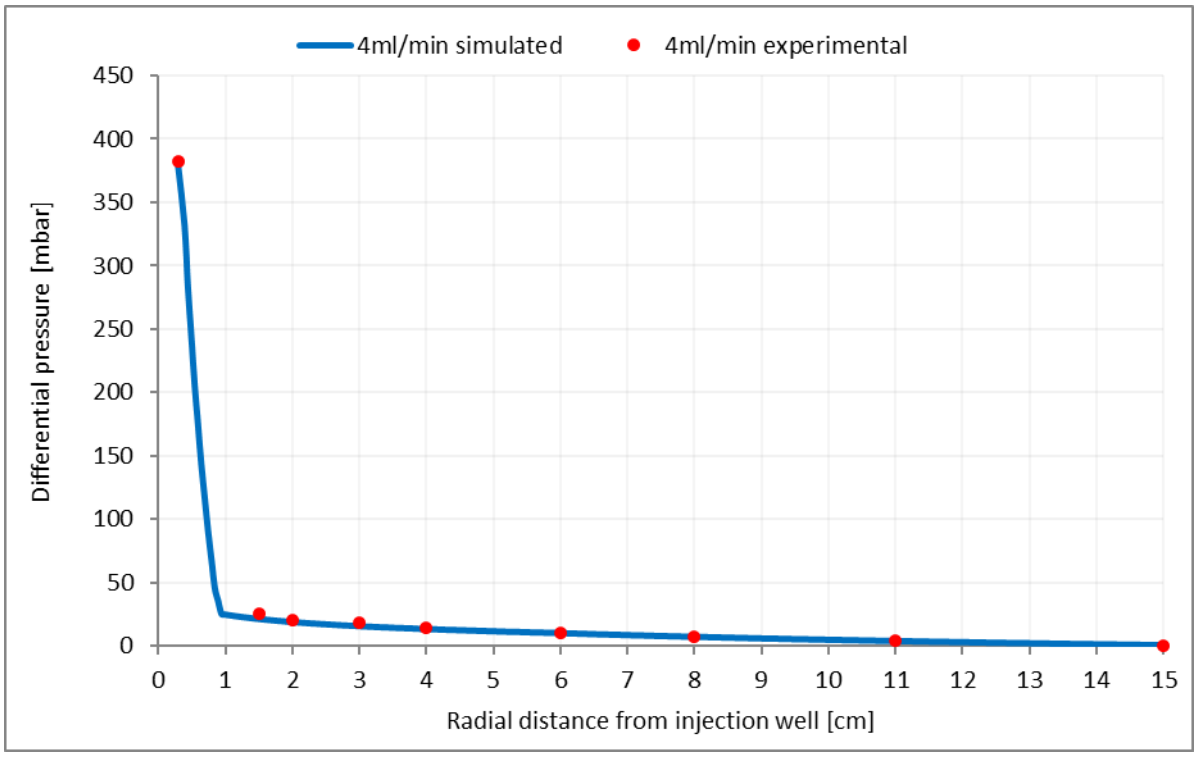

Figure A.25 Differential pressure match for 4ml/min HPAM solution injection rate

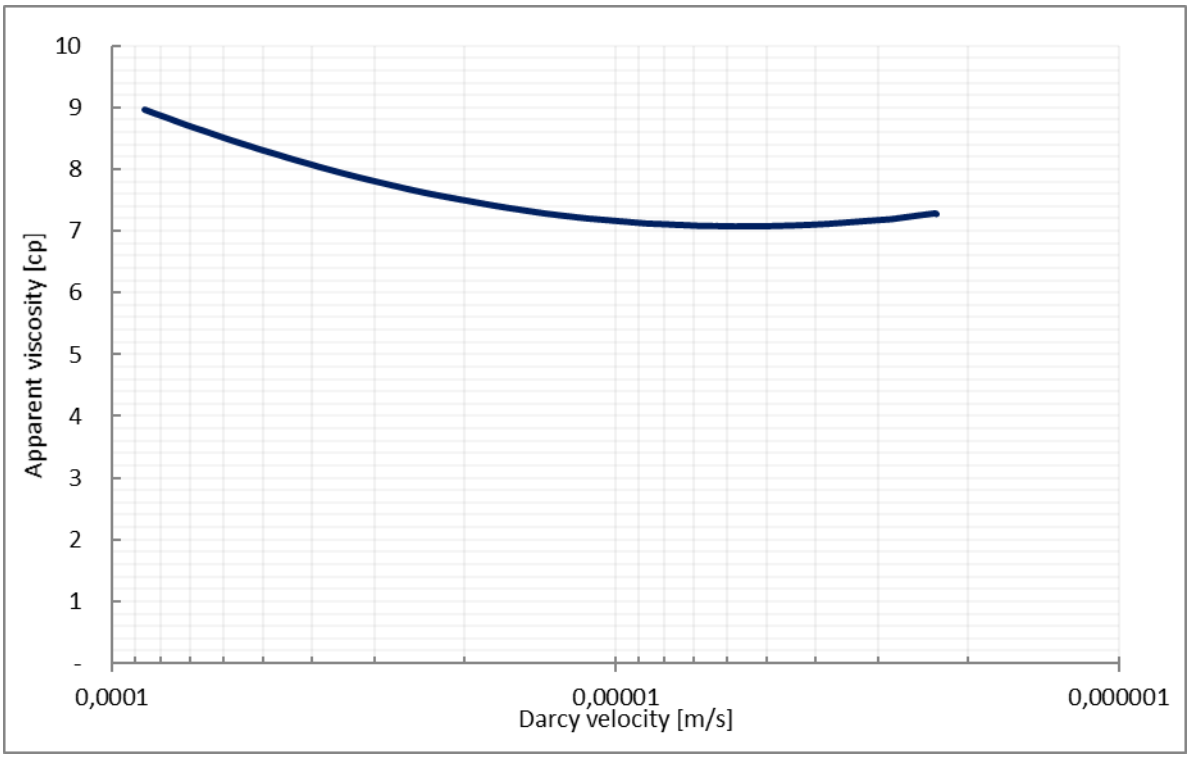

Figure A.26 4ml/min HPAM rheology curve

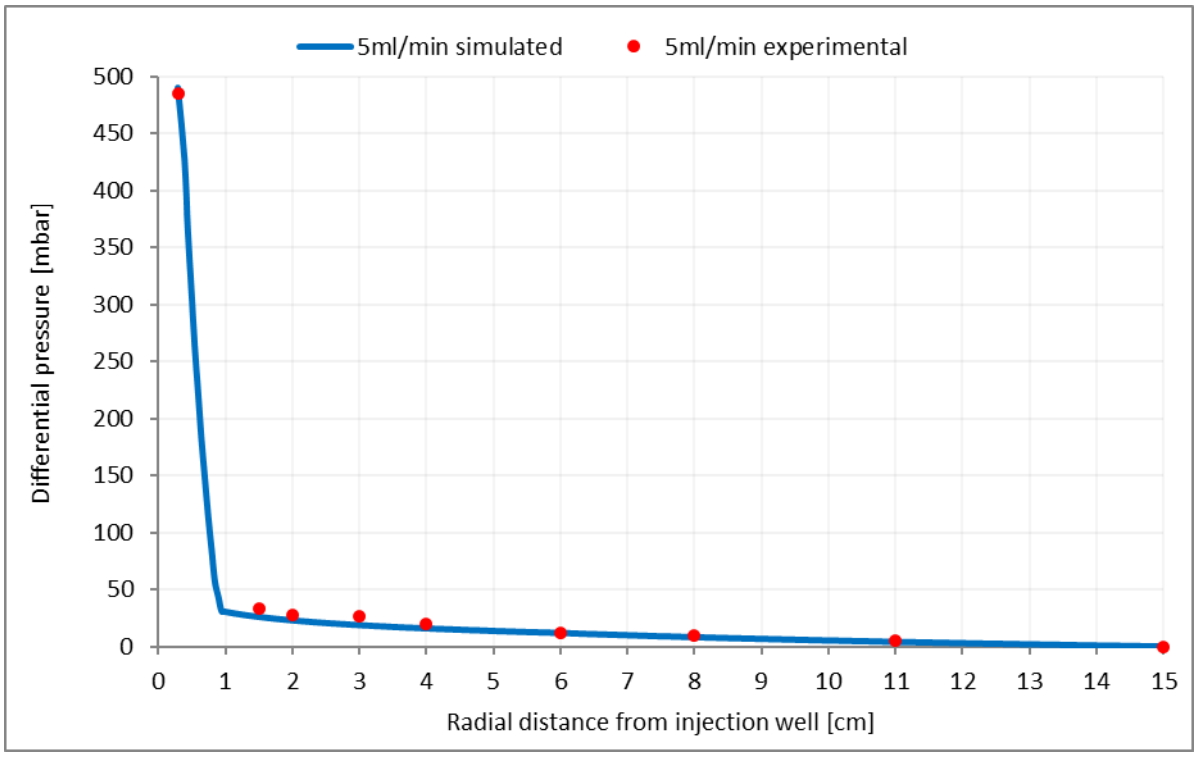

Figure A.27 Differential pressure match for 5ml/min HPAM solution injection rate

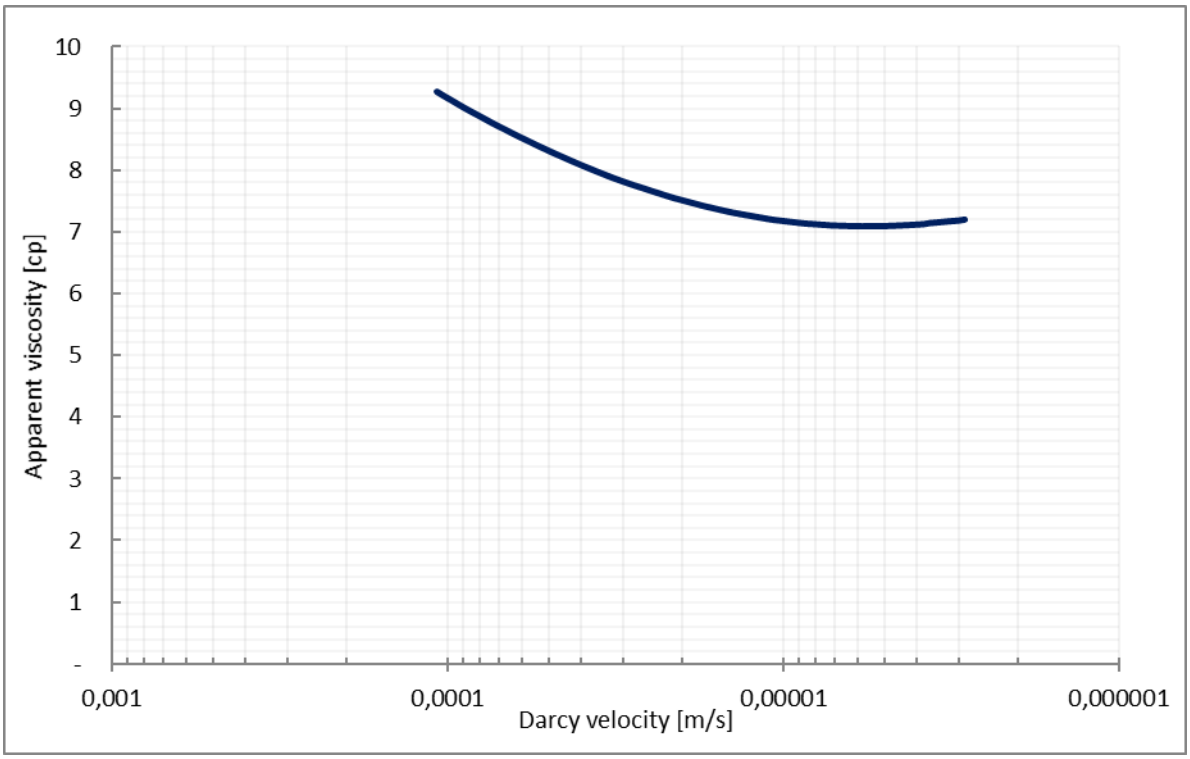

Figure A.28 5ml/min HPAM rheology curve

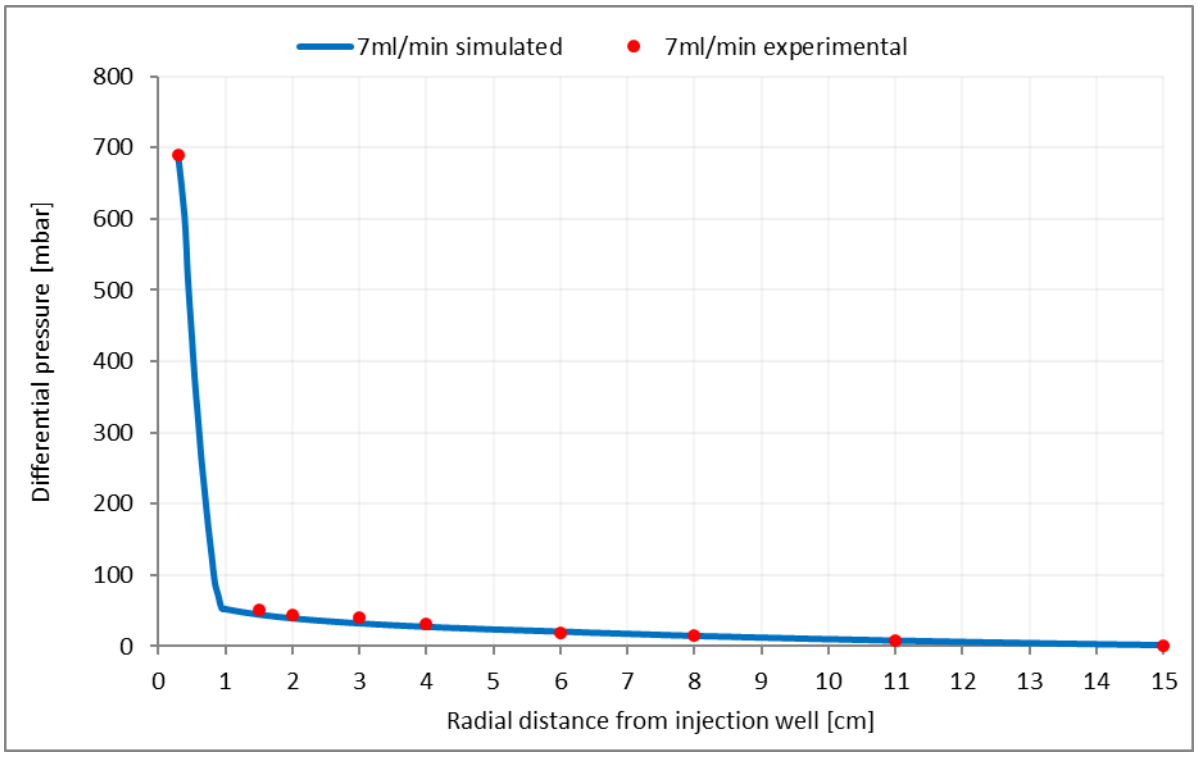

Figure A.29 Differential pressure match for 7ml/min HPAM solution injection rate

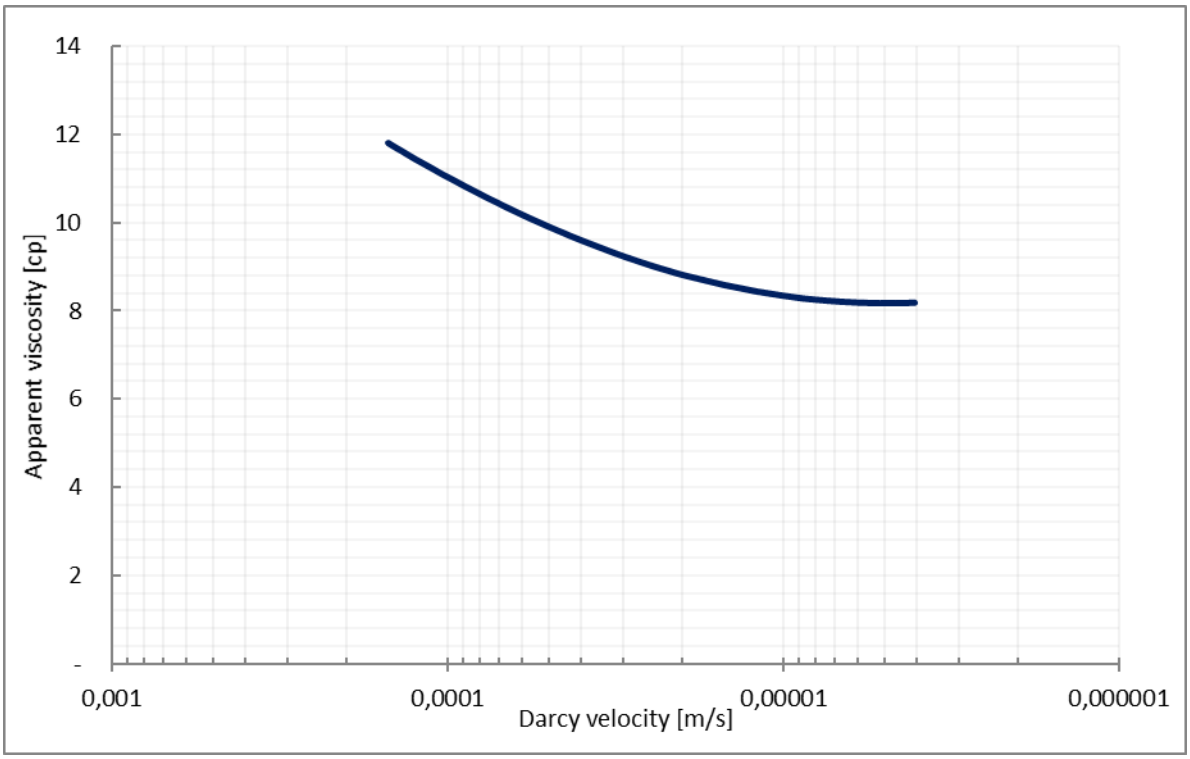

Figure A.30 7ml/min HPAM rheology curve

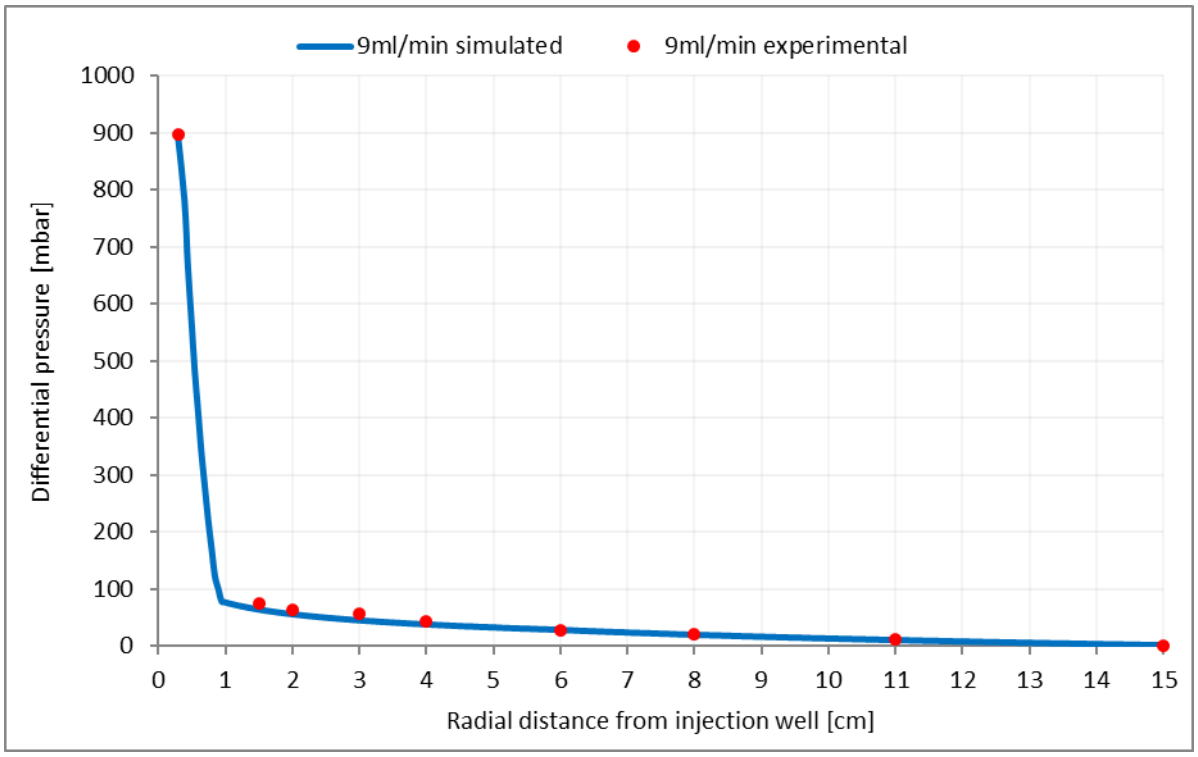

Figure A.31 Differential pressure match for 9ml/min HPAM solution injection rate

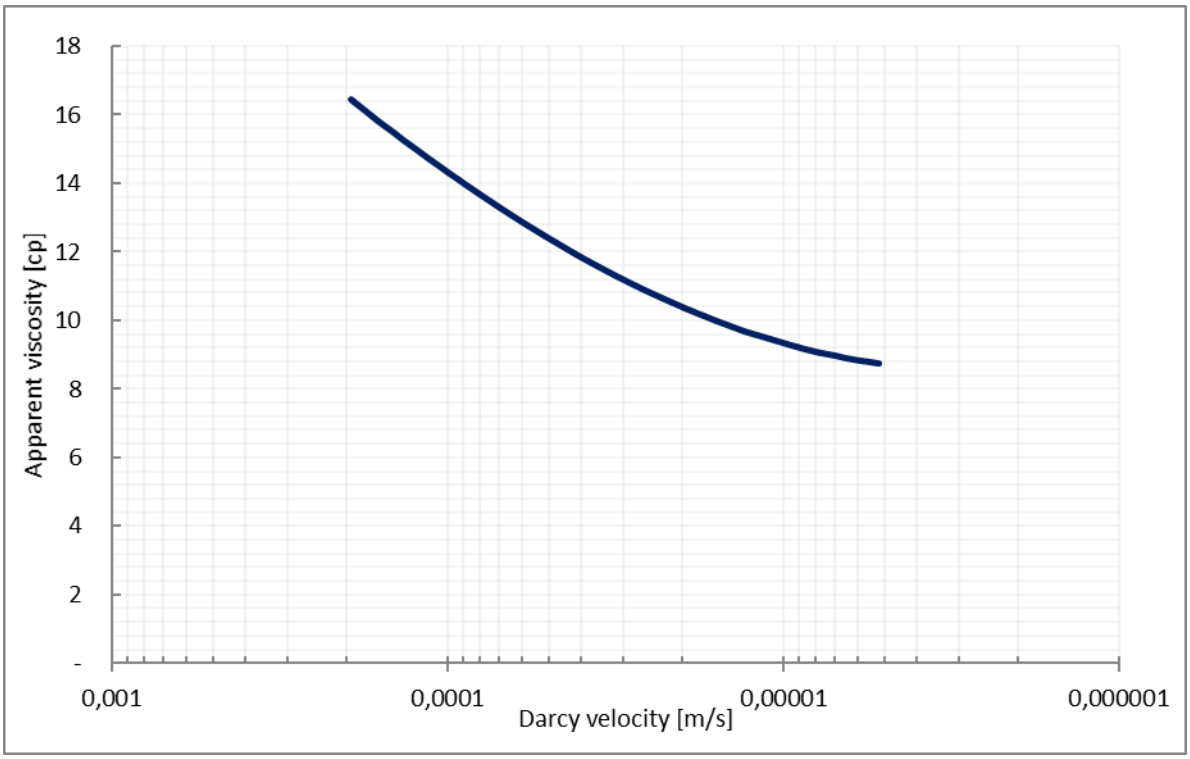

Figure A.32 9ml/min HPAM rheology curve

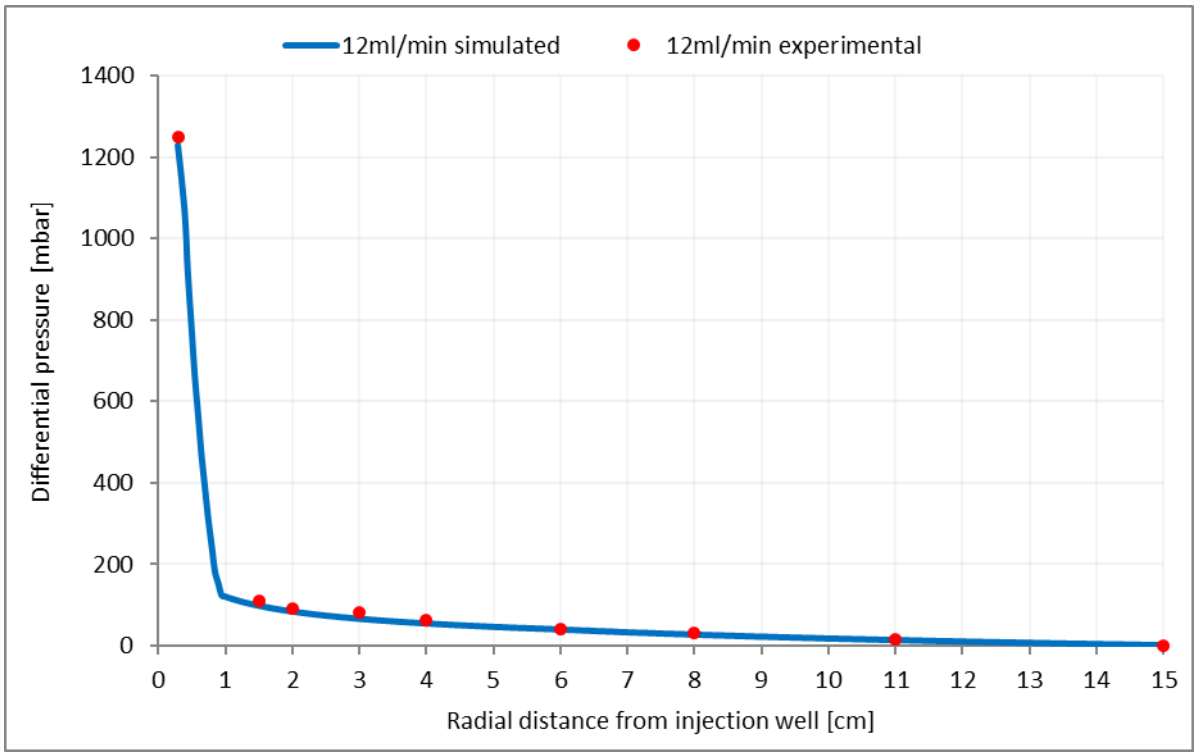

Figure A.33 Differential pressure match for 12ml/min HPAM solution injection rate

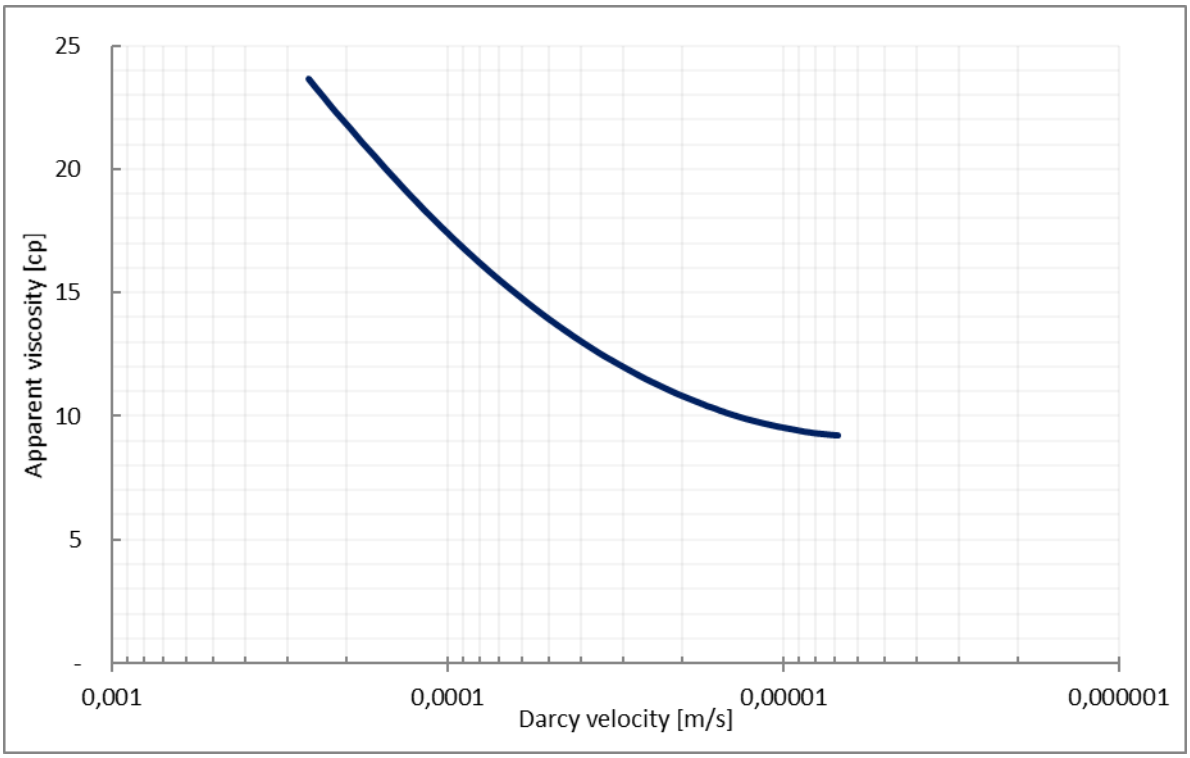

Figure A.34 12ml/min HPAM rheology curve

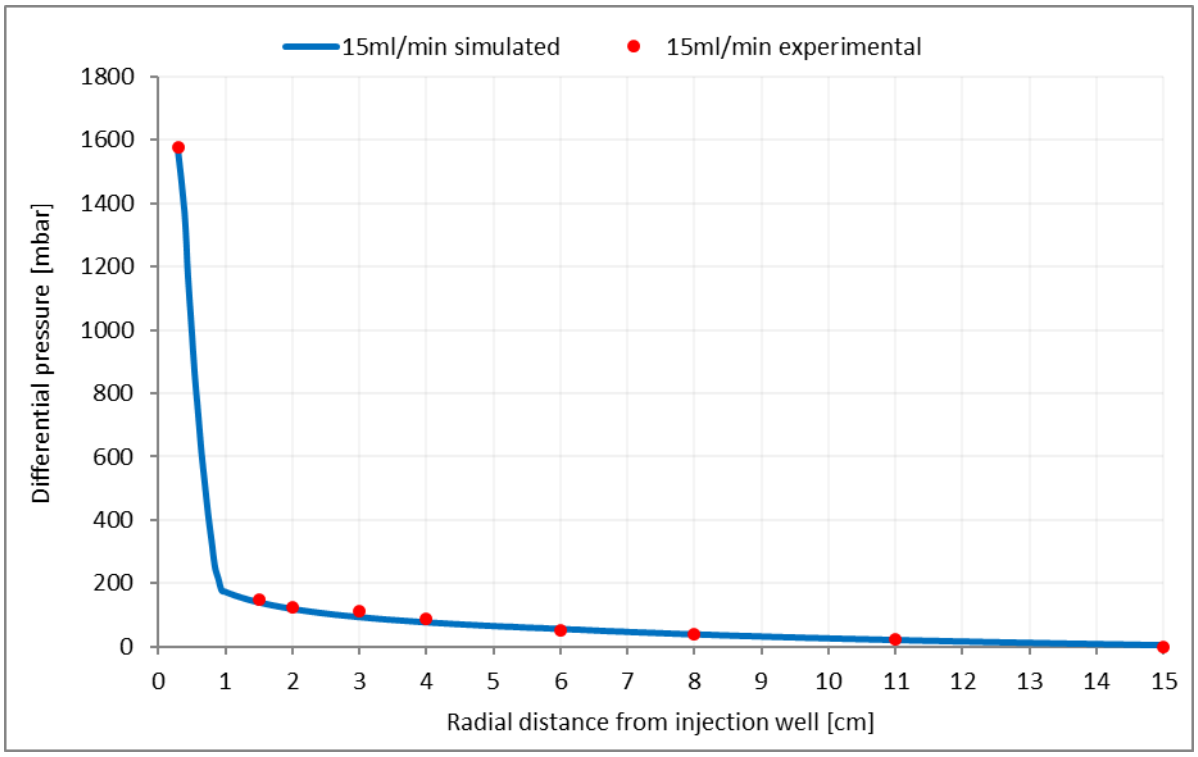

Figure A.35 Differential pressure match for 15ml/min HPAM solution injection rate

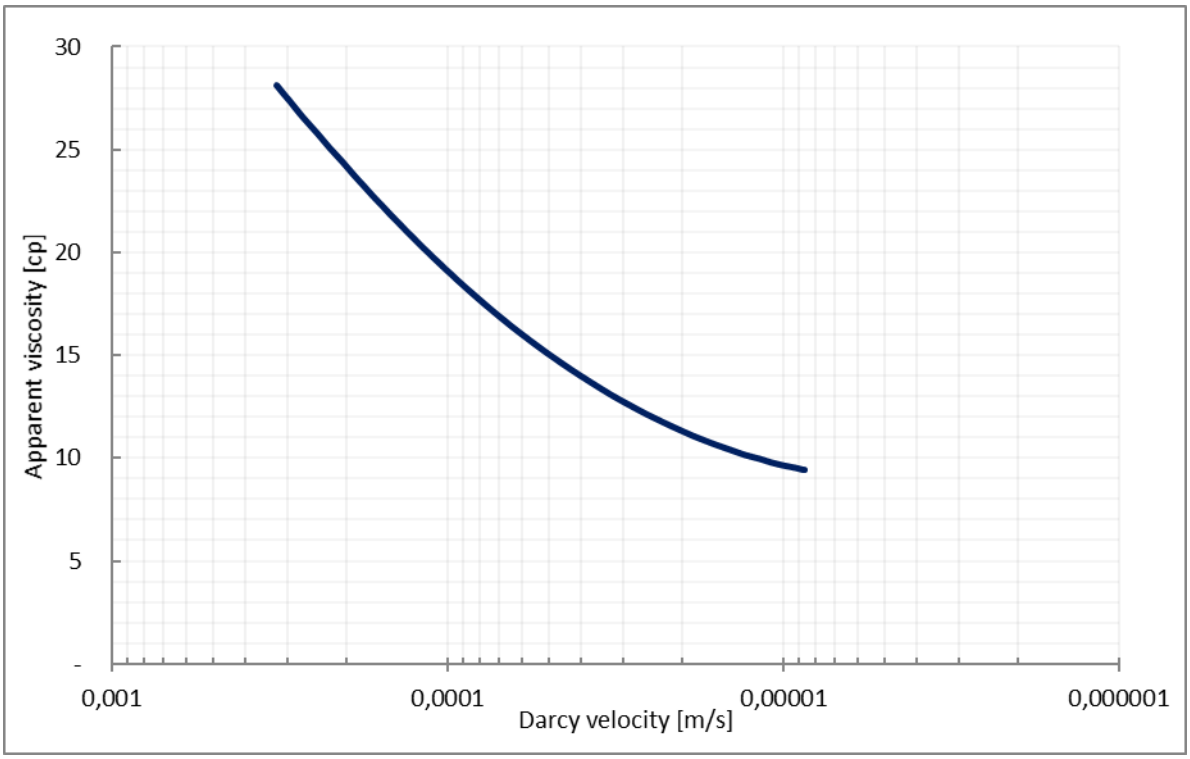

Figure A.36 15ml/min HPAM rheology curve

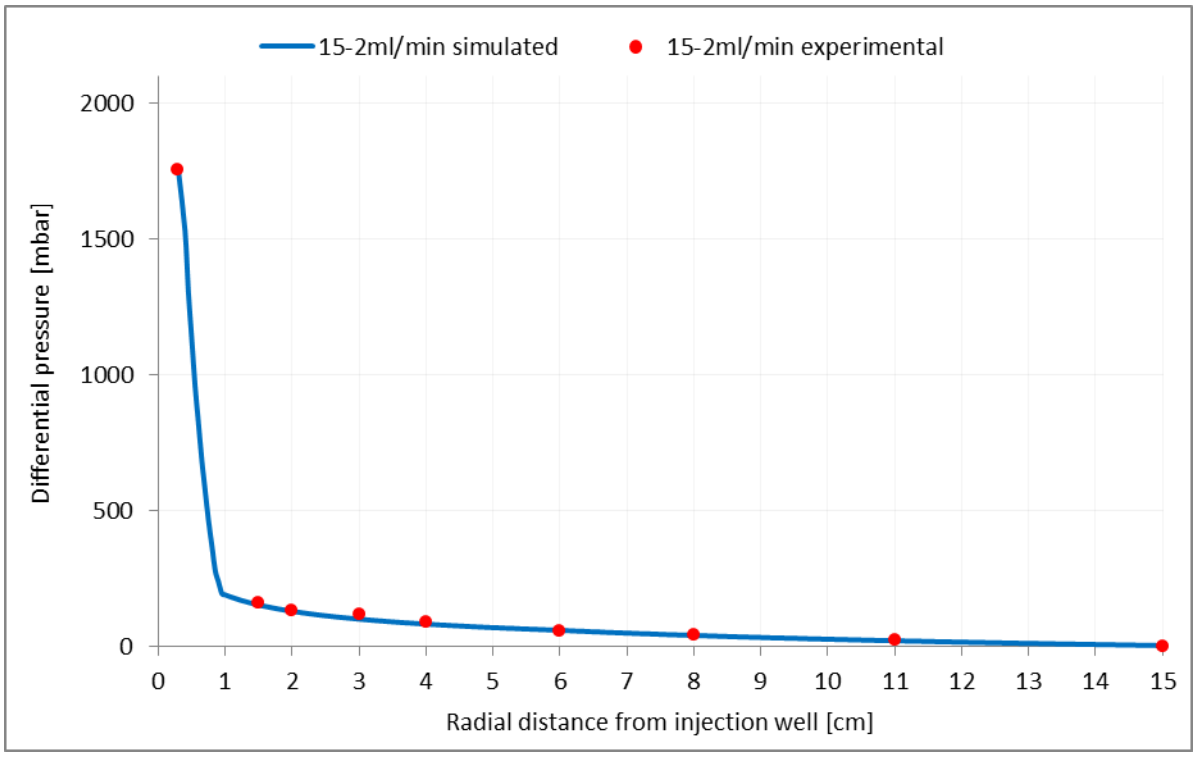

Figure A.37 Differential pressure match for 15-2ml/min HPAM solution injection

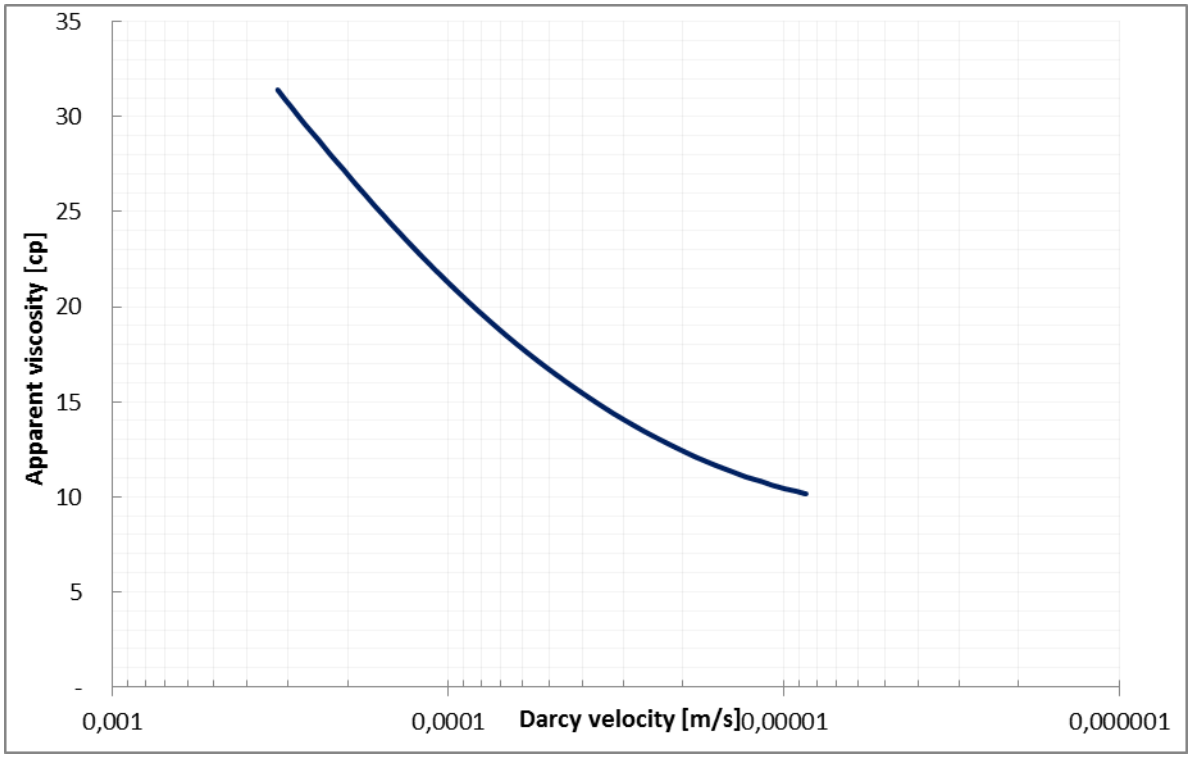

Figure A.38 15-2ml/min HPAM rheology curve

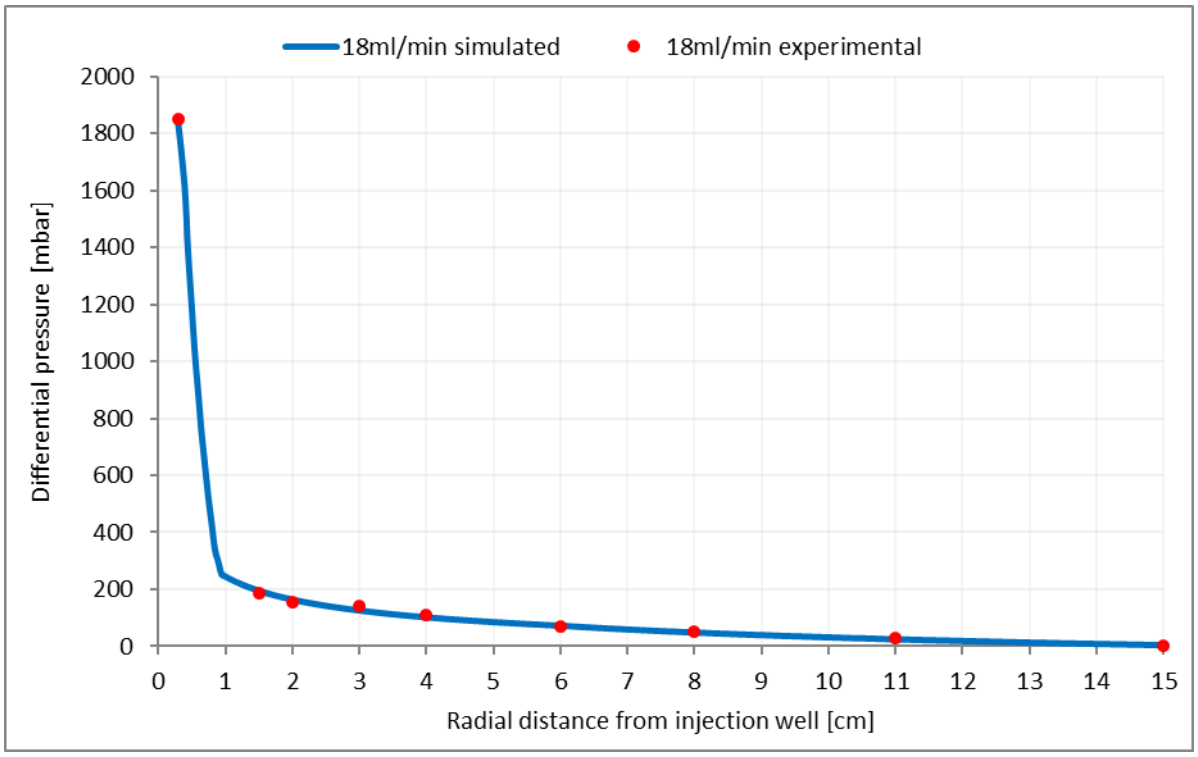

Figure A.39 Differential pressure match for 18ml/min HPAM solution injection rate

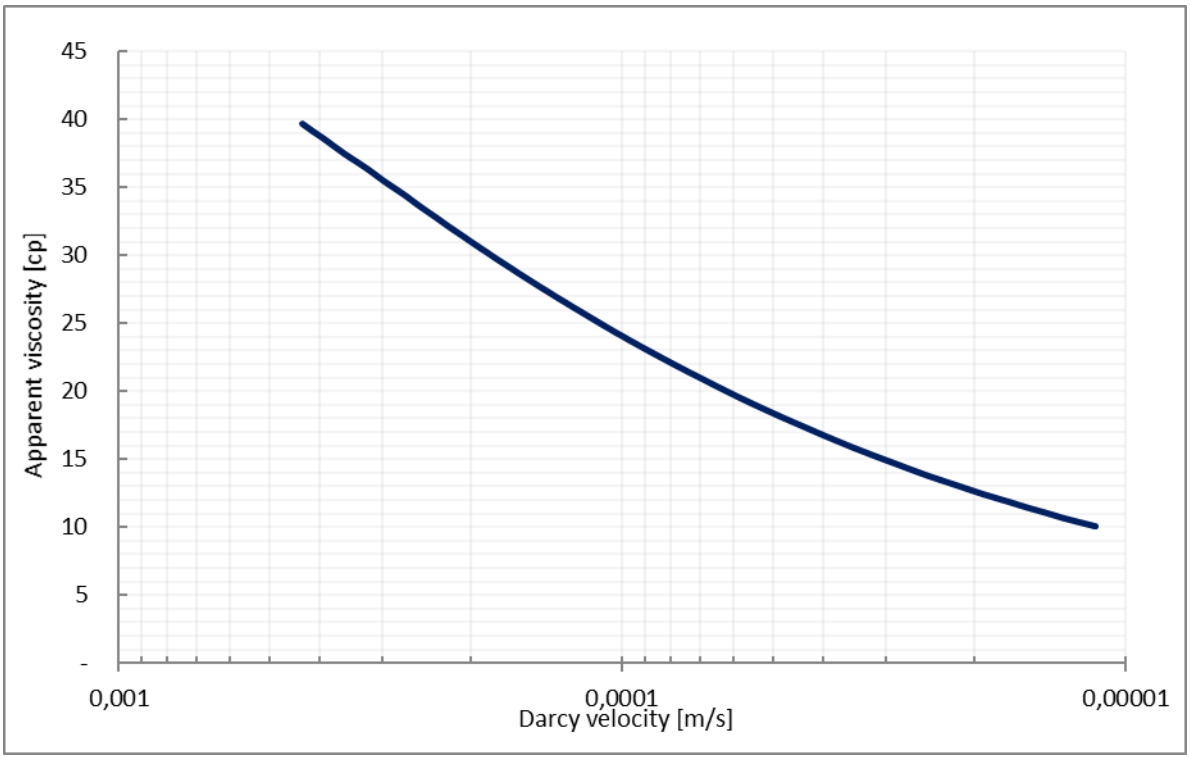

Figure A.40 18ml/min HPAM rheology curve

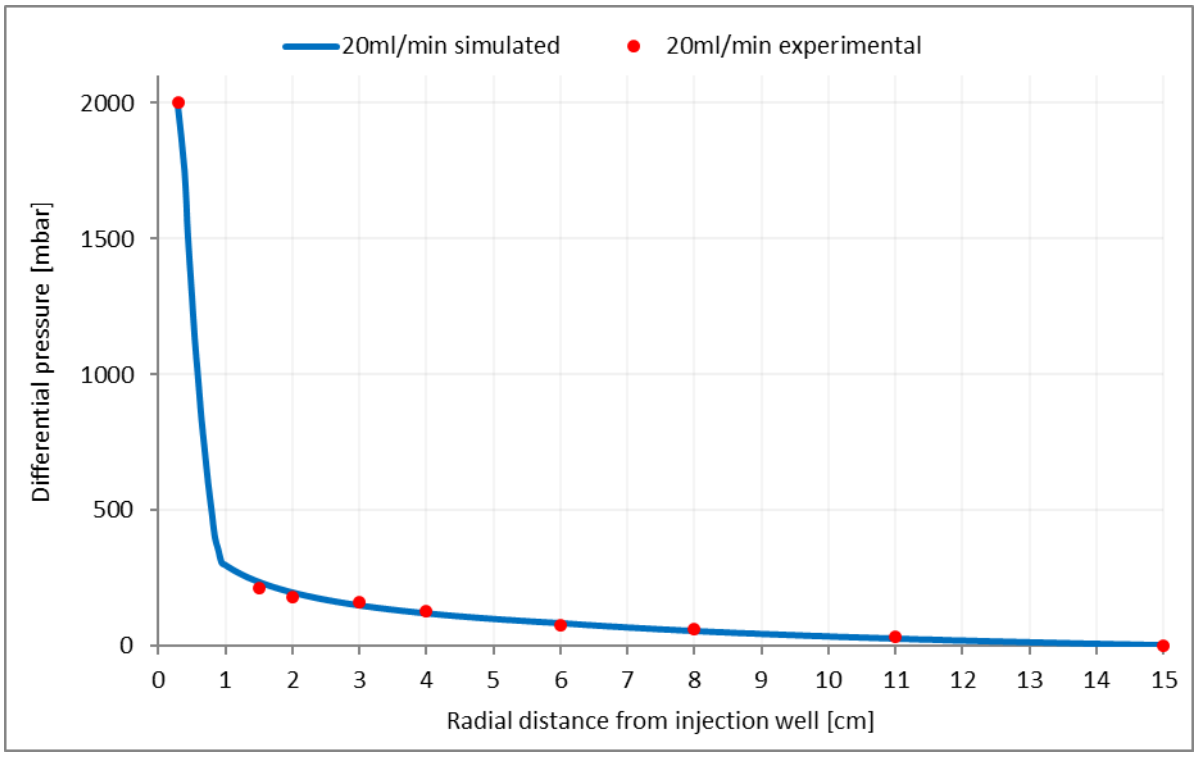

Figure A.41 Differential pressure match for 20ml/min HPAM solution injection rate

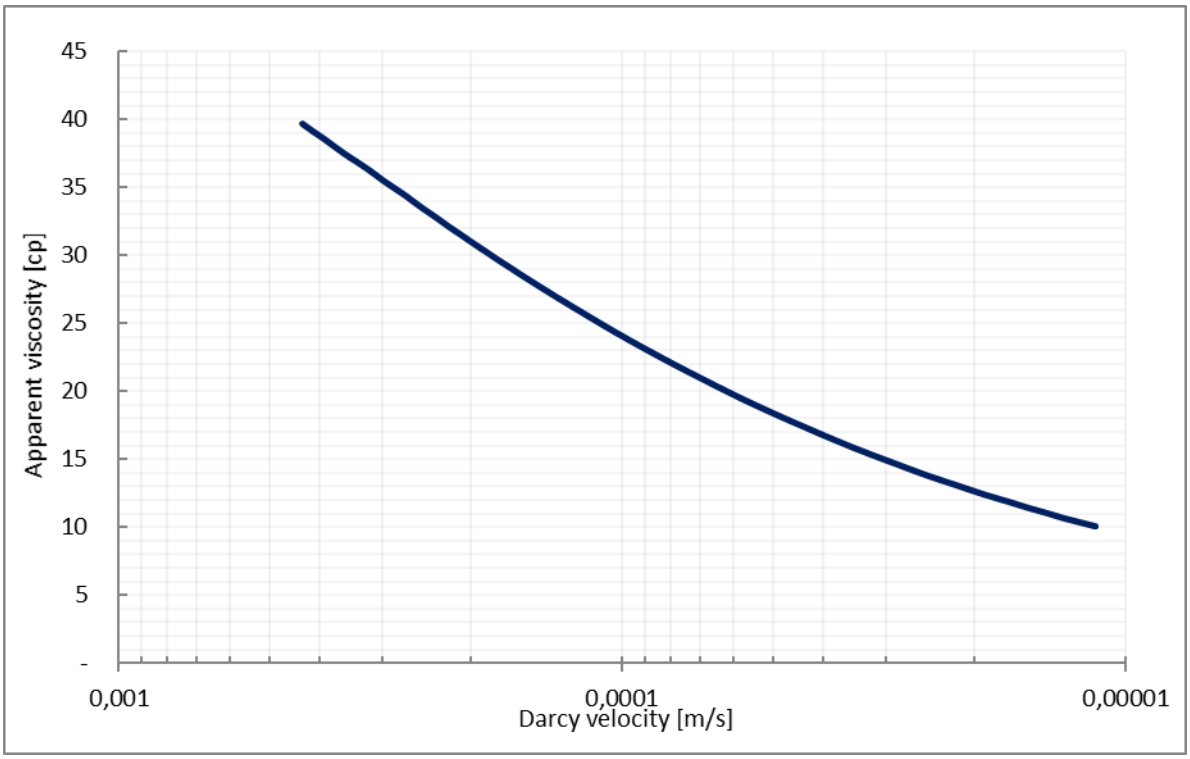

Figure A.42 20ml/min HPAM rheology curve

A.2 Xanthan Differential Pressure Matches and Corresponding Rheology Curves

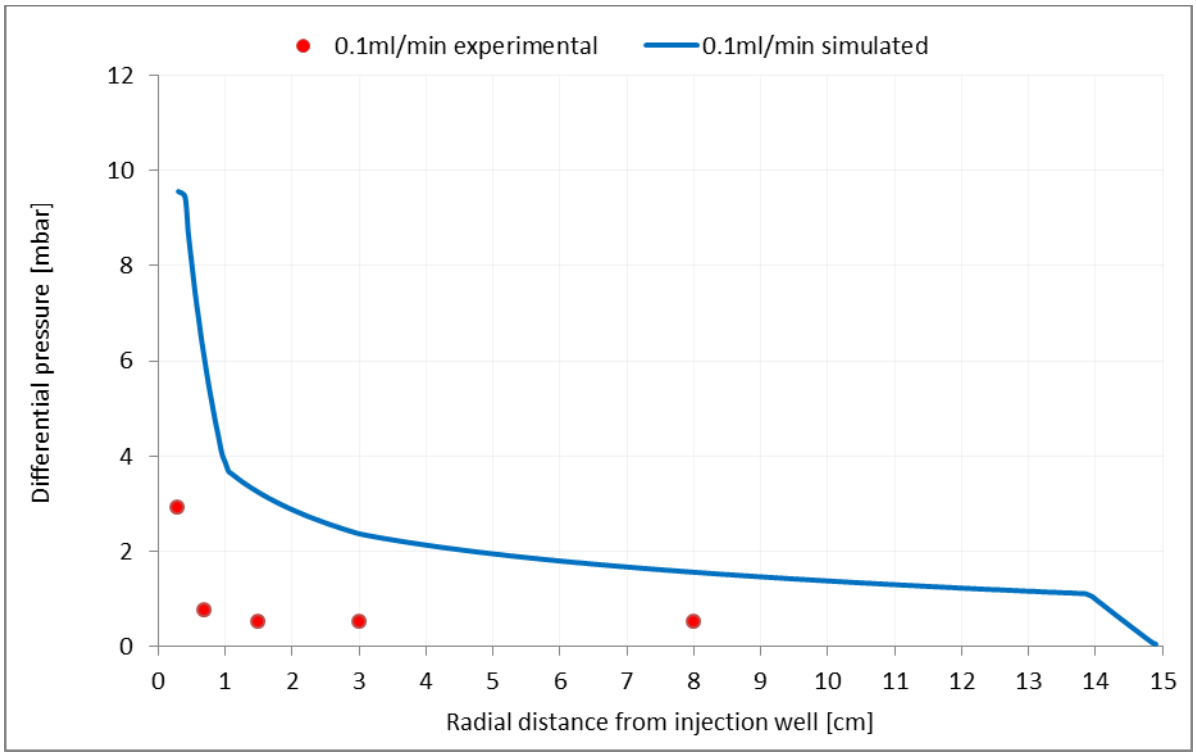

Figure A.43 Differential pressure match for 0.1ml/min xanthan solution injection rate

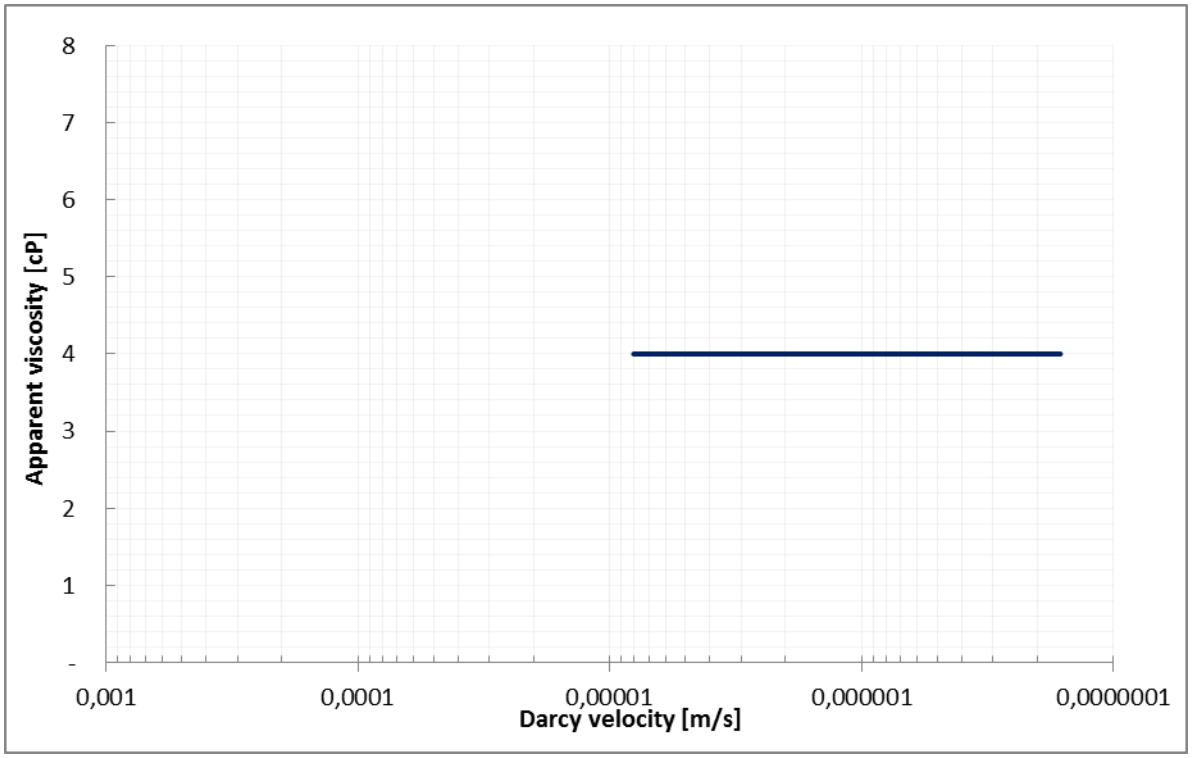

Figure A.44 0.1ml/min xanthan rheology curve

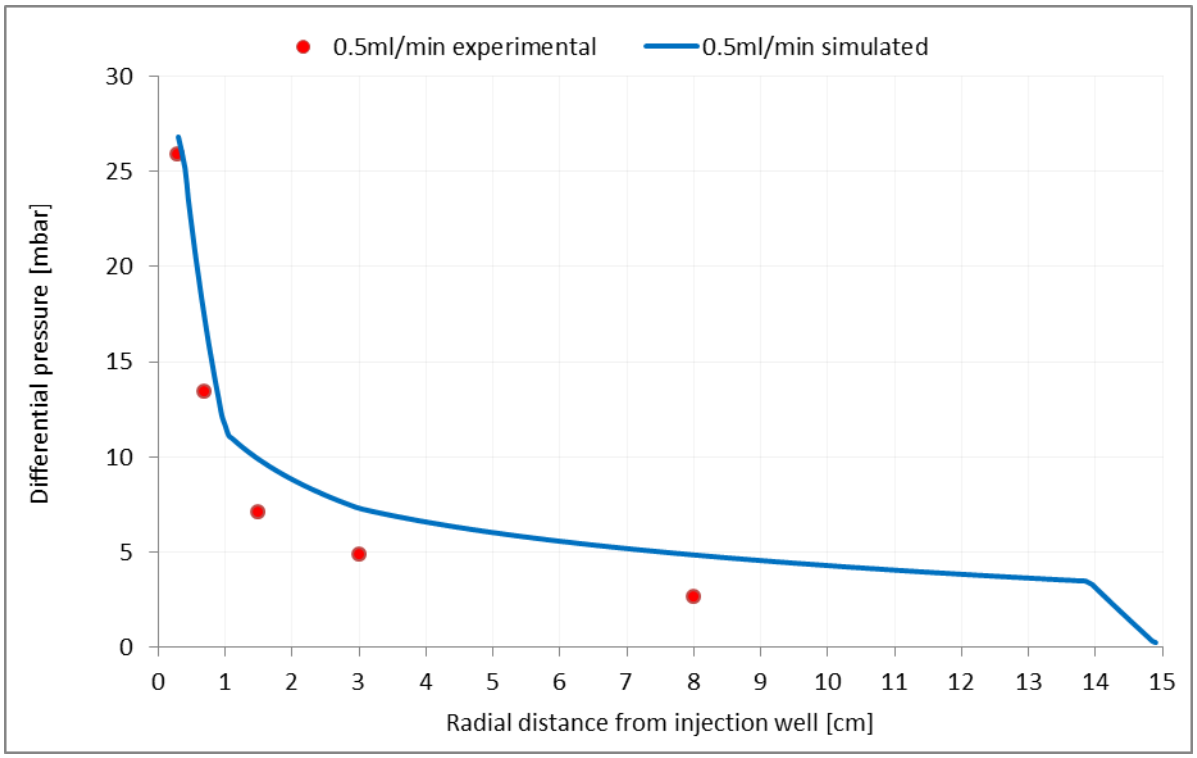

Figure A.45 Differential pressure match for 0.5ml/min xanthan solution injection rate

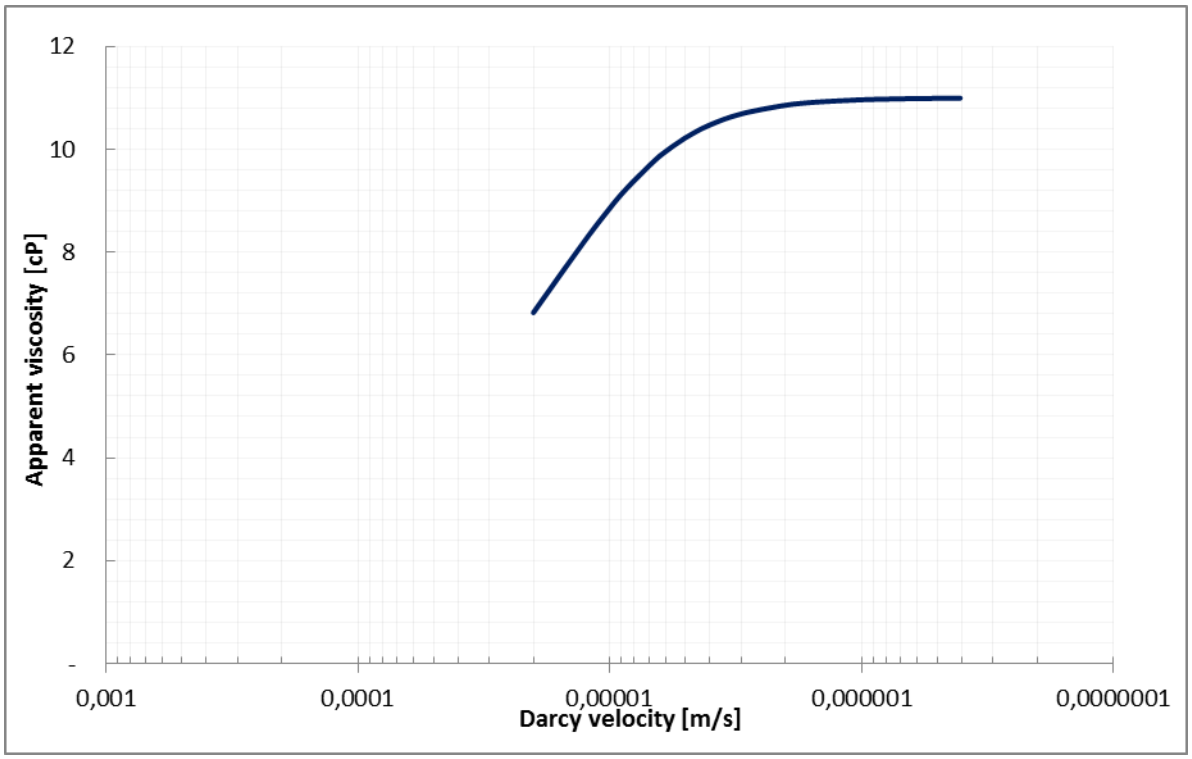

Figure A.46 0.5ml/min xanthan rheology curve

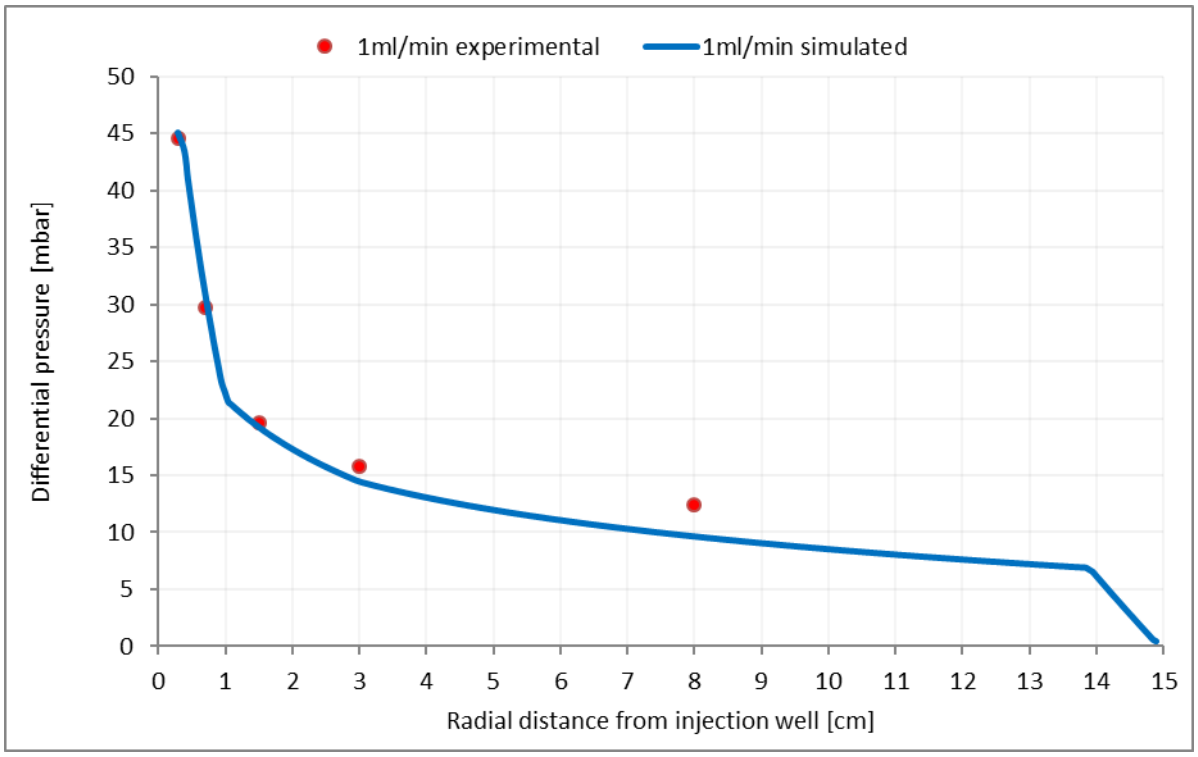

Figure A.47 Differential pressure match for 1ml/min xanthan solution injection rate

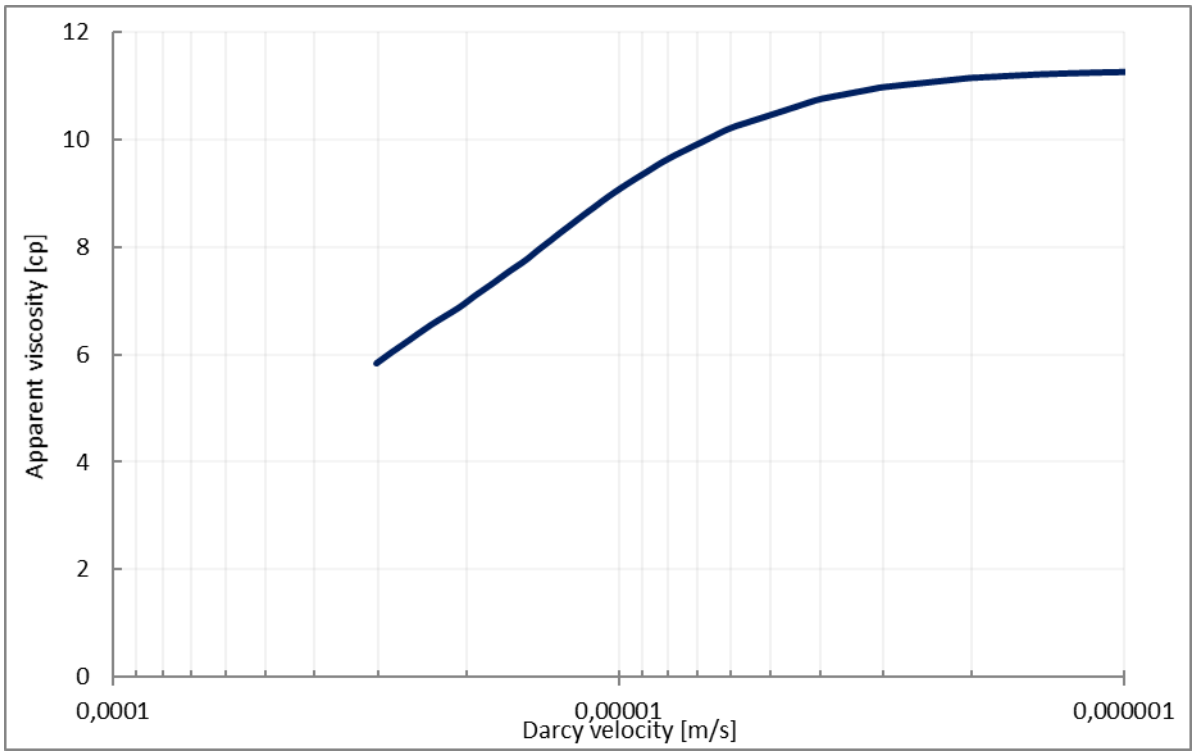

Figure A.48 1ml/min xanthan rheology curve

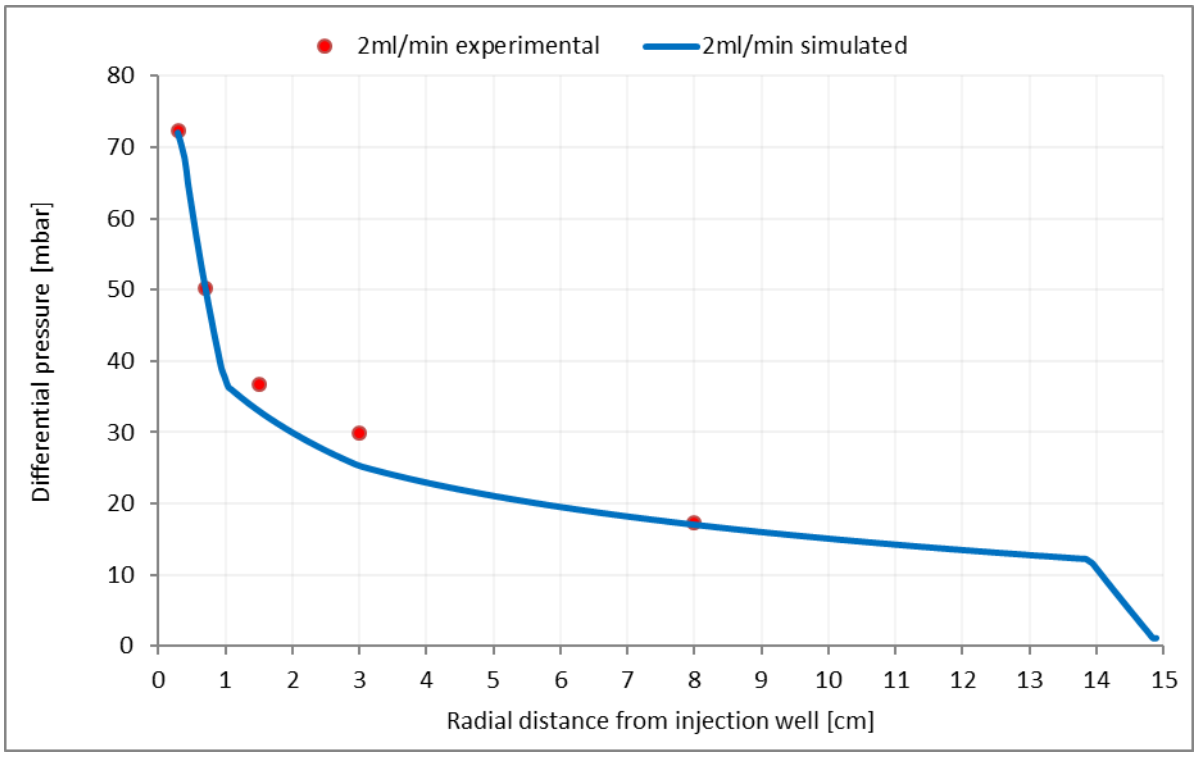

Figure A.49 Differential pressure match for 2ml/min xanthan solution injection rate

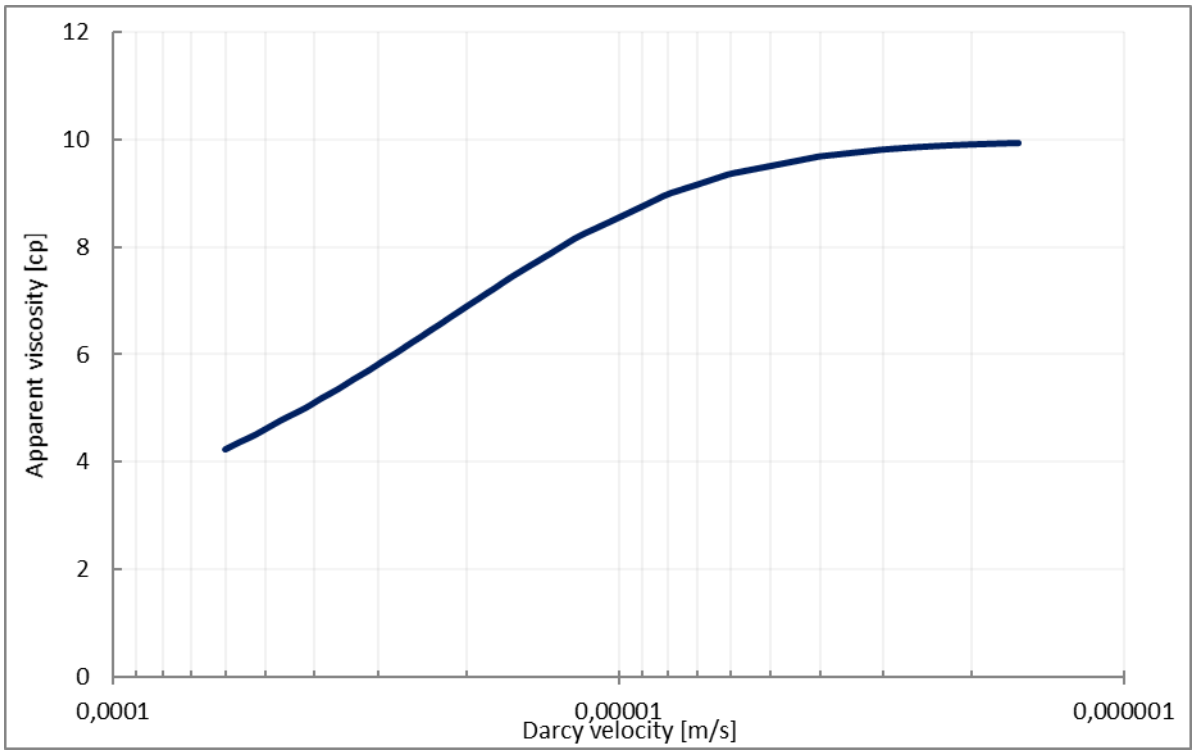

Figure A.50 2ml/min xanthan rheology curve

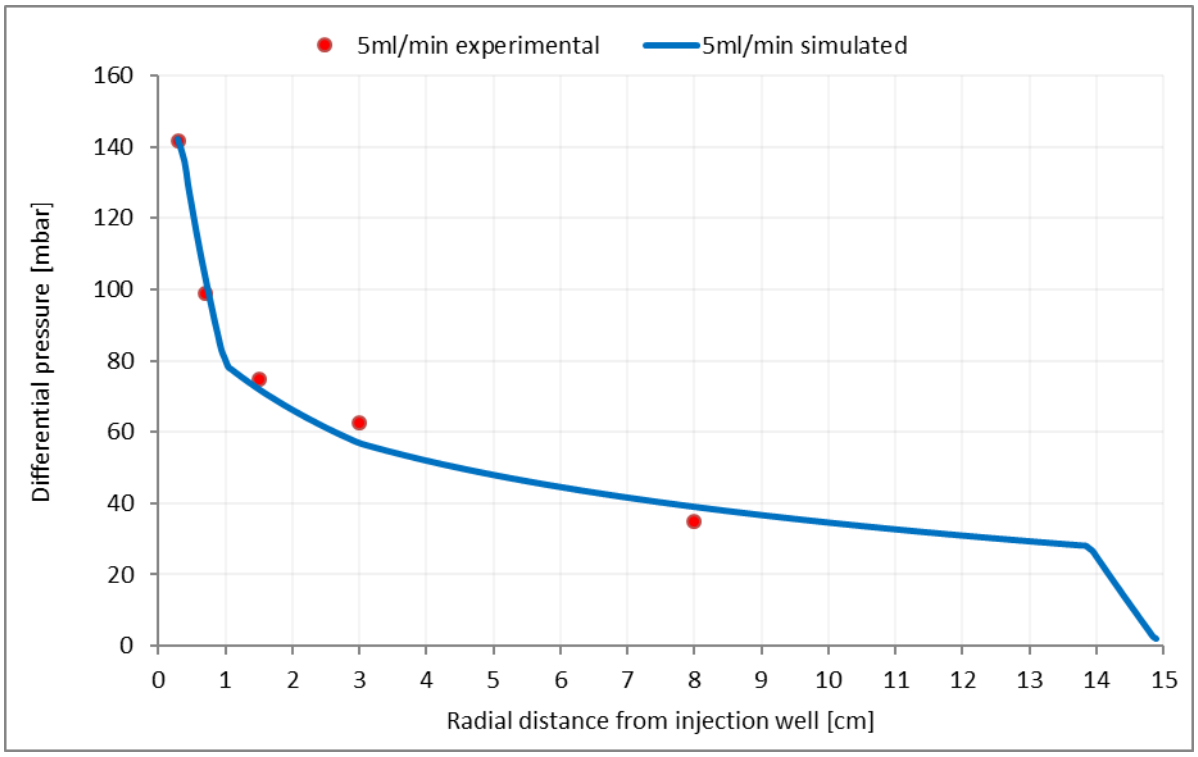

Figure A.51Differential pressure match for 5ml/min xanthan solution injection rate

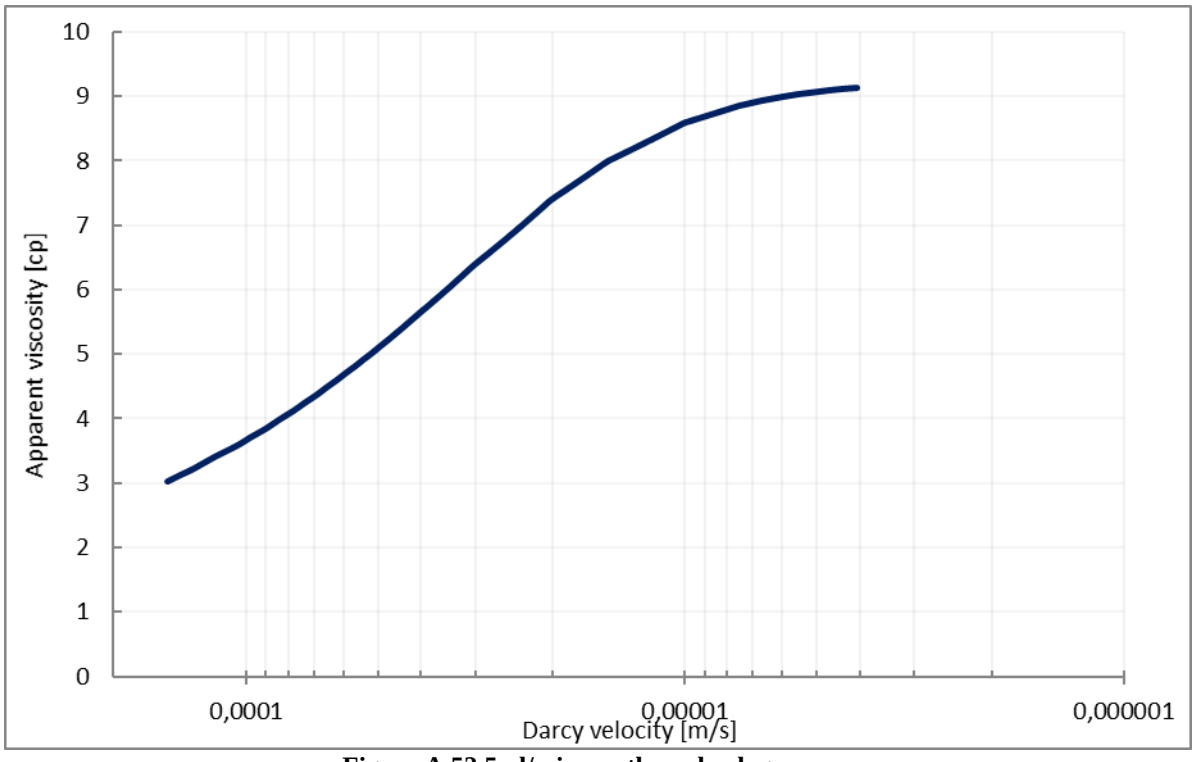

Figure A.52 5ml/min xanthan rheology curve

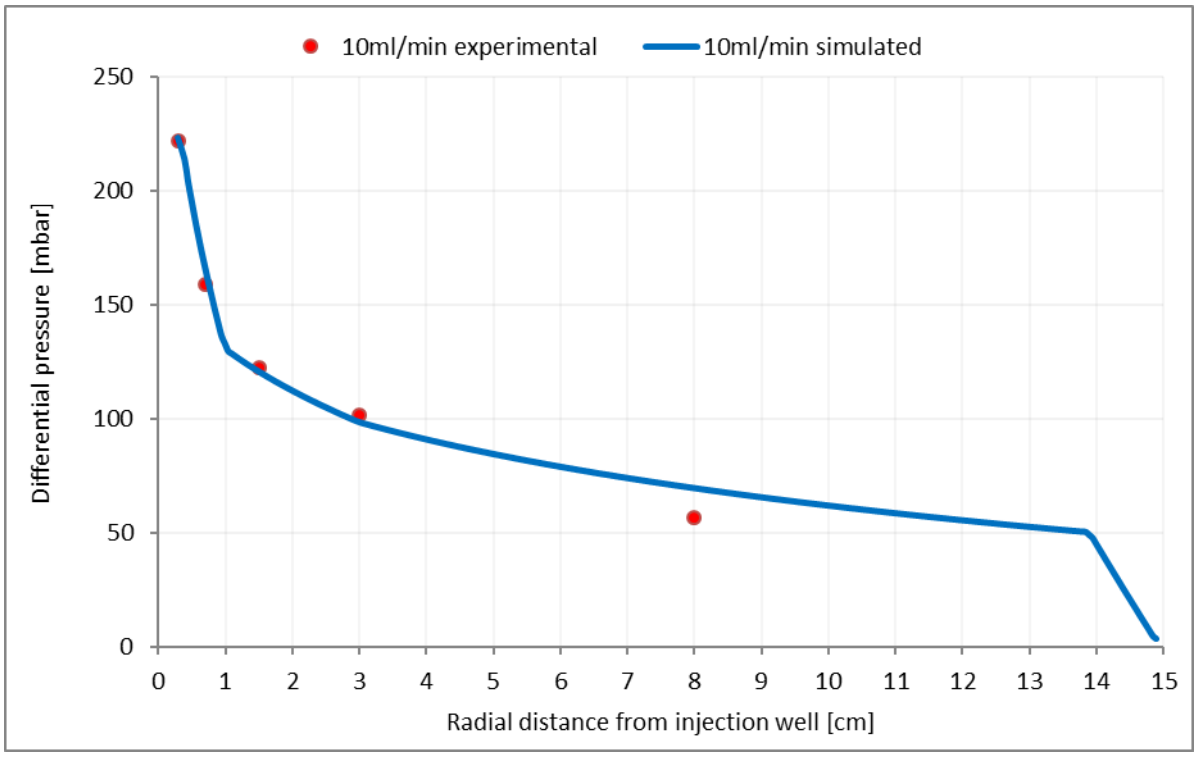

Figure A.53 Differential pressure match for 10ml/min xanthan solution injection rate

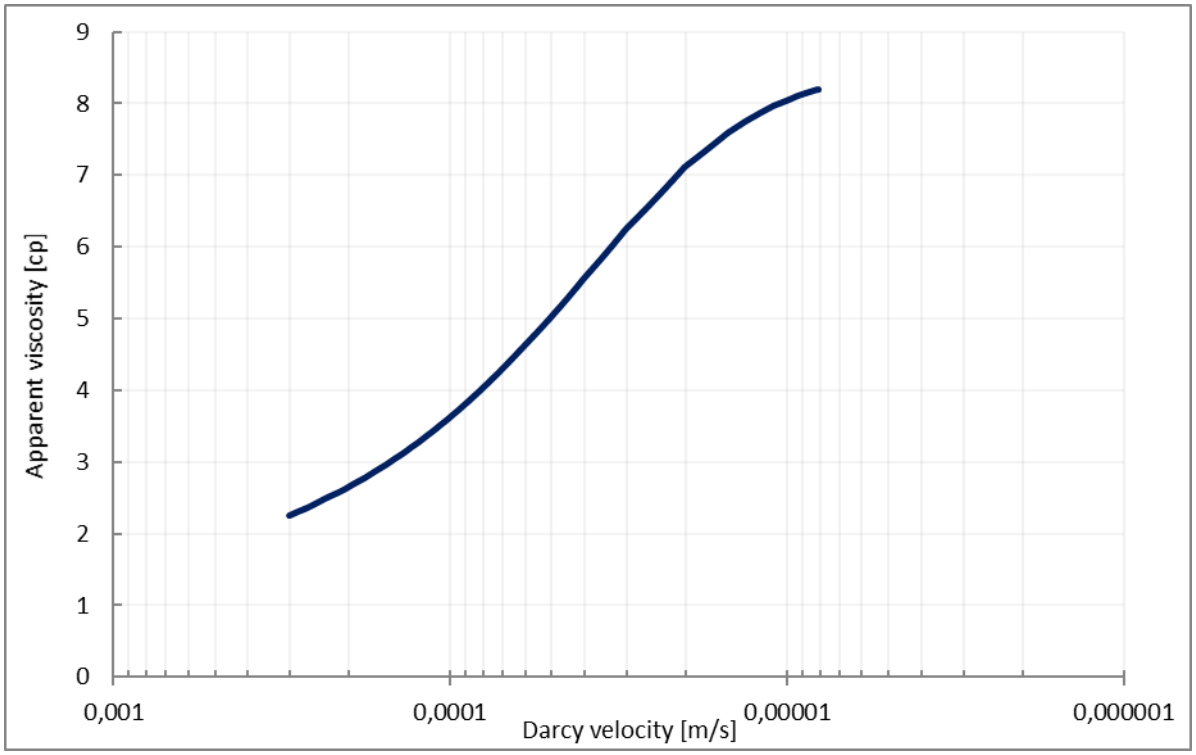

Figure A.54 10ml/min xanthan rheology curve

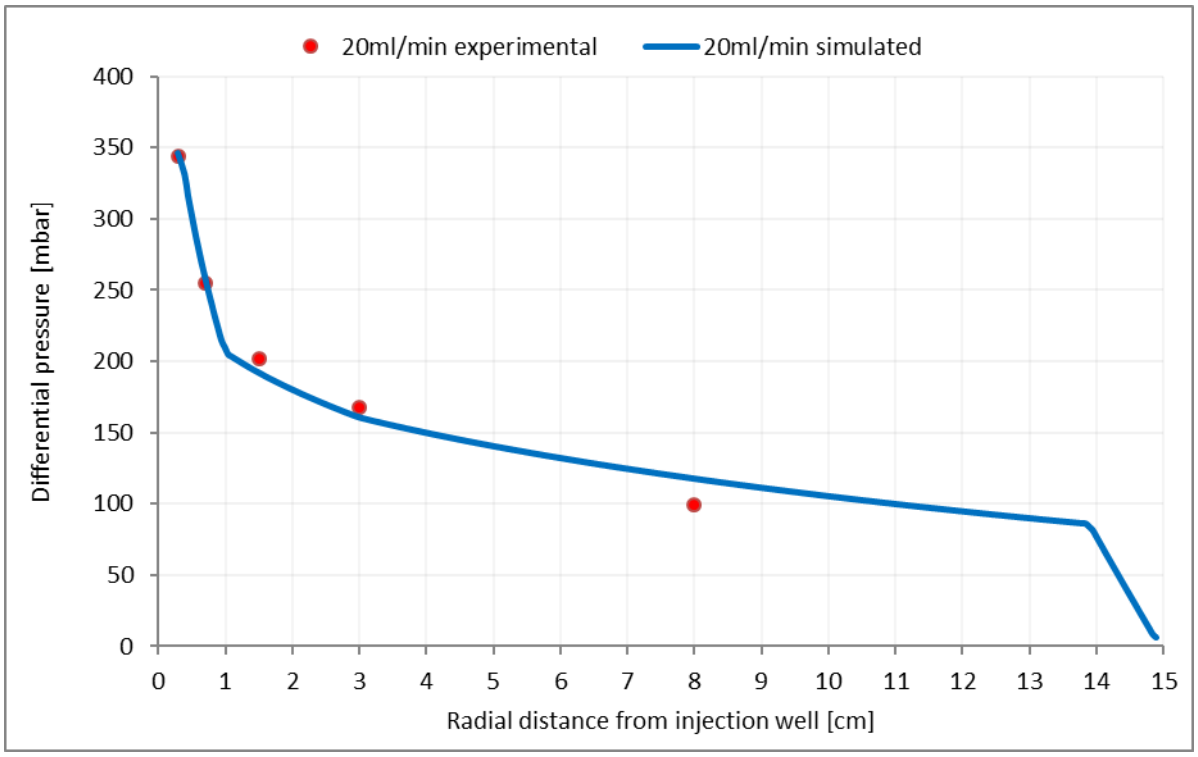

Figure A.55 Differential pressure match for 20ml/min xanthan solution injection rate

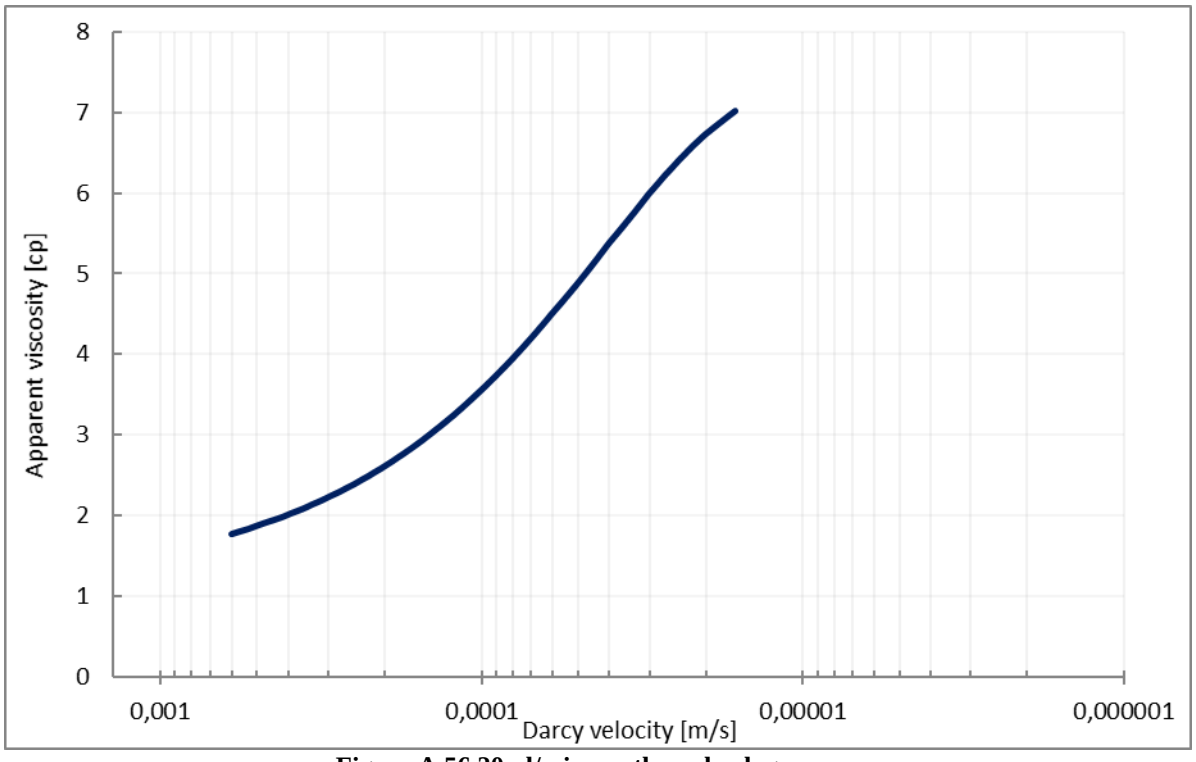

Figure A.56 20ml/min xanthan rheology curve

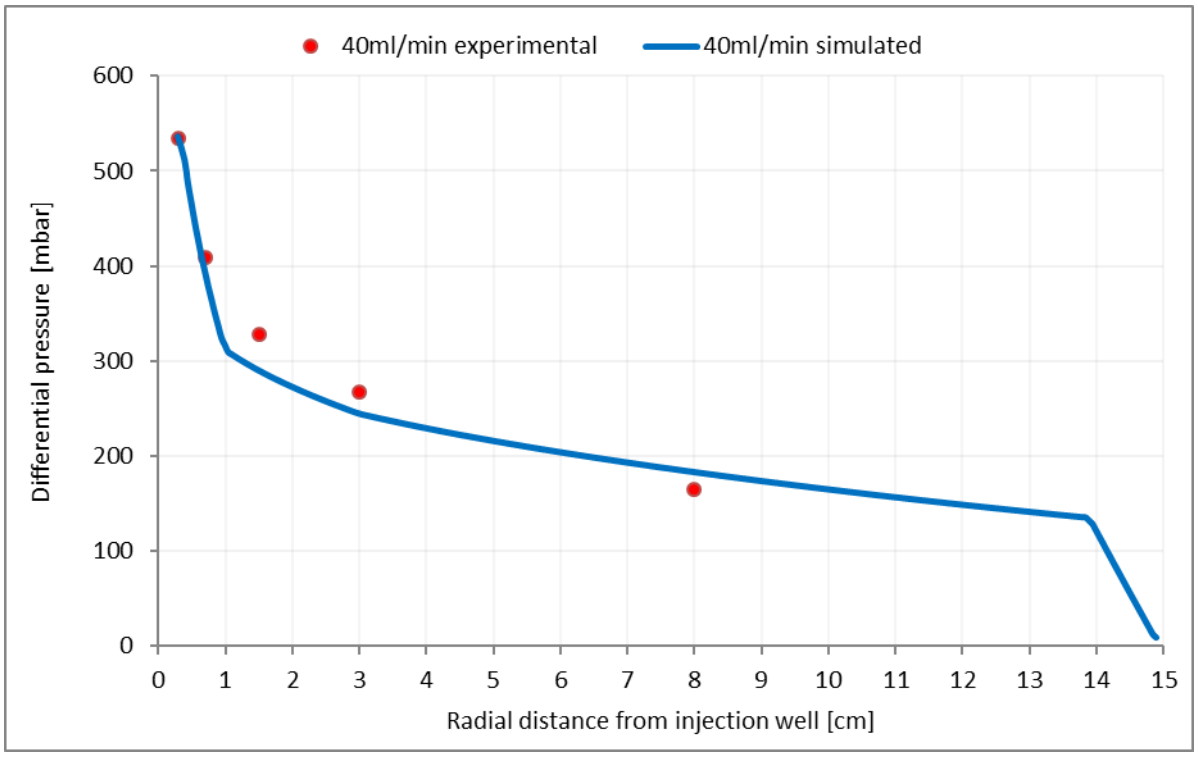

Figure A.57 Differential pressure match for 40ml/min xanthan solution injection rate

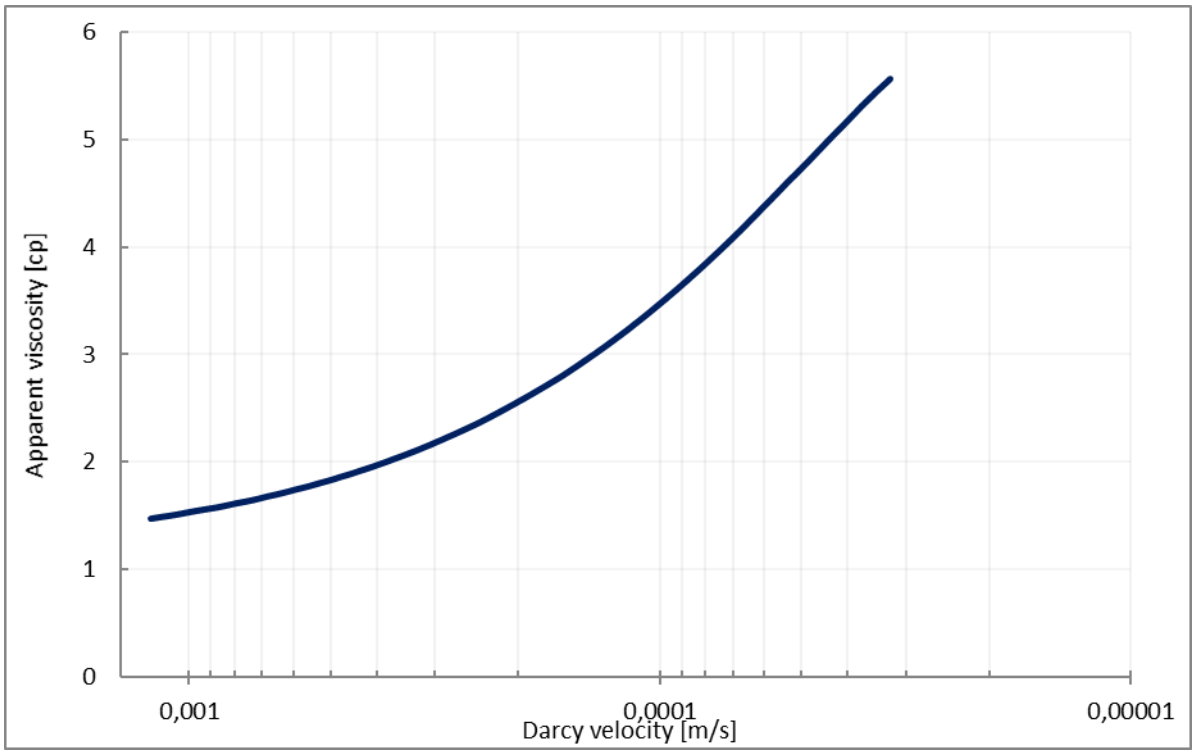

Figure A.58 40ml/min xanthan rheology curve

A.3 HPAM Differential Pressure Matches and Corresponding Rheology Curves for Constant Permeability Simulations

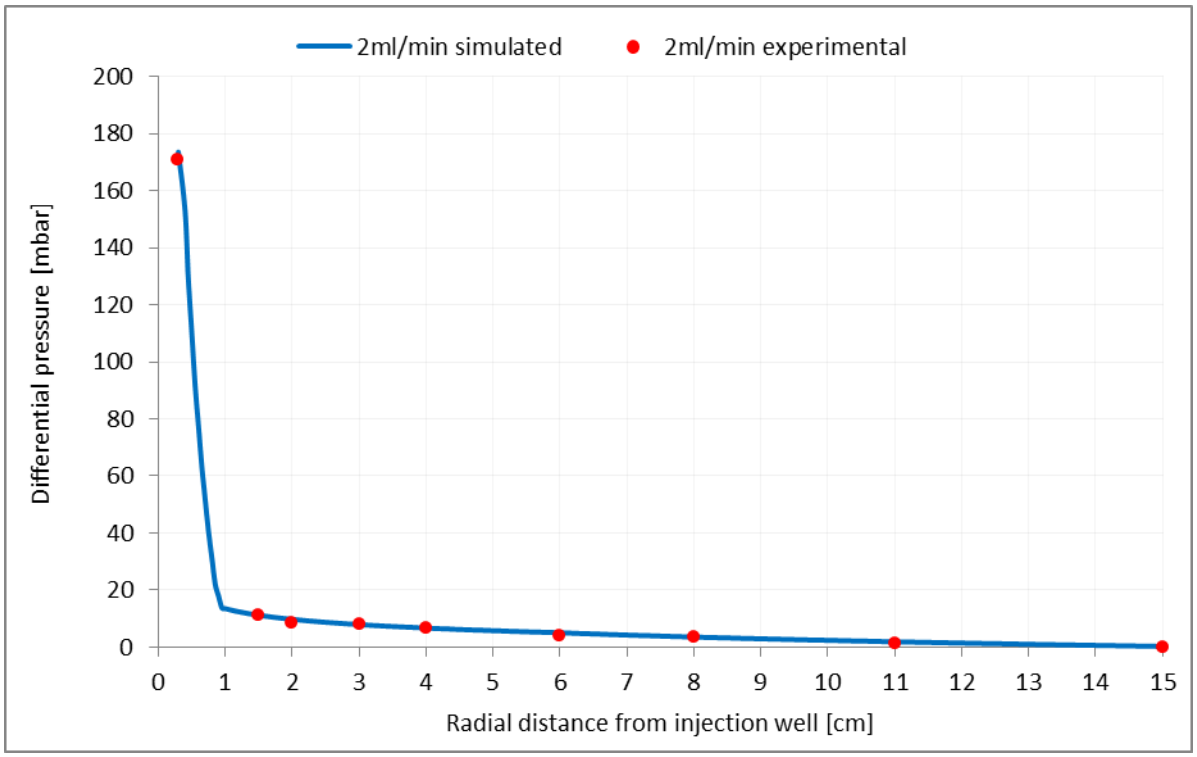

Figure A.59 Differential pressure match for 2ml/min HPAM solution injection rate from constant permeability simulations

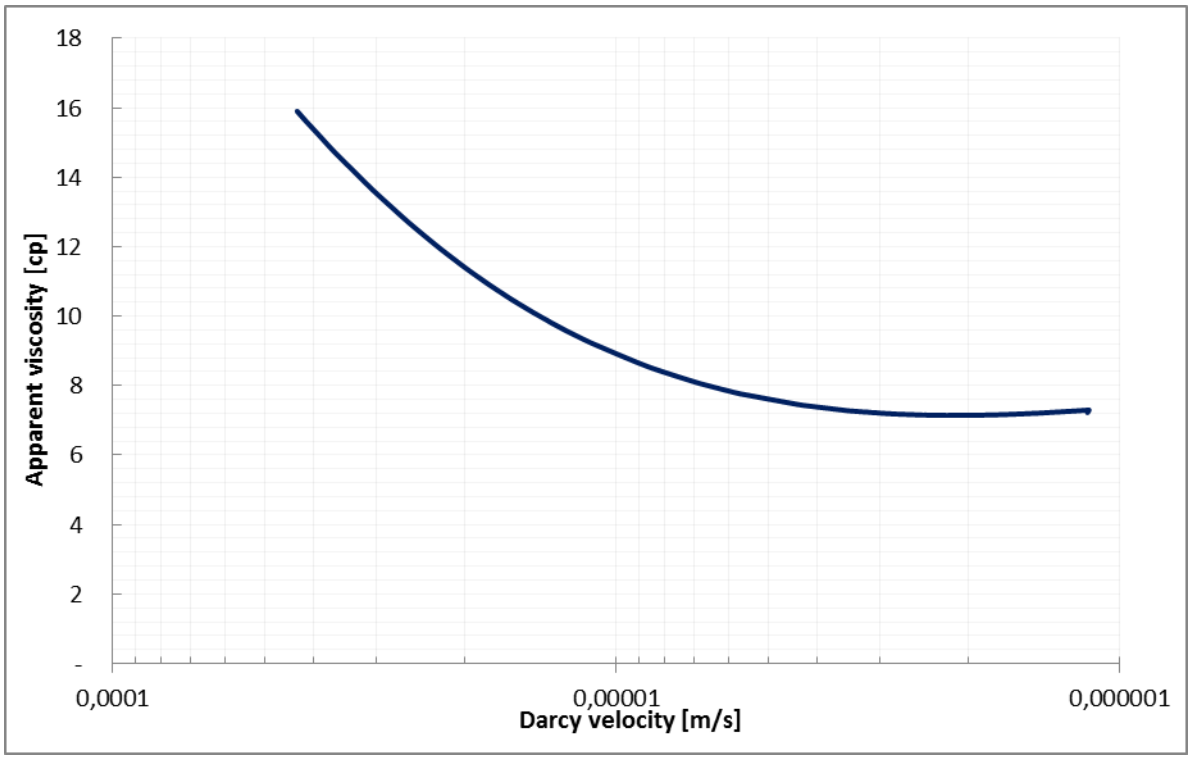

Figure A.60 2ml/min HPAM rheology curve from constant permeability simulations

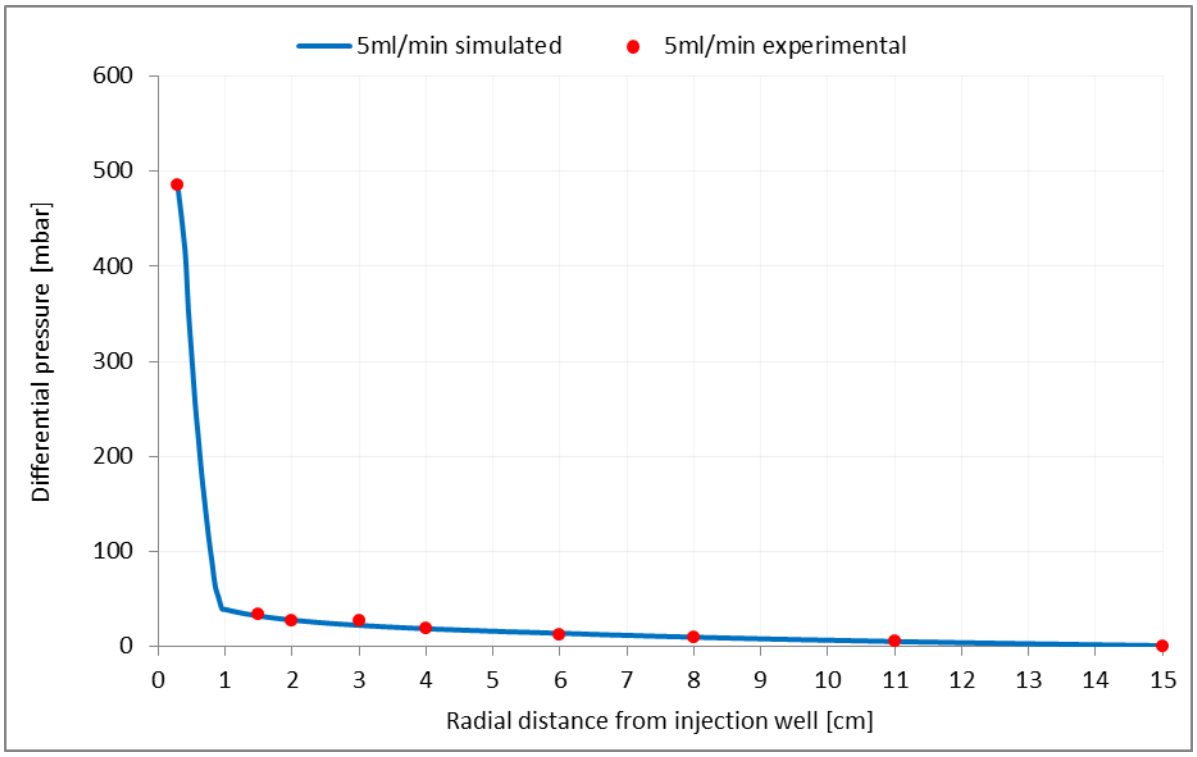

Figure A.61 Differential pressure match for 5ml/min HPAM solution injection rate from constant permeability simulations

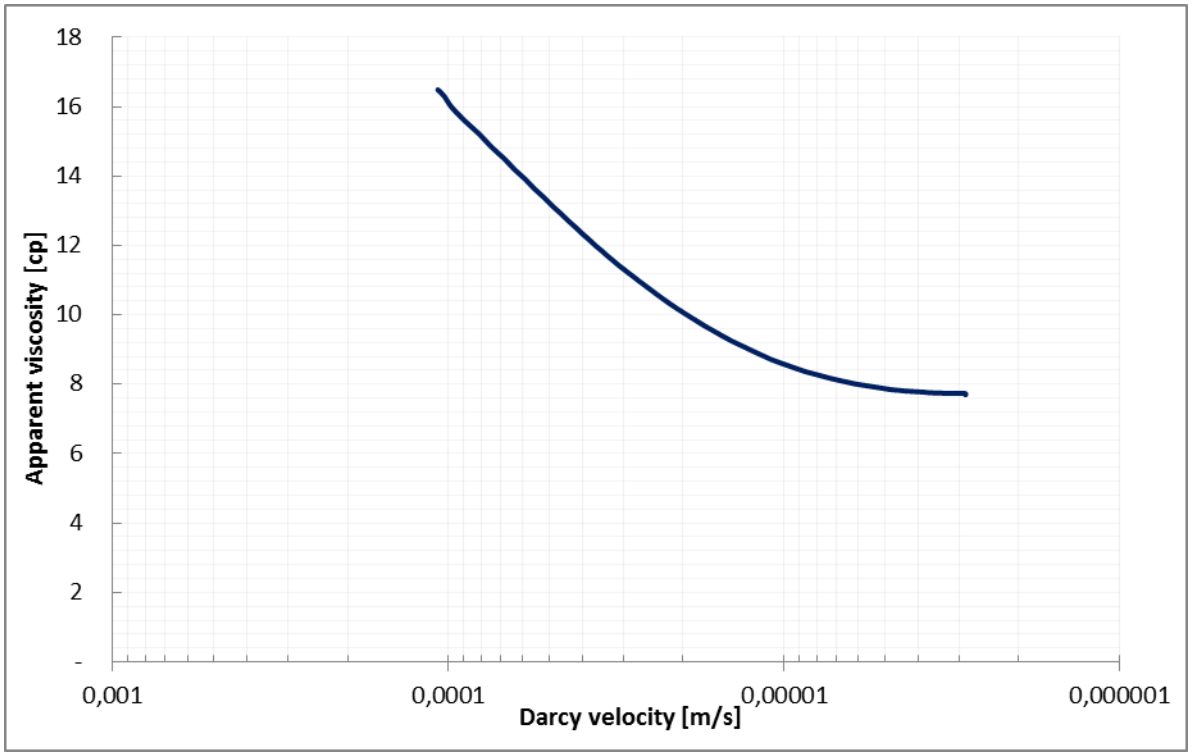

Figure A.62 5ml/min HPAM rheology curve from constant permeability simulations

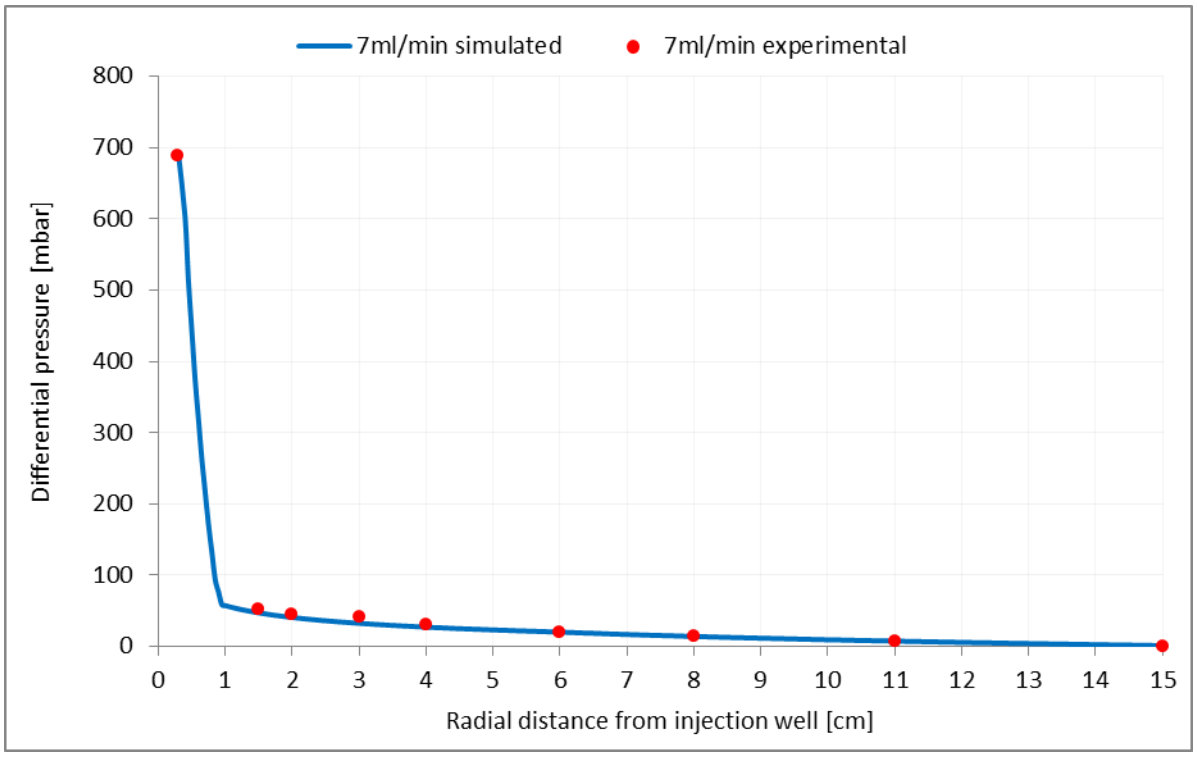

Figure A.63 Differential pressure match for 7ml/min HPAM solution injection rate from constant permeability simulations

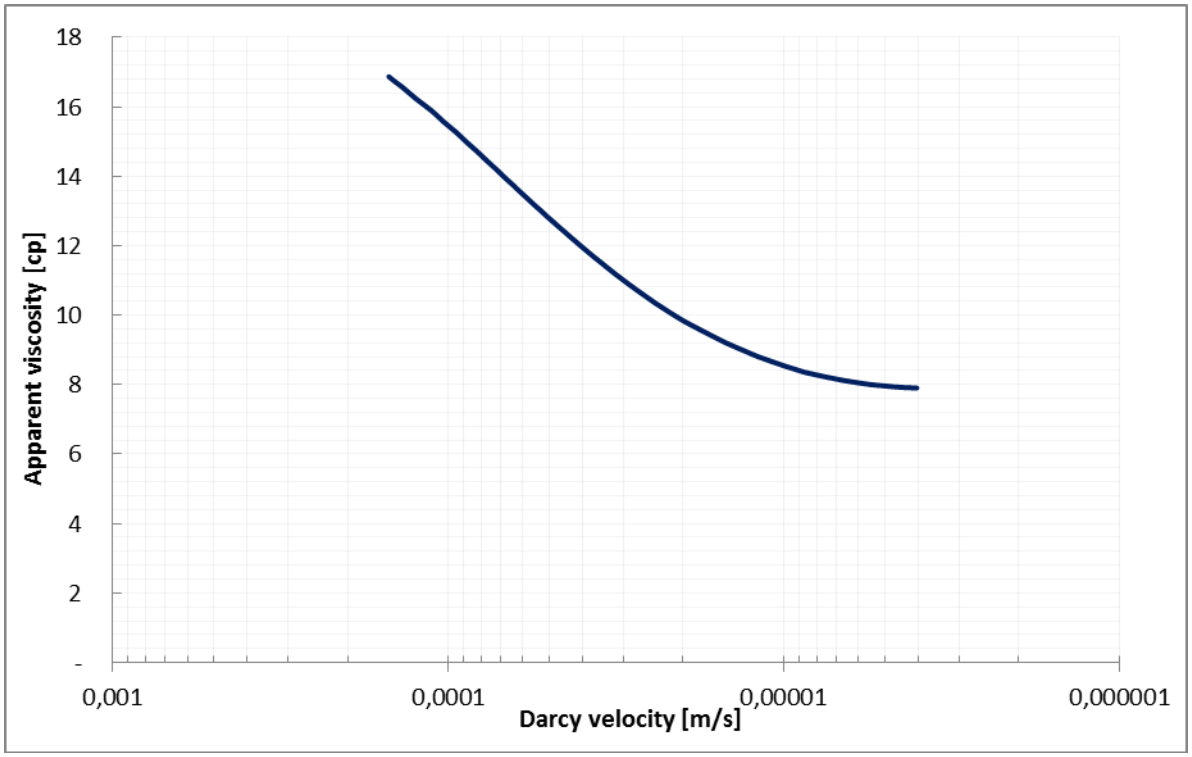

Figure A.64 7ml/min HPAM rheology curve from constant permeability simulations

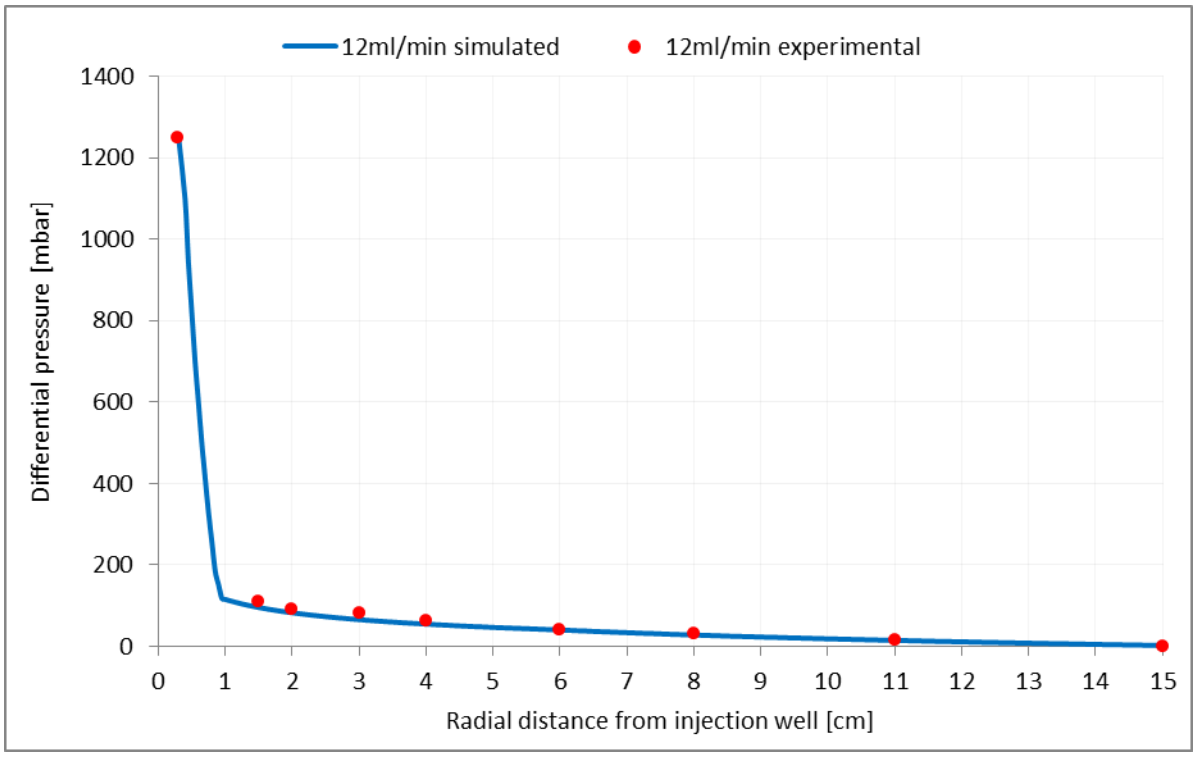

Figure A.65 Differential pressure match for 12ml/min HPAM solution injection rate from constant permeability simulations

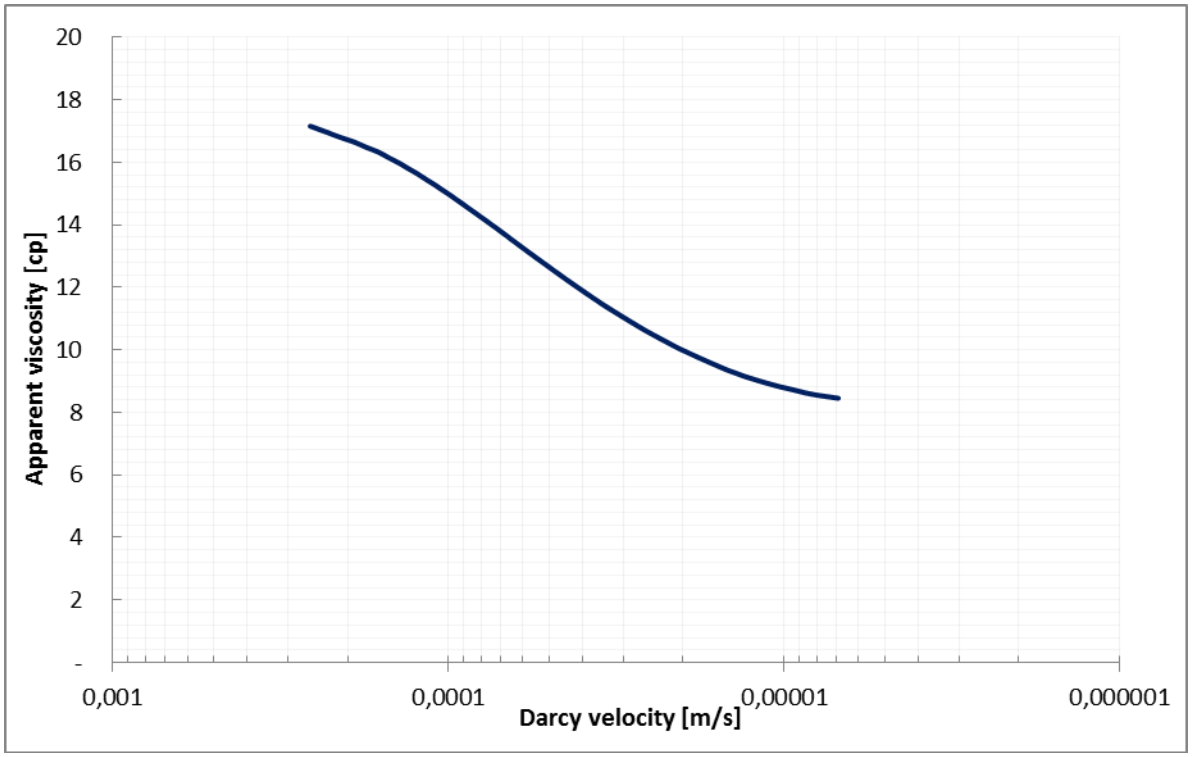

Figure A.66 12ml/min HPAM rheology curve from constant permeability simulations

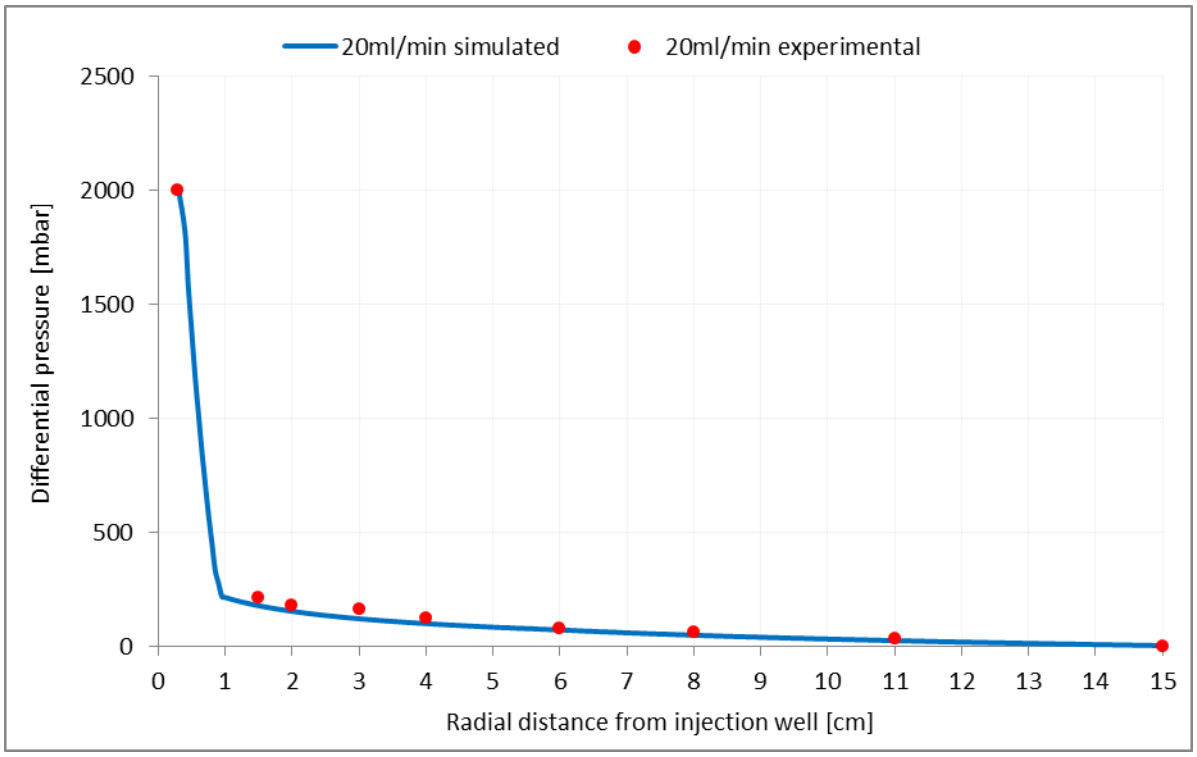

Figure A.67 Differential pressure match for 20ml/min HPAM solution injection rate from constant permeability simulations

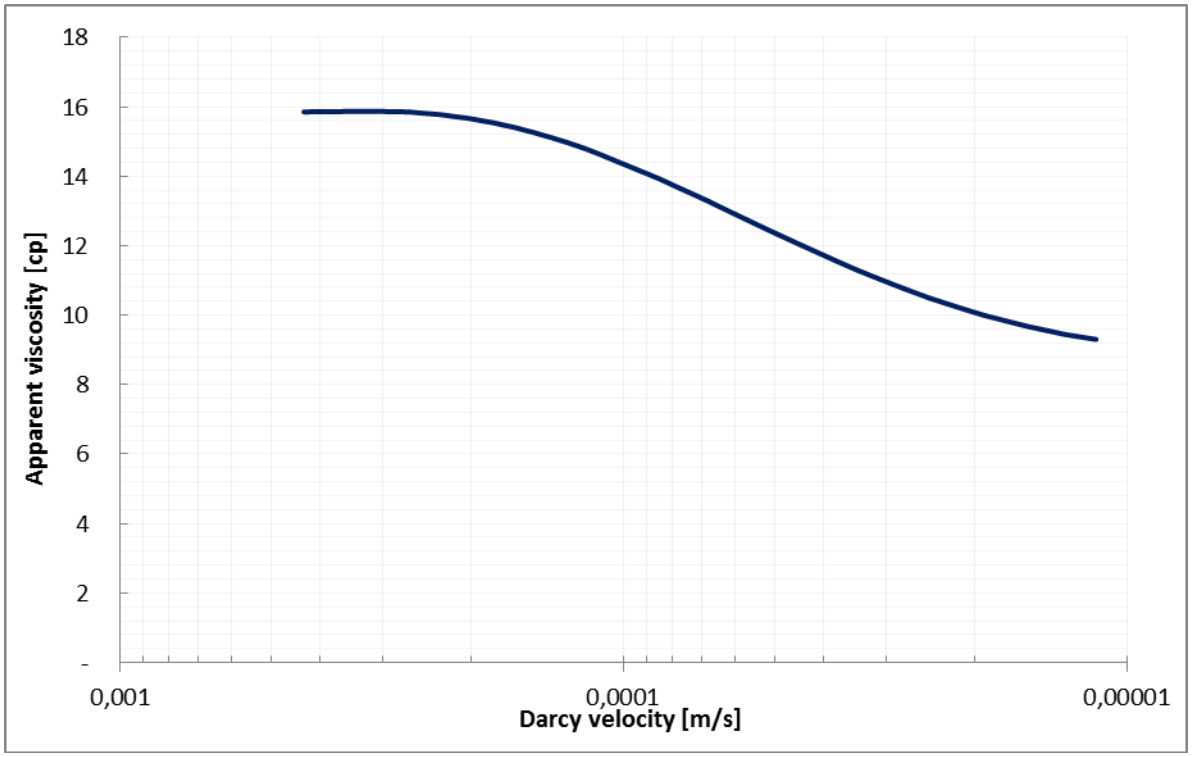

Figure A.68 20ml/min HPAM rheology curve from constant permeability simulations

A.4 H-1 Waterflooding Differential Pressure Matches

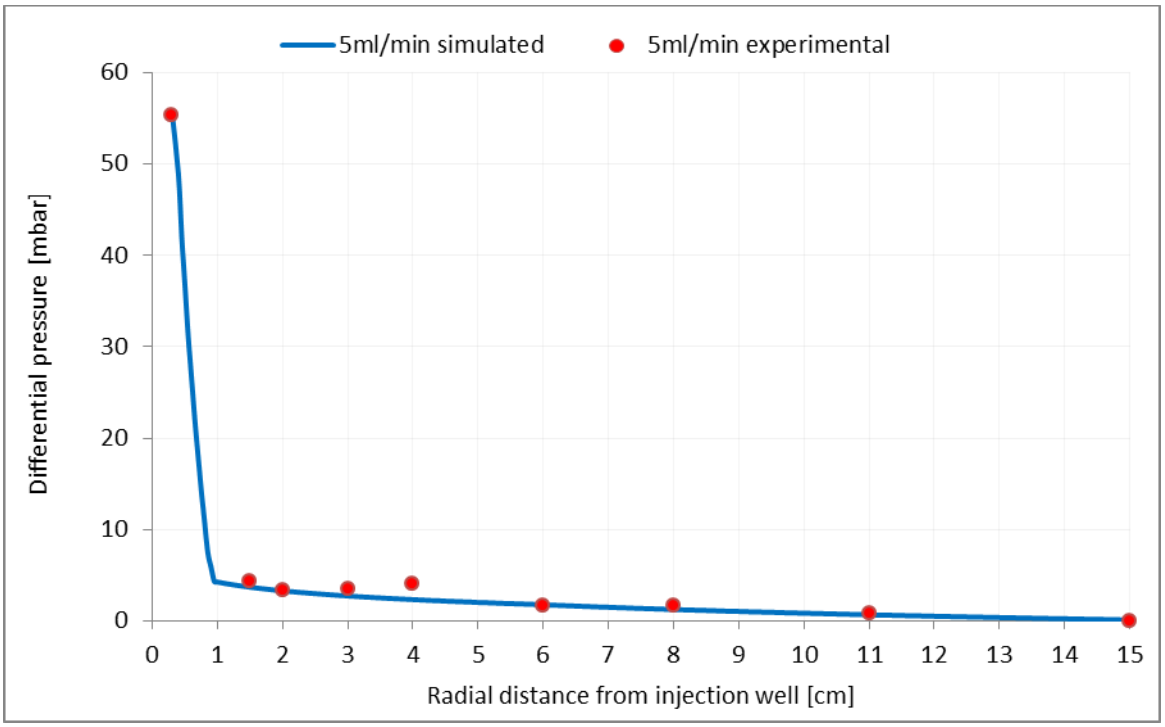

Figure A.69 H-1 5ml/min waterflooding differential pressure match

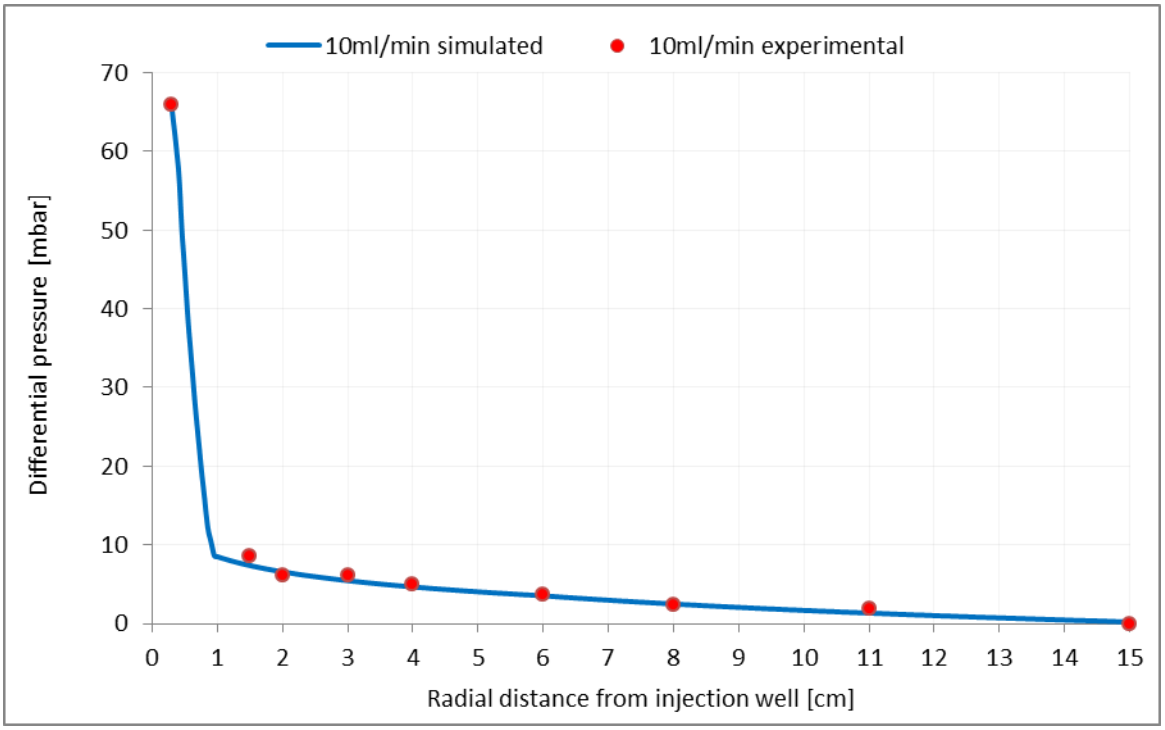

Figure A.70 H-1 10ml/min waterflooding differential pressure match

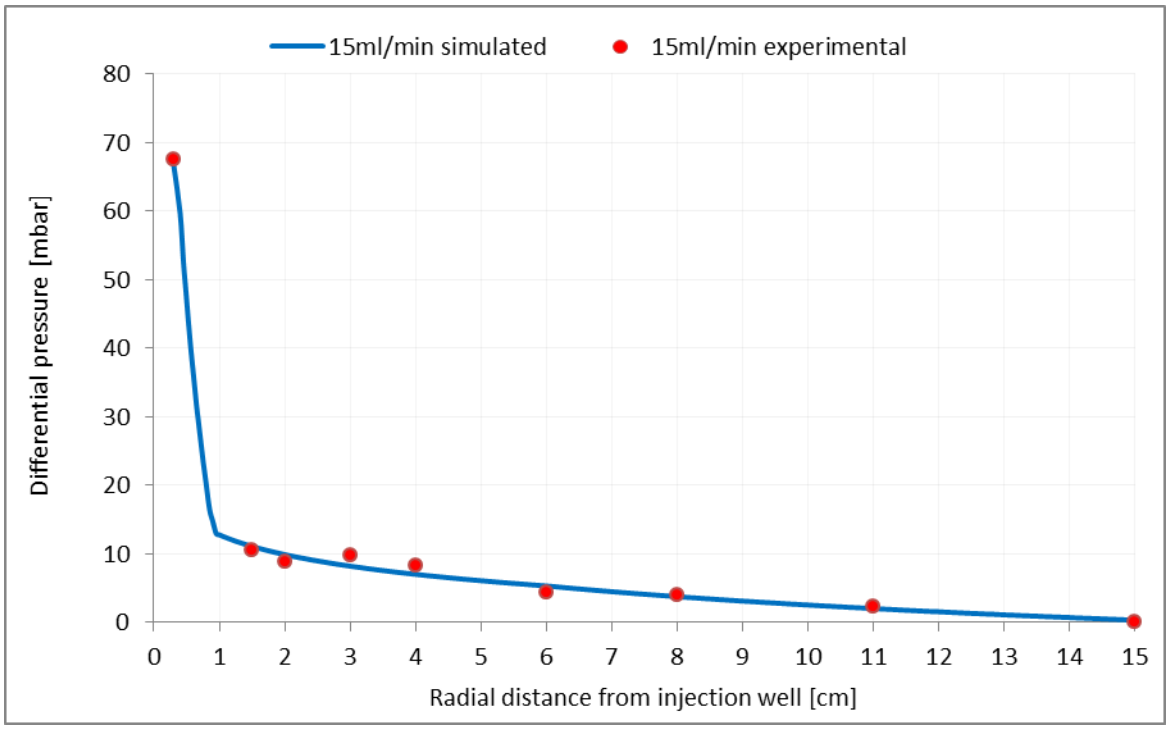

Figure A.71 H-1 15ml/min waterflooding differential pressure match

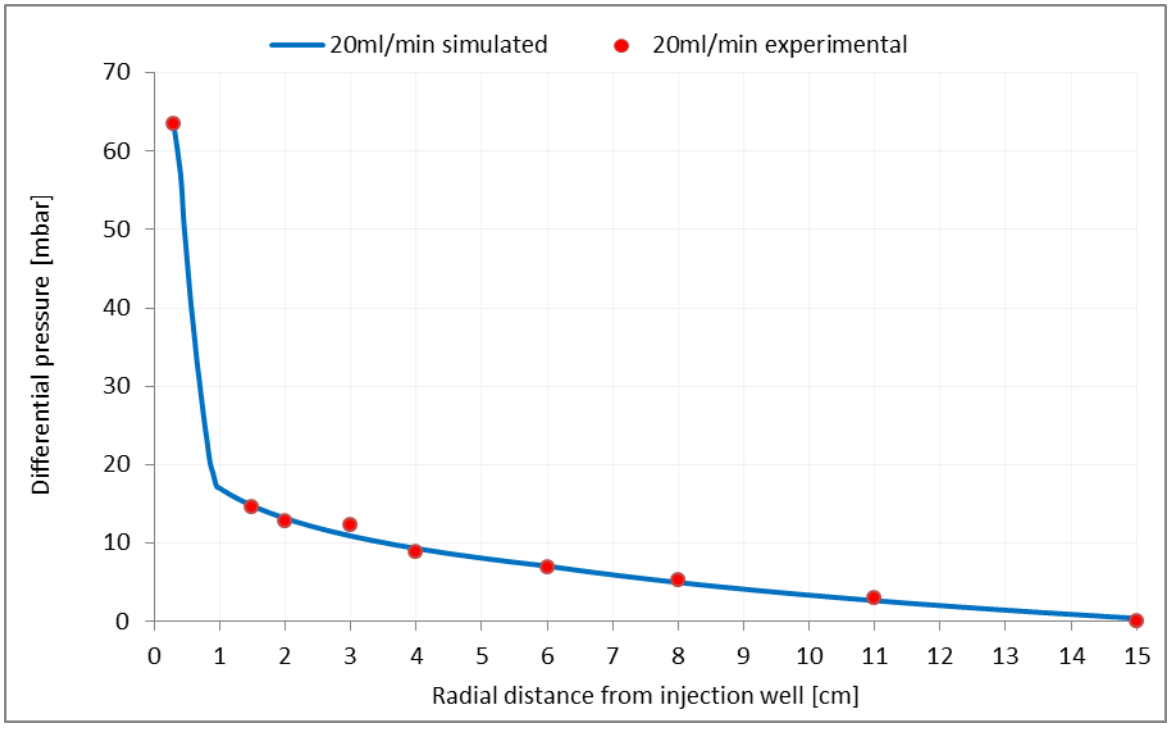

Figure A.72 H-1 20ml/min waterflooding differential pressure match

A.5 X-1 Waterflooding Differential Pressure Matches

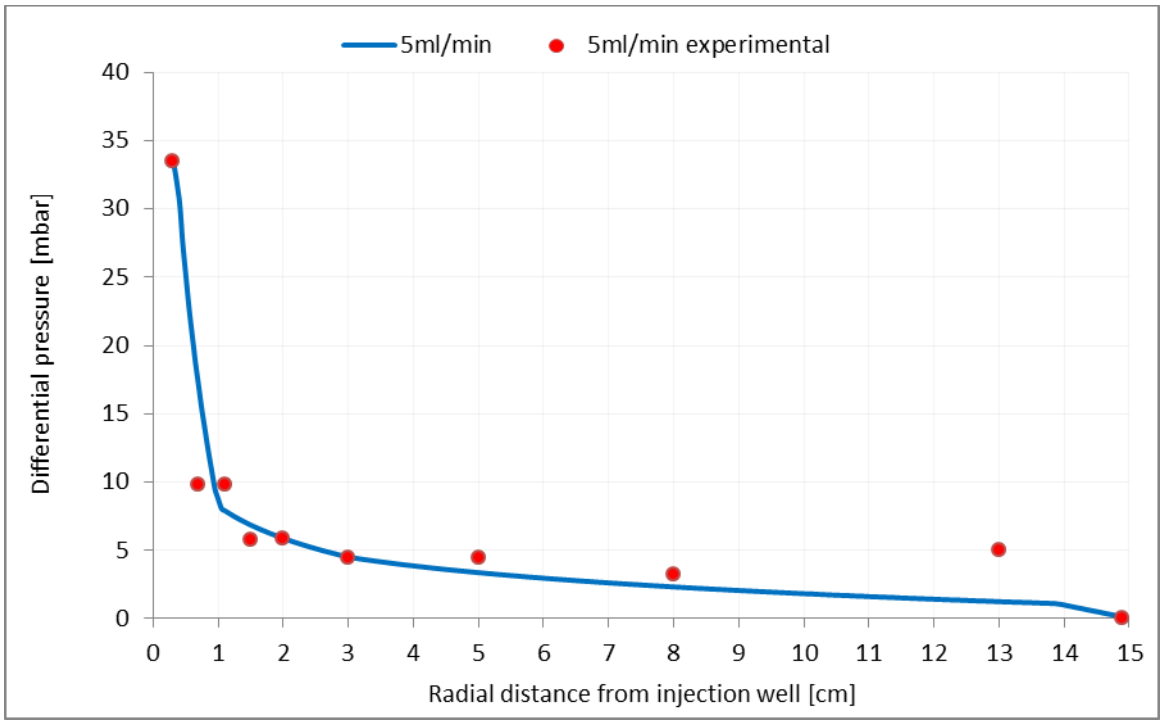

Figure A.73 X-1 5ml/min waterflooding differential pressure match

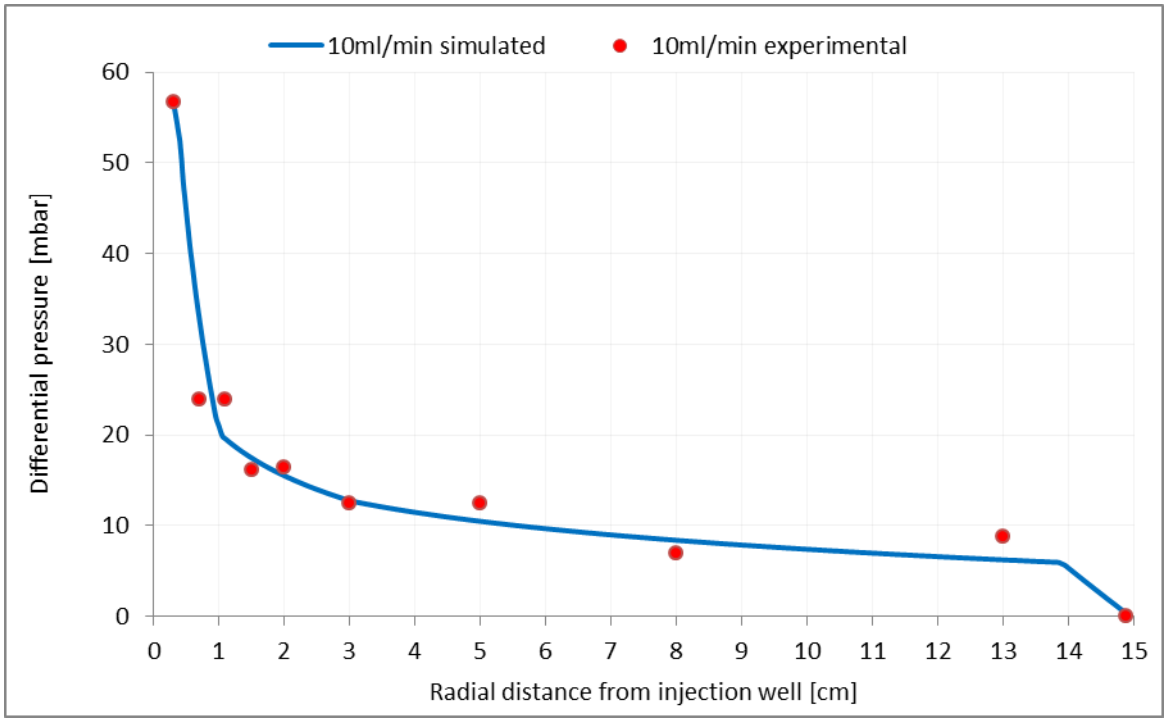

Figure A.74 X-1 10ml/min waterflooding differential pressure match

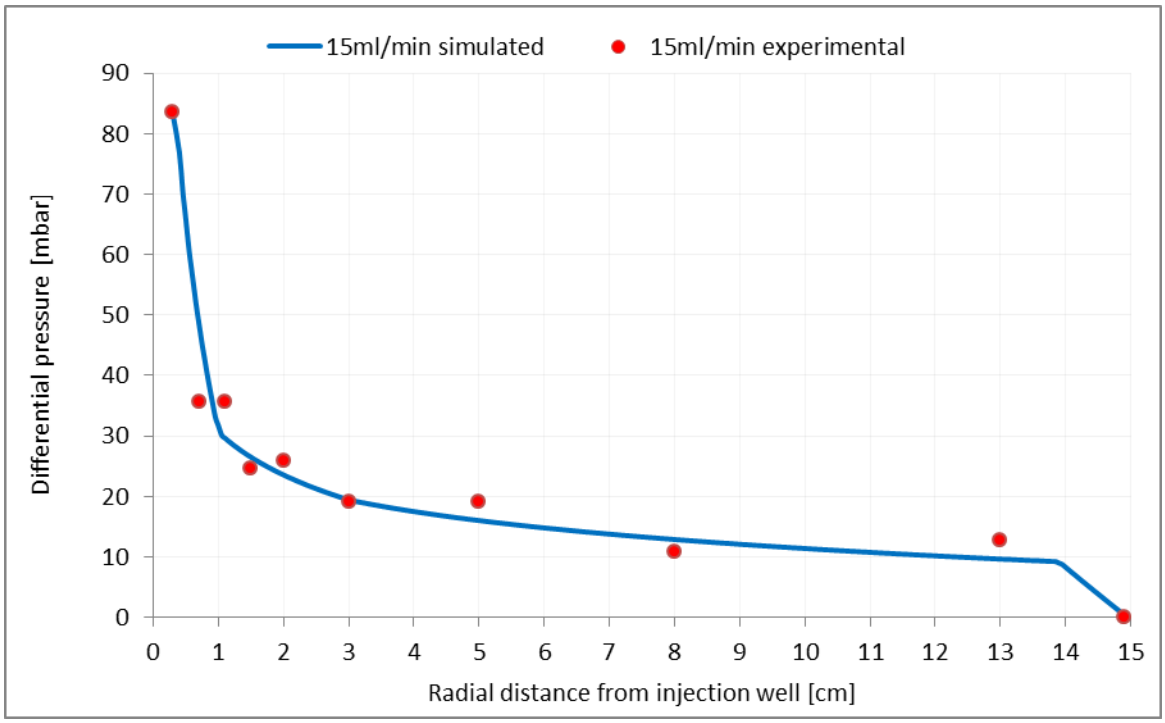

Figure A.75 X-1 15ml/min waterflooding differential pressure match

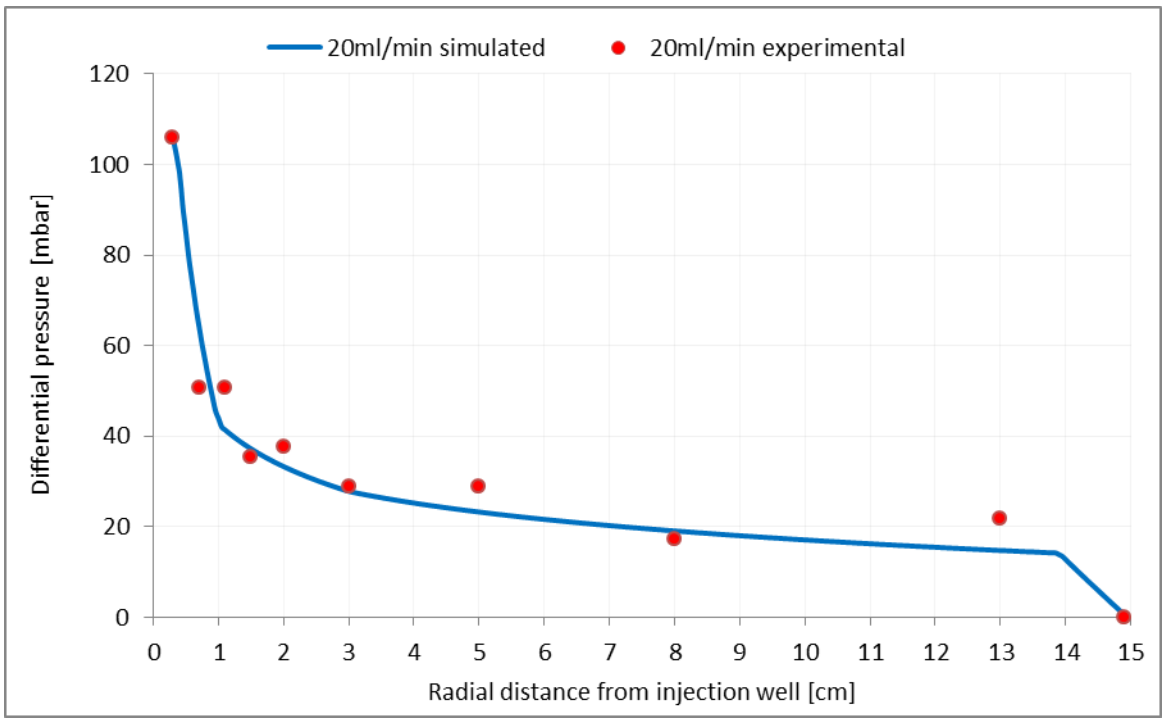

Figure A.76 X-1 20ml/min waterflooding differential pressure match

B. Calculations and Derivations

B.1 Derviation of Darcy's law in radial geometry

As indicated in figure 2.1, flow is radially away from a cylinder shaped well of radius r_w driven by a well pressure P_w towards an outer rim located at r_e with pressure p_e. At a distance r, in which $r_w<r<r_e$, there is a horizontal flow Q towards the outer rim through the cross-sectional area $A = 2\pi rh$, where h is the height of the perforated zone. Darcy's law (equation (2.1)) when neglecting the negative the minus sign gives;

$$Q = \frac{KA}{\mu}\frac{dp}{dr} = \frac{2\pi hK}{\mu} r \frac{dp}{dr} \tag{B.1}$$

Integrating over the cylinder shaped reservoir;

$$Q\int_{r_e}^{r_w}\frac{dr}{r} = \frac{2\pi hK}{\mu}\int_{p_e}^{p_w} dp \tag{B.2}$$

This gives Darcy's law for radial flow given in terms of the volumetric flow rate [15];

$$Q = \frac{2\pi hK}{\mu}\frac{p_w - p_e}{ln\left(\frac{r_w}{r_e}\right)} \tag{B.3}$$

B.2 Calculation of Polymer Mole Fraction

The polymer concentration used for the AMPS experiment and xanthan experiment was given as 1000ppm and 890ppm respectively. Calculation of polymer mole fractions may be calculated using equation;

$$X_i = \frac{n_i}{n_T}$$

Where X_i is mole fraction of component i in a mixture, and n_i and n_T is number of moles of component i and number of total moles present, respectively. The mole fraction is a

dimensionless quantity expressing the ratio of the number of m oles of one component to the number of moles for all components present. Further, the mole of a component may be expressed as the ratio of the mass, m, to the molecular weight, M_w, given by;

$$n = \frac{m}{M_w}$$

Recognizing that the ppm concentration unit may be written as (for AMPS concentration);

$$1000ppm = \frac{1000g\ (polymer)}{1000\ 000g\ (water)}$$

And assuming molecular weight of 10 000kg/mol, the number of moles for the AMPS polymer may be calculated as;

$$n_{AMPS} = \frac{1000g_{AMPS}}{10\ 000\ 000\ \ g/mol_{AMPS}} = 0.001moles$$

Further assuming a water viscosity of 1 centipoise and a molecular weight of 0.018kg/moles, as done for the work conducted in this thesis, the AMPS mole fraction can be calculated as;

$$X_{amps} = \frac{0.001moles_{AMPS}}{(55\ 508moles_{Water} + 0.001moles_{AMPS})} \approx 1.80 \cdot 10^{-8}$$

Giving the mole fraction of AMPS polymer in the polymer-water solution. Water moles in the above calculation was calculated in the same manner as the AMPS mole calculation above.

As total mole fraction sums to unity, the water mole fraction in the solution is simply calculated as;

$$X_{water} = 1 - X_{AMPS}$$

C. Simulation Scripts

C.1 Water Flooding Simulation Script

```
RESULTS SIMULATOR STARS 201401

** ============== INPUT/OUTPUT CONTROL ========================

TITLE1

'15ml/min Waterflooding'

INUNIT        LAB

OUTUNIT LAB

SHEAREFFEC SHV

WPRN          GRID TIME

OUTPRN        GRID PRES SW W X VISW

OUTPRN        WELL ALL

WPRN          ITER TIME

OUTPRN        ITER NEWTON

WSRF          WELL 1

WSRF          GRID TIME

**WSRF        SECTOR 1

OUTSRF GRID MASS ADSORP MOLE ADSORP PPM ADSPCMP KRO KRW KRW
MASDENW MOLDENW PRES RFW SHEARW

          SW VISCVELW VISW W X Y

OUTSRF WELL MOLE COMPONENT ALL

OUTSRF SPECIAL BLOCKVAR PRES 1,1,1

                BLOCKVAR PRES 3,1,1

              BLOCKVAR PRES 12,1,1
```

```
            BLOCKVAR PRES 17,1,1
            BLOCKVAR PRES 27,1,1
            BLOCKVAR PRES 37,1,1
            BLOCKVAR PRES 57,1,1
            BLOCKVAR PRES 77,1,1
               BLOCKVAR PRES 107,1,1
               BLOCKVAR PRES 147,1,1
               BLOCKVAR PRES 148,1,1
**$  Distance units: cm
**RESULTS XOFFSET          0.0000
**RESULTS YOFFSET          0.0000
**RESULTS ROTATION         0.0000  **$  (DEGREES)
**RESULTS AXES-DIRECTIONS 1.0 -1.0 1.0


** ========= RESERVOIR DESCRIPTION ============


GRID  RADIAL       148 1 1          RW 0.3                **Cylindrical grid
KDIR  DOWN
DI
IVAR 147*0.1 0.5
DJ
CON 360
DK
CON 3.08
```

DTOP

148*1

NULL

CON 1

POR

ALL 147*0.228 0.99

PERMI ALL

6*204 51*3150 90*2400 100000

PERMJ

EQUALSI

PERMK

EQUALSI

PINCHOUTARRAY CON 1

END-GRID

** ========== COMPONENT PROPERTIES ==========

MODEL 2 2 2 2

COMPNAME 'Water' 'Polymer'

CMM

0.018 8

PCRIT

0 0

TCRIT

0 0

PRSR 101

PSURF 101

MASSDEN

0.001 0.001

CP

0 0

AVISC

1 0

BVISC

0 0

VSMIXCOMP 'Polymer'

VSMIXENDP 0 1.80144e-006

VSMIXFUNC 0 0.1 0.2 0.3 0.4 0.5 0.6 0.7 0.8 0.9 1

** velocity viscosity

SHEARTAB

0.001 1

0.1 1

** ================= ROCK-FLUID PROPERTIES ==================

ROCKFLUID

RPT 1

SWT

0 0 1

0.1 0.1 0.9

0.2 0.2 0.8

0.3 0.3 0.7

0.4 0.4 0.6

0.5 0.5 0.5

0.6 0.6 0.4

0.7 0.7 0.3

0.8 0.8 0.2

0.9 0.9 0.1

1 1 0

**Polymer related keywords inhibited during Waterflooding

**ADSCOMP 'Polymer' WATER

**ADSPHBLK W

**ADSTABLE

** Mole Fraction Adsorbed moles per unit pore volume

** Mole Fraction Adsorbed moles per unit pore volume

** 0 0

** 4.508997705e-006 9.969376504e-008

**ADMAXT 9.96938e-008

**ADRT 2.49234e-009

**PORFT 1

**RRFT 1

** ============== INITIALIZATION =============

INITIAL

```
VERTICAL OFF

INITREGION 1

PRES  CON 101.1

TEMP CON 22

SW CON 1

MFRAC_WAT 'Water' CON          1


** ============  NUMERICAL CONTROL ==================


NUMERICAL

TFORM ZT

ISOTHERMAL

MAXSTEPS 50000

RUN


** ============  RECURRENT DATA  ====================

TIME 0

DTWELL 1e-4

DTMIN 1e-8

DTMAX 0.01


WELL 'Injector'

INJECTOR MOBWEIGHT EXPLICIT 'Injector'

INCOMP  WATER  1 0
```

```
TINJW  22.0
PINJW  101.1 **Pinjw = 5.89kPa
OPERATE  MAX  STW  15.0  CONT REPEAT
**          rad  geofac  wfrac  skin
GEOMETRY  K  0.3  0.2  1.0  0.0
PERF  GEO  'Injector'
** UBA     ff   Status  Connection
   1 1 1  1.0  OPEN    FLOW-FROM  'SURFACE'
WELL  'Producer1'
PRODUCER 'Producer1'
OPERATE  MIN  BHP  101.1  CONT REPEAT
**          rad  geofac  wfrac  skin
GEOMETRY  K  0.075  0.2  1.0  0.0
PERF  GEO  'Producer1'
** UBA       ff   Status  Connection
   148 1 1  1.0  OPEN    FLOW-TO  'SURFACE'
TIME 2
TIME 5
TIME 10
**WSRF        GRID 1
TIME 20
TIME 40
TIME 60
TIME 80
```

TIME 100

TIME 120

TIME 200

STOP

TIME 250

TIME 300

TIME 350

STOP

C.2 Polymer Flooding Simulation Script

RESULTS SIMULATOR STARS 201401

** ============== INPUT/OUTPUT CONTROL ========================

TITLE1

'20ml/min HPAM injection'

INUNIT LAB

OUTUNIT LAB

SHEAREFFEC SHV

WPRN GRID TIME

OUTPRN GRID PRES SW W X VISW

OUTPRN WELL ALL

WPRN ITER TIME

OUTPRN ITER NEWTON

WSRF WELL 1

WSRF GRID TIME

**WSRF SECTOR 1

OUTSRF GRID MASS ADSORP MOLE ADSORP PPM ADSPCMP KRO KRW KRW MASDENW MOLDENW PRES RFW SHEARWSW VISCVELW VISW W X Y

OUTSRF WELL MOLE COMPONENT ALL

```
OUTSRF SPECIAL   BLOCKVAR PRES 1,1,1
                 BLOCKVAR PRES 3,1,1
                 BLOCKVAR PRES 12,1,1
                 BLOCKVAR PRES 17,1,1
                 BLOCKVAR PRES 27,1,1
                 BLOCKVAR PRES 37,1,1
                 BLOCKVAR PRES 57,1,1
                 BLOCKVAR PRES 77,1,1
                 BLOCKVAR PRES 107,1,1
                 BLOCKVAR PRES 147,1,1
**$  Distance units: cm
**RESULTS XOFFSET 0.0000
**RESULTS YOFFSET 0.0000
**RESULTS ROTATION 0.0000  **$  (DEGREES)
**RESULTS AXES-DIRECTIONS 1.0 -1.0 1.0

** ========= RESERVOIR DESCRIPTION ==========
**Radial grid model
GRID  RADIAL 148 1 1 RW 0.3
KDIR  DOWN
DI
IVAR 147*0.1 0.3
DJ
CON 360
DK
CON 3.08
DTOP
148*1
```

```
**Properties assigned each grid block
NULL
CON 1
POR
ALL 147*0.228  0.99
PERMI
ALL 6*360 51*3150 90*2400 100000
PERMJ
EQUALSI
PERMK
EQUALSI
PINCHOUTARRAY CON 1
END-GRID
** ============= COMPONENT PROPERTIES ================
MODEL 2 2 2 2
COMPNAME 'WATER' 'POLYMER'
**Component molecular weights [kg/mol]
CMM
0.018 10
PCRIT
0 0
TCRIT
0 0
PRSR 101
PSURF 101
MASSDEN
0.001 0.001
CP
0 0
```

AVISC

1 9.466

BVISC

0 0

VSMIXCOMP 'POLYMER'

VSMIXENDP 0 1.8e-06

VSMIXFUNC 0 0.1 0.2 0.3 0.4 0.5 0.6 0.7 0.8 0.9 1

SHEARTAB

** [Darcy velocity (cm/min) Viscosity(cP)]

0.069 10.043

0.074 10.333

0.080 10.654

0.086 11.012

0.094 11.415

0.103 11.874

0.115 12.403

0.129 13.022

0.148 13.759

0.172 14.660

0.207 15.796

0.258 17.295

0.345 19.410

0.413 20.860

0.517 22.751

0.689 25.378

0.738 26.038

0.795 26.761

0.940 28.438

1.034 29.423

1.149 30.534

1.292 31.804

1.477 33.274

1.723 35.008

2.584 39.704

3.446 43.087

** =========ROCK-FLUID PROPERTIES ========

ROCKFLUID

RPT 1

SWT

**SW **krw **krow

0 0 1

0.1 0.1 0.9

0.2 0.2 0.8

0.3 0.3 0.7

0.4 0.4 0.6

0.5 0.5 0.5

0.6 0.6 0.4

0.7 0.7 0.3

0.8 0.8 0.2

0.9 0.9 0.1

1 1 0

** Polymer adsorption

ADSCOMP 'POLYMER' WATER

ADSPHBLK W

ADSTABLE

** Mole Fraction Adsorbed moles per unit pore volume

0 0

1.8e-06 9.8e-08

```
ADMAXT
9.8e-08
ADRT
9.8e-08
PORFT 1
RRFT 1
** ============== INITIALIZATION ================================
INITIAL
VERTICAL OFF
INITREGION 1
PRES
CON 101.1
TEMP
CON 22
SW
CON 1
MFRAC_WAT 'WATER' CON          1

** ============  NUMERICAL CONTROL ================================
NUMERICAL
TFORM ZT
ISOTHERMAL
MAXSTEPS 5000000
RUN
** ============  RECURRENT DATA  ================================
TIME 0
DTWELL 1.0e-4
DTMIN 1e-8
DTMAX 0.01
```

```
WELL 'Injector'
INJECTOR MOBWEIGHT EXPLICIT 'Injector'
INCOMP  WATER  0.9999982 1.8e-06
TINJW  22.0
PINJW  101.1
OPERATE  MAX  STW  20  CONT REPEAT
**          rad  geofac  wfrac  skin
GEOMETRY  K  0.3  0.2  1.0  0.0
PERF  GEO  'Injector'
** UBA ff  Status  Connection
   1 1 1  1.0  OPEN    FLOW-FROM  'SURFACE'
WELL  'Producer1'
PRODUCER 'Producer1'
OPERATE  MIN  BHP  101.1  CONT REPEAT
**          rad  geofac  wfrac  skin
GEOMETRY  K  0.075  0.2  1.0  0.0
PERF  GEO  'Producer1'
** UBA       ff   Status  Connection
   148 1 1  1.0  OPEN    FLOW-TO  'SURFACE'
TIME 2
TIME 5
TIME 10
**WSRF        GRID 1
TIME 20
TIME 40
TIME 60
TIME 80
TIME 100
TIME 120
```

TIME 200

STOP